Continuous models for multi-phase architectured/meta materials : homogenization for effective properties and damage evolution in three-dimensional lattices embedded in a softer matrix

Mario Spagnuolo

▶ **To cite this version:**

Mario Spagnuolo. Continuous models for multi-phase architectured/meta materials : homogenization for effective properties and damage evolution in three-dimensional lattices embedded in a softer matrix. Mechanics of materials [physics.class-ph]. Université Paris-Nord - Paris XIII, 2019. English. NNT : 2019PA131066 . tel-03357652

HAL Id: tel-03357652
https://theses.hal.science/tel-03357652

Submitted on 28 Sep 2021

HAL is a multi-disciplinary open access archive for the deposit and dissemination of scientific research documents, whether they are published or not. The documents may come from teaching and research institutions in France or abroad, or from public or private research centers.

L'archive ouverte pluridisciplinaire **HAL**, est destinée au dépôt et à la diffusion de documents scientifiques de niveau recherche, publiés ou non, émanant des établissements d'enseignement et de recherche français ou étrangers, des laboratoires publics ou privés.

UIVERSITE PARIS 13 SORBONNE PARIS CITE

N° attribué par la bibliothèque

|_|_|_|_|_|_|_|_|_|_|_|_|_|

THESE

Spécialité: MECANIQUE DES MATERIAUX

Préparée au **Laboratoire des Sciences des Procédés et des Matériaux**

dans le cadre de **l'Ecole Doctorale Galilée**

par

Mario SPAGNUOLO

TITRE

Modèles continus pour metamateriaux multi-phasés: homogénéisation pour les propriétés effectives et evolution de l'endommagement dans des reseaux tridimensionels inclus dans une matrice souple

Continuous models for multi-phase architectured/meta materials: homogenization for effective properties and damage evolution in three-dimensional lattices embedded in a softer matrix

Version provisoire

Soutenance prevue 10 Septembre 2019

Directeur de these: Patrick Franciosi, LSPM, UP 13 Villetaneuse

Codirecteur de these: Francesco dell'Isola, Università di Roma "La Sapienza"

Mario Spagnuolo has received funding from the European Union's Horizon 2020 research and innovation programme under the Marie Skłodowska-Curie grant agreement No 665850.

Continuous models for multi-phase architectured/meta materials: homogenization for effective properties and damage evolution in three-dimensional lattices embedded in a softer matrix

In this thesis, we present the result of the contact between two domains which in origin are very distant: the synthesis of new theory-driven conceived materials, the so-called metamaterials, and an homogenization framework based on some particular mathematical objects called Green operators, fruitfully used for describing the effective properties of composite materials. So, the main idea driving this thesis work is to design and study (and, possibly, to produce and measure) a mechanical system which we could call composite metamaterial. It should have both the enhanced properties of composite materials and of the smart architectures characteristic of metamaterials.

The idea above described is obviously of not simple actuation and it obliges to face with very hard mathematical and technical problems. In this thesis work, we try to explain the first tentative to reach this very ambitious project.

The first chapter of this thesis is devoted to the description of a particular metamaterial we have chosen as a reference for developing the composite. It is called the pantographic metamaterial and we are interested in its deformation enhanced properties, as, for example, large deformation ranges and late damage onset. We want to underline here that, from a mathematical point of view, the pantographic metamaterial is described by means of a generalized theory. Specifically, the presence of the microstructure makes it necessary to adopt a second gradient model for taking into account all its exotic effects.

Experimental tests for 3D pantographic structures are presented in the second Chapter. A comparison with the evaluations obtained by means of the model developed in the previous chapter is performed and the limits of this model are experimentally evaluated. The above mentioned tests are finally analysed by using the Digital Image Correlation techniques, which allow to measure in a very precise way the displacement and the deformation fields.

In the third and fourth chapters, the Green tensors homogenization framework is presented and used for modelling the pantographic-inspired material. This homogenization framework has some advantages: (i) it is very simple to be applied (in contrast with the Gamma convergence techniques needed to formally derived the homogenized description of the pantographic metamaterial); (ii) the result of this homogenization procedure consists in the direct access to the effective properties of the material; (iii) it is linear and, for this reason, the algorithmic code written to obtain the effective properties is very fast compared to the FEM based codes for numerically simulating the pantographic metamaterial.

In the last Chapter, the damage modelling in pantographic structures is approached. The discussion about damage presented in this thesis is related to the deformation features of the interconnecting pivots: this allows us to carry on some comparisons with the pantographic-inspired material, where, as it is shown in Chapter 4, the role of the pivots is played by the matrix phase. On the basis of simple criteria, the damage forecasting is made possible if the pivots have specific geometrical features.

MOTS-CLES:

Pantographic structures, Homogenization Methods, Green Operators, Fiber reinforced matrix, Effective properties, Damage analysis, Second gradient models, Digital Image Correlation

Modèles continus pour metamateriaux multi-phasés : homogénéisation pour les propriétés effectives et évolution de l'endommagement dans des réseaux tridimensionels inclus dans une matrice souple

Dans cette thèse, nous présentons le résultat du rencontre de deux domaines d'origine très éloignés : la synthèse de nouveaux matériaux de conception théorique, appelés métamatériaux, et un cadre d'homogénéisation basé sur des objets mathématiques particuliers appelés opérateurs de Green, utilisés pour décrire utilement les propriétés effectives des matériaux composites. L'idée principale de cette thèse est donc de concevoir et d'étudier (et, éventuellement, de produire et de mesurer) un système mécanique que l'on pourrait appeler métamatériau composite. Il doit posséder à la fois les propriétés renforcées des matériaux composites et les architectures sophistiquées caractéristiques des métamatériaux.

L'idée décrite ci-dessus n'est évidemment pas de simple actuation et elle oblige à se confronter avec des problèmes mathématiques et techniques très durs. Dans ce travail de thèse, nous essayons d'expliquer la première tentative pour atteindre ce projet très ambitieux.

Le premier chapitre de cette thèse est consacré à la description d'un métamatériau particulier que nous avons choisi comme référence pour développer le composite. C'est ce qu'on appelle le métamatériau pantographique et nous nous intéressons à ses propriétés de déformation renforcées, comme, par exemple, les grandes déformations et les endommagements différés. Nous voulons souligner ici que, d'un point de vue mathématique, le métamatériau pantographique est décrit par une théorie généralisée. Concrètement, la présence de la microstructure rend nécessaire l'adoption d'un modèle de second gradient pour prendre en compte tous ses effets exotiques.

Des essais expérimentaux pour les structures pantographiques 3D sont présentés dans le deuxième chapitre. Une comparaison avec les évaluations obtenues par le modèle développé dans le chapitre précédent est effectuée et les limites de ce modèle sont évaluées expérimentalement. Les tests mentionnés ci-dessus sont finalement analysés en utilisant les techniques de corrélation d'images digitales, qui permettent de mesurer de manière très précise le déplacement et les champs de déformation.

Dans les troisième et quatrième chapitres, le cadre d'homogénéisation des tenseurs de Green est présenté et utilisé pour modéliser le matériau d'inspiration pantographique. Ce cadre d'homogénéisation présente certains avantages : (ii) le résultat de cette procédure d'homogénéisation consiste en l'accès direct aux propriétés effectives du matériau ; (iii) il est linéaire et, pour cette raison, le code algorithmique écrit pour obtenir les propriétés effectives est très rapide comparé aux codes basés sur FEM pour la simulation numérique du métamatériau pantographique.

Dans le dernier chapitre, la modélisation des endommagements dans les structures pantographiques est approchée. La discussion sur les endommagements présentée dans cette thèse est liée aux caractéristiques de déformation des pivots d'interconnexion : ceci nous permet d'effectuer certaines comparaisons avec le matériau d'inspiration pantographique, où, comme il est montré au chapitre 4, le rôle des pivots est joué par la phase de la matrice. Sur la base de critères simples, la prévision des endommagements est rendue possible si les pivots ont des caractéristiques géométriques spécifiques.

Contents

Introduction

In this thesis, we present the result of the contact between two domains which in origin are very distant: the synthesis of new theory-driven conceived materials, the so-called metamaterials, and an homogenisation framework based on some particular mathematical objects called Green operators, fruitfully used for describing the effective properties of composite materials. So, the main idea driving this thesis work is to design and study (and, possibly, to produce and measure) a mechanical system which we could call composite metamaterial. It should have both the enhanced properties of composite materials and of the smart architectures characteristic of metamaterials.

The idea above described is obviously of not simple actuation and it obliges to face with very hard mathematical and technical problems. In this thesis work, we try to explain the first tentative to reach this very ambitious project. Clearly, we are far from the complete resolution of the problem, but an ideal scheme has been traced and many preliminary results have been obtained.

The Pantographic Metamaterial

As it is underlined in [1], mechanical metamaterials are a class of materials with exotic mechanical properties due to their architecture (or microstructure, as it is normally called in this field with no reference to the micro-scale) and they can be divided in many different sub-classes by means of their specific features. In this thesis we do not want to consider a general metamaterial, but we are interested in just one of them. It is called the pantographic metamaterial [2, 3] and we are interested in its deformation enhanced properties, as, for example, large deformation ranges and late damage onset. The pantographic metamaterial, or pantographic structure in its simplified version, can be regarded as a double array of parallel fibers, each array lying on a different plane. These two plains are parallel and the directions of the fibers are orthogonal in the reference configuration. The two plains are connected by means of some cylinders, generally called pivots in the relative literature, positioned in the

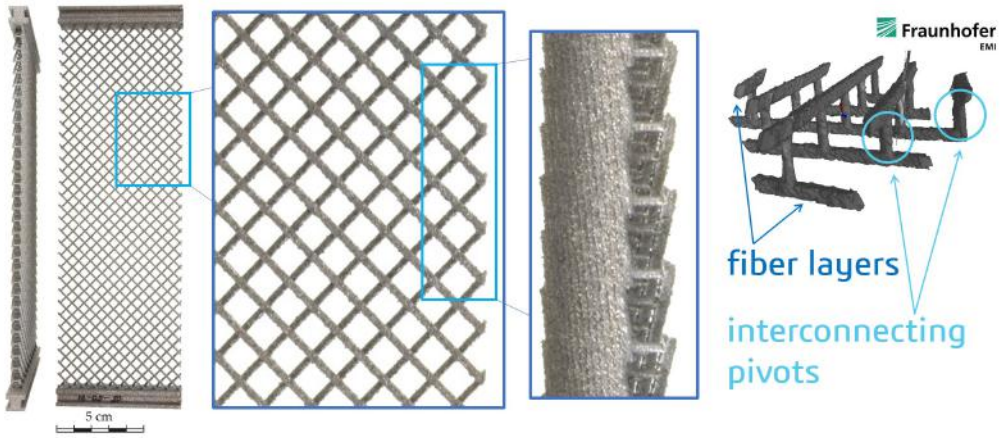

Figure 1: Example of a 3D printed (aluminum) pantographic structure: the two fiber layers and the interconnecting pivots are shown.

crossing points of the two arrays of fibers. An example of pantographic structure is shown in Fig. 1.

The first Chapter of this thesis is devoted to the description of this particular metamaterial. We want to underline here that, from a mathematical point of view, the pantographic metamaterial is described by means of a generalised theory. Specifically, the presence of the microstructure makes it necessary to adopt a second gradient model for taking into account all its exotic effects. However, it has to be considered that any model has its applicability limits and for different scales different models are needed. This last concept is well explained in Fig. 2.

An important consideration must be done in order to connect the domain in which the pantographic metamaterial has been introduced and developed and the domain where we aim to describe it for designing a pantographic composite metamaterial. The consideration is the following: the deformation in the pantographic metamaterial is extremely non-homogeneous and different zones with different deformation behaviours can be localised (see Fig. 3). In this thesis we approach the description of the pantographic composite metamaterial, or pantographic-inspired material, only for the homogeneous zones of the structure, where no bending of the fibers is observed and no second gradient contributions are needed for mathematical modelling it (the interface between the different zones is not treated, yet).

Experimental tests for 3D pantographic structures are presented in the second Chapter. A comparison with the evaluations obtained by means of the model developed in the previous chapters is performed and the limits of this model are ex-

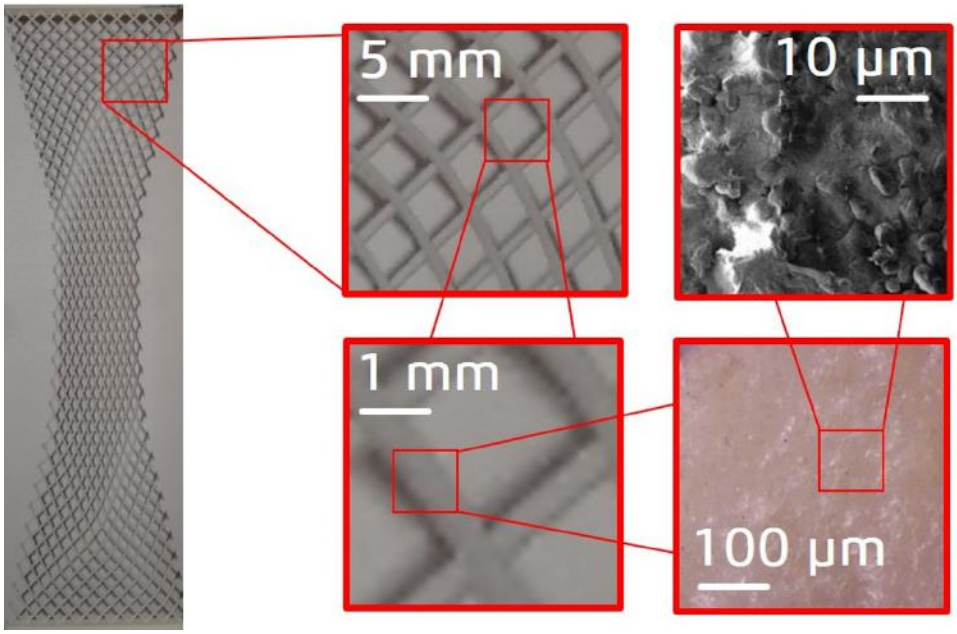

Figure 2: Multi-scale nature of pantographic metamaterials. Depending on the chosen scale, a different model (second gradient homogenised model, Euler-Bernoulli beam theory, Cauchy Continuum Mechanics, etc...) must be adopted.

perimentally evaluated. The above mentioned tests are finally analysed by using the Digital Image Correlation techniques, which allow to measure in a very precise way the displacement and the deformation fields. These last results have been obtained in the framework of a scientific collaboration with the LMT laboratory of the University of Paris Saclay.

Green tensors homogenisation framework

In the third and fourth chapters of this thesis, the Green tensors homogenisation framework is presented and used for modelling the pantographic-inspired material. This homogenisation framework has some advantages: (i) it is very simple to be applied (in contrast with the Gamma convergence techniques needed to formally derived the homogenised description of the pantographic metamaterial); (ii) the result of this homogenisation procedure consists in the direct access to the effective properties of the material; (iii) it is linear and, for this reason, the algorithmic code written to obtain the effective properties is very fast compared to the FEM based codes for numerically simulating the pantographic metamaterial.

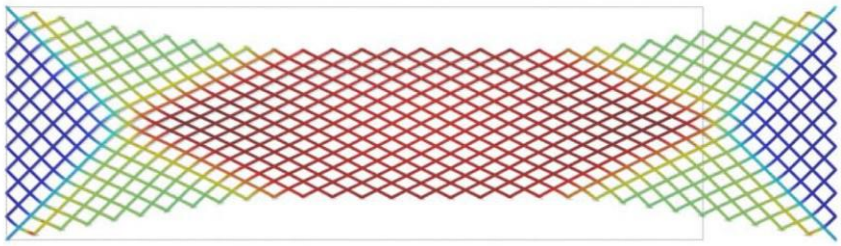

Figure 3: The three different deformation zones in the pantographic structure during an extension test: no deformation (blue), shear at macro level and relative rotation at micro level (red) and shear with a different angle (green). The bending of fibers is concentrated in the interface zones.

The fact that we compare a strongly non-linear system, as the pantographic metamaterial (large displacement and large rotations), with a linear system as the one described by means of the Green tensors must not lead to a misunderstanding. We adopt a linearised description of the pantographic-inspired material, where the internal geometry of the network is changed ad hoc step-by-step and linear deformations are considered for any step. The macroscopic response consists in a solution which is linear in increments, but globally non-linear.

In Chapter 3, we introduce the homogenisation framework and the Inverse Radon Transform (IRT), a method that allows to solve the integrals needed for the calculus of the Green tensors components in the Fourier space. This simplifies extremely the procedure and introduces a geometrical interpretation for the calculus of the Green tensors. As a first example of application we present the estimate of effective properties of a planar alignment and of a 1D bundle of infinite cylinders embedded in a softer matrix. Specially the first case is of primary importance for our work. It is, in fact, used in Chapter 4 to derive the Green tensor of the pantographic-inspired material.

In Chapter 4, an explicit expression of the Green tensor for the pantographic-inspired material is found and some applications are exhibited. One must remember that only the central homogeneous zone of the pantographic structure has an analogous in the described pantographic-inspired material (see Fig. 4). For this reason, the results obtained in the framework of the Green tensors homogenisation procedure are compared to numerical simulations obtained by means of a FEM code, originally developed to study wide-knit pantographic structures as composed by Euler-Bernoulli non-linear beams, where the bending of fibers has been forbidden. The details of

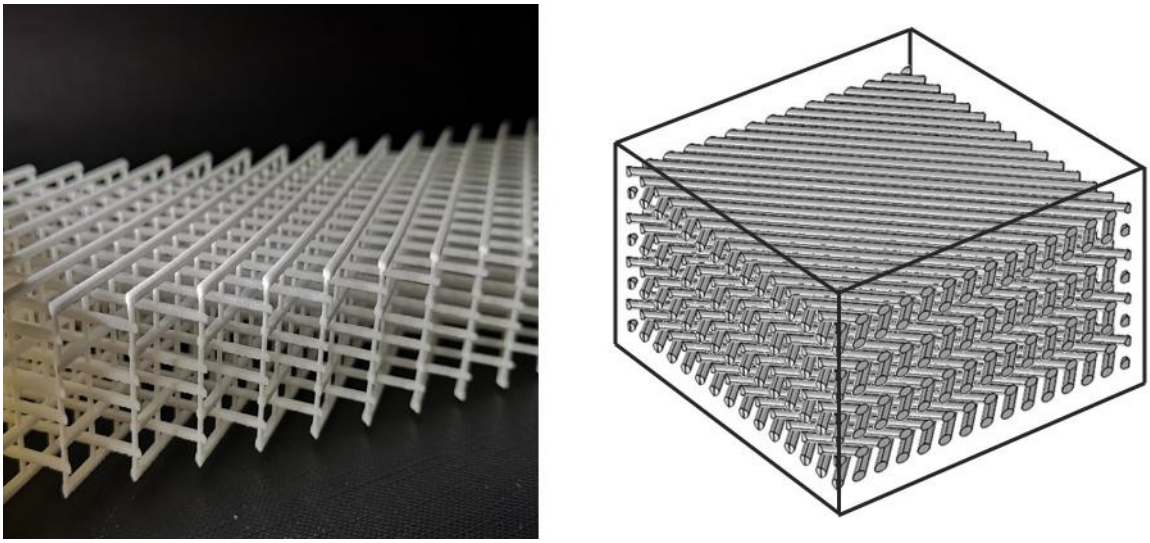

Figure 4: Particular of a 3D pantographic sample (left) which inspired the composite material treated by means of Green operators-based homogenization procedure (right).

this code can be found in [4] and are discussed in the first Chapter of this thesis.

Phenomenological and qualitative analysis of damage

In the last Chapter, a phenomenological analysis of damage is presented. The discussion about damage, on the basis of the Refs. [5, 6], is related to the deformation features of the interconnecting pivots: this allows us to carry on some comparisons with the pantographic-inspired material, where, as it will be shown in Chapter 4, the role of the pivots is played by the matrix phase. On the basis of simple criteria, the damage forecasting is made possible if the pivots have specific geometrical features.

Chapter 1

The Pantographic Metamaterial: an example of theory-driven design

The discussion presented in this Chapter is based on the Chapter "The Pantographic Metamaterial: a (not so) particular case" of the book [7].

1.1 Introduction

This Chapter is devoted to the discussion of a particular class of metamaterial, termed as the Pantographic Metamaterial. The research work on this type of metamaterial began in 2003. However recently, owing to the very rapid development of 3D printing technologies, this work has been enriched through experimental evidences. The current chapter will focus upon the theoretical developments alone since a part of the experiemental aspects, that include characterization and evaluation of pantographic metamaterials, deserves its own dedicated discussion in a seperate chapter.

Materials on demand In the last few years, the field of so-called metamaterials has been vigorously explored and exploited in many different ways. In the literature, metamaterials are, generally, treated as material systems endowed with particular microstructures, and, typically, the global properties of these material systems are analyzed using methods devised within the framework of classical or generalized mechanical theories. In contrast, it is more fascinating to regard metamaterials as material systems "on demand," which are expected to fulfill certain functional requirements. In this sense, we must first concieve the theoretical governing equations that describe the requirements and, subsequently, search for material system whose physics (or mechanical properties if the interest so demands) is specified, in some

way, perhaps not exactly, by the concieved equations. Clearly, this point of view opens the horizon to innumerable possibilities of applications. Moreover, the current capabilities to produce in a relatively simple way the designed microstructures makes possible to establish experimental foundations for certain mathematical theories which have been an object of different controversies up to recent times. Thus, the general problem to be solved for designing a new metamaterial is the following: given a desired behaviour, to first find the evolution equations that mathematically describes such a behavior, and to then specify the material (micro)structure governed by the chosen equations.

With the advancements in manufacturing techniques (e.g., 3D-printing technology and, more generally, of rapid prototyping techniques), the small scale production of materials with complex geometries has become more affordable than ever [8–11]. The exploitation of these new technologies has impelled, in the last few years, the development of material systems with many different sub-structures. Consequently, there has been an acceleration in the determination and study of new microstructures that, at a well-specified macroscopic scale, exhibit behaviors that are best described by non-standard mathematical models like generalized continuum theories. For instance, the motivations that led to the consideration of the pantographic microstructures, i.e. to be well-described at certain macroscopic spatial scale by second gradient continuum theories, have been extensively discussed in the literature [12–14]. As a rather significant consequence, these considerations have supported the development of a flourishing litrature on the history of such higher gradient and generalized continuum theories, some of which have shown that [15, 16] that many "generalized" theories were formulated before or together with the so-called "classical" ones and then lost, suggesting [17, 18] that some generalized theories were already known at least two centuries ago.

The Pantographic Metamaterial The mathematically-driven design of the pantographic metamaterial has clearly established that the pioneering efforts to give practical foundations to generalized continuum theories has shown the pathway to manufacture constructs (microstructures and mechanisms) using existing materials and emerging technology of additive manufacturing that have non-trivial, appealing and tailorable mechanical properties. A pantographic metamaterial (or fabric) concieved through this approach consists of a planar grid obtained by the superposition of two families of fibers (see Fig. 1.1) that are connected by means of small cylinders, called pivots. In the desin of these pantographic structures, the aim was to find a material system exhibiting mechanical properties described by a second gradient theory. This theory, which has been studied by Germain [19], Toupin [20], Mindlin [21] and

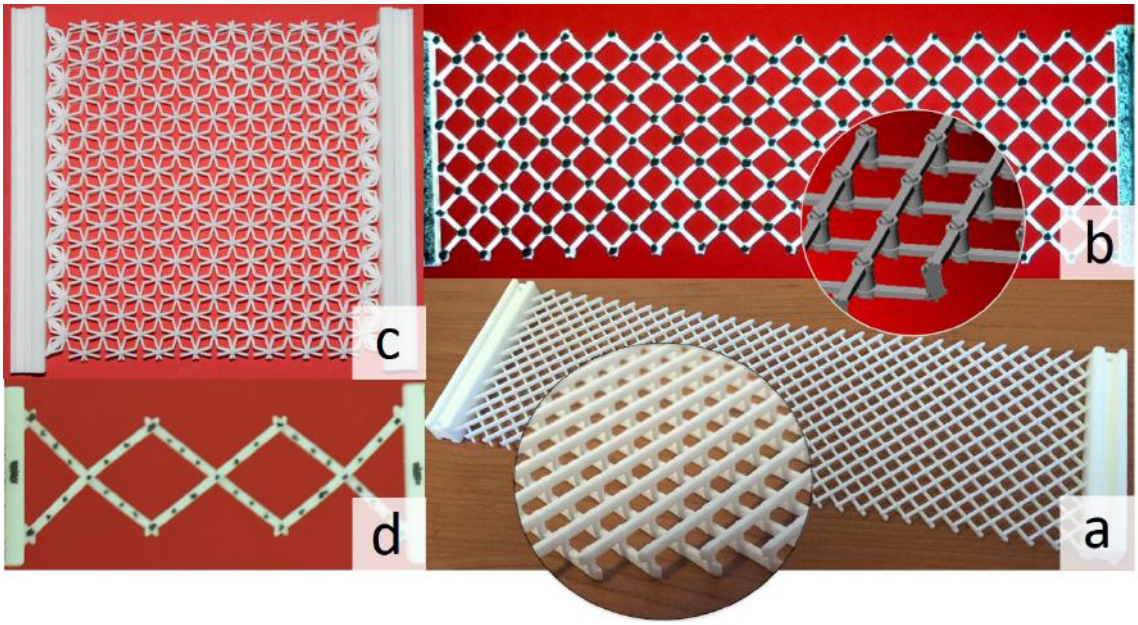

Figure 1.1: Example of polyamide 3D printed pantographic structures: (a) a "standard" pantographic fabric; (b) a pantographic structure with perfectly compliant pivots; (c) a bi-pantographic plate; (d) a "millimetric" pantographic structure.

Hellinger [22,23], is based upon the consideration that the strain energy depends not only on the displacement gradient but also on its second gradient. In what follows, we will first introduce the result of the theory-driven design since this is the main concern of this chapter.

At the first stage of the research effort, the problem was approached from a theoretical point of view. The mathematical models, which were initially introduced, belong to the class of generalized continua: as we have mentioned before. The introduced independent kinematic fields include not only the displacement field but, eventually, also microstretch and microrotation fields. In the second stage it was necessary to develop numerical integration schemes and the corresponding codes for solving, in physically relevant cases, the equations chosen to describe the desired behavior. Finally, it was necessary to physically realize the microstructures. We can schematize the whole research process in the following way:

i. design: modelling novel and exotic architectured metamaterials based on a mathematical understanding of the related mechanical problems and on suitably designed numerical simulations;

ii. production: building the designed prototypes by using 3D printing technology;

iii. testing: testing with experimental apparatuses the so-built prototypes;

iv. model calibration: producing a careful model fitting of the experimental data by means of the systematic use of numerical simulations;

v. validation: elaborating the obtained data with image correlation techniques for comparing the proposed models with experimental evidence.

The Pantographic Paradigm: an example of theory driven design We want now to point out a further peculiarity: the case of pantographic metamaterials constitutes a Scientific Paradigm, which can be translaed to very different fields. Every scientific theory can be produced on the basis of two different starting points: conjectures, if there are not initial experimental observations, or hypothesis, if everything begins by an effort to interpret some experimental phenomena. The subsequent development of a scientific theory is then always based on the validation of the proposed model by experiments. In this sense, the same word *theory* derives its meaning by the Greek one θεωρός (*observer*, more precisely a θεωρός was an envoy sent to consult the oracle: similarly, the word theory catches the sense of looking for obtaining some information), which is a word composed by θέα (*view*, sight) and the verb ὁράω (*to see*): we have to look at experimental observations to validate a scientific theory. From this point of view, it is interesting to consider the definition of theory as reported by Russo in his book [15], because it is possible there to find the same logic employed in the development of the theory of pantographic structures. The rationale is a very old one: it is the basis of the Science. In his book, Russo states that (literal citation):

> A theory has to be such that:
>
> 1. Its statements are not about concrete objects, but about specific theoretical entities. [...]
> 2. The theory has a rigorously deductive structure; it consists of a few fundamental statements (called axioms, postulates, or principles) about its own theoretical entities, and it gives a unified and universally accepted means for deducing from them an infinite number of consequences. [...]
> 3. Applications to the real world are based on correspondence rules between the entities of the theory and concrete objects. [...]

> Any theory with these three characteristics will be called a *scientific* theory. The same term will be used for some other theories, which we may call "of a higher order". They differ from the theories we have been considering so far in that they possess no correspondence rules for application to the real world - they are applicable only to other scientific theories.

For a very long time, second gradient materials have been treated as the objects of a theory whose set of described phenomena was empty, as experimental evidences able to well underline the necessity of recurring to a theory different from classical Cauchy elasticity were missing. Pantographic fabrics provide not only an example of real materials whose description needs the introduction of a second gradient theory, but also an easy-to-handle example of a powerful methodological approach, which can be used to analyse more complex and exotic structures.

1.2 Modeling Pantographic Structures: a *rèsumè* of obtained results

Pantographic structures have been studied from different points of view during the last decade. Here we give an overview on the models developed to describe the different aspects of this particular metamaterial. Specifically, the fundamental nucleus of the Chapter is constituted by the presentation of the three main 2D models: the basic Hencky-type discrete model; an intermediate "meso-model" in which the pantographic structure is considered as composed by Euler-Bernoulli beams; a continuum second gradient model, which is derived by an euristic homogenization of the discrete one. This last model representsone of the main reasons for the development of the research on pantographic structures. In fact, the theoretical interest in pantographic structures is due to the fact that, for a correct description of their peculiar phenomenology, it is necessary to use higher gradient continuum theories [24, 25] with the relative problem of homogenization [26] and of different possibilities of numerical integration [27, 28]. The presentation of the three 2D models is anticipated by an overview on some existing works which inspired the further formulation. Finally, we give some details on two elastic surface models representing a generalization of the 2D model, formulated in order to take into account the possibility that the structures undergo some out-of-plane deformations (*e.g.* buckling or wrinkling modes).

1.2.1 Pantographic (micro-)structures: the original path

The very first theorisation of a pantographic structure as micro-model associated to a macroscopic second gradient continuum model can be found in [13]. The fundamental idea was the following: to find the micro-model leading to, in the sense of some homogenization procedure, the simplest second gradient continuum model. The described development can be classified as a multiscale procedure. The history of Mechanics offers many examples of multiscale procedures, developed principally to set the relations between macro-models and micro-models. Among the first examples, as reported by Benvenuto in his book about the history of Structural Mechanics [29], are due to Maxwell and Saint-Venant [30].

In the field of multiscale procedures, a very efficient approach consists in the *asymptotic identification*. Once the micro and macro models have been postulated *a priori*, a kinematic correspondence is found between them and, subsequently, the equality of the power expended in the corresponding (micro- and macro-) motions is enforced. Through this approach it is possible to evaluate the parameters of constitutive equations of the macro-model in terms of the ones of the basic cells which compose the micro-model. Before proceeding with the description of the model employed in [13], we want to remark a peculiar fundamental aspect of this approach. In this approach, we first postulate the macro-model as a second gradient continuum, and only after that we look for a possible micro-model which produces via homogenization the macro-model. This theory-driven approach is, in our opinion, very powerful: we do not look at random microstructures hoping to find one which is good for our purposes, rather having in mind the theory we want to obtain, build the needed microstructure to conform to the theoretical predictions.

At the time the pantographic structures were proposed as metmaterials, second gradient models were already present in the literature. As we already remarked in the chapter about mechanical metamaterials, we can refer to the *elastica* studied by Euler, Bernoulli and Navier as the very first example of second gradient model: so, it is necessary to go (at least) back to the beginning of the eighteenth century to find the roots of second gradient theories. The model proposed by Euler is a 1D model. It was after almost one century that the first (incomplete) second gradient 2D and 3D model attributed to the Cosserat brothers [31] were proposed, although it is notable that the origins of 3D higher gradient - and even peridynamic - models can be traced back at least to Piola [32]. We call a material an *incomplete second gradient material* if its deformation energy depends only on $\nabla\mathbf{u}$ and $\nabla\omega(\mathbf{u})$, where $\omega(\mathbf{u})$ is the skew-symmetric part of the gradient $\nabla\mathbf{u}$ of the displacement, $\omega(\mathbf{u})= \nabla\mathbf{u}-\varepsilon(\mathbf{u})$ with $\varepsilon(\mathbf{u})$ the symmetric part of $\nabla\mathbf{u}$. It is possible to encounter complete 2D and 3D second gradient models in the description of capillarity or also in the theory of damage and

plasticity (because of the well-posedness of mathematical problems related to second gradient models).

The simplest second gradient continuum model is the 1D planar beam studied by Casal in [33, 34] and quoted by Germain in [19]. We can write its (quadratic) deformation energy as

$$\mathcal{E}(u,v) = \frac{\alpha}{2}\int_0^L \left((u'')^2 - 2\beta u''v'' + (v'')^2\right) dx \tag{1.1}$$

where u and v are, respectively, the axial and transversal components of the displacement and α and β some parameters with $\alpha > 0$ and $|\beta| < 1$. The usual energetic term due to elongation, proportional to the square of the first derivative of the axial displacement $(u')^2$, is not present in this formulation. From a phenomenological point of view this means that we have a material with a very particular behaviour, that is, it can be stretched without expending any energy. This is one of the most remarkable ways to characterize the pantographic microstructure. Indeed, during the research involved in the development of pantographic fabrics, the objective was to find a microstructure which could be stretched at zero energy (a so-called *floppy mode*).

As a generalization of the simple example proposed by Casal, it can be considered a material with the following elastic energy

$$\mathcal{E}(u) = \int_\Omega A\nabla\nabla u \cdot \nabla\nabla u \tag{1.2}$$

which is a pure second gradient energy, i.e. it is not involving at all the first gradient of the displacement field. This material is in general subject to a volumic force f and to a generalized boundary force (traction, double forces...) F. We remark that, indeed, when considering a similar material, the mechanical interactions with external world which are involved are not only traction forces but also generalized ones (like, for example, double forces). If we set $\sigma = 2A\nabla\nabla u$ for semplicity (σ is a third order tensor) then we can write the variational formulation as

$$\forall v,\ \int_\Omega \sigma \cdot \nabla\nabla v - \int_\Omega f \cdot v - \int_{\partial\Omega} F \cdot v = 0 \tag{1.3}$$

Through successive integrations by parts we get the boundary conditions in second gradient theories

$$div\left(div(\sigma)\right) - f = 0 \quad \text{on } \Omega \tag{1.4}$$

$$-div^s(\sigma \cdot n)_{/\!/} - div(\sigma)\cdot n = F \quad \text{on } \partial\Omega \tag{1.5}$$

$$(\sigma \cdot n)\cdot n = 0 \quad \text{on } \partial\Omega \tag{1.6}$$

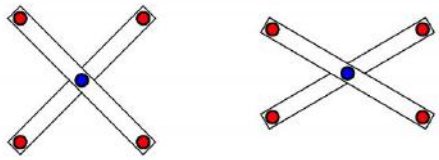

Figure 1.2: Basic module of a pantographic structure and its stretched configuration.

These boundary conditions are not interpretable on the basis of the standard Cauchy Continuum Mechanics, and clearly new mechanical interactions arise in higher order theories (we refer to [25] for more details).

The pantographic structure, see its basic module in Fig. 1.2, has been first introduced in the field of homogenized generalized media in [13, 35].

For obtaining the corresponding homogenised macro-model it is necessary to consider a structure composed by n pantographic modules and to study its behaviour when n tends to infinity.

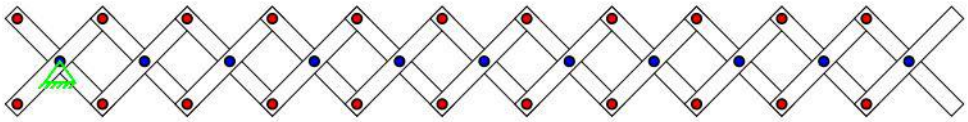

Figure 1.3: Pantographic microstructure of a 1D planar beam.

Some formal asymptotic expansion procedures, are systematically used in [13,35] for determining the effective properties of periodic structures consisting of welded linear elastic bars. Remarkably, for the case when the bending and torsion stiffnesses of isotropic homogeneous elastic bars are lower than the extensional one, interesting macro-models are obtained. In finding macro-models for micro-architectured metamaterials there is usually a complex estimate that needs to be established, that is, is the energy associated to second gradient of displacements negligible with respect to first gradient energy? For a long time it was believed that second gradient emergies were *always* negligible [18]. This belief was proven to be ungrounded at the dawn of modern continuum mechanics by Gabrio Piola [32,36]. However the results by Piola have been ignored for a long time in the orthodox Cauchy-Truesdell school.

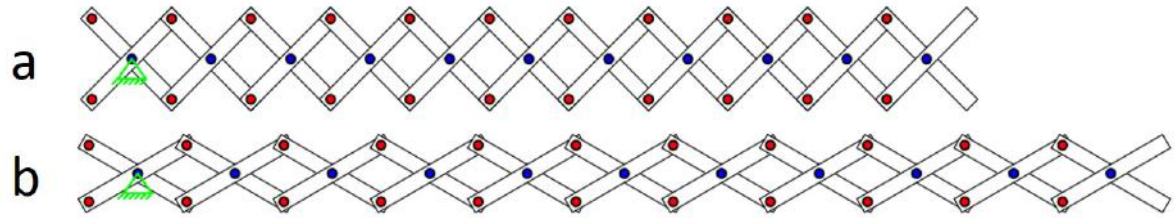

Figure 1.4: Reference configuration (a) and deformed configuration (b) of a pantographic beam. The deformed configuration (b) represents a so-called *floppy mode*.

In order to make clear that synthesizing second gradient metamaterials with non-negligible second gradient energy is not only possible, but can be addressed mathematicly, it has been proven that [13, 37]

i. pantographic micro-structures allow for the synthesis of Casal-type beams (see deformation energy in Eq. (1.1));

ii. using two families of pantographic substructures it is possible to synthesize second gradient plates: *i.e* plates whose deformation energy depends on second gradients of in-plane displacements[1];

iii. in presence of pefect pivots the macro deformation energy of short beam pantographic structures does not include *at all* first gradient terms and that in pantographic fabrics one can observe so called "floppy-modes": *i.e.* homogeneous local deformations corresponding to vanishing deformation energy (see alos the remark below);

iv. the mathematical treatment of second gradient linearized elastic continua (synthesized as described in this Chapter) requires the introduction of anisotropic Sobolev spaces [**?**, 38].

Remark *In so called long-fibers pantographic metamaterials (see Fig. 1.4) there is only a* 1*-parameter family of floppy modes while in short-fibers pantographic metamaterials (see Fig. 1.5) there are* ∞^3 *floppy modes.*

We underline here that we did not find the pantographic micro-structures via a

[1]In classical plate theory the second gradients of transverse displacements only appear in the deformation energy.

data-driven procedure, or some trial and error. Instead, being guided by classical mechanics, we built some mechansims whose degrees of freedom would produce "floppy modes" at micro-level in the designed and desired metamaterials. Adding some extra contraints (*i.e.* considering the boundary conditions needed for second gradient continua, see [13, 25, 37], one "blocks" macro floppy modes but leaves them active at local (micro) level. We therefore obtain theory-driven synthesis of second gradient materials.

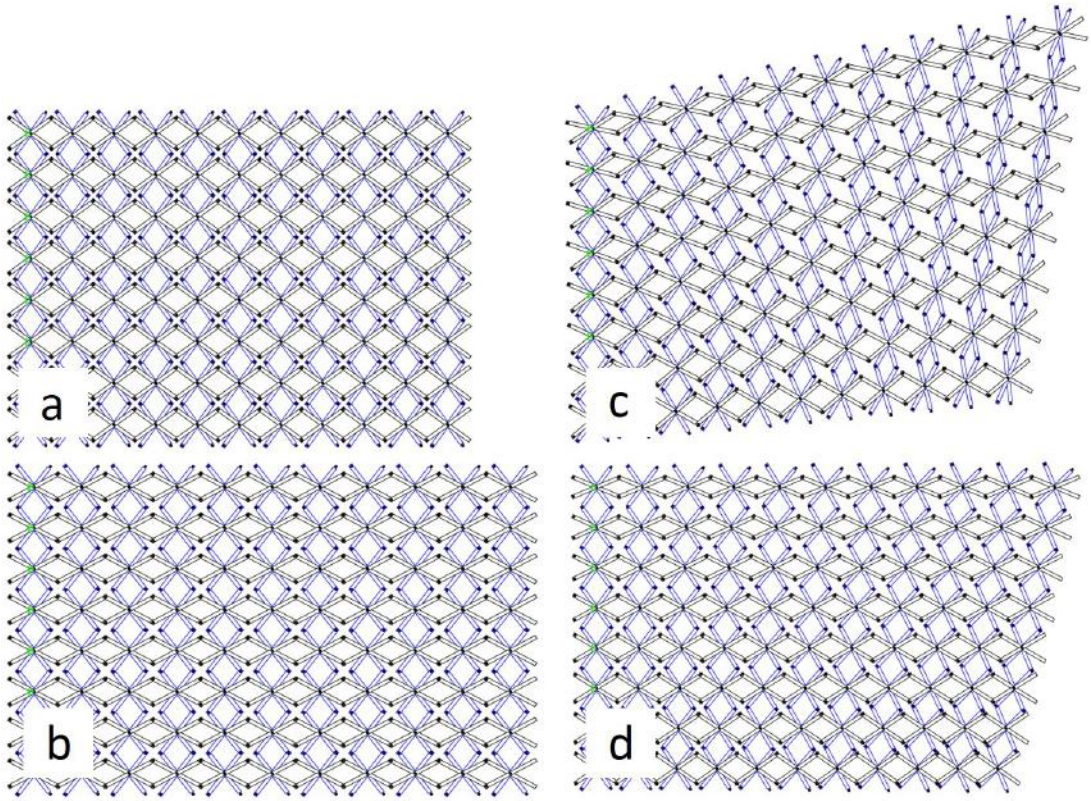

Figure 1.5: Reference configuration (a) and deformed configurations (b) of a pantographic 2D structure. The deformed configurations (b) represent some of the *floppy modes*.

As a second example of synthesis of higher gradient materials, in [13] it is shown how, by considering a modified (Warren-type) pantographic structure as micro-model, it is possible to obtain a third gradient planar beam model (Fig. 1.6) as homogenized macro-model. An interesting difference between the two models is

that the pantographic beam does not store any energy when undergoing uniform extension, while the Warren-type pantographic beam undergoes a floppy-mode when undergoing uniform flexure.

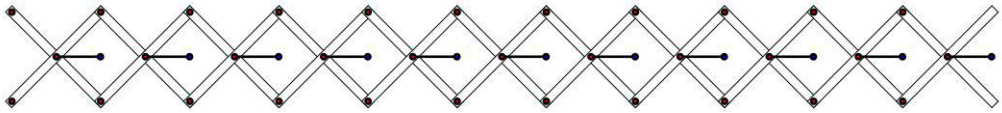

Figure 1.6: Warren-type pantographic microstructure, producing as homogenized model a third gradient planar beam model.

1.2.2 Pipkin's higher gradient plate modeling systems with inextensible fibers

The model we have previously presented is a linear model (see the energy reported in Eq. 1.1). We now descibe the generalization to the non-linear case. The effort in that direction are based upon work by Pipkin et al. [39–46] on inextensible fibers. Taking inspiration from the work of Pipkin et al, 2D continua composed by two orthogonal families of inextensible fibers has been studied in [47], which was further extended and applied to pantographic lattices in [12, 48]. The concept of a continuum model regarded as composed by fibers needs further explanations. Let us consider a $2D$ continuum with a rectangular domain $\Omega \subset \mathbb{R}^2$ as reference shape. The sides of the rectangle are in a ratio of 1:3 (so chosen since some remarkable features arise if we consider structures whose sides ratio is at least 1:3 because, as we will describe in the Chapter dedicated to experimental methods). To invesigate the planar motions of this continuum, we introduce a suitably regular function $\boldsymbol{\chi} : \ \Omega \to \mathbb{R}^2$ (we call it "macro-placement") which associates the reference positions to the current ones $(X_1, X_2) \overset{\boldsymbol{\chi}}{\mapsto} (x_1, x_2)$.

An orthogonal frame of reference $(\mathcal{O}, \xi_1, \xi_2)$, whose axis ξ_1 and ξ_2 are oriented along the inextensible fibers in the reference configuration, is introduced. Accordingly, we have the following non-dimensional coordinates

$$\xi_1 \coloneqq \frac{1}{l}(X_1 - X_2) + \frac{1}{2} \ , \ \ \xi_2 \coloneqq \frac{1}{l}(X_1 + X_2) + \frac{1}{2}. \tag{1.7}$$

A graphical explanation of the introduced quantities is given in Fig. 1.7. The Cartesian frame $(\mathcal{O}, \xi_1, \xi_2)$ is chosen so that the members of its associated basis, namely the ordered couple of vectors (D_1, D_2), are oriented, in the reference configuration, as the two families of fibers. The inextensibility constraint can be introduced by

considering that a curve γ is inextensible for a placement $\boldsymbol{\chi}$ if, for every part γ_1 of γ, $\boldsymbol{\chi}(\gamma_1)$ has the same length as γ_1. The presence of this "inextensibility constraint" allows us to discuss of *inextensible* fibers.

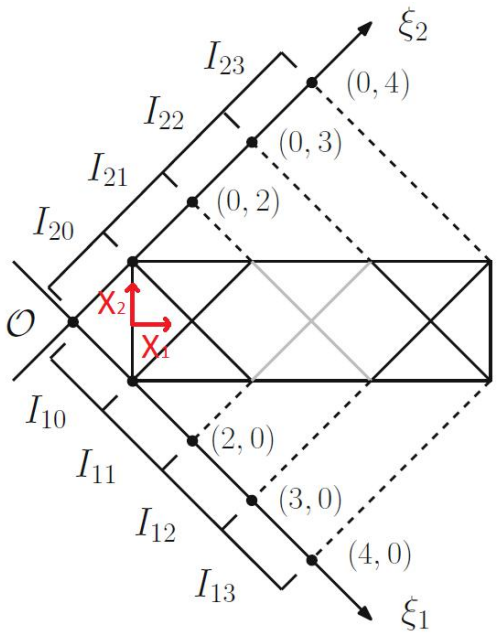

Figure 1.7: The inextensible fiber configuration and relative Lagrangian coordinates.

By definition, d_1 and d_2 are considered to be the transformed vectors in the current configuration, of the vectors D_1 and D_2, respectively, i.e. $d_\alpha = FD_\alpha,\ \alpha = 1, 2$, where $F = \nabla\boldsymbol{\chi}$. From their definition, which needs that $\boldsymbol{\chi}$ is at least locally continuously differentiable, it follows that the vectors d_α are tangent to the fibers in the current frame. Moreover, the inextensibility constraint implies that $\|d_1(\xi_1, \xi_2)\| = \|d_2(\xi_1, \xi_2)\| = 1$ for all (ξ_1, ξ_2). It can be shown (see Rivlin [49] for a formal demonstration) that, if we restrict our analysis on a open simply linearly connected set Δ of Ω, where $\boldsymbol{\chi}$ is twice continuously differentiable the inextensibility of fibers allows the following representation formula

$$\boldsymbol{\chi}^\Delta(\xi_1, \xi_2) = \boldsymbol{\chi}_1^\Delta(\xi_1) + \boldsymbol{\chi}_2^\Delta(\xi_2) \tag{1.8}$$

Moreover, if we denote with $\mu_1^\Delta(\xi_1)$ and $\nu_1^\Delta(\xi_1)$ the projections of $\boldsymbol{\chi}_1^\Delta(\xi_1)$ on D_1 and D_2, respectively, and $\nu_2^\Delta(\xi_2)$ and $\mu_2^\Delta(\xi_2)$ the projections of $\boldsymbol{\chi}_2^\Delta(\xi_1)$ on D_1 and D_2,

respectively, then

$$\boldsymbol{\chi}_1^{\Delta}(\xi_1) = \mu_1^{\Delta}(\xi_1)D_1 + \nu_1^{\Delta}(\xi_1)D_2 \text{ and } \boldsymbol{\chi}_2^{\Delta}(\xi_2) = \nu_2^{\Delta}(\xi_2)D_1 + \mu_2^{\Delta}(\xi_2)D_2 \tag{1.9}$$

As we have already noted, the constraint of inextensibility can be expressed imposing that the norm of d_1 and d_2 is equal to one. Therefore, we can introduce two quantities $\vartheta_1^{\Delta}(\xi_1)$ and $\vartheta_2^{\Delta}(\xi_2)$ such that

$$d_1^{\Delta} = \cos\vartheta_1(\xi_1)D_1 + \sin\vartheta_1(\xi_1)D_2 \quad \text{and} \quad d_2^{\Delta} = \sin\vartheta_2(\xi_2)D_1 + \cos\vartheta_2(\xi_2)D_2 \tag{1.10}$$

We can now study the Pipkin continuum by considering some boundary conditions. In a standard bias extension test[2] we fix the left short side of the rectangle (denoted by Σ_1) and we impose a non-vanishing displacement u_0 on the right short side (denoted by Σ_2). Because of fiber inextensibility, the boundary conditions on Σ_1 and Σ_2 can be used to determine directly the placement field in the interior of Ω [47], i.e. on the regions Δ_{00} and Δ_{33} of Fig. 1.8. The determination of the function χ in the other regions then follows in a straightforward manner.

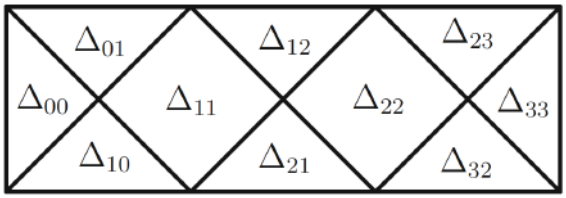

Figure 1.8: Domain pattern induced by the boundary conditions.

Due to the fiber inextensibility we can also estabilish a relation between the functions μ_i^{Δ} and ν_i^{Δ}

$$\|F \cdot D_1\|^2 = 1 \Rightarrow \left(\mu_{1,1}^{\Delta}\right)^2 + \left(\nu_{1,1}^{\Delta}\right)^2 = 1 \Rightarrow \nu_{1,1}^{\Delta} = \pm\sqrt{1 - \left(\mu_{1,1}^{\Delta}\right)^2} \tag{1.11}$$

$$\|F \cdot D_2\|^2 = 1 \Rightarrow \left(\mu_{2,2}^{\Delta}\right)^2 + \left(\nu_{2,2}^{\Delta}\right)^2 = 1 \Rightarrow \nu_{2,2}^{\Delta} = \pm\sqrt{1 - \left(\mu_{2,2}^{\Delta}\right)^2} \tag{1.12}$$

Hence, the admissible placements in the Pipkin's plate are only determined by the globally continuous and piecewise twice continuously differentiable fields $\mu_1(\xi_1)$ and $\mu_2(\xi_2)$. Eqs. (1.10)-(1.12) allow us to restrict our study to the ordinary differential equations

$$\frac{\mathrm{d}\mu_\alpha(\xi_\alpha)}{\mathrm{d}\xi_\alpha} = \cos\vartheta_\alpha(\xi), \ \alpha = 1, 2 \tag{1.13}$$

[2]It should be clear now that the BIAS extension test plays a central role in the study of deformable fabrics.

In fiber-inextensible 2D Pipkin continua it is customary to introduce the *shear deformation* γ as a strain measure, defined as the scalar product of the fiber directions in the deformed configuration. Recalling the inextensibility assumption and Eq. (1.10), the *shear deformation* γ reads as

$$\gamma(\xi_1, \xi_2) \coloneqq d_1 \cdot d_2 = \cos\left(\frac{\pi}{2} - \vartheta_1(\xi_1) - \vartheta_2(\xi_2)\right) = \sin\left(\vartheta_1(\xi_1) + \vartheta_2(\xi_2)\right) \tag{1.14}$$

Further, the following kinematic constraint should be enforced

$$-\frac{\pi}{2} < \vartheta_1 + \vartheta_2 < \frac{\pi}{2} \ \left(\implies -1 < \gamma < 1\right) \tag{1.15}$$

if the case $\vartheta_1 + \vartheta_2 = \pm\frac{\pi}{2}$, which stands for overlapping fibers, is to be avoided. Now that the fields $\vartheta_1(\xi_1)$ and $\vartheta_2(\xi_2)$ uniquely describe admissible placements, the strain energy density $W\left(\vartheta_1, \vartheta_2, \dfrac{\mathrm{d}\vartheta_1}{\xi_1}, \dfrac{\mathrm{d}\vartheta_2}{\xi_2}\right)$ may be introduced. We postulate that W has the following form

$$W\left(\vartheta_1, \vartheta_2, \frac{\mathrm{d}\vartheta_1}{\xi_1}, \frac{\mathrm{d}\vartheta_2}{\xi_2}\right) = \alpha g(f(\gamma)) + \beta g(\|\nabla f(\gamma)\|) \tag{1.16}$$

with $g(x) = \frac{1}{2}x^2$. Different functions f have been studied [12, 48], among which:

S $\quad f(\gamma) = \gamma$

Q $\quad f(\gamma) = \arcsin\gamma$

T $\quad f(\gamma) = \tan(\arcsin\gamma)$

The two cases $(\alpha = 1, \beta = 0)$ and $(\alpha = 0, \beta = 1)$ are referred to as pure *first gradient energy* (1g) and pure *second gradient energy* (2g), respectively. Numerical results [50–54] show that the equilibrium configurations obtained by considering second gradient energies are substantially different if compared to the ones obtained with the first gradient approach (see Fig. 1.9). An experimental validation is needed to decide which model produces the best representation of reality.

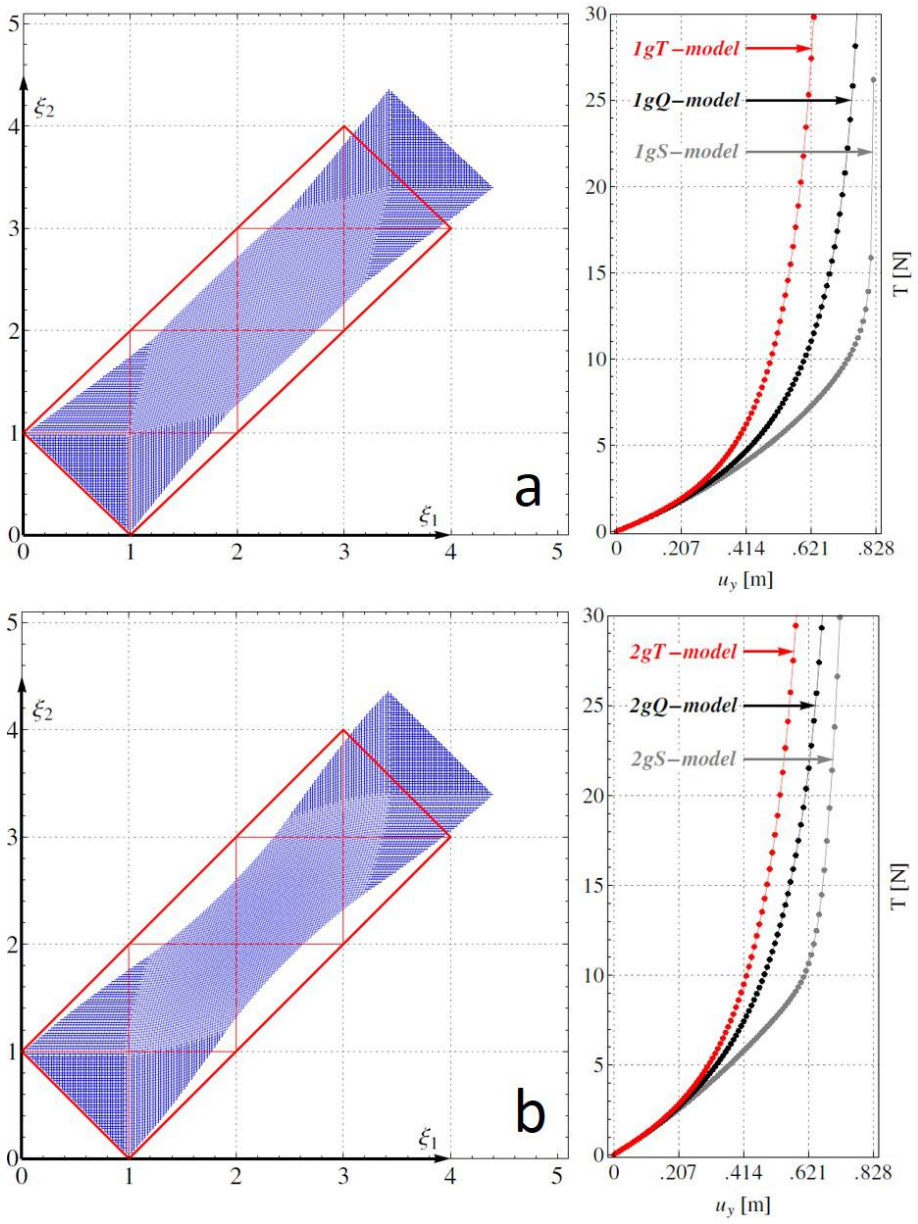

Figure 1.9: Deformed equilibrium configurations and resultant (normal) forces on the short side for a BIAS extension test for the first gradient 1gT (a) and second gradient 2gT (b) models.

1.3 Three scales, three models: micro, meso and macro models for non-linear 2D pantographic sheets

Using the theoretical framework we have discussed as our basis, we can now consider the non-linear 2D second gradient continuum model of a pantographic lattice with extensible fibers. Clearly we can approach the problem from different points of view. We note that we have introduced the necessary concepts needed to develop a micro model and its homogenized second gradient macro model. We also are able to find homogenization procedure to connect the two different scales. Finally, a third approach has been proposed to model a particular class of pantographic structures (when the fibers of the same family are not too close one to the other).

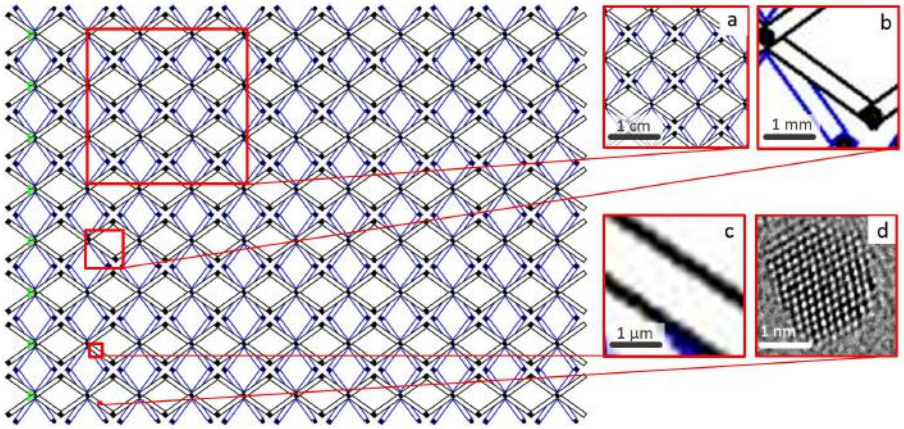

Figure 1.10: Different REVs for different scales imply different models: (a) Second Gradient Continuum model; (b) Beam Theory; (c) standard Cauchy Continuum Mechanics; (d) Quantum Mechanics.

It is therefore, important at this juncture to review how the modelling process relates with reality. Via a process of design and subsequent manufacturing (we will address this in the Chapter about experimental methods), it is possible to obtain real samples which are ultimately 3D objects composed by fibers with a non zero cross section area and which are posed in two parallel planes. Remember that in the models we refer to all the fibers of one plane as a "family" of fibers. The fibers of any plane are all parallel one to the other and the two planes are separated by cylinders (or the pivots) which connect the fibers of one family to the ones of the second family.

Reality plays a fundamental role in the definition of the Representative Elementary Volume (REV). As it can be observed in Fig. 1.10, at different scales we need different models for properly describing the phenomena. So, for example, we can use a homogenized continuum model if we regard the structure as a plate (Fig. 1.10.a) but we will have to introduce a beam model to describe it if the chosen REV is the one depicted in Fig. 1.10.b or we will clearly use the standard Cauchy continuum model in the description of a little part of a fiber (Fig. 1.10.c) and we likely have to use some atomistic method if our REV only contains few atoms.

Clearly, the real sample *is* not a 2D continuum, but it will be *modelled* in the sequel as it was. Obviously, when the fibers are too far one with respect to the other (see Fig. 1.11.a) we can think that the continuum model is no more appliable and for this specific case a "meso" model which describes the structure as composed by coninuous fibers (so it is not continuous in the sense of a 2D plate, but only in the description of fibers) has been developed.

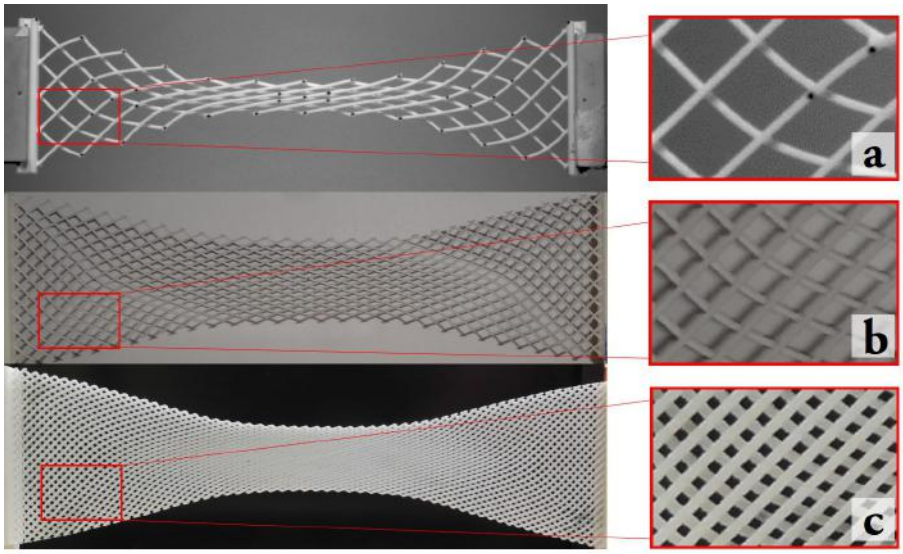

Figure 1.11: Three pantographic structures which differ for the density of fibers.

Current research is directed toward the investigation of the validity limits of the second gradient continuum model. First evidences show that it is in a good agreement with experimental measurements also for structures not at all dense (in the sense of distribution of fibers) as the one in Fig. 1.11.a. We will show in the following, after the presentation of the three models, a very preliminary result along this research path.

1.3.1 Discrete Hencky-type model

In the spirit of the multiscale procedures, a discrete approach can be considered for modeling pantographic structures [35, 55, 56]. In the previously presented models we had an inextensibility constraint for the fibers composing the structure. Here, to obtain a better agreement with experimental evidences [12, 35] extension of fibers is accounted for by modeling the fibers as composed by material particles connected by extensional springs. Moreover, for describing at the micro level the bending of fibers, we introduce rotational springs at each node of the lattice.

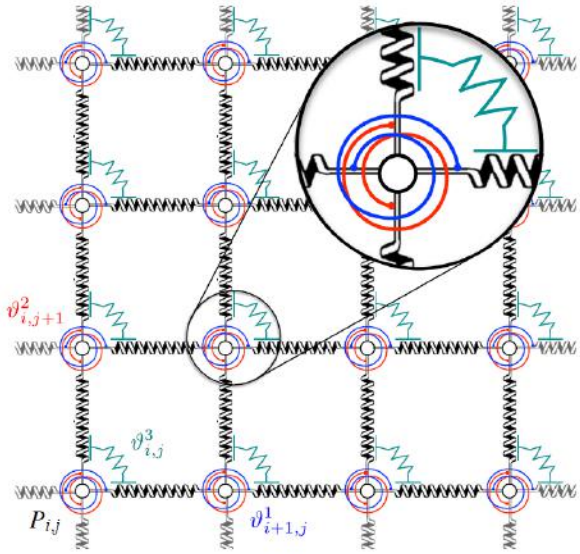

Figure 1.12: Graphical representation of the discrete Hencky-type model of a pantographic sheet (in detail the three rotational springs are pointed out).

Let us consider a Lagrangian Cartesian orthonormal coordinate system with its associated basis of unit vectors (D_1, D_2) representing the fibers directions in the reference configuration. In this configuration the lattice body points have the following positions

$$P_{i,j} = (i\epsilon, j\epsilon), \quad i = 0, 1, ..., N \text{ and } j = 0, 1, ..., M \tag{1.17}$$

where ϵ is the distance between two adjacent body points, and N and M are the numbers of points along the fibers directions (see Fig. 1.12). In the current configurations, we denote the positions of the body points (whose position in the reference configuration is labeled by $P_{i,j}$) with $p_{i,j}$. The body points at the nodes $P_{i,j}$ are connected by extensional springs along the two directions (Fig. 1.12). These extensional

springs, characterized by the rigidities $k^1_{i,j}$ and $k^2_{i,j}$ for the two directions, provide energetic terms depending on the distances between adjacent contiguous points in the current configuration, i.e. the distance $\|p_{i,j+1} - p_{i,j}\|$ for the fibers which are oriented along D_1 in the reference configuration, and on the distance $\|p_{i+1,j} - p_{i,j}\|$ for the fibers oriented D_2 in the reference configuration. Further energetic terms are provided by rotational springs which are positioned at each node. For a good representation of bending and shear of the structure, we have to consider three rotational springs, characterized by the rigidities $b^1_{i,j}$ and $b^2_{i,j}$ (bending of fibers) and $b^3_{i,j}$ (torsion of pivots), at each node. Their deformation energies depend, respectively, on the angles:

1. $\vartheta^1_{i,j}$ between the vectors $p_{i-1,j} - p_{i,j}$ and $p_{i+1,j} - p_{i,j}$,

2. $\vartheta^2_{i,j}$ between the vectors $p_{i,j-1} - p_{i,j}$ and $p_{i,j+1} - p_{i,j}$,

3. $\vartheta^3_{i,j}$ between the vectors $p_{i,j+1} - p_{i,j}$ and $p_{i+1,j} - p_{i,j}$.

We then postulate the following strain energy for the microscopic Lagrangian discrete system

$$\begin{aligned} U(\{p_{i,j}\}) = &\sum_j \sum_i \frac{k^1_{i,j}}{2}(\|p_{i+1,j} - p_{i,j}\| - \epsilon)^2 + \sum_j \sum_i b^1_{i,j}(\cos\vartheta^1_{i,j} + 1) + \\ &+ \sum_j \sum_i \frac{k^2_{i,j}}{2}(\|p_{i,j+1} - p_{i,j}\| - \epsilon)^2 + \sum_j \sum_i b^2_{i,j}(\cos\vartheta^2_{i,j} + 1) + \\ &+ \sum_j \sum_i \frac{b^3_{i,j}}{2}\left|\vartheta^3_{i,j} - \frac{\pi}{2}\right|^\xi \end{aligned} \tag{1.18}$$

where ξ is a parameter that is equal to 2 for a generic linear case. In [55, 56], the above described discrete model made of extensional and rotational (i.e. torsional) springs is solved at each iteration by energy minimization.

As a numerical application of the described model, we show Figs. 1.13 and 1.14. In Fig. 1.13 the deformed shape of a pantographic structure is shown resulting from a BIAS extension test simulation using the discrete energy in Eq. (1.18). In the same manner, in Fig. 1.14 we show the deformed shape of a pantographic structure resulting from a shear test simulation.

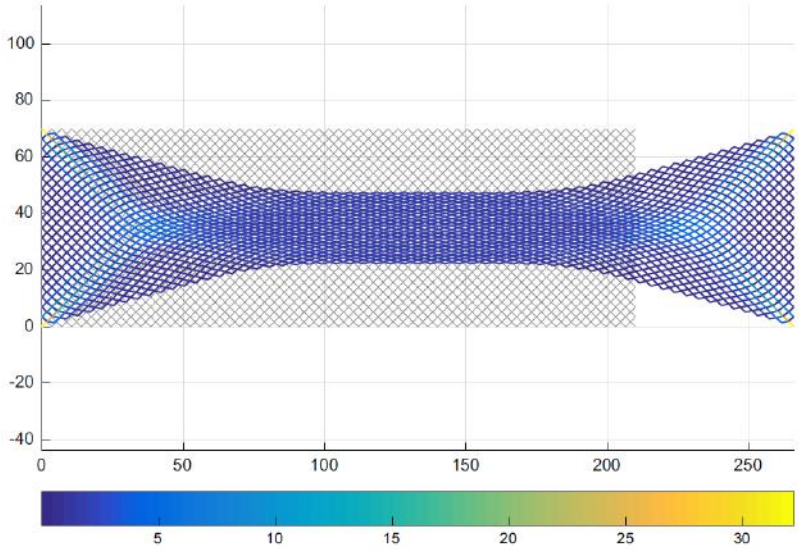

Figure 1.13: BIAS extension test numerical simulation of a pantographic structure described by the discrete Hencky-type model: reference configuration (in *gray*) and current shape.

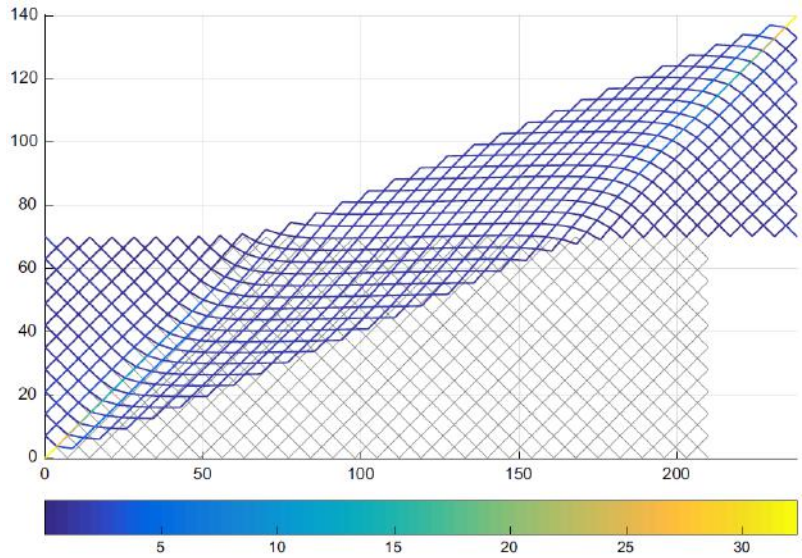

Figure 1.14: Shear-extension test numerical simulation of a pantographic structure described by the discrete Hencky-type model: reference configuration (in *gray*) and current shape.

1.3.2 Euler-Bernoulli non-linear beam theory meso-model

As we remarked, a homogenized model cannot be properly (exactly) used to describe all the details of structures as the one in Fig. 1.15 (even if we already hinted that the error in some sense in rather small). To expose certain additional details for this kind of structures one can consider so-called "meso-models", which is an intermediate model between the discrete and the homogenized ones. This model, along with an example of its numerical application, was first presented in [4]. In this case, the fibers of the pantographic structure are modeled as non-linear Euler-Bernoulli beams.

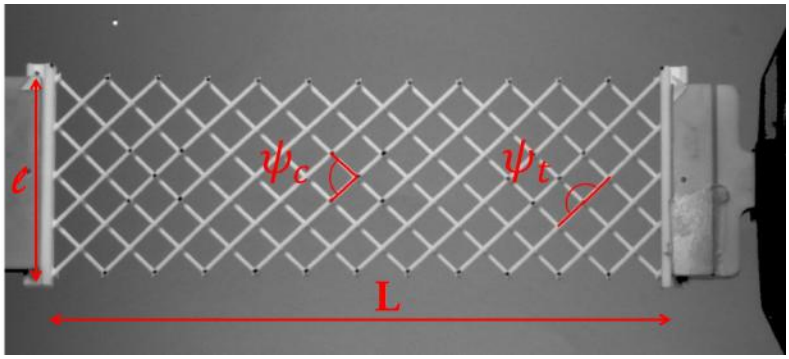

Figure 1.15: Specimen in the reference configuration.

This model, which we discuss here briefly, allows to describe structures composed by two families of fibers (which are not very close one to the other, see Fig. 1.15) interconnected by some cylinders (the real pivots) whose torsion and flexion are *a priori* non negligible. Pivots are modelled by adding in every interconnection a torsional spring (accounting for the shear of the pantographic structure at a macro level) and, possibly, an extensional spring (allowing for the sliding of a fiber with respect to the corresponding one in the other family, *i.e.* the fiber in the other family connected to it by the pivot, see Fig. 1.16). Each fiber element of length L_i (L_i is the distance between two adjacent pivots in the current configuration) is then modeled as an Euler-Bernoulli beam, endowed with a stretching energy W_s^i and a bending energy W_b^i. The total number of fiber elements is denoted with M.

The deformation energy, which by a numerical minimization makes possible to determine equilibrium configurations, is defined as follows: for a single fiber element i of length L_i we have an elastic energy depending quadratically on axial strain (stretching energy)

$$W_s = \sum_{i=1}^{M} \frac{1}{2} \int_0^{L_i} EA\epsilon^2 \, dx \tag{1.19}$$

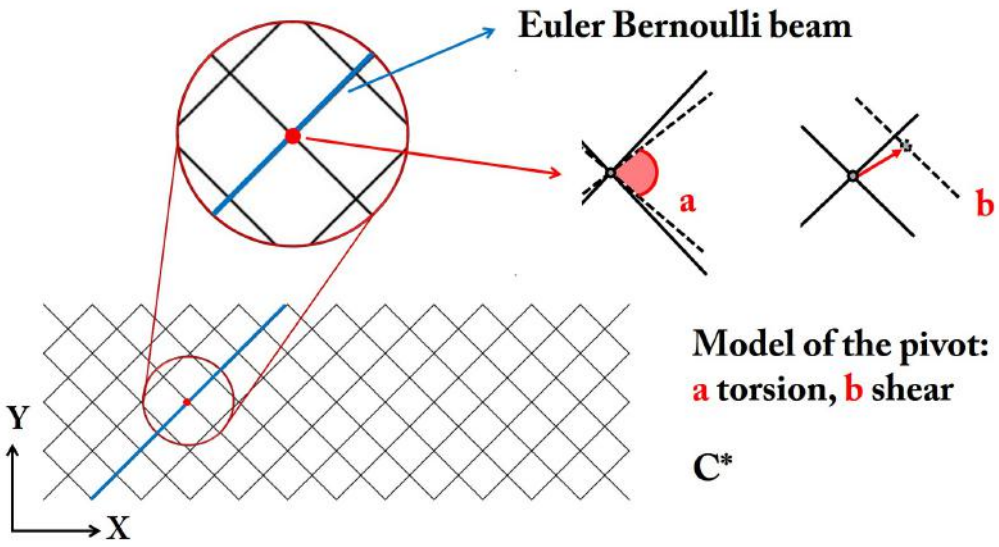

Figure 1.16: Reference configuration of the pantographic structure and representation of the pivot mechanisms.

and curvature (bending energy)

$$W_b = \sum_{i=1}^{M} \frac{1}{2} \int_0^{L_i} EI\kappa^2 \, dx \tag{1.20}$$

By referring to Fig. 1.17.a, a pivot torsion energy term can be written as follows

$$W_p = \sum_{i=1}^{N_p} \frac{1}{2} k_p \left(\frac{\pi}{2} - \Delta\alpha_i \right)^2 \tag{1.21}$$

where $\Delta\alpha_i$ represents the change of the angle between two intersecting fibers in the deformed configuration with respect to the reference configuration. In [4] an additional energetic term is considered that allows us to describe the (possible) sliding of fibers in correspondence of interconnecting pivots. We will explore this possibility in the last Chapter about experimentas and analysis of damage.

The total potential energy is thus given as

$$W = W_s + W_b + W_p \tag{1.22}$$

By now considering the minimum of potential energy

$$\delta W = 0 \tag{1.23}$$

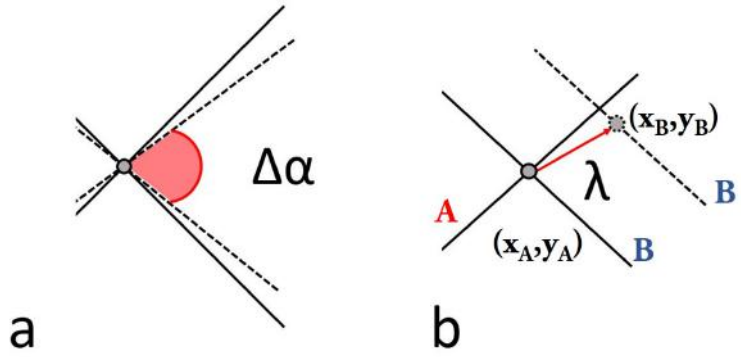

Figure 1.17: Representation of pivot energetic terms.

we can obtain the equilibrium configurations. It is evident that the presented problem cannot be solved analytically. The Ritz approach is employed in [**?**] to solve this problem, and consists in discretizing the energy (1.22) and minimizing it, after having introduced some shape functions for the displacement. For all the details we refer the reader directly to the article. In Fig.1.18, the superposition between the calculated deformed shapes and the measured ones are shown.

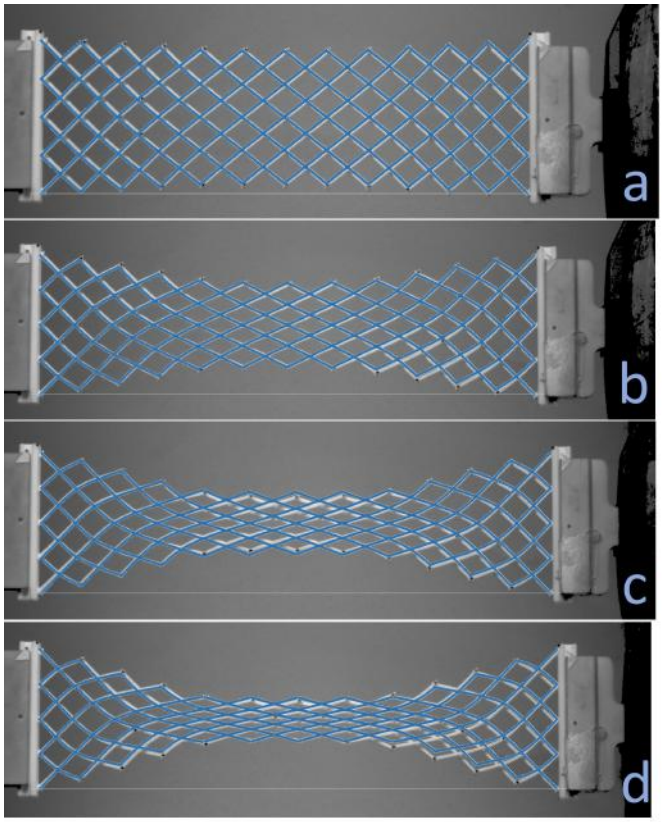

Figure 1.18: Comparison between experimental (gray) and numerical (blue) shapes of the pantographic structure. They differ for the imposed displacement: (a) $0.014\,m$, (b) $0.037\,m$, (c) $0.048\,m$, (d) $0.054\,m$.

1.3.3 Second gradient homogenized model

We now present the central point in the field of the pantographic metamaterial which is the $2D$ continuum macro-model obtained via homogenization of discrete Hencky-type micro-model presented in a previous section. Expanding in truncated Taylor series the kinematic map as it is explained in [35], we can compute the micro-placement field of material particles at the nodes of the referential lattice by using the values, in such nodes, of a regular macro-placement and its first gradient. Such a map determines a unique micro-motion once a macro-motion is given. The micro-macro transition is obtained by equating the micro-strain energy with the macroscopic counterpart, thus obtaining a macroscopic Lagrangian surface density

of strain energy in terms of the constitutive coefficients appearing in the postulated expression of the micro-strain energy. Numerical simulations with both discrete and homogenized models show that the homogenized model is representative of the microscopic response [55, 56]. Following the notation introduced above, we now consider a $2D$ continuum whose reference shape is given by a rectangular domain $\Omega = [0, N\epsilon] \times [0, M\epsilon] \subset \mathbb{R}^2$. Very often, it is assumed that $N = 3M$, which, as we have already remarked, is the standard relation between the width and height of a fabric specimen for experimental and numerical tests. If we want to study only planar motions, then the current shape of the rectangle Ω is mathematically described by regular macro-placement $\boldsymbol{\chi} : \ \Omega \to \mathbb{R}^2$. Following the so-called Piola's Ansatz, it is chosen that $p_{i,j} = \boldsymbol{\chi}(P_{i,j}) \quad \forall i = 1, ..., N, \forall j = 1, ..., M$. Assuming that $\boldsymbol{\chi}(\cdot)$ is at least twice differentiable at $P_{i,j}$, the following second order approximations are obtained

$$\|p_{i+1,j} - p_{i,j}\| = \|\boldsymbol{\chi}(P_{i+1,j}) - \boldsymbol{\chi}(P_{i,j})\| \backsimeq \epsilon \|F(P_{i,j})D_1 + \frac{\epsilon}{2}\nabla F(P_{i,j})|D_1 \otimes D_1\| \tag{1.24}$$

$$\|p_{i,j+1} - p_{i,j}\| = \|\boldsymbol{\chi}(P_{i,j+1}) - \boldsymbol{\chi}(P_{i,j})\| \backsimeq \epsilon \|F(P_{i,j})D_2 + \frac{\epsilon}{2}\nabla F(P_{i,j})|D_2 \otimes D_2\| \tag{1.25}$$

where we have denoted with F the deformation gradient $\boldsymbol{\nabla\chi}$. Further details can be found in [35, 55, 56]. In Eq.(1.24)-(1.25) it is presented the ϵ-truncated Taylor expansion of the first and the third addends in Eq. (1.18) (extensional terms). Letting $\epsilon \to 0$ one finally recovers the homogenized terms. To homogenize the bending and torsional energetic terms, it is necessary to rewrite the three angles $\vartheta^{\alpha}_{i,j}$ ($\alpha = 1, 2$) and $\vartheta^{3}_{i,j}$ as functions of the macro-placement $\boldsymbol{\chi}$. Specifically, we express the cosinus of these angles in terms of $\boldsymbol{\chi}$. Using analogous Taylor expansions as those in Equation (1.25), neglecting $o(\epsilon^2)$ terms, and writing all quantities in terms of the displacement $\boldsymbol{\chi}$, the strain energy of the micro-model becomes

$$\begin{aligned} U(\{p_{i,j}\}) = &\sum_j \sum_i \sum_\alpha \frac{k^{\alpha}_{i,j}}{2}\epsilon^2 (\|F(P_{i,j})D_\alpha + \frac{\epsilon}{2}\nabla F(P_{i,j})|D_\alpha \otimes D_\alpha\| - 1)^2 \\ &+ \sum_j \sum_i \sum_\alpha b^{\alpha}_{i,j} \left[\frac{\|\nabla F(P_{i,j})|D_\alpha \otimes D_\alpha\|^2}{\|F_{i,j}D_\alpha\|^2} - \left(\frac{F(P_{i,j})D_\alpha \cdot \nabla F(P_{i,j})|D_\alpha \otimes D_\alpha}{\|F_{i,j}D_\alpha\|^2} \right)^2 \right] \frac{\epsilon^2}{2} \\ &+ \sum_j \sum_i \frac{b^{3}_{i,j}}{2} \left| \arccos \left(\frac{F(P_{i,j})D_1 \cdot F(P_{i,j})D_2}{\|F(P_{i,j})D_1\| \cdot \|F(P_{i,j})D_2\|} \right) - \frac{\pi}{2} \right|^{\xi}, \end{aligned} \tag{1.26}$$

Rescaling the rigidities as

$$k_{i,j}^{\alpha} = \mathbb{K}_e^{\alpha};\ b_{i,j}^{\alpha} = \mathbb{K}_b^{\alpha};\ b_{i,j}^{3} = \mathbb{K}_p \epsilon^2 \tag{1.27}$$

and letting $\epsilon \to 0$, the strain energy of the macroscopic system reduces to

$$\begin{aligned} U(\boldsymbol{\chi}(\cdot)) = & \int_\Omega \sum_\alpha \frac{\mathbb{K}_e^\alpha}{2} \|FD_\alpha - 1\|^2 \mathrm{d}S + \\ & + \int_\Omega \sum_\alpha \frac{\mathbb{K}_b^\alpha}{2} \left[\frac{\|\nabla F | D_\alpha \otimes D_\alpha\|^2}{\|FD_\alpha\|^2} - \left(\frac{FD_\alpha \cdot \nabla F | D_\alpha \otimes D_\alpha}{\|FD_\alpha\|^2} \right)^2 \right] \mathrm{d}S + \\ & + \int_\Omega \frac{\mathbb{K}_p}{2} \left| \arccos\left(\frac{FD_1 \cdot FD_2}{\|FD_1\| \cdot \|FD_2\|} \right) - \frac{\pi}{2} \right|^\xi \mathrm{d}S. \end{aligned} \tag{1.28}$$

The homogenized energy in Eq. (1.28) can be used to perform numerical simulations: in Fig. 1.19, numerical simulations of the BIAS extension test and shear test are shown. Such homogenization process can be used as an argument for supporting that the description of pantographic fabric at a certain macro-level requires the use of second gradient continua.

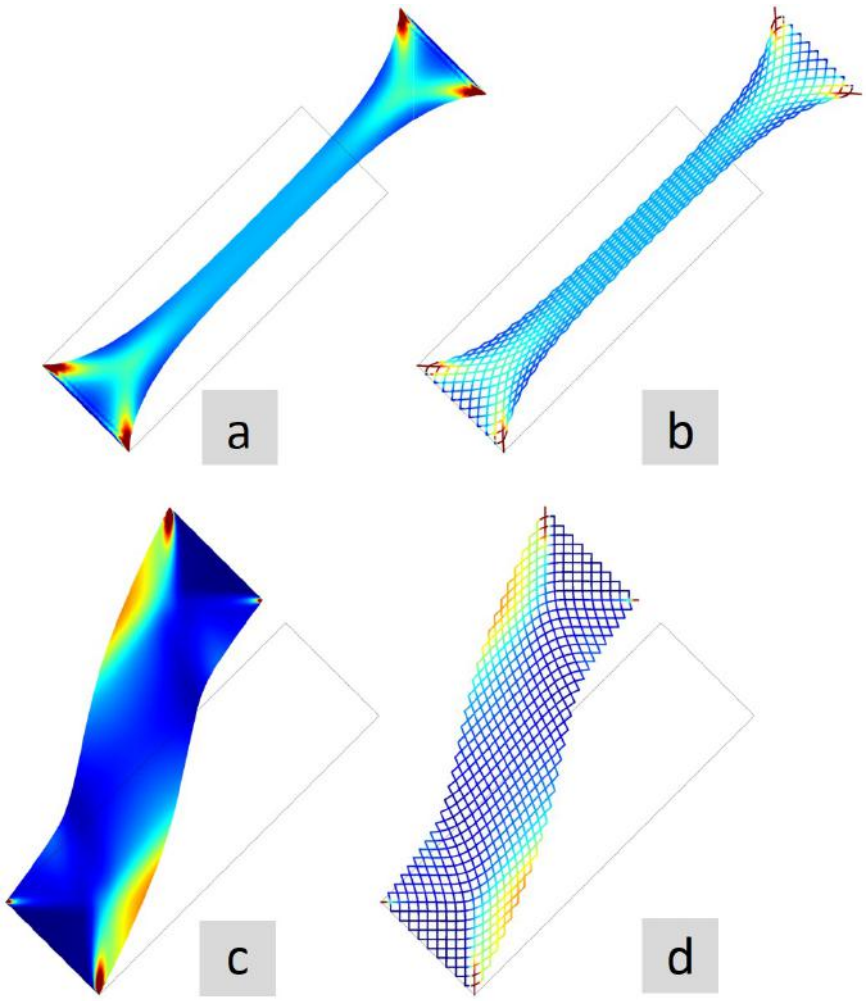

Figure 1.19: BIAS extension test (a) and shear test (b) of a pantographic lattice. In the right images the "fibers" directions are explained.

Astounding power of the second gradient homogenized model As a preliminary conclusion of this Chapter we show the astounding simulations in Fig. 1.20. In this figure, which inspired the analysis in [57], two comparisons between numerical simulations performed with two different models in the same BIAS extension test are shown. We have already described the results in Fig. 1.20.a: obtained by using a model which consider the fibers composing the pantographic fabrics modeled as non-linear Euler-Bernoulli beams. We have remarked that this particular "meso" model has been used in the case of pantographic structures which are composed by

very few fibers. In that case, in fact, the hypothesis of continuum (an effective 2D continuum) is not well-suited and we are obliged, at least in principle, to use a model which is intermediate between the discrete and the continuum ones.

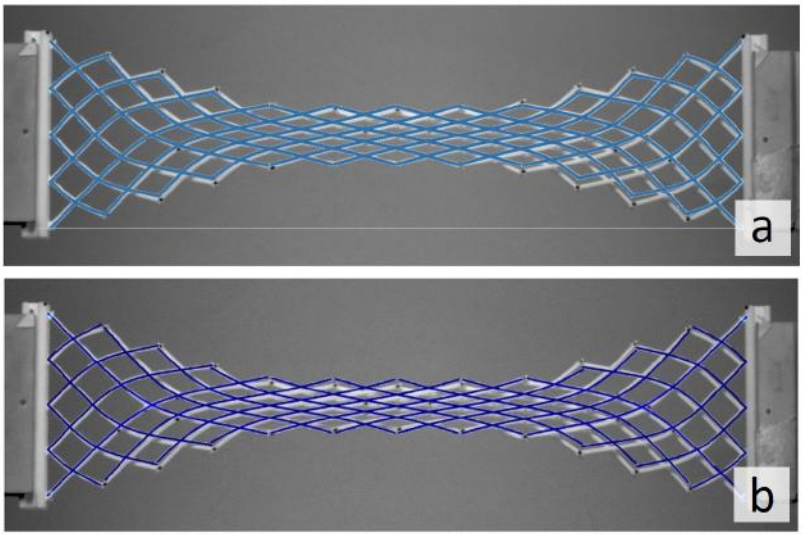

Figure 1.20: Comparison between simulation performed by using the "meso" non-linear Euler-Bernoulli beam theory-based model (a) and the homogenized second gradient model (b).

Let us consider Fig. 1.20.b. The simulation presented in that figure has been performed by minimizing the second gradient energy reported in Eq. (1.28, modified by an additional term which takes into account the possibility that the fibers of the two families slide one with respect to the other in correspondence of their interconnecting pivots. This additional term has been considered for the first time in [5]. The consequence of including this additional term will be further discussed in the final Chapter of this thesis about experimental methods in pantographic structures and their damage/fracture behavior based upon the results obtained in [5]. We remark that in [4], which has been presented above, an analogous additional term can be recognized. However, it is remarkable and surprising that a continuum homogenized model is capable of replicating results in the case of a specimen with so few fibers. Clearly, the inclusion of second gradient terms enriches the model sufficiently to capture phenomena that is otherwise not modelled based upon the standard Cauchy theory.

1.4 Conclusion

The Pantographic Metamaterial represents a class of metamaterials precisely defined by its microstructure. In this Chapter we have limited our attention to 1D and 2D pantographic metamaterials. The extension to the synthesis of such 3D constructs is quite feasible regardless of the theoretical and technological challenges. In the third and fourth Chapters, it will be shown how to model a 3D pantographic-inspired material, by means of a completely different homogenisation framework.

A fundamental characteristic of the Pantographic Metamaterial, which is also a motivation for dedicating a whole chapter to this metamaterial, is the fact that it represents an archetype of theory-driven design. We have widely remarked that at the genesis of pantographic structures was in response to a very simple question. Can we concieve and realize a material system whose energy consists of a purely second gradient type? At the level of a micro-structure, as we have shown, it is necessary to consider a structure which exhibits, locally, a wider class of floppy modes than just rigid motions. This is the rationale that first stimulated us to concieve an ideal pantograph. In an strict adherence to the spirit of the theory-driven research approach nothing has been randomly explored. We have shown here how the answer to basic posed question originating in the theory was developed and, further, how this development lead to the many theoretical predictions found through numerical computations. To validate the followed approach, an essential aspect is to devise methods for experimentally demonstrating the predictions. In the next Chapter of this thesis, some experimental observations and their relation with the modelling will be treated in detail.

The following Chapters (3 and 4) are devoted to answer to a fundamental question: is it possible to conceive a composite material whose essential features are inspired to the ones of the pantographic structures? This apparently simple question will need a whole change of perspective to be answered. In fact, as it will be clear in the fourth Chapter, a fiber-reinforced composite material, whose fibers are arranged in a pantographic-inspired network, can be designed and studied by means of homogenization methods typically used in the framework of composite materials which are heterogeneous at the micro-scale and homogeneous at a macroscopic scale (this was also a main feature in pantographic metamaterials). These methods have been rarely used to describe materials as unusual as pantographic structures, where the second (or higher) gradient energetic terms are substantial. For this reason, it was very challenging to properly model this composite metamaterial. In this thesis we have approached the problem in simplified way: no second gradient effects are taken into account (at the current state of the research, but this represents the main

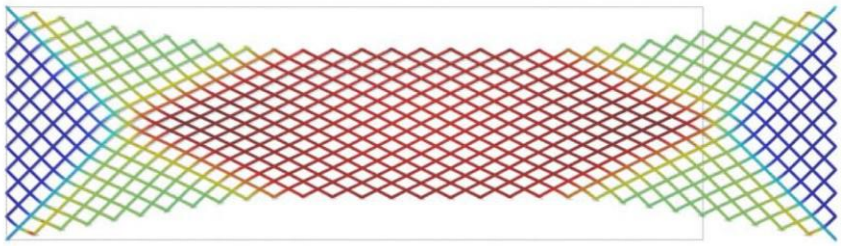

Figure 1.21: The three different deformation zones in the pantographic structure during an extension test: no deformation (blue), shear at macro level and relative rotation at micro level (red) and shear with a different angle (green). The bending of fibers is concentrated in the interface zones.

perspective of this work). Simplifications and approximations are justified by first very promising results obtained thanks to the determination of the Green operators related to the specific considered fiber network embedded in a softer matrix. As it will be shown, by means of these operators it is possible to properly describe the deformation evolution and to compare it to the one relative to a simplified pantographic structure.

As it has been remarked in the Introduction of this thesis, the global deformation of a pantographic structure can be considered as composed by localized different behaviors. In Fig. 1.21, three behavior-zones can be observed: (i) the blue ones, where the angle between the fibers is unchanged along the deformation; (ii) the red one, where only relative rotation between the fibers is observed; (iii) the green ones, where again only relative rotation between the fibers is observed, but a different angle with repect to the one of the red zone (these two angles are, for instance, related by means of suitable geometrical relations). If, then, only relative rotations between the fibers are considered (as it will be done in the fourth Chapter) the three behavior-zones can be properly modelled. The only information that, at the current state of the research, is not present consists in the description of the interfaces between the different zones: on these interfaces, in fact, the bending of fibers is concentred and, as it is now clear after the topic discussed along the present Chapter, the bending is the one responsible for the second gradient energetic term.

Chapter 2

From experimental evidences to a new theoretical modeling

2.1 Introduction

In this Chapter, we present some relevant experimental results which aimed the search for homogenization procedures different from the ones introduced in the previous Chapter. Specifically, experimental tests were performed on 3D multi-layer pantographic networks (see, for instance, Fig.2.1).

Experiments are integral to the development of physical theories. They serve the critical role of verifying and validating the principles and assumptions that form the basis of theoretical developments. The predictive ability of a physical theory must be tested against experiments to establish its applicability and credibility.

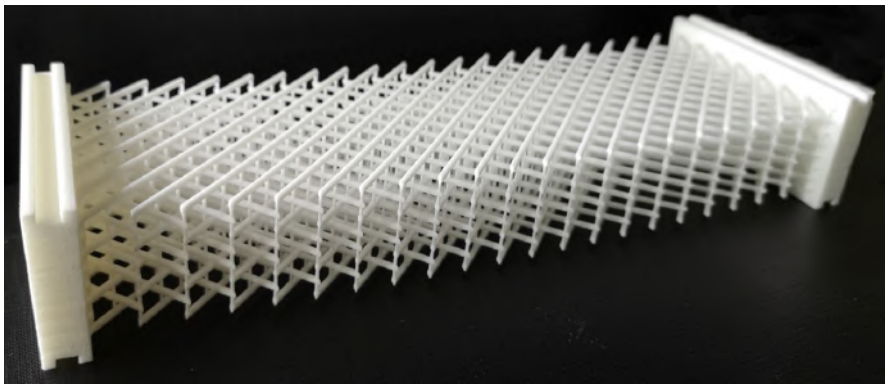

Figure 2.1: Example of multi-layer pantographic network.

The sample presented in Fig. 2.1 has the same basic geometry of the pantographic structures described in the previous Chapter, but it consists in an assembly of different layers of fibers, which are alternately misoriented. The array of fibers are, also in this case, interconnected by means of cylinders, which we will call again pivots.

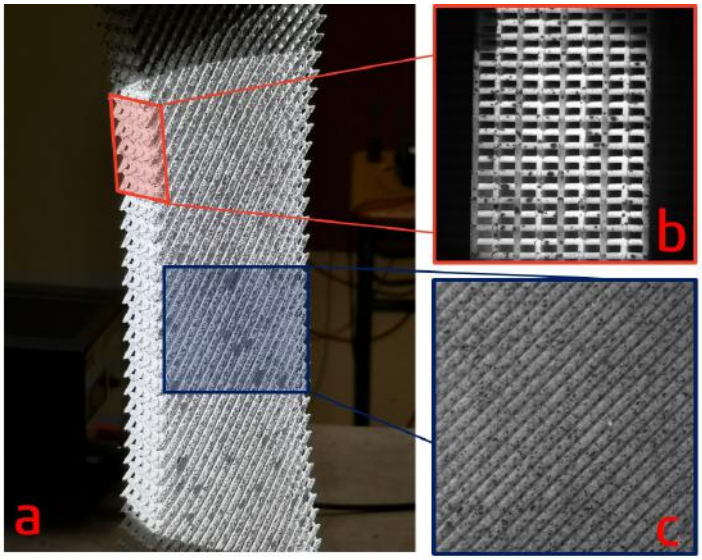

Figure 2.2: Definition of the two sides of the multi-layer pantographic network: (b) *lateral side* and (c) *face*.

The interest in this structure lies in the fact that it can be modelled both by means of the second gradient continuum model presented in the previous Chapter, both by using a completely different homogenization framework, typically used for composite materials. This pantographic network represents, then, the perfect joint-point between the pantographic metamaterial and the pantographic-inspired composite material. In the following we will refer to two different sides of the pantographic 3D network. By referring to Fig. 2.2, we will call *lateral side* of the structure the part shown in the left-up corner and *face* the part in the right-up corner.

This Chapter can be considered as motivational for the next two, which deal with the methods of homogenization through the Green operators. In fact, the models presented in these Chapters have been adopted as a consequence of the experimental observations we present here.

2.2 Experimental measurements

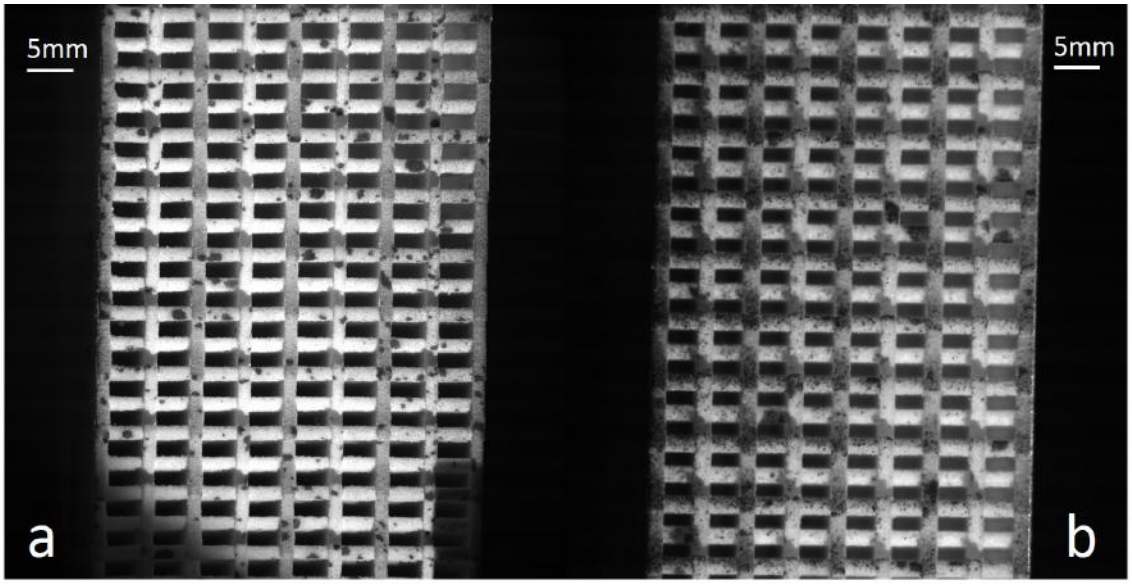

Figure 2.3:

BIAS extension tests have been performed on different samples of 3D pantographic structures as the one in Fig. 2.1. Here we present results of two of the tests. The only difference between the two samples is the height of the pivots h_p (specifically, we have $h_p = 2mm, 3mm$, while the other, common, geometrical features are reported in Tab. 2.1). In Fig. 2.3, it is shown the lateral side of the samples for $h_p = 3mm$ (a) and $h_p = 2mm$ (b).

r_p	a	b	n_f	n_l
$0.5mm$	$0.9mm$	$1.7mm$	20	9

Table 2.1: Common geometrical parameters of the tested samples.

A fundamental result, which is shown in Fig. 2.4, consists in the fact that the average reaction force measured during the BIAS extension test decreases when the pivot's height increases. This can be easily explained by introducing a new degree of freedom for pivots. Until now pivots can only rotate, exhibiting some torsional stiffness or without any effort, if they are perfect. To correctly describe the phenomenology shown in Fig. 2.4, it is necessary to introduce an additional type of

pivot deformation: a shear deformation. In fact, if the height of the pivot is sufficiently large (or, more precisely, if the ratio $h_p/(2r_p)$ between the height and radius of the pivot is sufficiently greater than 1), then the displacement imposed at the edges of the pantographic structure will induce locally a shear deformation in the pivot[1].

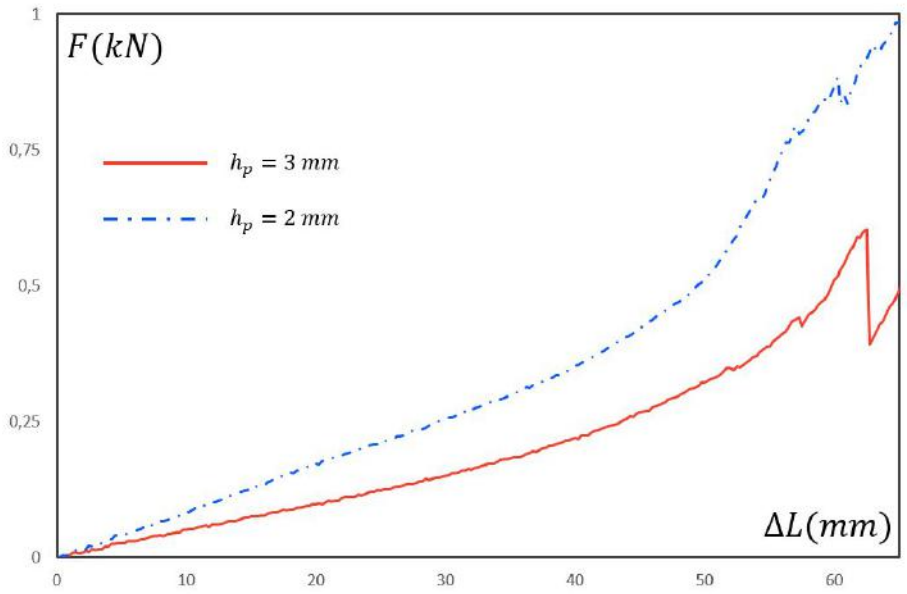

Figure 2.4: Force-displacement experimental curves: it is observed that the average reaction force decreases when the pivot's height increases.

This new possibility of deformation allows the pantographic structure to stretch with less variation of the angle between the fibers, resulting in a lower overall energy compared to the case in which the shear deformation of the pivots is not present (if the ratio $h_p/(2r_p)$ is less than or equal to 1). In fact, as it has been shown in the first Chapter, most of the deformation energy of the pantographic structure is concentrated in the pivots and is due to their torsion.

The phenomenological ansatz we have introduced to explain the difference between the reaction force plots is amply demonstrated by the observation of the deformation in the lateral part of the pantographic network.

[1]This phenomenological explanation will be discussed and extended in the last Chapter of this thesis.

In Fig. 2.5, it is shown the side of the structure with $h_p = 3mm$. In Fig. 2.5a we show the reference configuration, while the current, deformed, configuration is presented in Fig. 2.5b.

Figure 2.5: Side of the structure with $h_p = 3mm$. Reference (a) and current (b) configurations. In (b) it is clearly visible that, due to the shear of the pivots, the overall width of the lateral side of the structure has decreased during the deformation.

The shear deformation of the pivots is therefore highly visible. This proves that the deformation mechanism we postulated to account for the decrease in the reaction force at a h_p increase is well founded.

A second observation can be carried out by observing Fig. 2.5. In fact, in (b) it is clearly visible that, due to the shear of the pivots, the overall width of the lateral side of the structure has decreased during the deformation. This effect will be strongly taken into account in Chapter 4, when it will be modelled the pantographic-inspired material by means of Green operators.

In the next section, we present some results obtained by using the Digital Image Correlation technique.

2.3 Digital Image Correlation Analyses

Digital Image Correlation (DIC for short, see [58,59]) can be used to quantify evolution of displacement field at prescribed resolution of a deformed specimen. Recently, this technique has been applied to extract the displacement fields as the pantographic structure is deformed in the experimental tests [2,60]. For the pantographic structures, displacement fields can be derived at macroscopic and mesoscopic scales. These displacement fields can then be compared with those predicted via numerical simulations. By this comparison it is possible to validate the considered constitutive model.

2.3.1 Principle of Digital Image Correlation

DIC is based upon the analysis of digital images of surfaces at different stages of deformation in experiments, with an aim to obtain a precise estimation of the deformations. One of the limits of DIC comes from its ill-posedness. Generally, only limited information is available from gray level images. For this reason, it is not possible to measure displacement fluctuations beyond certain spatial resolution. Consequently, it is necessary to find a compromise between the uncertainty level and the spatial resolution [61]. Unrefined descriptions of displacement fields based on discretizations coarser than the scale of pixels are usually required. Additional information is necessary to achieve finer resolutions. For example, it is possible to consider continuous displacement fields and decompose them on convenient kinematic bases (e.g., finite element shape functions). The calculation time is increased in this global approach, but the uncertainties can be reduced [61].

Global DIC

The registration of two gray level images in the reference (f) and deformed (g) configurations is based on the conservation of gray levels

$$f(\boldsymbol{x}) = g(\boldsymbol{x} + \boldsymbol{u}(\boldsymbol{x})) \tag{2.1}$$

where $\boldsymbol{u}$ is the (unknown) displacement field to be measured and $\boldsymbol{x}$ the position of pixels. The sought displacement field minimizes the sum of squared differences Φ_c^2 over the region of interest (ROI)

$$\Phi_c^2 = \sum_{\text{ROI}} \varphi_c^2(\boldsymbol{x}) \tag{2.2}$$

where φ_c defines the gray level residuals $\varphi_c(x) = f(\boldsymbol{x}) - g(\boldsymbol{x} + \boldsymbol{u}(\boldsymbol{x}))$ that are computed at each pixel position $\boldsymbol{x}$ of the ROI. The minimization of Φ_c^2 is a nonlinear and ill-posed problem. This is the reason for considering a weak formulation in which the displacement field is expressed over a chosen kinematic basis

$$\boldsymbol{u}(\boldsymbol{x}) = \sum_n \boldsymbol{u}_n \boldsymbol{\psi}_n(\boldsymbol{x}) \tag{2.3}$$

where $\boldsymbol{\psi}_n$ are vector fields and u_n the associated degrees of freedom, which are gathered in the column vector $\boldsymbol{u}$. Thus the measurement problem consists in the minimization of Φ_c^2 with respect to the unknown vector $\boldsymbol{u}$. This problem is nonlinear and to obtain a solution Newton's iterative scheme can be implemented.

In the following analyses, the vector fields correspond to the shape functions of 3-noded triangular elements (i.e., T3 elements). Consequently, the unknown degrees of freedom are the nodal displacements of the T3 elements.

Regularized DIC

The previous approach can be penalized when the image contrast is not sufficient to achieve low spatial resolutions. This is, for instance, the case in the analyses reported hereafter. Regularization techniques can then be selected [62]. They consist of adding to the global correlation functional Φ_c^2 penalty terms. In the following, a first penalty, which is based on the local equilibrium gap, is added for the inner nodes of the finite element mesh and those belonging to the free edges

$$\Phi_m^2 = \{\mathbf{u}\}^\top [\mathbf{K}]^\top [\mathbf{K}] \{\mathbf{u}\} \tag{2.4}$$

where $[\mathbf{K}]$ is the rectangular stiffness matrix restricted to the considered nodes. For the other edges, a similar penalization is considered

$$\Phi_b^2 = \{\mathbf{u}\}^\top [\mathbf{L}]^\top [\mathbf{L}] \{\mathbf{u}\} \tag{2.5}$$

where $[\mathbf{L}]$ is a second operator acting on the nodal displacements of the boundaries that are not traction-free [62].

The global residual to minimize then consists of the weighted sum of the previous three functionals (i.e., Φ_c^2,Φ_m^2 and Φ_b^2). Because the dimensions of the first functional is different from the other two, they need to be made dimensionless. It follows that the penalization weights acting on Φ_m^2 and Φ_b^2 are proportional to a regularization length raised to the power 4 [62]. The larger the regularization length, the more weight is put on the penalty terms. This penalization acts as a low-pass mechanical filter, namely, all high frequency components of the displacement field that are not

mechanically admissible are filtered out. Similarly, for low-contrast areas mechanical regularization provides the displacement interpolation. Examples of results obtained via DIC analyses in the field of pantographic structures are reported in Appendix A.

2.3.2 DIC analyses

For the experimental tests for which we have shown the displacement force curves in the previous section, we present here some measurements of displacement and strain fields by means of the DIC techniques above described.

In Fig. 2.6 the experimental apparatus used to acquire the images analyzed by DIC is shown. As it can be observed, we used two fixed cameras for aquiring the pictures of the face and of the lateral side of the pantographic 3D network. It has to be remarked that the specimen, for the properties of large deformations typical of pantographic structures, so, due to the fact that the cameras are fixed, part of the structure which is aquired in the first images will not be in the last images. For this reason, only a small part of the pictures can be analysed by means of DIC.

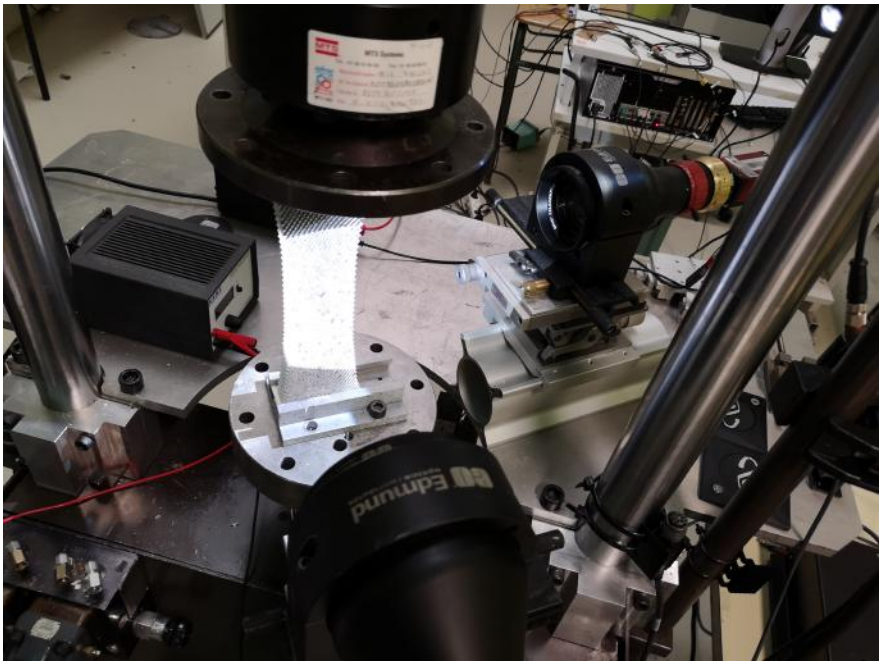

Figure 2.6: Experimental apparatus used to acquire the images analyzed by DIC.

In Fig. 2.7 the reference and deformed configurations of the face of the pantographic multi-layer network, for which the DIC analyses are shown in the following,

are presented. As it is remarked in Appendix A, different mesh can be adopted for performing the analyses. In Figs. 2.8-2.9 two possibilities are shown.

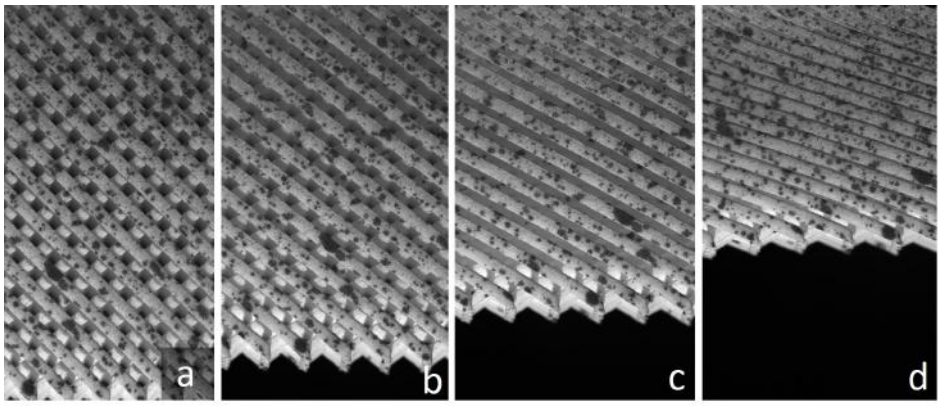

Figure 2.7: Reference configuration (a) and three deformed configurations (b,c,d) of the face of the pantographic multi-layer network. The DIC analyses will be shown for the (b,c,d) pictures.

In Fig. 2.8 a macroscopic mesh for the face of the pantographic network is shown. The density of the finite elements can be changed to obtain resultsmore or less detailed.

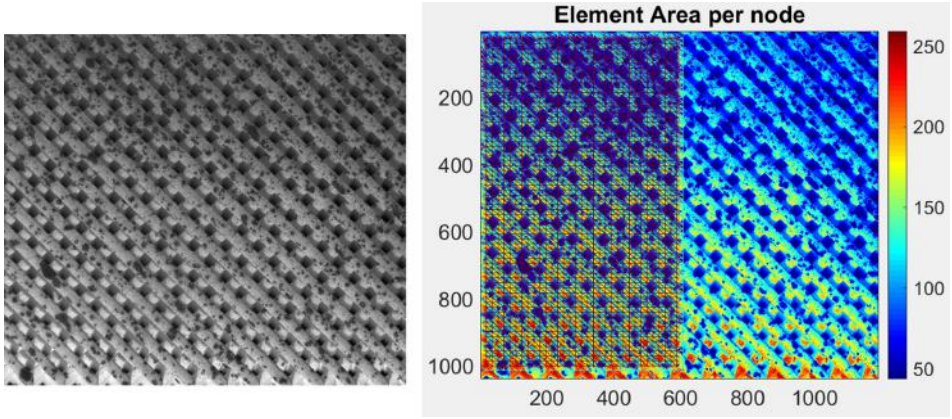

Figure 2.8: Macroscopic mesh for the face of the pantographic network.

In Fig. 2.9 an adapted mesoscopic mesh for the lateral side of the pantographic network is shown. In this case a macroscopic mesh would not be useful to obtain correct results.

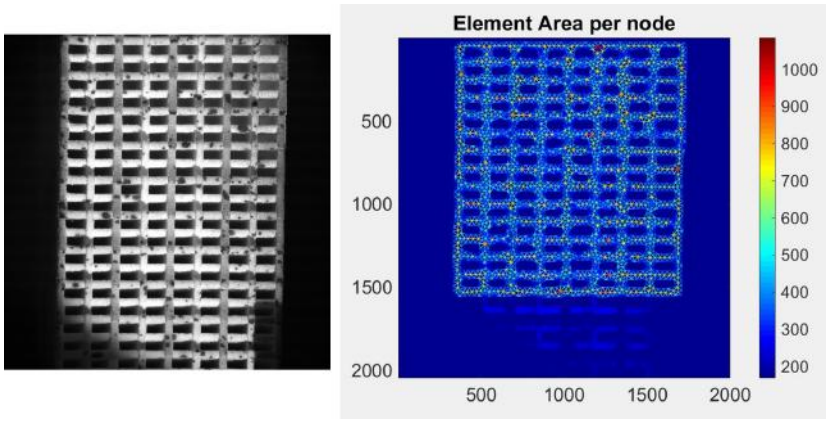

Figure 2.9: Adapted mesh for the lateral side of the pantographic network.

Using the mesh shown in Fig. 2.8, the displacement and strain fields have been measured on the pictures of the face of the pantographic network. The results are shown for three of the images (see Fig. 2.7 b,c,d).

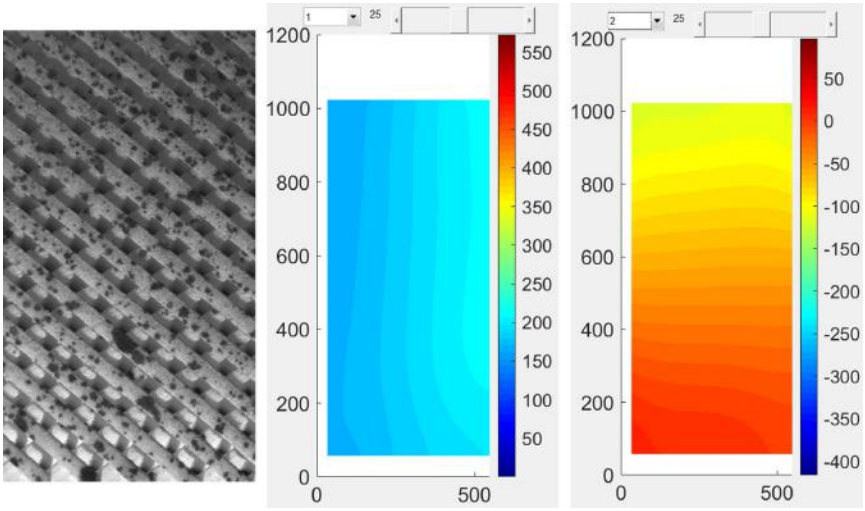

Figure 2.10: Longitudinal (left) and transverse (right) displacement fields measured for the image of Fig. 2.7 b. The fields are shown on the reference configuration.

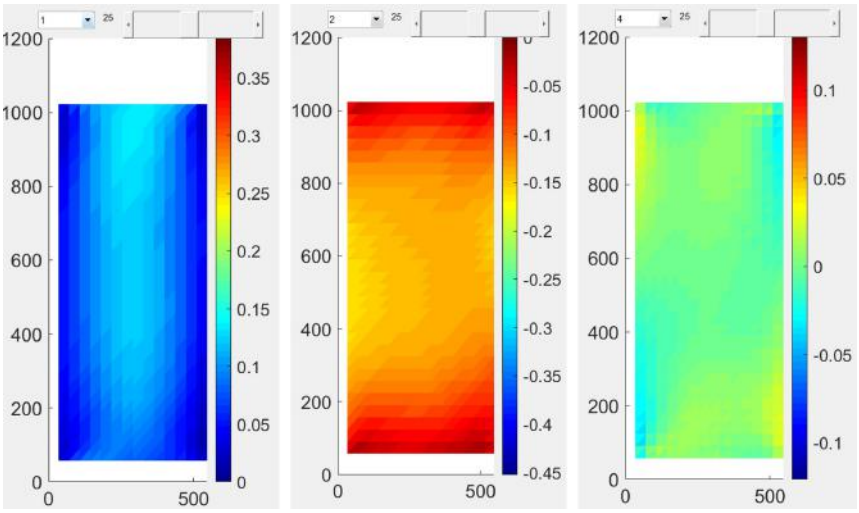

Figure 2.11: Longitudinal (left), transverse (center) and shear (right) strain fields measured for Fig. 2.7 b. The fields are shown on the reference configuration.

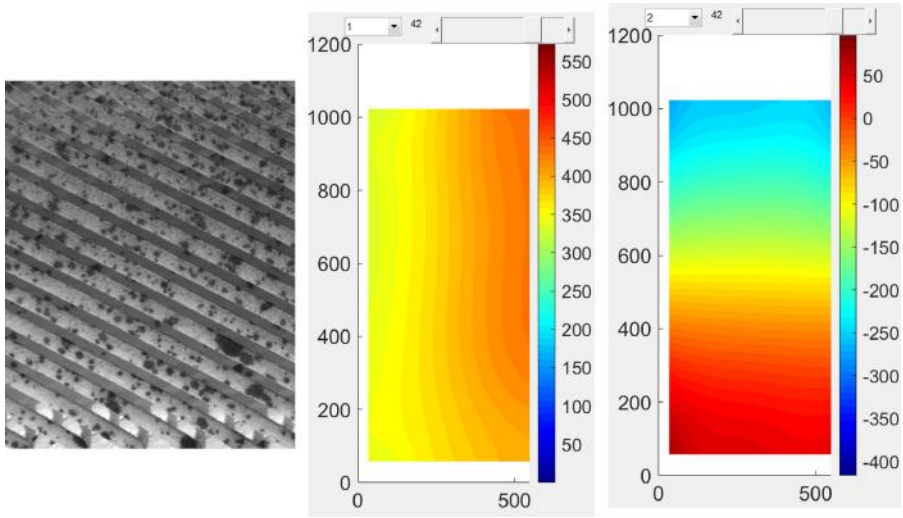

Figure 2.12: Longitudinal (left) and transverse (right) displacement fields measured for the image of Fig. 2.7 c. The fields are shown on the reference configuration.

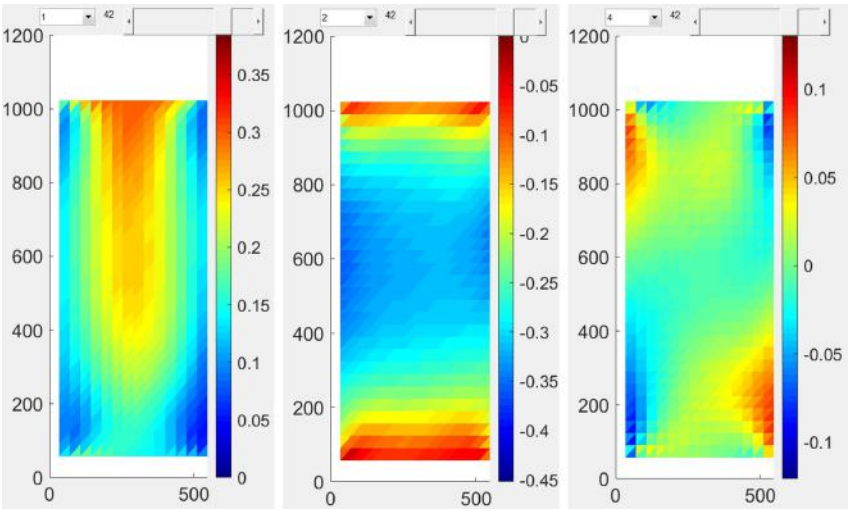

Figure 2.13: Longitudinal (left), transverse (center) and shear (right) strain fields measured for Fig. 2.7 c. The fields are shown on the reference configuration.

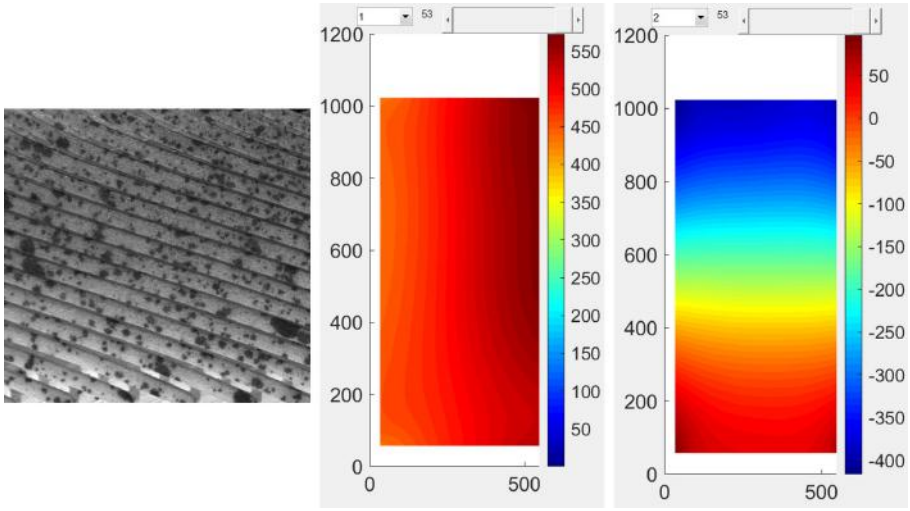

Figure 2.14: Longitudinal (left) and transverse (right) displacement fields measured for the image of Fig. 2.7 d. The fields are shown on the reference configuration.

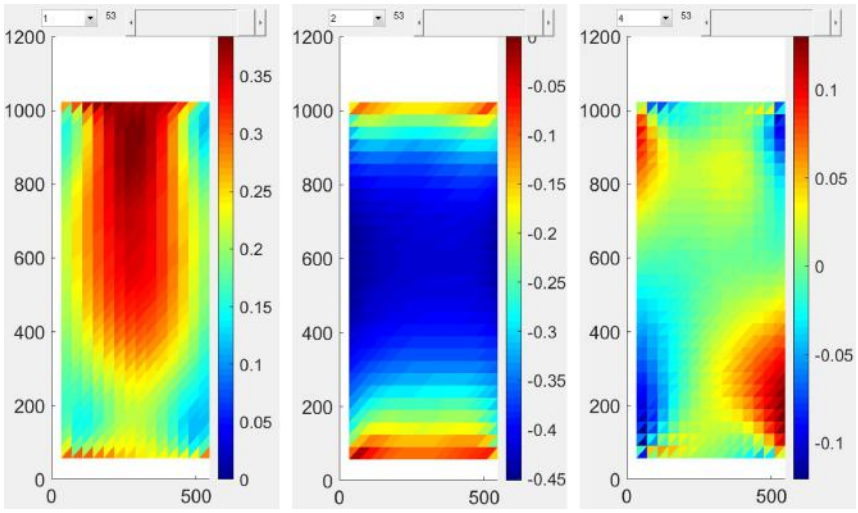

Figure 2.15: Longitudinal (left), transverse (center) and shear (right) strain fields measured for Fig. 2.7 d. The fields are shown on the reference configuration.

Figs. from 2.7 to 2.15 show the measured displacement and strain fields. In Fig. 2.16 the gray level residual fields are finally shown. More details about the analyses here and above presented can be found in Appendix A.

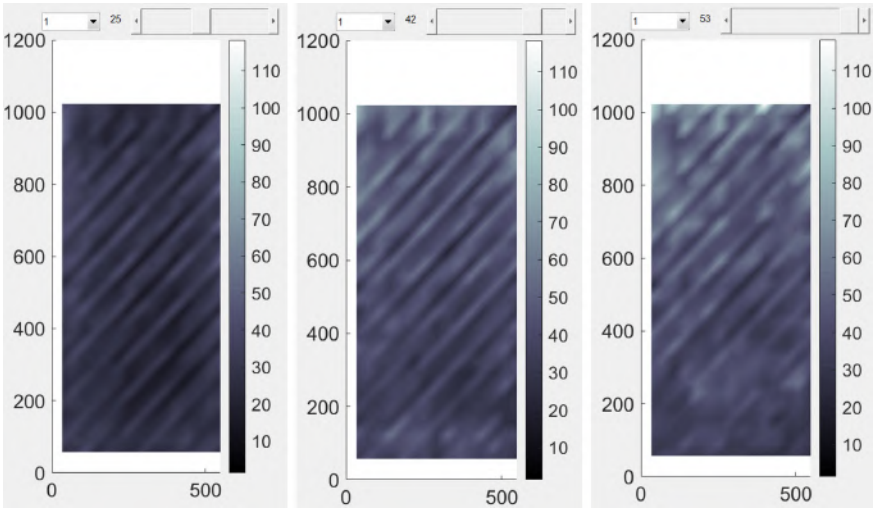

Figure 2.16: Gray level residual fields measured for Fig. 2.7 b,c,d. The fields are shown on the reference configuration.

2.4 Conclusion

In this Chapter we have presented some experimental data and their analysis by means of DIC techniques. The experimental tests presented here have been the basic motivation for the theoretical analyses that follow in the next Chapters. Some of the fundamental ideas presented in Chapter 4 were derived from the observation of the phenomenology of the pantographic multi-layer network.

From this point of view, this Chapter constitutes the ideal link between the previous one, concerning the pantographic metamaterial, and the following two, concerning the modelling of a pantographic-inspired composite material.

Experimental evidence will be taken up in the last Chapter of this thesis, where the emerging and causes of damage and fracture in the pantographic metamaterial will be analyzed.

Chapter 3

Mean Green operators homogenization technique for deformable fiber networks embedded in a compliant matrix

The discussions presented in this Chapter are based on the articles [63, 64].

3.1 Introduction

Particular attention is paid in this Chapter to those composite structures in which the domains that are embedded in a homogeneous matrix can be considered as infinite fibers of a same second phase, as exemplified in Fig. 3.1. This is, in fact, the first step to model the pantographic-inspired composite.

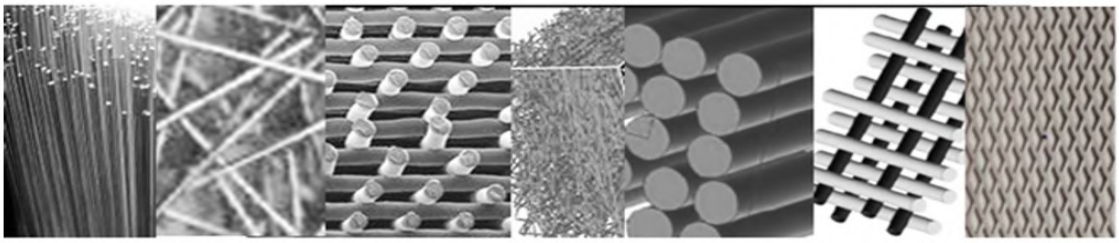

Figure 3.1: Some (dimensionless) examples of 1-directional (1D) fiber bundles and of 2D and 3D fiber networks

They are assumed to be arranged such as to make either a one-directional bundle or interpenetrated ones along several directions of space, so realizing various sorts of lattice network in 1, 2 or 3 dimensions, the modeling of which, in terms of effective property estimate, is still highly challenging, owing to the phase continuity [65–68]. Whether it be random or periodically ordered, a one-directional bundle of infinite fibers makes the composite medium bi-continuous in the fiber direction and phase co-continuity is ensured in all fiber directions of multi-directional such networks which are through-sample spanning. Such networked fiber structures can be found in vary many different materials the matrix phase of which can have different (elasto-visco-plastic) behavior type, including possible damage, and most cases the fiber phase combines both stretching and bending straining modes at least in some ranges of deformation [69–72].

Here, this first step in the investigation of effective property estimates for matrices reinforced with fiber-networks will be restricted to purely elastic regime and bending mode analyses are delayed to subsequent works.

Now, when in heterogeneous structures of the general (inclusion or fiber) reinforced-matrix type the embedded domains are too dense in the matrix, the interactions between these domains cannot be disregarded in the estimation of some effective properties. The considered network-reinforced matrices suffer the specific difficulty that in addition to classical pair interaction effects between elements, changes in the network structure can be important, what is likely to further affect the interactions in return. For example, thanks to a compliant matrix and also depending on various possible interconnections between elements (from simple contacts to physical links), the network elements can significantly change their orientations and their inter-distances under straining, so deserving to currently account for the interaction changes.

How much pair interactions in clusters of inclusions or fibers affect the overall material behavior remains an open question. The fact that only the nearest neighbors to an inclusion are in practice considered to significantly matter has been pointed as excessively simplifying, even when no long range order exists [73]. For embedded domains that become aligned and get close to each other when the embedding matrix is soft enough to suffer a large deformation, interactions may become of non negligible effect even if the embedded domains are initially in quite dilute concentration. In some circumstances, when for example the interactions between domains increase in certain directions and oppositely decrease and vanish in other ones, it is certainly important to account for the current evolution of the interactions in estimating effective properties of composites and meta-materials. These interactions are not that easy to estimate. They can be accounted for either in some average or statistical

way or in fully deterministic manner, from the calculation of the interaction Eshelby tensors or related operators [74, 75] between all element pairs in a pattern, when there is some particular organization of the elements.

In many homogenization frameworks, the main role to estimate effective properties of heterogeneous structures of the reinforced matrix type is carried by the Eshelby tensors [76] which characterize the shapes of characteristic domains in an infinite medium. These domains can be either inclusions representative of the embedded phases (inhomogeneities) or also domains which represent a particular spatial distribution or organization symmetry of the embedded phases. Widely used, Eshelby tensors are non-uniform except for ellipsoidal domains or symmetries and no interactions. When a domain V does not represent a single inclusion but a pattern of them, the interaction Eshelby tensors between all element pairs constituting the pattern are also needed to fully obtain the global tensor for V [77]. While the interior Eshelby tensor of a V domain (say $\boldsymbol{E}^V(\boldsymbol{r})\,,\ \boldsymbol{r} \in V$) is not easily at hand for a general V shape even in the simplest cases of a matrix with isotropic properties, the interaction tensor between domain pairs is generally much harder to access, even with computational help. In order to estimate effective properties of reinforced matrices, it is often enough to consider, rather than the entire tensor field $\boldsymbol{E}^V(\boldsymbol{r})$ over V, a mean tensor form, say $\overline{\boldsymbol{E}^V}$, which can be computed in a simpler way: this mean global tensor comprises the appropriately weighted sum of all the mean interior tensors for the pattern elements and of all the mean pair interaction tensors between the elements.

The product $\boldsymbol{E}^V(\boldsymbol{r}) : \boldsymbol{C}^{-1}$ between the Eshelby tensor and the compliance (inverse stiffness) tensor $\boldsymbol{C}^{-1}$of the matrix in which V is embedded defines the so-called *modified Green operator integral*, derived from the Green tensor, to be denoted $\boldsymbol{t}^V(\boldsymbol{r})$ [78–80]. Again, if a mean global operator can be considered, then we have that $\overline{\boldsymbol{E}^V} : \boldsymbol{C}^{-1} = \overline{\boldsymbol{t}^V}$. The knowledge of $\boldsymbol{t}^V(\boldsymbol{r})$ is quite equivalent to the knowledge of $\boldsymbol{E}^V(\boldsymbol{r})$ with several advantages of the former on the latter as super-symmetry and positive definiteness [75, 81, 82] among others, some of which showing up when making use of the Radon transform (RT) method and inversion (IRT) formula [83] as the dissociation of geometry and property contributions which results in easier calculations.

We here use for short the terms "interior", "pair interaction" and "global interaction" operator, to name respectively, the mean (or uniform when so) modified Green operator integral representative of an embedded domain in a matrix, the mean interaction operator integral between any two such embedded domains and the whole mean interaction operator integral within a pattern of several domains.

In this context, mean operators of large, infinite-like, patterns, as those obtained

in earlier already cited works for spheres, spheroids or finite cylinder alignments are here shown of major interest. It will be specified which finite part of infinite patterns contributes to the global interaction, owing to an influence distance above which element interactions become negligible. On the contrary to a domain that represents a spatial distribution of inclusions or of patterns within which the element arrangement will somehow also evolve with their spatial distribution, this influence (or interaction cut-off) distance defines (unless changes in the matrix symmetry properties) a size and shape invariant influence zone around any element, and circumscribes a finite varying part of the infinite pattern. This limited influence zone conversely allows the use of the mean operator of infinite patterns as soon as the element number is large enough.

The present Chapter aims at being a preliminary examination of inter-penetrated fiber bundles with the goal of arriving, in the next Chapter, at describing the pantographic-inspired composite material. It will be pointed that the concept of infinite patterns suffering element interactions over a finite and invariant influence zone has specific interest for continuous fiber networks in which by definition a finite pattern cannot be specified while an interaction domain of finite size can be introduced.

3.2 Mean Green operator and effective properties of a planar alignment of fibers

The access to interaction estimates between the elements of such fiber networks imposes to solve analytically the interaction problem between two infinite parallel fibers with at first a circular cross section, a basic case which surprisingly was not present in explicit form in the literature so far, to the authors knowledge, even for cylinders of same cross section radius, and although the single cylindrical inclusion case has been already treated [84,85]. It is noteworthy that from the RT/IRT method, this one-cylinder problem is solved (the cylinder operator is obtained) in simple manner and with no calculations.

We start by solving the two-cylinder basic problem (the mean global cylinder pair operator), after which the exact analytical solution for the mean global Green operator of n-planar alignments of parallel infinite cylinders (up to infinite fiber number) is presented, in a quite simple derivation from the pair interaction. The operator solution for infinite one-directional bundles of parallel infinite cylinders is then obtained and shown to allowing applications for embedded structures of interpenetrated bundles in terms of effective properties.

Finally, in order to show how, with these available mean operators for infinite patterns, one can describe quite simply effective properties for the sorts of deformable fiber networks we are concerned with and how one can follow the effective property evolutions resulting from deformation of the fiber arrangement, a homogenization framework is necessary. Among the simplest homogenization frameworks which are likely to be used for such property estimates, we will use of the framework of Ponte-Castaneda and Willis (PC-W) [75], a type of mean field approximation which has also been shown to apply for patterns. While the validity of these homogenization frameworks is generally considered restricted to dilute inhomogeneity concentrations since the interactions are not, or not sufficiently, accounted for, the application to patterns allows the account of the interactions interior to the pattern, such that only the interaction between patterns remains to be improved for large concentrations. If when the larger is the representative pattern the lower is the disregarded interaction part, the use of infinite-like patterns with all interior pair interactions possibly accounted for at any concentration of the elements is expected to substantially correct, if not suppress, these restrictions. It will be shown that the PC-W estimate form remains relevant at the limit of infinite representative patterns when the representative spatial distribution symmetry is taken to be the one of the interaction domain.

3.2.1 Introduction of the Green operator and of the Radon transform

Consider an infinite homogeneous elastic medium described by its elastic moduli tensor C_{ijkl}. We describe the displacement field $\boldsymbol{u}(\boldsymbol{r})$ due to a punctual force $\boldsymbol{f}(\boldsymbol{r'})$ applied to a different point of the medium, where $\boldsymbol{u} = (u_1, u_2, u_3)$ and similarly for $\boldsymbol{r}$,$\boldsymbol{r'}$, as

$$u_i(\boldsymbol{r}) = G_{ij}(\boldsymbol{r}, \boldsymbol{r'}) f_j(\boldsymbol{r'}) \tag{3.1}$$

The Green strain tensor $G_{ij}(\boldsymbol{r}, \boldsymbol{r'})$ in Eq. (3.1) is defined from the stress equilibrium relation $\sigma_{ij,j}(\boldsymbol{r}) = \left(C_{ijkl}(\boldsymbol{r})\, u_{k,l}(\boldsymbol{r})\right)_{,j} = 0$ such that, with $C_{ijkl}(\boldsymbol{r}) = C_{ijkl} + \delta C_{ijkl}(\boldsymbol{r})$

$$C_{ijkl} G_{kh,lj}(\boldsymbol{r}, \boldsymbol{r'}) + \delta(\boldsymbol{r}, \boldsymbol{r'})\, \delta_{ih} = 0 \tag{3.2}$$

in which the double derivative of the Green tensor $G_{ij}(\boldsymbol{r}, \boldsymbol{r'})$ is called the modified Green operator

$$\Gamma_{klhj}(\boldsymbol{r}, \boldsymbol{r'}) = \frac{\partial^2 G_{kh}(\boldsymbol{r}, \boldsymbol{r'})}{\partial x_l \partial x_j} \tag{3.3}$$

We next consider a bounded domain V into the medium. Integrating the operator $\Gamma_{pqjn}(\boldsymbol{r}, \boldsymbol{r'})$ over this domain, formally yields the so-called modified Green operator

integral

$$t^V_{pqjn}(\boldsymbol{r}) = \int_V \Gamma_{pqjn}(\boldsymbol{r}, \boldsymbol{r'})\ d\boldsymbol{r'} \tag{3.4}$$

An explicit calculus of the mean value of $\boldsymbol{t}^V(\boldsymbol{r})$ over V starts by Fourier transforming Eq. (3.2) making use of the Fourier transform for the Green tensor $\hat{G}_{pj}(\boldsymbol{k}) = \int G_{pj}(\boldsymbol{r})\, e^{i\boldsymbol{k}\cdot\boldsymbol{r}}\ d\boldsymbol{r}$. The Fourier transform of Eq. (3.2) is then

$$C_{mnpq}\hat{G}_{pj}(\boldsymbol{k})\, k_q k_n = \delta_{mj} \tag{3.5}$$

Introducing spherical coordinates (k, ϑ, φ) in the Fourier basis further yields

$$C_{mnpq}\omega_q\omega_n\hat{G}_{pj} = \delta_{mj} = M_{mp}\hat{G}_{pj} \tag{3.6}$$

where $\boldsymbol{\omega} = (\sin\vartheta\cos\varphi\ , \sin\vartheta\sin\varphi\ , \cos\vartheta\ )$ and a new tensor M_{mp} is defined by contraction. Finally, introducing the elementary operator $t^e_{pqjn}(\omega) = M^{-1}_{pj}\omega_q\omega_n$, one arrives at

$$t^V_{pqjn}(\boldsymbol{r}) = \frac{1}{8\pi^3}\int_V \left(\int_\Omega t^e_{pqjn}(\omega)\int_{k=0}^{\infty} k^2 e^{-i\boldsymbol{k}\cdot\left(\boldsymbol{r}-\boldsymbol{r'}\right)} dk\ d\omega\right) d\boldsymbol{r'} \tag{3.7}$$

This last equation can be simply rearranged by permuting the V and Ω integrals and by introducing a weight function $\psi(\omega, \boldsymbol{r})$ such as to finally write

$$t^V_{pqjn}(\boldsymbol{r}) = \int_\Omega t^e_{pqjn}(\omega)\,\psi(\omega, \boldsymbol{r})\, d\omega \tag{3.8}$$

where

$$\psi(\omega, \boldsymbol{r}) = \frac{1}{8\pi^3}\xi_V(\omega, \boldsymbol{r}), \qquad \xi_V(\omega, \boldsymbol{r}) = \int_V \left(\int_{k=0}^{\infty} k^2 e^{-i\boldsymbol{k}\cdot\left(\boldsymbol{r}-\boldsymbol{r'}\right)} dk\ d\omega\right) d\boldsymbol{r'} \tag{3.9}$$

Eq. (3.8) is the inverse Radon transform (IRT) form of $t^V_{pqjn}(\boldsymbol{r})$. In Eq. (3.9) it has been defined the weight function $\psi(\omega, \boldsymbol{r})$, in which all the geometrical information of the considered embedded inclusion pattern is contained. The powerfulness of this IRT transform is to separate the concerned operator in two parts: while the $t^e_{pqjn}(\omega)$ operators are only material property orientation-dependent (for each material property case, a table of them can be calculated once and for all), the weight function $\psi(\omega, \boldsymbol{r})$ of a specific inclusion or pattern V is valid regardless of the properties of the embedding matrix, whether them be isotropic or not and whether them be elastic or else. Although both operator parts are at analytical hand for quite many

cases, the integral resolution in Eq. (3.8) can remain quite complicated especially for general property anisotropy.

The main problem from now amounts to well characterize $\psi(\omega, \boldsymbol{r})$ in order to describe the pattern or network organization in the matrix of the composite of concern. Using the Radon inversion formula in its fully geometrical form, the function $\psi^V(\omega,r)$ can be written

$$\begin{aligned}
\psi^V(\omega, r) &= -\int_V \frac{\delta''(\omega \cdot (r - r'))}{8\pi^2} d\boldsymbol{r}' \\
&= -\int_{z'=D_V^-(\omega)}^{z'=D_V^+(\omega)} \left(\int_{\boldsymbol{s}_V(z',\omega)} \boldsymbol{s}_V(z', \omega) \right) \frac{\delta''(\boldsymbol{z} - \boldsymbol{z}', \omega)}{8\pi^2} d\boldsymbol{z}' \\
&= -\frac{\tilde{\boldsymbol{s}}_V''(\boldsymbol{z}, \omega)}{8\pi^2}
\end{aligned} \tag{3.10}$$

where $\mathrm{s}_V(z,\omega)$ is the planar section area of V through r and of ω-normal, by the plane of equation $z = \omega \cdot r$. Then, $\tilde{\mathrm{s}}_V{}''(z,\omega) = \frac{\partial^2}{\partial z^2} s_V(z,\omega)$ is the second z-derivative of $\mathrm{s}_V(z,\omega)$, indicated by the tilde to be understood as a regularized form of it. Next setting $\mathrm{d}\mathbf{r} = \mathbf{ds}_V(z,\omega)\ \mathrm{dz}$ as having set $\mathrm{d}\mathbf{r}' = \mathbf{ds}_V(z',\omega)\ \mathrm{dz}'$ in Eq. (3.2), the mean value of this weight (or shape) function over V reads, $\forall \omega \in \Omega$

$$\overline{\psi^V}(\omega) = -\frac{1}{8\ \pi^2 \mathrm{v}} \int_{D_V^-(\omega)}^{D_V^+(\omega)} \tilde{\mathrm{s}}_V{}''(z,\omega)\ s_V(z,\omega)\ dz = \frac{1}{8\ \pi^2 v} \int_{D_V^-(\omega)}^{D_V^+(\omega)} \left(\tilde{s}_V{}'(z,\omega)\right)^2\ dz \tag{3.11}$$

The interval $\left[\mathrm{D}_V^-(\omega),\ \mathrm{D}_V^+(\omega)\right] = 2\mathrm{D}_V(\omega)$ corresponds to the breadth of V in the ω direction (*i.e.* the distance between the two opposite tangent planes to V, of ω-normal), which characterizes the support function of V when strictly convex ($\mathrm{D}_V(\omega) = \max_{r \in V}(\omega \cdot r)$), or more generally, in particular when V is a pattern of inclusions, of the convex hull of V.

It is noteworthy that Eq. (3.9) formally holds whether $\boldsymbol{r}$ is an interior or an exterior point to V, with the difference that the boundary of V always contributes at exterior points when it only contributes at interior points when V is not a simply connected convex body. So it is as well for the Green operator given by Eq. (3.8).

Thus a similar discussion can be considered in the case of a pair of inclusions and from it to any inclusion number n in a pattern up to infinite sets which can be seen as multiply connected (non convex) inclusions V. At any interior point $\boldsymbol{r}$ of such a V pattern of n (possibly infinite) V_i inclusion number, the weight function and the related Green operator comprises the interior term from Vi when $\boldsymbol{r}$ is interior to V_i

and all the exterior contributions from the other V_j domains ($j \neq i$). At exterior points to V both the weight function and the Green operator assemble the n exterior contributions from all the V_j domains which constitute V. As far as the mean Green *interior* operator (mGO) of a general V pattern is of concern here, the mean weight function for an (up to infinite) number of inclusions then reads from Eq. (3.10)

$$\bar{\psi}^V(\omega) = \frac{1}{8\pi^2 v} \int_{D_V^-(\omega)}^{D_V^+(\omega)} \left(\sum_{i=1}^{n} \tilde{s}'_{V_i}(z,\omega) \right) \left(\sum_{j=1}^{n} \tilde{s}'_{V_j}(z,\omega) \right) dz \tag{3.12}$$

$$\bar{\psi}^V(\omega) = \sum_{i=1}^{n} \frac{v_i}{v} \bar{\psi}^{V_i}(\omega) + \sum_{i=1}^{n} \sum_{j=1}^{n} \frac{v_i + v_j}{v} \bar{\psi}^{V_i,V_j}(\omega) \tag{3.13}$$

From comparing Eq.(3.12) with Eq. (3.11), it is immediate to see that

$$\overline{\psi^{Vi}}(\omega) = \int_{D_{Vi}^-(\omega)}^{D_{Vi}^+(\omega)} \frac{\left(\tilde{\mathrm{s}}_{Vi}{}'(z,\omega)\right)^2}{8\ \pi^2 v_i}\ dz \tag{3.14}$$

$$\overline{\psi^{Vi,Vj}}(\omega) = \int_{\sup(D_{Vi}^-(\omega), D_{Vj}^-(\omega))}^{\inf(D_{Vi}^+(\omega), D_{Vj}^+(\omega))} \frac{\tilde{\mathrm{s}}_{Vi}{}'(z,\omega)\tilde{s}_{Vj}{}'(z,\omega)}{8\ \pi^2 (v_i + v_j)}\ dz \tag{3.15}$$

The pattern mGO follows as

$$\overline{t^V} = \sum_{\mathrm{i}=1}^{\mathrm{n}} \frac{\mathrm{v_i}}{\mathrm{v}} \overline{\mathrm{t^{Vi}}} + \sum_{i=1}^{n} \sum_{j=i+1}^{n} \left(\frac{\mathrm{v_i} + \mathrm{v_j}}{\mathrm{v}} \right) \overline{\mathrm{t^{Vi,Vj}}}, \quad \text{with } \mathrm{v} = \sum_{\mathrm{i}=1}^{\mathrm{n}} \mathrm{v_i} \tag{3.16}$$

Infinite series in Eqs (3.16) formally provide the mean weight function and the related mGO for infinite inclusion patterns. The first (simple sum) term corresponds to the interior parts from the individual pattern elements and reduces to a single term when all elements are identical. The second (double sum) term represents the global interaction part in the pattern mGO. Only the interaction term depends on the element inter-distances.

3.2.2 Application to single and pairs of ellipsoids

For ellipsoids V_0, which include the infinite cylinders with elliptic or circular cross section at limit (together with zero-thickness platelets at the other extreme), the interior uniform weight function takes the simple form (where $z = \omega \cdot \mathbf{r}$ and $\left[-\mathrm{D_V^{\mathit{ell}}}(\omega), \mathbf{D_V^{ell}}(\omega)\right]$

is the breadth of V_0 in the ω-normal direction)

$$\psi_{\mathrm{V0}}^{\mathrm{ell}}(\omega)=\left(-\frac{1}{8\pi^2}\right)\frac{\partial^2}{\partial \mathrm{z}^2}\left(\frac{3\ \mathrm{v}}{4\ \mathrm{D}_{\mathrm{V0}}^{ell}(\omega)}\ \left(\mathbf{1}-\left(\frac{\mathbf{z}}{\mathbf{D_{V0}^{ell}}(\omega)}\right)^{\mathbf{2}}\right)\right)=\left(\frac{3}{4\ \pi}\right)^2\left(\frac{\mathrm{v}}{3\ \mathrm{D}_{\mathrm{V0}}^{ell}(\omega)^{\mathbf{3}}}\right) \tag{3.17}$$

Accordingly, the mean pair interaction operator $\overline{\mathbf{t}_{\mathrm{V}}^{\mathrm{V1,V2}}}=\int_{\mathbf{\Omega}}\overline{\psi_{\mathrm{V}}^{\mathrm{V1,V2}}}(\omega)\mathbf{t^P}(\omega)\mathbf{d}\omega$ between two general inclusions, V_1 and V_2, is the cross part of the global interior mean operator $\overline{\mathbf{t}^{\mathrm{V}}}$ for the domain $\mathrm{V}=\mathrm{V}_1\bigcup\mathrm{V}_2$ ($\mathrm{V}_1\bigcap\mathrm{V}_2=\emptyset$), of volume $V=V_1+V_2$ and reads

$$\overline{\mathbf{t}^{\mathrm{V}}}=\frac{1}{\mathrm{v}}\sum_{\mathbf{i=1,2}}\sum_{\mathbf{j=1,2}}\int_{\mathbf{Vi}}\int_{\mathbf{Vj}}\mathbf{\Gamma}(\mathbf{r}-\mathbf{r}')\mathbf{dr}'\mathbf{dr}=\frac{\mathrm{v1}}{\mathrm{v}}\overline{\mathbf{t^{V1}}}+\frac{\mathbf{v2}}{\mathbf{v}}\overline{\mathbf{t^{V2}}}+\overline{\mathbf{t_V^{V1,V2}}} \tag{3.18}$$

For V_1 and V_2 congruent to a same V0 shape one has for the interior operator parts, similarly to the weight function parts $\frac{\mathrm{v1}}{\mathrm{v}}\overline{\mathbf{t^{V1}}}+\frac{\mathbf{v2}}{\mathbf{v}}\overline{\mathbf{t^{V2}}}=\overline{\mathbf{t}^{\mathrm{V0}}}$. We now on specialize to pairs of spheroids.

In contrast with previously considered axially symmetric inclusion pairs and patterns with regard to the x_3 axis (θ=0), we here consider two congruent spheroids V1, V2, of x_2-oriented symmetry axis (see Fig. 3.2)), say ($\theta=\pi/2$, $\varphi=\pi/2$) and lying in plane x_2-x_3. The calculations, according to the IRT method, for the mean pair interaction weight function and operator between two parallel identical spheroids at the limit of 2 infinite cylinders, are reported in Appendix B.

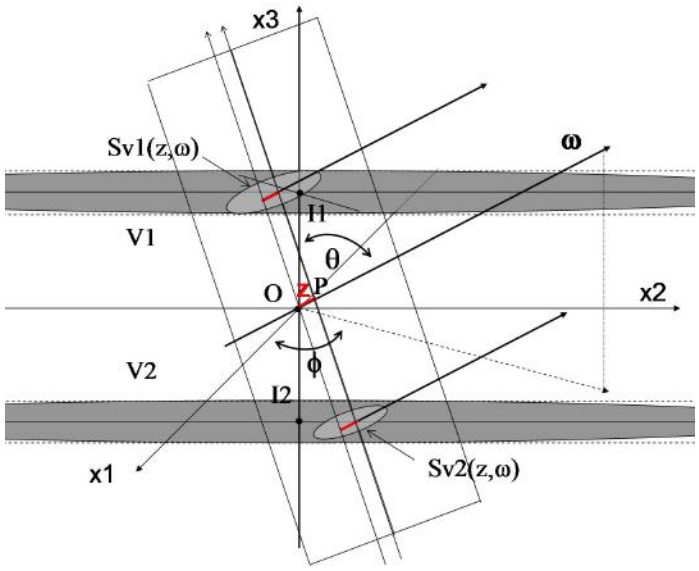

Figure 3.2: Pair of x_2-oriented parallel identical prolate (infinite-like) spheroids V_1, V_2 in plane $x_2 - x_3$ and section areas by the plane of equation z = $\omega \cdot \mathbf{r}$.

All calculations done, one thus obtains for $\zeta \to \infty$ the needed independent two functions

$$I^{1,0}_{2cyl\infty} = C_2 = \sum_{i(m,n)=1}^{3} {}^{\zeta^\infty} I^{1,0}_{i(m,n)} = -\frac{{\rho_0}^2}{10} \tag{3.19}$$

$$I^{2,0}_{2cyl\infty} = C_4 = \sum_{i(m,n)=1}^{3} {}^{\zeta^\infty} I^{2,0}_{i(m,n)} = -\frac{{\rho_0}^2}{20} - \frac{9{\rho_0}^4}{280} \tag{3.20}$$

from which the three other involved trigonometric functions result as $S_2 = -I^{1,0}_{2cyl\infty}$, $S_2C_2 = I^{1,0}_{2cyl\infty} - I^{2,0}_{2cyl\infty}$, $S_4 = I^{2,0}_{2cyl\infty} - 2I^{1,0}_{2cyl\infty}$. These 5 functions yield the terms of the mean pair interaction operator for the x_2-oriented cylinders reported in Tab 3.1, using the two constant $A = -\frac{1}{2\mu(1-v)}$ and $B = \frac{1}{\mu}$ for isotropic elastic-like matrices of shear modulus μ and Poisson ratio ν (or the single one $B = \frac{1}{D}$ for dielectric-like ones, with dielectric modulus D). The first column of Tab. 3.1 reports the interior operator for an x_2-oriented fiber of elliptic cross sections having their two axes along the x_1 and x_3 axes. The coefficient η is the stretch in direction x_3. Infinite (resp. null) aspect ratio η yields the laminate operator with normal x_1 (resp. x_3). The interior operator of the single infinite x_2-oriented cylindrical fiber (η=1) is retrieved from using the first of the three elements of the integral in Eq. (B1.3b), taking

θmin(φ)=0 (resp. xmax(φ)=1), for all φ values, as the min (resp. max) integration bound, say ρ_0=1, what gives 1/2 and 3/8 for p=1 and p=2 respectively. Then, the different terms of the global operator for the cylinder pair fully result from Tab. 3.1 for the x_2-oriented cylinders from adding the interior (for η=1) and the interaction operator, and then for any orientation using the appropriate rotation matrix. The sphere and sphere pair terms are also reported for comparison. Here, as the limit case when $\zeta = 1$, they simply correspond to the θ or x integrals, with the φ-integrals simply multiplying the θ-integral results by a factor $\frac{2}{\pi}\int_0^{\pi/2}\cos^{2q}\phi d\phi$, q=0,1,2).

The dimensionless non zero terms of the elasticity mean global (interior plus interaction) pair operator for parallel identical cylinders (say multiplied by the shear modulus μ) are plotted in Fig. 3.3 as a function of the normalized distance L/R and for Poisson coefficient of 0.3 and 0.5 (limit incompressible case). At large enough distance L, the interaction part vanishes and the global operator reduces to the interior one. The influence or cut-off interaction distance is typically ten times the cylinder radius, with no significant effect of Poisson ratio in the range $v \in (0.3 - 0.5)$. Note that as defined in Table 1, the operators are, from left to right, for an elliptic cylinder that flattens normally to x_3 (resp. x_1) axis with increasing (resp. decreasing) η, for a circular x_2-cylinder pair that lays in the x_2-x_3 plane and for a sphere pair aligned along the x_3 axis. From Eq. (3.6), the terms of the pair interaction operator obeys the polynomial decomposition in ρ_0

$$\overline{\mathbf{t}_{\rho_0}^{\mathrm{cyl,cyl}}} = \mathrm{v0}{\rho_0}^2 + \mathrm{w0}{\rho_0}^4 \tag{3.21}$$

while for the sphere pair case it was of the form $\overline{\mathbf{t}_{\rho_0}^{\mathrm{sph,sph}}} = \mathrm{v0}{\rho_0}^3 + \mathrm{w0}{\rho_0}^5$ (with different tensors $\mathbf{v}0, \mathrm{w}0$). As for spheres, the $\mathbf{w}0$ part is only present for elastic-like material properties, in which case certain $(ijkl)$ components (when $\mathrm{v0_{ijkl}}$ and $\mathrm{w0_{ijkl}}$ have opposite signs) of the interaction operator can exhibit an optimum for $\rho_{0*} < 1$ which depends on the Poisson ratio through the A/B coefficient ratio. The next section examines patterns of parallel infinite cylindrical fibers and gives their global mean operator in exact analytical form as well.

	x_2 η-elliptic cylinder interior $\mathbf{t}^{x_2\eta-cyl}$	x_2 cylinder general pair interaction form	x_2 cylinder pair interaction form $\mathbf{v}0\rho_0{}^2 + \mathbf{w}0\rho_0{}^4$	Sphere Interior $\mathbf{t}^{sph}$	Sphere pair interaction form $\mathbf{v}0\rho_0{}^3 + \mathbf{w}0\rho_0{}^5$
1111	$\frac{(2+\eta)A}{2(1+\eta)^2} + \frac{B}{1+\eta}$	AS4+ BS2 =A(C4-2C2) - BC2	$\frac{2\lvert B\rvert - 3\lvert A\rvert}{20}\rho_0{}^2 + \frac{9\lvert A\rvert}{280}\rho_0{}^4$	$\frac{3A+5B}{15}$	$\frac{2\lvert B\rvert - 3\lvert A\rvert}{48}\rho_0{}^3 + \frac{3\lvert A\rvert}{160}\rho_0{}^5$
1122	0	0	0	$\frac{A}{15}$	$-\frac{\lvert A\rvert}{48}\rho_0{}^3 + \frac{\lvert A\rvert}{160}\rho_0{}^5$
1133	$\frac{\eta A}{2(1+\eta)^2}$	AS2C2 = A(C2-C4)	$\frac{\lvert A\rvert}{20}\rho_0{}^2 - \frac{9\lvert A\rvert}{280}\rho_0{}^4$	$\frac{A}{15}$	$\frac{\lvert A\rvert}{24}\rho_0{}^3 - \frac{4\lvert A\rvert}{160}\rho_0{}^5$
2222	0	0	0	$\frac{3A+5B}{15}$	$\frac{2\lvert B\rvert - 3\lvert A\rvert}{48}\rho_0{}^3 + \frac{3\lvert A\rvert}{160}\rho_0{}^5$
2233	0	0	0	$\frac{A}{15}$	$\frac{\lvert A\rvert}{24}\rho_0{}^3 - \frac{4\lvert A\rvert}{160}\rho_0{}^5$
3333	$\frac{\eta(1+2\eta)A}{2(1+\eta)^2} + \frac{\eta B}{1+\eta}$	AC4 + BC2	$\frac{-2\lvert B\rvert + \lvert A\rvert}{20}\rho_0{}^2 + \frac{9\lvert A\rvert}{280}\rho_0{}^4$	$\frac{3A+5B}{15}$	$-\frac{2\lvert B\rvert}{24}\rho 0^3 + \frac{8\lvert A\rvert}{160}\rho 0^5$
2323	$\frac{\eta B}{4(1+\eta)}$	(B/4)C2	$-\frac{\lvert B\rvert}{40}\rho 0^2$	$\frac{2A+5B}{30}$	$\frac{4\lvert A\rvert - \lvert B\rvert}{96}\rho_0{}^3 - \frac{4\lvert A\rvert}{160}\rho_0{}^5$
3131	$\frac{\eta A}{2(1+\eta)^2} + \frac{B}{4}$	AS2C2	$\frac{\lvert A\rvert}{20}\rho_0{}^2 - \frac{9\lvert A\rvert}{280}\rho_0{}^4$	$\frac{2A+5B}{30}$	$\frac{4\lvert A\rvert - \lvert B\rvert}{96}\rho_0{}^3 - \frac{4\lvert A\rvert}{160}\rho_0{}^5$
1212	$\frac{B}{4(1+\eta)}$	(B/4)S2 = -(B/4)C2	$\frac{\lvert B\rvert}{40}\rho_0{}^2$	$\frac{2A+5B}{30}$	$\frac{\lvert B\rvert - \lvert A\rvert}{48}\rho_0{}^3 + \frac{\lvert A\rvert}{160}\rho_0{}^5$

Table 3.1: Interior operator of η-elliptic x_2-cylinder (col.1) and sphere (col.4); Mean pair interaction operator for 2 circular x_2-cylinder (col. 2 and 3) and spheres (col. 5) aligned along x_3.

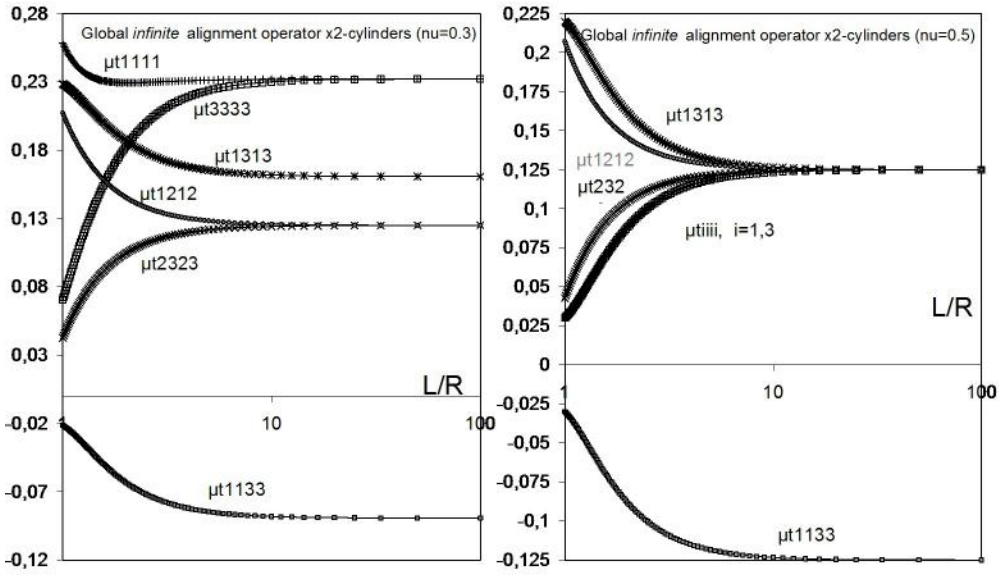

Figure 3.3: Global (interior plus interaction) operator for an alignment of parallel infinite x_2-cylinders in plane of normal x_1.

3.2.3 Planar alignments of C-fibers and of SQ-beams and their interaction mGOs

As far as the matrix phase is considered to have isotropic elastic-like properties, all the non-vanishing components of the mGO for any inclusion pattern depend on two independent trigonometric functions only and can therefore be written in terms of two functions. Thanks to these simplifying characteristics, a first case of infinite pattern (say coaxial alignments of non necessarily all size-identical oblate spheroids including spheres) was explicated in [86], in the case of isotropic matrix properties, and prolate spheroids being treatable identically. The case of aligned coaxial fiinite cylinders with same radius was next treated in [87, 88] still for isotropic (elastic-like or dielectric-like) matrix properties.

In the case of inclusion patterns made of parallel fibers in a plane, these two functions can be written as $C_2(x)$ and $C_4(x)$ say, with x standing for a normalized characteristic element inter-distance (isotropic dielectric-like properties only call for the $C_2(x)$ function). Furthermore, these two functions share into an x-independent part $(C^{(2)}, C^{(4)})$ which corresponds to the interior mGO term and into a global interaction part, the rest of it, between all the pattern element pairs. This rest is the

	1111	1133	3333	2323	1313	1212
$\bar{\boldsymbol{t}}_{C^M}^{Genfiber,x2}$	$AS^{(4)}+BS^{(2)}$	$A(S^{(2)}C^{(2)})$	$AC^{(4)}+BC^{(2)}$	$BC^{(2)}/4$	$A(S^{(2)}C^{(2)})+B/4$	$BS^{(2)}/4$
$\bar{\boldsymbol{t}}_{C^M}^{C-fiber,x2}$	$\frac{3A+4B}{8}$	$\frac{A}{8}$	$\frac{3A+4B}{8}$	$\frac{B}{8}$	$\frac{A+2B}{8}$	$\frac{B}{8}$
$\bar{\boldsymbol{t}}_{C^M}^{SQ-Beam,x2}$	$\frac{(6-\pi)A+4B}{8}$	$\frac{(\pi-2)A}{8}$	$\frac{(6-\pi)A+4B}{8}$	$\frac{B}{8}$	$\frac{(\pi-2)A+2B}{8}$	$\frac{B}{8}$
$\boldsymbol{t}_{C^M}^{Lam,x2-x1}$	0	0	A+B	B/4	B/4	0

Table 3.2: Non zero interior mGO terms for x2-oriented generic fibers, C-fiber, SQ-beams and x2-x1 laminate in isotropic media ($B = 1/\mu$,$A = -B/2(1-v)$), $S^{(2)} = 1 - C^{(2)}$,$(S^{(2)}C^{(2)}) = C^{(2)} - C^{(4)}$,$S^{(4)} = 1 - 2C^{(2)} + C^{(4)}$.

x-dependent part of the mGO.

Now on, the reported work strictly specializes to 3D structures made from piling FPAs of n infinite parallel fibers of same cross section shape and size and equally inter-distant, with n being large enough to be taken as infinite. The mGOs for such FPAs in isotropic elastic-like matrices were previously solved in exact analytical form in [85] for beams with rectangular cross sections and for cylinders in [63], the related effective properties for both FPA types being also explicated. Here, the exact mGO solution for cylindrical fibers (to be denoted C-fibers) will be recalled for comparison with an accurately approximate analytical mGO form for infinitely many parallel beams of same square cross section (now on denoted SQ-beams), which is here newly introduced for being used (fiber cross sections in pantographic structures are more likely rectangular than circular and square is a good compromise) and in easier way than the exact one.

The interior parts of the C2 and C4 functions for the SQ-beam case read simply $C^{(2)}_{\mathrm{SQB}} = \frac{1}{2}$ and $C^{(4)}_{\mathrm{SQB}} = \frac{6-\pi}{8}$. The C2 interior function equals the C-fiber one, $C^{(2)}_{\mathrm{CFib}} = \frac{1}{2}$and the C4 one does not differ much from $C^{(4)}_{\mathrm{CFib}} = \frac{3}{8}$. The resulting six non zero components of the interior mGO of x2-oriented infinite fibers are reported in Tab. 3.2 in generic form and for the circular and square cross sections here of concern. The uniform interior GO of laminates with x_3 normal is also recalled.

In [63] it has been shown that the global mGO for a planar n-alignment of parallel

	$C_2(x)$	$C_4(x)$
Q	-0.1	-0.05
S	0.	-0.0321

Table 3.3: Coefficients of C_i(x) functions for C-fiber infinite PAs in Eq. (3.25).

infinite identical cylinders can be written as

$$\begin{aligned}\overline{\boldsymbol{t}_{\rho_0}^{ncyl}} &= \frac{1}{n}\left(n\boldsymbol{t}^{cyl}+2\sum_{i=1}^{n-1}(n-i)\overline{\boldsymbol{t}_{\rho_i}^{cyl-cyl}}\right)=\boldsymbol{t}^{cyl}+2\sum_{i=1}^{n-1}\frac{(n-i)}{n}\left(\frac{\boldsymbol{v}_0}{i^2}\rho_0^2+\frac{\boldsymbol{w}_0}{i^4}\rho_0^4\right)\\ &= \boldsymbol{t}^{cyl}+2\left(\sigma_2^{(n)}\boldsymbol{v}_0\rho_0^2+\sigma_4^{(n)}\boldsymbol{w}_0\rho_0^4\right)=\boldsymbol{t}^{cyl}+\left(\boldsymbol{v}_0^{(n)}\rho_0^2+\boldsymbol{w}_0^{(n)}\rho_0^4\right)\end{aligned} \tag{3.22}$$

That is, while the interior part of the mGO is invariant, the interaction operator for n elements is directly obtained from the pair interaction operator, with two multipliers $2\sigma^{(2)}$(n) and $2\sigma^{(4)}$(n) respectively applying on the functions $C_2(x)$ and C_4(x) (the x variable in the functions $C_j(x)$ stands for $\rho_0 = R/L$ in Eqs. (3.19)-(3.20).

For $n = 2$, $i = 1$, $2\sigma(2)_2 = 2\sigma_4^{(2)} = 1$ and $\overline{\boldsymbol{t}_{\rho_0}^{2cyl}} = \boldsymbol{t}^{cyl} + (\boldsymbol{v}_0\rho_0^2 + \boldsymbol{w}_0\rho_0^4)$, where the $\boldsymbol{v}_0 = \boldsymbol{v}_0^{(2)}and\boldsymbol{w}_0 = \boldsymbol{w}_0^{(2)}$ tensorial notations represent the coefficients of the different non zero terms of the operator. For $n \to \infty$, the limit for the infinite series, $\Sigma(q) = \lim_{n\to\infty}\sigma_q^{(n)} = \lim_{n\to\infty}\sum_{i=1}^{n-1}\frac{(n-i)}{n}\left(\frac{1}{i^q}\right)$ is the Riemann Zeta function $Z(q) = \lim_{n\to\infty}\sum_{i=1}^{n-1}\left(\frac{1}{i^q}\right)$, which is finite, $\forall q > 1$. At the limit of an infinite alignment of parallel cylinders one obtains with $Z(2)$=π2/6, $Z(4)$=π^4/90

$$\overline{\boldsymbol{t}_{\rho_0}^{\infty cyl}} = \boldsymbol{t}^{cyl} + \left(\boldsymbol{v}_0^{(\infty)}\rho_0^2 + \boldsymbol{w}_0^{(\infty)}\rho_0^4\right) = \boldsymbol{t}^{cyl} + 2\left(Z(2)\boldsymbol{v}_0\rho_0^2 + Z(4)\boldsymbol{w}_0\rho_0^4\right) \tag{3.23}$$

with the particular (not always the maximal) values when all the cylinders are at contact

$$\overline{\boldsymbol{t}_{\rho_0=1}^{\infty cyl}} = \boldsymbol{t}^{cyl} + 2\left(Z(2)\boldsymbol{v}_0 + Z(4)\boldsymbol{w}_0\right) \tag{3.24}$$

More synthetically, the functions $C_2(x)$ and $C_4(x)$ for the interaction part of the mGO for infinite FPAs of C-fibers can be written, with $x = \rho_0$ and the Q_i, S_i coefficient values given in Tab. 3.3, as the polynomial form

$$C_i(x) = Q_i x^2 + S_i x^4, i = 2, 4 \tag{3.25}$$

In Fig. 3.4, it is shown the behavior of the $C_2(x)$ and $C_4(x)$ functions for the interaction part of the mGO for FPAs of C-fibers, according to Eqs. (3.25). The variations of the global mGO non zero terms with the C-fiber inter distance (1/x=L/R) according to Eq. (3.24) are plotted in Fig. 3.5(left) from [63] for a Poisson ratio of 0.5. When the fiber inter-distance increases, the global mGO reduces to its interior part. At fiber contact, the mGO interaction part is optimal, but terms can either be positive or negative.

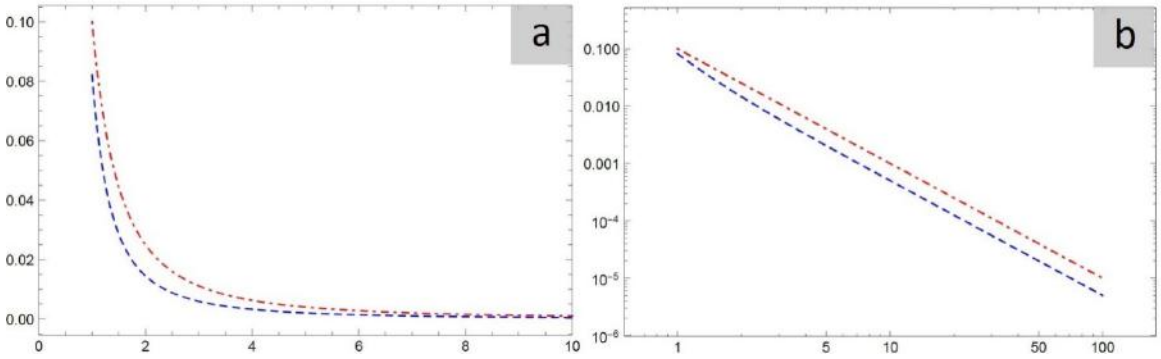

Figure 3.4: The (left) C2(x) (red) and C4(x) (blue) mGO interaction function parts for C- fibers; (right)log/log plot.

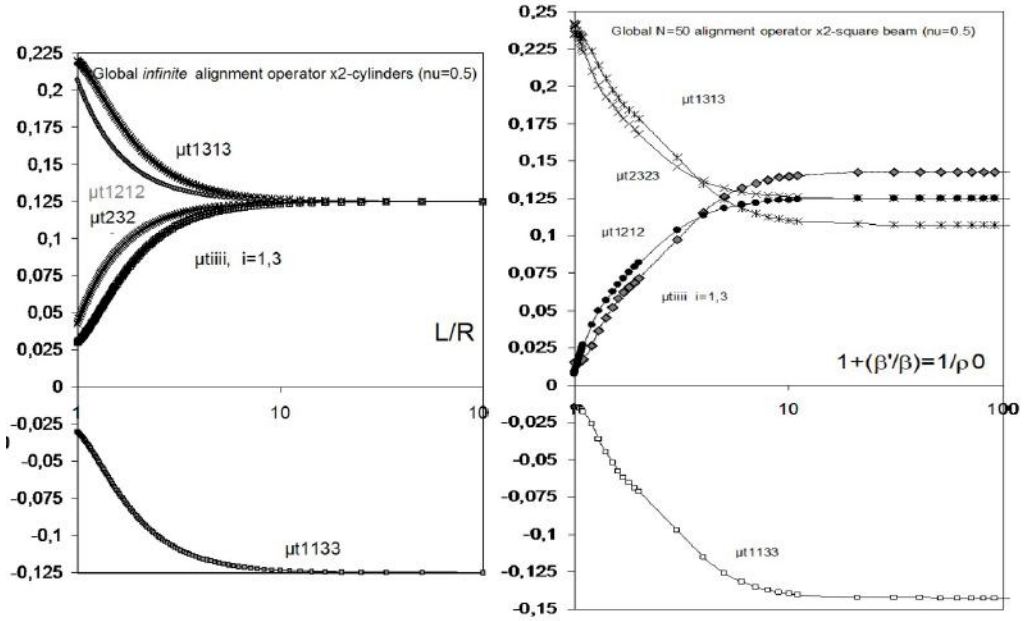

Figure 3.5: Variation with fiber inter-distance 1/x of the global mGO terms for an infinite FPA of x_2-parallel infinite (left) C-fibers in plane of normal x_1 from [63] and of (right) SQ-beams of square cross section in plane of normal x_3 (indices 1 and 3 are to be inverted), from [85].

The Fig.3.5(right) reports from [85], the corresponding global mGO non zero term variations for SQ-beams with the normalized inter-distance (1/x) [1]. As for the cylinder alignments, this Figure shows that the influence zone for all the pair interactions between SQ-beams in an infinite PA is also ten to twenty times the beam width, depending on the wished precision. These variations of the mGO interaction part in the global mGO for SQ-beams were obtained from using the exact although complicated solution reported in the cited reference, not to be repeated here. From a graphical analysis of the numerical plots reported in Fig. 3.4 (from that exact solution for the mGO interaction part of infinite SQ-beam PAs) a simplified form of easier use is shown to write from two functions $C_i(x)$ (i=1,2) which can be expressed as

$$C_i\left(x\right) = x^2\left(R_i x^{-2} + Q_i x^{-1} + S_i\right)\frac{1}{1+\alpha_i\left(x^{-3}-1\right)} \tag{3.26}$$

[1] Indices 1 and 3 are inverted since the alignment is of normal x1 for C-fibers and of normal x3 for SQ-beams.

	$C_2(x)$	$C_4(x)$
R	0.786	0.162
Q	-1.330	-0.376
S	1.043	0.656
α	0.162	0.049

Table 3.4: Coefficients of C_i(x) functions for SQ-beams infinite PAs in Eq. (15a).

where the involved coefficients are reported in Tab. 3.4 for the two functions $C_2(x)$ and $C_4(x)$.

For the reason that in pantographic structures the fiber inter distance is generally at most of the order of ten times the fiber dimension, it is here possible to consider a shortened form of Eq. (3.26), without the α-correction (which mostly corrects the long-range behavior), say the rank-2 polynomial form

$$C_i\left(x\right) \simeq x^2\left(R_i x^{-2} + Q_i x^{-1} + S_i\right) = R_i + Q_i x + S_i x^2 \tag{3.27}$$

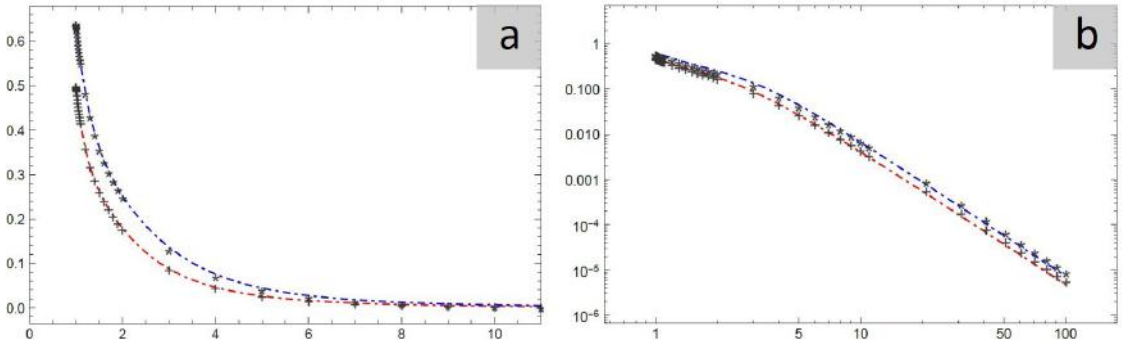

Figure 3.6: The (left), approximate C2(x) (red dashes and symbol "+" for numerics) and C4(x) (blue dashes and symbol "*" for numerics) mGO interaction function parts for squared beams; (right) log/log plot.

The Tab. 3.5 reports the generic form of the interaction mGO $\boldsymbol{t}_{\boldsymbol{C}^M}^{int(8Align(0))}$ for a planar alignment of x_2-oriented fibers in the plane of normal x_3.

The corresponding global mGO $\boldsymbol{t}_{\mathrm{C^M}}^{8\mathrm{Align}(0)}$ for an infinite (C- or SQ-) fiber planar alignment (FPA) is the sum of the interaction part $\boldsymbol{t}_{\boldsymbol{C}^M}^{int(\infty Align(0))}$ from Tab. 3.4 and of the corresponding interior one $\bar{\boldsymbol{t}}_{\boldsymbol{C}^M}^{Genfiber,x2}$ from Table 1, both specializing as explicated for C-fibers or SQ-beams.

	1111	1133	3333	2323	1313	1212
$\boldsymbol{t}_{\boldsymbol{C}^M}^{int(\infty Align(0))}$	$A(C_4 - 2C_2) - BC_2$	$A(C_2 - C_4)$	$AC_4 + BC_2$	$\left(\frac{B}{4}\right) C_2$	$A(C_2 - C_4)$	$-\left(\frac{B}{4}\right) C_2$

Table 3.5: Generic non zero interaction mGO terms for a planar alignment of x_2-oriented fibers in the

$x_1 - x_2$ *plane in isotropic media* ($B = 1/\mu A = -B/2(1-v)$), *with*

$S_2 = -C_2$,$(S_2C_2) = C_2 - C_4$,$S_4 = -2C_2 + C_4$.

3.2.4 Effective Properties of the planar alignment of C-fibers and of SQ-beams

As far as one considers a homogeneous medium embedding one (or more) phase(s) under the form of inclusions or inclusion patterns, in random manner, using the mean field two-point statistics approximation from [75] allows to estimating effective properties accounting for each phase volume fraction, properties and representative domain shape as well as for some global anisotropy of the spatial distribution symmetry of these phases. Considering elastic (or other kind of, *e.g.* dielectric) properties, this here so-called PC-W estimate, for n included phases in matrix with properties $\boldsymbol{C}^M$, takes the generic form

$$\boldsymbol{C}_{effPCW}^{nV_i/SDist} = \boldsymbol{C}^M - \left(\left(\sum_{i=1}^{n} \left(f_i \left(\left(\boldsymbol{C}^M - \boldsymbol{C}^i \right)^{-1} - \boldsymbol{t}_{\boldsymbol{C}^M}^{V_i} \right) \right)^{-1} \right)^{-1} + \boldsymbol{t}_{\boldsymbol{C}^M}^{SDist} \right)^{-1} \quad (3.28)$$

In Eq. (3.28), $\boldsymbol{t}_{\boldsymbol{C}^M}^{V_i}$ is the mean operator of the representative domain V_i for phase i (a single inclusion of phase i, or a finite pattern of them) having $\boldsymbol{C}^i$ properties and f_i volume fraction, and $\boldsymbol{t}_{\boldsymbol{C}^M}^{SDist}$ is the operator representing some common spatial distribution for all the V_i domains in the matrix. This spatial distribution needing be formally ellipsoidal to obtain Eq. (16a), this $\boldsymbol{t}_{\boldsymbol{C}^M}^{SDist}$ operator is uniform[2]. This distribution symmetry operator can also be seen as the operator of the representative (ellipsoidal) elementary matrix volume V_M containing the pattern V_i. This latter interpretation fixes a concentration limit for the validity of the PC-W estimate, related to the minimal reference volume size capable of containing the representative pattern of the embedded phases, in the sense of an (ellipsoidal) envelop of this pattern. When the domains Vi are single inclusions, the PC-W estimate statistically

[2] Spatial distributions of inclusions are unlikely ellipsoidal and are unlikely multimodal at non dilute concentrations (Franciosi and Lebail, 2004).

accounts for a part of their interactions through their spatial distribution, but the larger are the chosen representative patterns V_i, the more the pair interactions can be accounted for precisely at the pattern scale. As far as the considered patterns are finite sets, the estimate still regards the pair interactions between any two patterns through their spatial distribution. Interactions between pairs of infinite patterns become a marginal contribution to effective property estimates when the element interactions in the pattern are accounted for. Thus, Eq. (3.28) will be enough in the following for the purpose of using infinite patterns to represent the embedded phase, and especially the two-phase form of it which simplifies to

$$\boldsymbol{C}^{V/SDist}_{effPCW} = \boldsymbol{C}^M - f_V\Big(\Big(\big(\boldsymbol{C}^M - \boldsymbol{C}^V\big)^{-1} - \boldsymbol{t}^V_{\boldsymbol{C}^M}\Big) + f_V \boldsymbol{t}^{SDist}_{\boldsymbol{C}^M}\Big)^{-1} \tag{3.29}$$

In Eq. (3.29), the single included phase has volume fraction $f_V = 1 - f_M$ and properties $\boldsymbol{C}^V$, a representative inclusion or pattern V with *mean* global Green operator $\boldsymbol{t}^V_{\boldsymbol{C}^M}$, and these patterns are spatially distributed according to some (ellipsoidal) symmetry represented by the operator $\boldsymbol{t}^{SDist}_{\boldsymbol{C}^M}$. Assuming statistical homogeneity of the individual elements, regardless of the pattern, f_V must also be the inclusion concentration in the pattern, say the volume fraction of V in its elementary matrix volume V_M (a difference would represent some inclusion clustering in the patterns, the statistical homogeneity assumption applying at the pattern distribution scale). When such a composite is deformed, both the characteristic embedded inclusion pattern and their spatial distribution evolve. In the particular case of infinite inclusion patterns it was shown in [63] that when the pattern evolution is well accounted for, its distribution symmetry can be kept constant (and determined by the influence zone symmetry around each fiber element) as far as the symmetry and anisotropy characteristics of the embedding matrix do not change.

3.3 Application to effective property estimates of a soft matrix reinforced by a fibre network

We exemplify simple cases of a matrix embedding fiber bundles or networks where planar alignments can be identified such as to make use of the global fiber pattern operators obtained in the previous sections for determining effective property estimates. As far as one considers a homogeneous medium embedding one, or several other, phase(s) under the form of inclusions or inclusion patterns, in random manner, using the mean field PC-W [75] two-point statistics approximation allows to estimating effective properties in accounting for each phase volume fraction, properties and representative domain shape as well as for some global anisotropy of the

spatial distribution symmetry of these phases. Considering elastic-like or dielectric-like properties, this here on called "PC-W" estimate, for n included phases in matrix with properties C^M, takes the generic form

$$C_{effPCW}^{nVi/SDist} = C^M - \left(\left(\sum_{i=1}^{n} \left(f_i \left(\left(C^M - C^i \right)^{-1} - t_{C^M}^{Vi} \right) \right)^{-1} \right)^{-1} + t_{C^M}^{SDist.} \right)^{-1} \quad (3.30)$$

In Eq. (3.30), $t_{C^M}^{Vi}$ in the mean operator of the representative domain Vi for phase i (a single inclusion of phase i, or a finite pattern of them) having C^i properties and f_i volume fraction and $t_{C^M}^{SDist.}$ is the (formally ellipsoidal) operator representing some common spatial distribution for all the Vi domains in the matrix. This distribution symmetry operator can also be seen as the operator of the representative (ellipsoidal) elementary matrix volume V_M containing the pattern Vi. This latter understanding fixes a concentration limit for the validity of the PC-W estimate, related to the minimal reference volume size capable of containing the representative patterns of the embedded phases, in the sense of an (ellipsoidal) envelop of these patterns. When the domains Vi are single inclusions, the PC-W estimate statistically accounts for a part of their interactions through their spatial distribution, but the larger are the chosen representative patterns Vi, the more the pair interactions can be accounted for precisely at the pattern scale. As far as the considered patterns are finite sets, the estimate still regards the pair interactions between any two patterns through their spatial distribution. Eq. (3.30) will be enough for the following discussion purpose about the use of infinite patterns, and especially the two-phase form of it which simplifies to

$$C_{effPCW}^{V/SDist} = C^M - f_V \left(\left(\left(C^M - C^V \right)^{-1} - t_{C^M}^{V} \right) + f_V t_{C^M}^{SDist.} \right)^{-1} \quad (3.31)$$

In Eq. (3.31), the single included phase has volume fraction $f_V = 1 - f_M$ and properties C^V, a representative inclusion or pattern V with mean global operator $t_{C^M}^{V}$, and these patterns are spatially distributed according to some (ellipsoidal) symmetry represented by the operator $t_{C^M}^{SDist.}$. Assuming statistical homogeneity of the individual elements, regardless of the pattern, f_V must also be the inclusion concentration in the pattern, say the volume fraction of V in its elementary matrix volume V_M (a difference would represent some inclusion clustering in the patterns, the statistical homogeneity assumption applying at the pattern distribution scale).

Now, when a composite comprises a compliant matrix and a stiffer embedded phase, the inclusion arrangement inside the representative pattern is expected to evolve (changes of the inclusion shape being considered as negligible in comparison),

with an effect on the element interactions. The description of such evolutions can be simplified when global operators for typical large (infinite-like) inclusion patterns are available in closed form, as those for aligned spheres and spheroids [86], for coaxial finite cylinders [88] and for planar arrays of infinite fibers (this present work) to which we here pay special attention. In what follows we assume the individual fibers to not deform (they remain straight and of fixed circular cross section) and to remain parallel when so initially in the directional bundle or array they belong to. That is we disregard all possible bending, flexion and torsion modes for the fibers or for their arrays, to which a separate analysis needs and will be dedicated. We furthermore disregard any interface de-cohesion between the fibers and the embedding matrix which is assumed compliant enough for so doing.

3.3.1 Description of 1D fiber-reinforced matrices from infinite planar arrays of fibers

A one-directional bundle of parallel fibers can be described in different manners, as exemplified in Fig. 3.7, by cross section views of normal $\omega_i = (\theta_i, \phi_i)$. On the left side example, the fibers are taken as randomly distributed in isotropic manner (no spatial arrangement is accounted for if any) with ignored specific pair interactions what means a validity restriction to dilute enough concentrations. The representative volume element is a cylinder embedding a single fiber and straining such a material amounts to modify the spatial fiber distribution from isotropic to elliptic according to the stretch or compression direction. In the central description, a regularly enough arrangement of the fibers which are aligned and with nearly equal inter-distances in parallel planes is taken into account with using a finite pattern representative of the major interactions between neighboring fibers in the pattern. Pair interactions between patterns are only accounted for through their spatial distribution what holds for dilute enough pattern concentrations even when taking as large patterns as possible. Taking a nearly 2D-isotropic initial pattern, a 2D isotropic initial matrix domain can be attributed to the pattern and any transversally applied deformation will transform both the pattern and its dedicated matrix domain from 2D isotropic to elliptic, according to the stretch or compression direction. In the third right hand side example of Figure 3.7, the pattern is assumed being infinite but only a finite part of it contributes to the interaction estimate (due to the finite interaction or influence distance), which is the part interior to the invariant (here 2D isotropic) influence zone, as obtained from calculating the interactions in any equivalent direction normal to the fiber orientation. In contrast with the two previous cases, the pattern of interest is evolving within the matrix reference domain

which remains constant, the influence zone, defined by the interaction cut-off relative length, approximately ten to twenty times the fiber radius as here estimated.

For the second and third estimates, the fiber concentration limit is given by the attained arrangement under deformation at which fibers become in contact. Since they cannot overlap each other, further evolutions will depend of the fiber rearrangement possibilities what is not in the present scope. For cylinders of same radius, the compact piling corresponds to a concentration $f_{\max} = \pi/2\sqrt{3} \approx 0,906$. This concentration limit is further decreased when the fibers are not in hexagonal piling, as described next.

If the fibers can be assumed regularly enough arranged such as to appear aligned and with nearly equal inter-distances in parallel planes, these planes are characterized by an ω_j-oriented normal around the ω_i fiber axis. Thus, such fiber arrangements around any selected fiber can be fully represented by an appropriately weighted average $\langle . \rangle_{\omega j}$ over a set of orientations ω_j around the ω_i axis of the layer operators $t_{C^M}^{\infty Fib(\omega_i,\omega_j,\rho 0)}$, what provides a global bundle operator $t_{C^M}^{\infty Fib\langle\omega_i,\rho 0_i\rangle_{\omega j}}$. This can be simplified in only considering the 3 densest planar arrays of fibers. As is shown on Fig. 3.7 right, for any finite pattern with size smaller than the cut-off interaction distance, a part of the element interactions would be lost (the white elements) and the more in the directions where the elements become closer to each other and for which the number of interacting fibers increase. Conversely, new (grey) elements enter the cut-off interaction distance, deserving being accounted for. Also, the main densest planar arrays do not necessarily remain the initial ones, as visible in Fig.3.7c right where the vertical array (dotted parallel lines) becomes denser than the horizontal one. The use of the global operators for large enough (infinite-like) planar alignments allows to considering as representative volume the one defined by the cut-off interaction distance itself (2D isotropic in the cylindrical fiber case) and with accounting for all the elements being currently inside this volume, as indicated by the same dotted circle in Fig. 3.7a,b,c, right, within which the number of fibers varies in anisotropic manner. Making use of the operators for the infinite planar arrays is beneficial to follow these evolutions, the key parameter being then the inter-distances between the elements of each of the densest planar alignments, together with the orientation of the selected set of densest alignments. The global operator for such an infinite bundle, $t_{C^M}^{\infty Fib\langle\omega_i,\rho 0_i\rangle_{\omega j}}$ say, can be obtained from appropriately summing all the constitutive infinite planar alignments around their common fiber direction.

Using the PC-W estimate with considering nearly 1D infinite fiber bundles organized according to the 2D isotropic influence zone yield effective properties of the

form

$$C_{effPCW}^{\infty Fib\langle\omega_i,\rho 0_i\rangle_{\omega j}} = \mathrm{C}^M - f_F\left(\left(\mathrm{C}^M - \mathrm{C}^F\right)^{-1} - \mathrm{t}_{\mathrm{C}^M}^{\infty Fib\langle\omega_i,\rho 0_i\rangle_{\omega j}} + f_F \mathrm{t}_{\mathrm{C}^M}^{SDist.}\right)^{-1} \quad (3.32)$$

It is without loss of generality and not even much loss of precision that the global bundle operator $t_{C^M}^{\infty Fib\langle\omega_i,\rho 0_i\rangle_{\omega j}}$ can be in general simplified with only considering in the sum, the three layer orientations that correspond to the elementary triangular patterns of near-neighboring fiber triplets, say to the three major (indicated) possibilities of considering the structure as a piling of planarly fiber-reinforced layers, generally having three different inter-distances $L_j = R/\rho_j$. The (simply equally weighted since the three elements of the pattern have equal volume fractions in it) average of these three main planar pattern operators describing the bundle arrangement is likely sufficient to provide a quite simple close approximation for $t_{C^M}^{\infty Fib\langle\omega_i,\rho 0_i\rangle_{\omega j}}$, owing to the simple operator form for planar arrays. When the composite is strained in homogeneous enough manner, the variation of this characteristic triplet of currently densest fiber arrays allows quite easily to varying the pattern operators according to the composite response, in varying the three main layering orientations together with varying accordingly the fiber inter-distance in these layers. All the interactions in the influence zone are always automatically accounted for with using the evolving infinite planar operators.

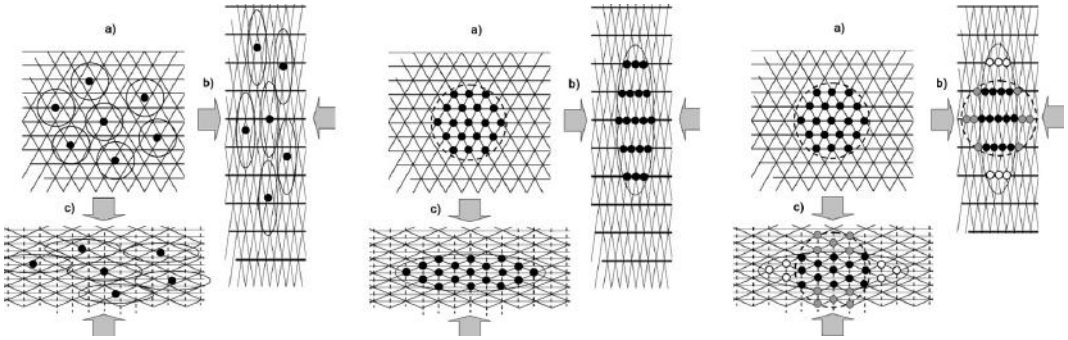

Figure 3.7: 2D isotropic (a) and horizontally (b) or vertically (c) strained elementary volume of 1D fiber-reinforced matrix using a RVE comprising, from left to right : a single fiber, a finite fiber pattern and the finite part of an infinite fiber pattern contained in a (2D isotropic) influence zone.

The pattern evolution can be simplified in considering the 3-element pattern of Fig. 3.8, from which simple geometry provides all the necessary evolution parameters from initial equilateral symmetric arrangement to flattened one along x_3 axis: the

alignment of normal x_1 keeps the φ angle to 0 while for the two other ones, $\kappa 0$ evolves from $\pm 2\pi/3$ to $\pm\left((\pi/2)+\tan^{-1}(1/\eta\sqrt{3})\right)$. The fiber inter-distances respectively vary as $\frac{HK_\eta}{HK_1}=\frac{1}{\sqrt{\eta}}$ and $\frac{AH_\eta}{AH_1}=\frac{AK_\eta}{AK_1}=\sqrt{\frac{3\eta^2+1}{4\eta}}$. The matrix is considered as almost incompressible and the area of the elliptic disk is assumed to remain constant ($\pi R^2=\pi ab=\pi b^2\eta=\pi a^2/\eta$) where $a=OA$ and b is the second ellipse semi-axis. If the fiber (radius r) concentration when η=1 ($IH_1=L_1$) is $f=\frac{0.5\pi r^2}{{L_1}^2\sqrt{3}}=\frac{0.5\pi {L_1}^2\rho^2}{{L_1}^2\sqrt{3}}=\frac{\pi\rho^2}{2\sqrt{3}}=f_{\max}{\rho_0}^2\leq f_{\max}$, it decreases for η>1 since $IH_\eta=L_\eta=L_1/\sqrt{\eta}$ provides the new first contact limit. The fiber volume fraction at this contact corresponds to $\rho_\eta=r/L_\eta=\sqrt{\eta}\,(r/L_1)=\rho\sqrt{\eta}$ the limit is at $\rho_\eta=1$, thus $\rho^2={\rho^2}_\eta/\eta=1/\eta$ say $f_{\lim}=\frac{\pi}{2\sqrt{3}}\frac{{\rho^2}_\eta}{\eta}=f_{\max}/\eta$ (it decreases similarly for η<1, what corresponds to the case (b) situations in Fig. 3.7, orthogonal to the here treated case (c)).

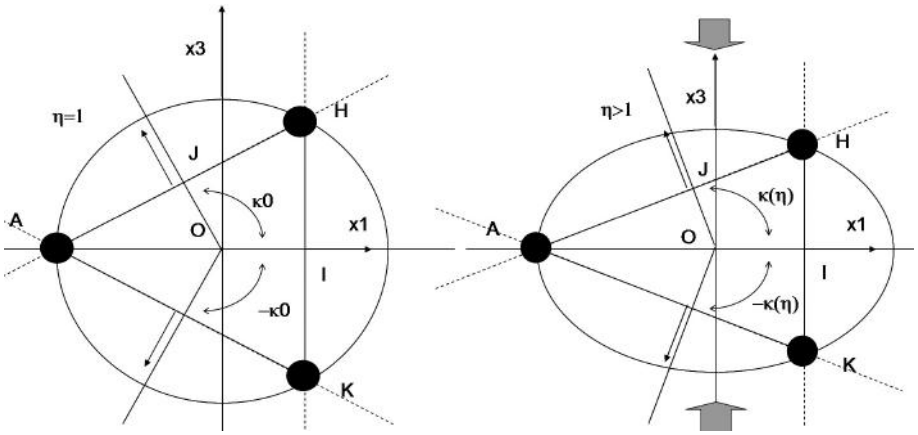

Figure 3.8: The 3-element cylinder pattern deformation under compression of x3 axis for quasi incompressible matrix and related 3 main infinite alignments (dashed lines) representing the pattern.

3.3.2 Estimates of effective properties of 1D fiber-reinforced matrices

Based on the three structure descriptions shown in Fig. 3.7 for a 1D fiber bundle with some spatial arrangement of the fibers, we compare the corresponding estimates of effective properties, using the generic Eq. (3.32) for the three of them, in the case of a matrix straining that corresponds to the cases (c) in Fig. 3.7 (vertical compressive mode):

i. For the representative volume with a single fiber in elliptic description with aspect ratio η>1 (Fig. 3.7, left), the distribution operator is given in Tab. 3.1 column 1, which also gives the cylindrical fiber operator when taking η=1;

ii. For the middle case of Fig. 3.7, the same η-elliptic fiber operator describes the finite pattern distribution, while the pattern mean operator is the sum of the pair interaction operators in the pattern. We assume the pattern to have the same "elliptic" symmetry (η) as the distribution operator, taken to correspond with planes, the normal of which are at angles kappa as defined in Fig. 3.8 . This pattern, when reduced to its minimum, is the triangular set of main (densest) fiber planar alignments (dashed lines in Figure 6) specified by the 3 inter-distances and the 3 plane orientations (in equal weights for the three interactions given by the 3 volume fractions of 1/3 for each fiber in the minimal pattern of three fibers). Although this pattern should be finite and delimited by an elliptic contour, each of the three constitutive main alignments can be considered made of n elements, with n ranging from 2 to any value that makes the distance between the central fiber and a most distant nth one larger than the cut-off interaction distance, even in the case the n fibers are at contact! According to the here estimated distance, n should be larger than the ten to twenty critical number of fibers, n_{critic} say. In this latter case ($n > n_{critic}$), the interaction terms can be taken as being those of the infinite alignment. We report the data obtained for the two extreme assumptions (n=2 and n "infinite" for $n > n_{critic}$).

iii. For the third right hand side case on Fig. 3.7, the invariant 2D isotropic distribution is represented by the cylinder operator while the operator for the infinite bundle with elliptic symmetry is described from considering the three planar alignments with same normal orientations κ as in the middle case). We only consider the case of an infinite fiber number n in the three main alignments, the difference with the previous estimates is that the spatial distribution of these infinite patterns is taken represented by the invariant (here 2D isotropic) influence zone for interactions.

For the isotropic matrix, the only elastic property of interest is the Poisson ratio v^M, while only the relative elastic stiffness moduli of the fibres $\mathbf{C}^F/\mu^M$ are needed, μ^M being the matrix shear modulus. Although $\mathbf{C}^F$ can be taken of general anisotropy, we here consider isotropically incompressible elastic fibers for sake of simplicity ($v^F = 0.499$) and since the matrix is assumed highly compliant in comparison to the fibers, one consideres $\mu^F = 50\mu^M$. We arbitrarily choose $v^M = 0.49$ for keeping a nearly

incompressible matrix. This also allows to only presenting and discussing the effective shear moduli variations from one estimate to another.

The results that suffice to illustrate the here addressed point are plotted in Figs. 3.9-3.10 (further analyses are let out of the present scope). The Fig. 3.9 only ensures that all four estimates coincide at $\eta = 1$, what is due to the known fact that the global mean interaction part in highly symmetric (as 3D or 2D isotropic) patterns simply vanishes.

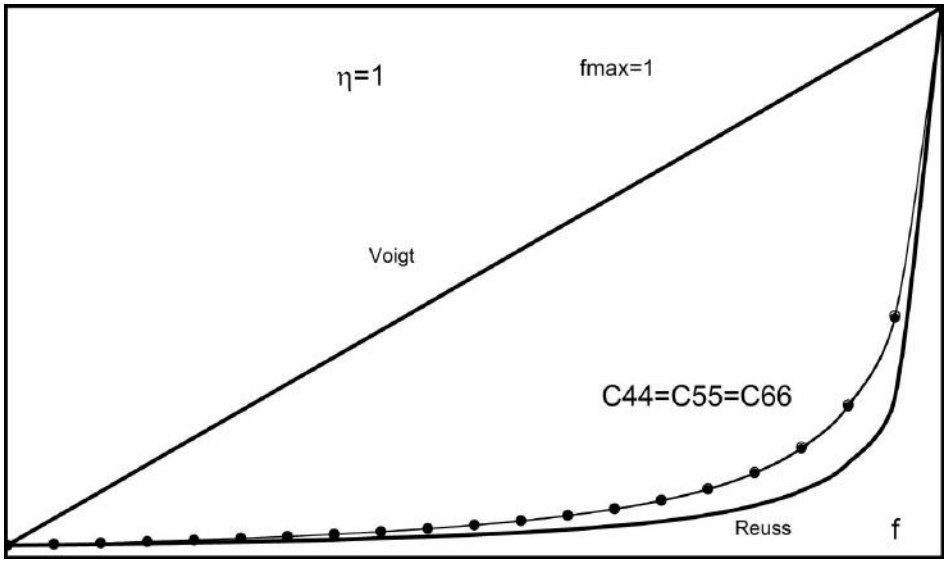

Figure 3.9: Effective shear properties for a 1D bundle of isotropic and incompressible fibers in a compliant isotropic nearly incompressible matrix from the four estimates.

For each of these four (yet three types of) estimates, four elliptic anisotropies $\eta = 1.5,\ 2,\ 2.5,\ 3$ have been compared, in addition to the reference 2D isotropic state for $\eta = 1$. For an increasing η value, the concentration range of validity decreases as specified in what precedes. This range is the same for all four estimates, including the first one as well, as far as the request of all fibers being of same radius is applying. Conversely, for each specific fiber concentration f, the allowed range of stretch η varies, in reducing with increasing f. The Figs. 3.10 a,b,c represent the evolution with the stretch η of the 3 shear moduli for the examined fiber bundle according to the four descriptions previously presented, at three different fiber concentrations of 40%, 60% and 80%. The plotted η range decreases with increasing f but it is kept larger than the allowed one to show the evolutions beyond the limit. Fig. 3.10a is characteristic of the moduli variations at low and moderate concentrations $0 < f <$

50%. The moduli evolve without becoming unreasonable. All results are close to the Reuss lower bound, as expected for hard inclusions in a soft matrix. For higher concentrations (Figs. 3.10b and c) the range of allowed stretch decreases drastically and the moduli become to diverge more rapidly, with some of them possibly violating either Reuss or Voigt bound, although the latter one is much higher, not plotted (but values are given in the Figures). It clearly appears for all reported concentrations that:

i. considering, in a varying pattern spatial distribution (reference matrix volume), a shape-varying finite pattern of three fibers instead of a single fiber pattern, the moduli estimates go faster towards the bounds of the validity range, and so it is as well in reinforcing the three-fiber pattern as a three infinite planar alignments (say in substituting the three-fiber pattern operator with the three-alignment pattern operator);

ii. considering the three-alignments infinite pattern in a "constant" (shape-invariant) reference domain (defined on the interaction cut-off distance between the fibers) goes oppositely compared to the estimates from the single fiber pattern operator; there is much less divergence in this case than in the other ones at increasing fiber concentrations, what has the result of suppressing or delaying the violation of the extremal Voigt and Reuss bounds for an extended formal validity range for this estimate.

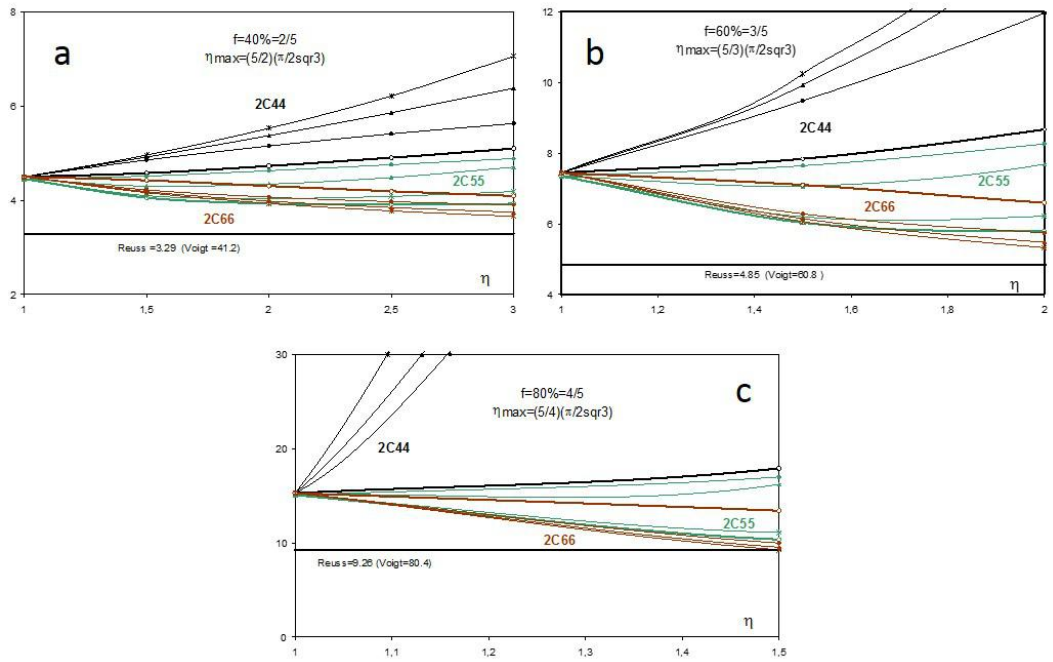

Figure 3.10: Evolution with a stretch $\eta > 1$ of the 3 effective shear moduli at 40% (a), 60% (b) and 80% (c) fiber volume fraction from the four compared estimates (single fiber, 3-elements and n>n$_{critic}$ -elements in η -elliptic distribution are represented by black dots, triangles and crosses, the infinite pattern in a fixed influence zone by white dots on a bold line).

It is noteworthy that all pair interactions could be accounted for and that most of them are in this infinite pattern description of the fiber arrangement such that in that respect we have a mean field estimate which is no more a dilute approximation. As the arrangement is described, the fiber concentration limit is given by the impossible overlapping of any two fibers. If the composite structure can deform further and if the fiber arrangement evolution can still be described from planar alignments, the modelling can be pursued with the appropriate representative (infinite and fully interacting) pattern.

In the extreme case when the fibers are dense in a single set of parallel planes (of normal ω_j) and with large enough distances between the planes to neglect transverse interactions, the structure can be treated as a laminate structure made of fiber-reinforced layers of matrix with distribution symmetry represented by the platelet operator $t_{C^M}^{p\omega_j}$ (from Tab. 3.1, column 1, with $\eta = 0$ or infinite according to the laminate normal orientation x_1 or x_3 respectively). A property estimate from the

PC-W framework for such a laminate structure reads

$$C_{effPCW}^{\infty Fib(\omega_i,\omega_j,\rho 0_i)} = \mathrm{C}^M - f_F \left(\left(\mathrm{C}^M - \mathrm{C}^F \right)^{-1} - \mathrm{t}_{\mathrm{C}^M}^{\infty Fib(\omega_i,\omega_j,\rho 0_i)} + f_F \mathrm{t}_{\mathrm{C}^M}^{p\omega_j} \right)^{-1} \tag{3.33}$$

using the single $t_{C^M}^{\infty Fib(\omega_i,\omega_j,\rho 0_i)}$ operator for the infinite planar pattern of fibers and for the distribution, the laminate operator $t_{C^M}^{p\omega_j}$ of same normal (from Tab. 3.1, column 1 with appropriate η value and rotated orientation).

3.4 Conclusion

In order to estimating effective properties of compliant matrices reinforced with deformable fiber networks, we have first analytically derived global (interior plus interaction parts) mean Green operators for large, and up to infinite, planar alignments of parallel cylindrical fibers of infinite length in isotropic matrices, the also solved case of rectangular beams being to be presented separately. The mean pair interaction operator between two infinite parallel cylinders is the first obtained and here presented original result, from which the mean interaction operator for infinite planar alignments of parallel identical cylinder (with equal inter distances) appears of very simple closed form (thanks to the used Radon Transform and inverse transform method). This interaction operator for infinite planar alignments of cylinders is similar to the interaction operator for infinite alignments of equally distant identical spheres, from the general sphere pair operator, as reported in a previous work. Owing to the infinite nature of the fibers and to the co-continuity they ensure with the matrix in the fiber directions, the operator for infinite planar alignments opens on specific interest for network-reinforced matrices.

It has been shown that the influence distance between two fibers, that is the fiber neighbourhood within which interactions matter in a global pattern operator, is typically one order of magnitude (ten to twenty times) larger than the fiber cross section radius. This allows to making use of the infinite alignment operator for any planar fiber array larger than ten to twenty fibers (depending on the wished accuracy). The inter-distance between the fibers is the key parameter that modifies the number of fibers in this fixed influence zone, the 2D shape of which is assigned by the fiber cross section shape and by the symmetry properties of the matrix.

It has been then shown how these operators for planar alignments provide operators for one-directional fiber bundles (averaging a finite operator set for coaxial dense planar alignments) that can be quite easily used in simple homogenization frameworks for effective property estimates of directionally fiber reinforced matrices. The use, as representative element, of an infinite pattern which accounts for

all (if necessary) or for the major pair interactions between the inclusions extends the validity range of the used mean field estimates from the literature farther than the usually restrictive dilute and no interaction approximation they suffer. A key interest is also the possibility to quite easily follow the effective property changes related to the deformation of such fiber networks when embedded in a soft matrix.

It is finally shown how extension to determining, from the obtained effective properties for 1D bundles, the effective properties for a matrix reinforced with interpenetrated multi-directional fiber networks is possible, thanks to the building of global mean operator for the whole network and to the use of laminate system and fiber system schemes. The case of networks with interconnected fibers, as in particular typical pantographic-like beam structures of increasing interest, is the topic of the next Chapter.

Chapter 4

A Green operator-based elastic modeling for two-phase pantographic-inspired bi-continuous materials

This Chapter is based on [64].

4.1 Introduction

In this Chapter, still restricting our attention to the homogeneous behavior range of these structures, the concern is to determine effective elastic-like properties for two-phase materials that comprise an isotropic compliant matrix and a 3D fiber pantographic-inspired network co-continuous with the embedding matrix. This assemblage is a new type of bi-continuous composites or composites with interpenetrating phases. An example of such a new structure in that family is shown in Fig. 4.1, drawing at left and additive manufacturing (AM) realization at right[1], for the case when the fiber network symmetry is orthogonal, what may in general correspond to a reference undeformed situation (the embedding matrix is made invisible on all the Figures to come).

[1] By courtesy of Prof. T. Lekszycki, Warsaw University of Technology.

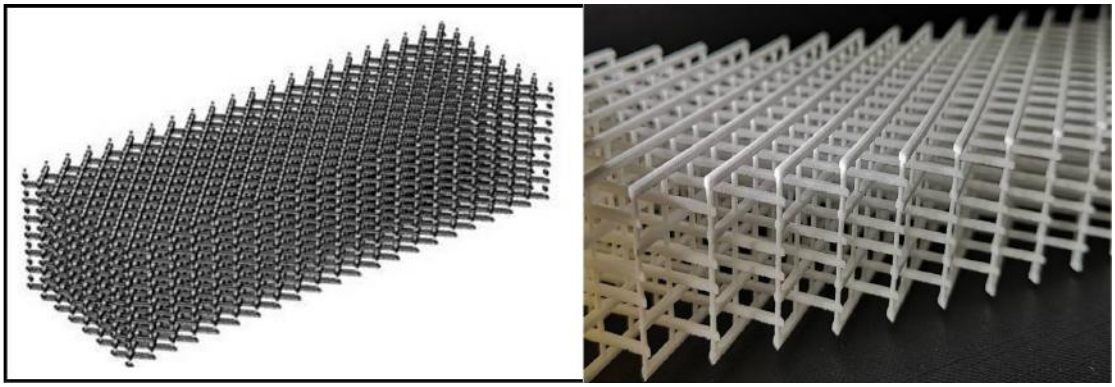

Figure 4.1: Drawing (left) and AM realization (right) of a multilayer pantographic-inspired 3D fiber network (to be embedded in a matrix not visible on the figure.

The Fig. 4.1 anticipates on the fact that, in the main here examined structure, one of the 3 (initially orthogonal) fiber families is treated differently from the two other ones, as seen in the following. In the general case when all three fiber directions play similar roles, the idealized current structure for such a 3D network when allowed to substantially deform homogeneously thanks to the mechanical characteristics of the fiber interconnections is the one of a triclinic lattice as shown in Fig. 4.2. This triclinic lattice can be seen as basically made of three inter-penetrated and interconnected assemblages of parallel fibers under the forms of either 1D fiber bundles or fiber planar alignments (FPAs), with 1D bundles being also possibly seen as assemblages of coaxial FPAs.

The fiber-like elements can be either rods or beams and the connections between fibers of different orientations are symbolized on the Fig. 4.2 by hinges which hide the details of the operating mechanism for deforming the network, only the geometrical and related stiffness descriptors of which need be specified for constitutive equation formulations.

The deformation of the general triclinic network of Fig. 4.2 type, with elements assumed to remain straight in the average (to be commented later on), will typically be characterized by the evolutions of 3 element inter distances in 3 complementary families of FPAs and of 3 angles between the orientations of the elements in these different FPAs. Only considering here fiber-like elements which are either of circular or of square cross sections, we reduce the examined situations to cases when the FPA assemblages are alternated (...*L*-*R*-*L*-*R*...) layers in one (x-y say) plane, with in-plane 2ϑ-misoriented u- and v- identical (rod or beam) elements.

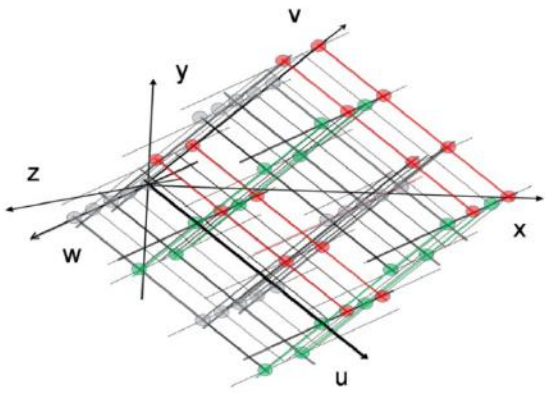

Figure 4.2: A triclinic lattice made of inter-penetrated and interconnected planar alignments or 1D fiber bundles.

The inter connecting hinges are taken to be aligned along a third family of w-oriented fiber-like elements of the 3D network which may be inclined on the z normal to the x-y plane. From a structure symmetry assumption, the element inter-distance is kept identical for the two FPA families parallel to the x-y plane and the FPAs are assumed to remain planar and parallel (neither out-of-plane twist nor flexion of the FPAs). Thus, the unit pantographic-like constitutive domain of the structure is a *L-R* (or *R-L*) pair of contiguous FPAs, as exemplified in Fig.4.3 in the orthogonal reference case, with a layer inter distance not necessarily equal to the in-layer fiber inter distance.

Although these features are disregarded in a first step, it is worthy to keep from now in mind for the final discussion, that variations of the 2ϑ misorientation angle between successive(*L,R,L,...*) parallel FPAs can also be related to torsion and bending (inclination) along the third interconnecting element family, related to some torsion and bending aptitude for these swiveling interconnections.

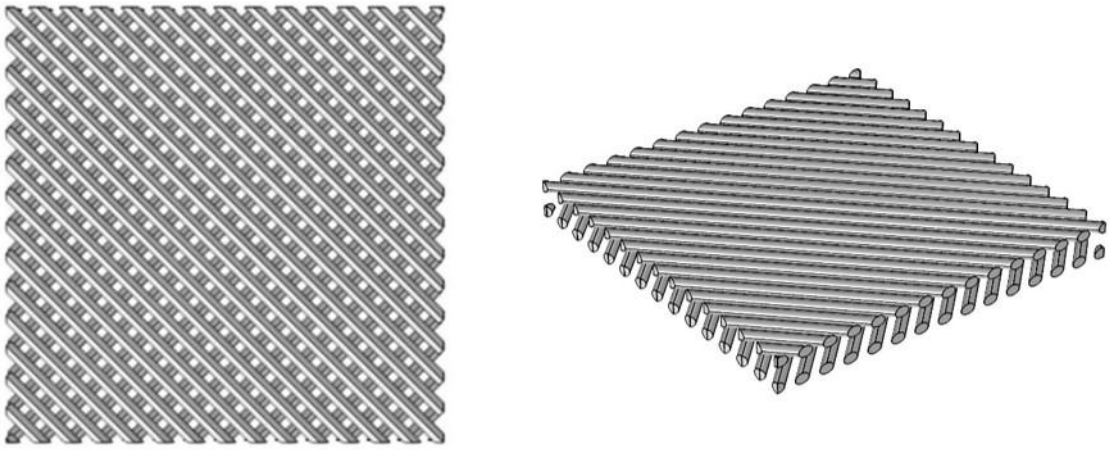

Figure 4.3: Representation of a double fiber planar alignment, constituting the typical pantographic-inspired bi-layer (no interconnections are visible).

We here mainly consider the in-plane (x-y) homogeneous extension of a matrix reinforced by such a network, the overall in-plane behavior of 2D pantographic structures during extension or shear being known to be in first approximation piece-wise homogeneous extension, each homogeneous domain possibly supporting additionally a specific body rotation with regard to the main axis, as illustrated in Fig.4.4 (where identically colored fibers are those belonging to a same - L or R - FPA in any contiguous pair): apart of the end domains (as *NMP, RTU* in Fig.4.4) which in first approximation do not deform, each sub-domain lattice straining corresponds to an equal and opposite variation of angles (u,x) and (v,x) (resp. y), Fig.4.2, which are related to an evolution of a same element inter-distance in the two FPA families. A homogeneous shear x/y (or y/x) on such sub-domains also corresponds to a similar extension (as the central pantograph part *PQRS* in Fig.4.4), with the extension direction being additionally in-plane rotated (from z to z'). Lateral domains also deform by combining extension and rotation. Simple angular relations are collected in Appendix C. It is also noteworthy that specific end conditions for clamping the fiber layers when applying axial extension on the structure can suppress the end and lateral sub-domains and yield an overall homogeneous extension.

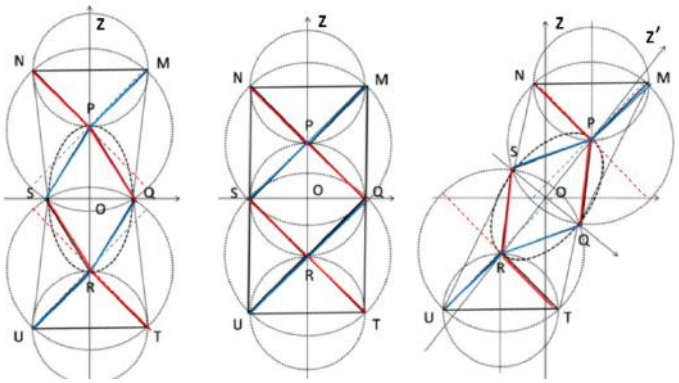

Figure 4.4: Scheme of axial extension (left) or transverse shear (right) for a 2D pantographic bilayer structure (central), with piece-wise homogeneous extension-like deformation of sub-domains PQRS, MPQ=SRU, NPS=QRT, with rotations. Fiber colors indicate L or R planar alignments (PAs). Interconnecting pivots are normal to the FPAs.

The exemplified configuration keeps the through-layers connecting third fiber bundle normal to the FPAs. This corresponds to the one-placement-field assumption frequently used for the strength of the layer interconnections [35], while inclinable interconnections would correspond to a two-placement-field assumption as discussed in [5] and more generally to a currently triclinic supporting lattice as the one of Fig.4.2.

As is also observed on the simple 2D views of Fig.4.4, the homogeneously deformed sub-domains are in-plane connected along boundaries where second gradient effects are localized, the nature of which is related to a local bending of the aligned fibers. These singularities are disregarded in the present work.

Since the piece-wise homogeneously deformed network of concern is embedded in a matrix which is also assumed to deform piece-wise homogeneously (with homogeneous sub-domains of the two phases being coincident), the overall (effective) behavior of such a composite structure can be approached, as far as attention is paid to homogeneous applied deformation (that is at the scale of the homogeneously deforming sub-domains in first approximation), in using homogenization frameworks applicable to reinforced matrices, with the two phase co-continuity deserving some particular considerations [89–91].

The embedded network being considered as substantially deformable, its representative pattern, although taken to remain piece-wise homogeneous, is expected to not remain invariant along any deformation path and so it is as well then for the effective elastic properties of the structure in each such domain.

If one further disregards the damage features possibly related to debonding between the fibers and the matrix, as well as to the matrix or fiber fracture, the major issue to estimate the current effective properties of such structures from a homogenization procedure is to well enough describe the reinforcing networked pattern in terms of its mean Green operator (mGO) and in the present case to have an expression of easy use to follow at the best the expected variations of this operator with the pattern structure evolution under homogeneous deformation.

In the case when the fibers are cylinders, global mGOs for fiber planar alignments (FPAs) of n (up to infinite) parallel, identical and equally distant, ones (C-fibers) as exemplified in Fig. 4.5 have been calculated in [63], for all fiber inter distance values from infinity to contact, with all fiber pair interaction accounted for in the FPAs, for the case of matrices which are at least isotropic around the fiber direction.

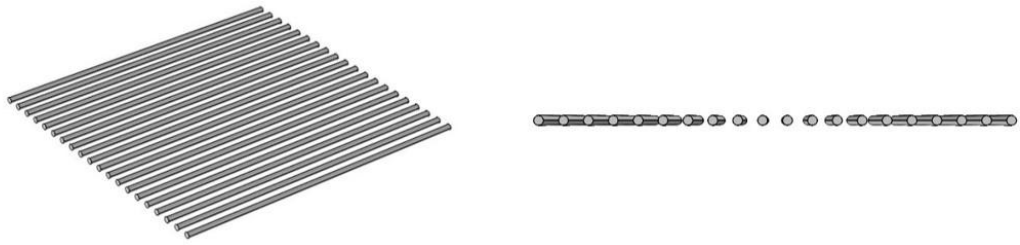

Figure 4.5: Representation of a planar alignment of C-fibers.

These mGOs for FPAs of C-fibers were shown to have a simple expression, with application examples given for estimate variations of effective stiffness properties of 1D fiber bundles when compressed or extended transversally with regard to the fiber direction.

For FPAs of parallel beams with various polygonal, and in particular rectangular (including square), cross sections, the mGOs were calculated in [85][2], for any inter distance as well, the exact form of which being not reducible to a simple one. An accurate approximation of easier use will be here given for the case of square cross sections (SQ-beams) which is close to the most frequently chosen shapes when elaborating pantographic-like networks from 3D printing [12].

As for all inclusion patterns, the mGOs of FPAs share into a main term and a global pair-interactions contribution. On the geometrical ground, the main term only depends on the element shape and the interaction part depends on the inter-distance between the elements in the pattern, that is between the parallel elements

[2] From a newly introduced "decomposition method" derived from the Radon transform framework.

in the FPAs[3]. In having considered FPAs up to an infinite number of elements in the cited references, it was shown that the critical inter distance above which a fiber or a beam can be considered as isolated was typically (depending on the wished precision) ten to twenty times the C-fiber radius or the SQ-beam side. This length defines the influence zone around any element out of which the rest of the alignment does not contribute much to the interaction and thus to the pattern mGO. This limited influence zone conversely allows the use of the mGO of infinite patterns as soon as the element number is large enough. The knowledge of this mGO for infinite PAs of C-fibers or SQ-beams was thus the very first necessary information to attempt performing the homogenization-based estimate of effective properties for the two-phase pantographic-inspired structure here of concern.

The second necessary information for the network deformation to be pantographic-inspired is to well enough describe the behavior of the through-layer interconnections for they rule the in-layer behavior under straining. Hence, this amounts in the one hand to well accounting for the through-layer stiffness of the FPA assemblage and on the other hand to describe the in-plane relations between the fiber network extension, the fiber inter-distances in the FPAs, the misorientations between the alternated FPAs, and the volume fraction changes for the fiber network in the matrix.

The chosen description must represent the specific characteristics which are carried by the inter-connections between the elements of the piled FPAs in the assemblage, called pivots at the scale of each two consecutive L-R or R-L layer pairs as exemplified in Fig. 4.1, and which constitute the fiber-like pivot arrays possibly described, in the average, as a 1D fiber bundle going through and somehow interconnecting the layers.

4.2 Homogeneous pantographic-inspired 3D architecture of two-phase composite

Making use of the mGO of an infinite FPA of either C-fibers or SQ-beams with any inter-distance value between elements, we can model a simple layered composite material whose representative inclusion pattern basically consists in such two parallel FPAs with fibers oriented along two 2ϑ-misoriented directions, initially orthogonal ($2\vartheta = 90°$) and possibly evolving with an applied strain on the structure, together with other geometrical characteristic of the FPA assemblage, as in particular the

[3] Interactions between not parallel fibers are localized "around" the shortest distance between the two fibers. They are disregarded in the modeling for sake of simplifying, but their effect will be estimated from computational simulations.

fiber inter-distance in the fiber layers. The resulting network made from such a "pantographic-inspired" layering as representative reinforcement patterns can finally be embedded in a softer matrix phase with the specific characteristic for such a composite that both matrix and fiber network phases are co-continuous.

Provided that the mGO for an infinite planar alignment of fibers is known for any fiber inter-distance in it, a classical procedure to perform a homogenization-based modeling of such a composite structure is similar to the one for a laminate structure with alternated layers [67,74,92]. Owing to the heterogeneous structure of the layers, this procedure would here be a two-level homogenization route. Effective properties of laminated structures have an exact solution from the used homogenization method when the phase properties (the layers) are exactly known, otherwise it is also an estimate. Grossly speaking, effective properties of a laminate elastic structure are close to the Reuss lower bound for the properties normal to the layers while they attain the upper bound within the layers plane [93, 94]. As shown in the following, the difference between the effective properties of two-phase laminates and the Voigt upper bound, which only concerns the properties normal to the layers, results from cross coupling terms between the layers.

But these terms do not represent any bundle-like stiffness through-layer (possibly inclination-dependent) contribution to the overall stiffness of the composite corresponding to the 3D networks here of concern, since the layers will not remain connected if the embedding matrix has vanishing stiffness.

In the particular present case of layers only differing by an in-plane orientation, the layer properties normally to the layers remain uniform (Voigt and Reuss bounds coincide on them) and they directly yield the effective properties of the structure in that direction.

A relevant modeling alternative (allowed by the fact that the embedded phase is co-continuous with the matrix) consists in constructing a global mGO for a pantographic (L-R or R-L) bi layer from an arithmetic averaging of those of the two fiber alignments rotated by angles of $\pm\vartheta$ (initially equal to $\pm 45°$ prior to any applied straining).

This simpler scheme does not, by construction, exhibit any through-layer cross coupling terms as those showing up in the laminate scheme. But since the layers have uniform properties normally to the layer plane, the arithmetic average (say the Voigt bound) is still given by the layer normal properties, as is the harmonic average (Reuss bound) as well since both bounds coincide with regard to that normal direction.

Consequently, both these two modeling procedures identically give Voigt effective properties within the layers and uniform ones normally to them, say normally to the fiber alignments that reinforce the highly compliant matrix in the fiber planes only.

But none of these fiber layer assemblage descriptions accounts for more transversal stiffness than the matrix-due one without additionally introducing in the structure a *specific* description of through-layer interconnections.

As commented in the beginning, through-layer interconnections of the pantograph pivot type can be mimicked by a sort of third 1D w-oriented fiber bundle going through the layers, corresponding to the interconnecting pivot arrays which are more or less fiber-like aligned in the average, even if their arrays can become inclined and even if they are expected to twist or/and bend alternately between layer pairs as commented and illustrated later on. Of course, such through-layer interconnections between the fibers of each neighboring two layers in the ...*L*-*R*-*L*-*R*... piling will also have determinant in-plane effects on the behavior and evolution of the structure under external loading or straining.

Accounting for these in-plane effects consists in considering the geometric constraints implied by such interconnections on these structural behavior and evolution. This description of in-plane effects of the through layer interconnections is a fundamental point in the here proposed description: the interconnection mechanics rules the structure deformation (extension or shear) in simultaneously modifying the relative angles 2ϑ of the alternated layers and the in-layers fiber inter-distance (say the in-layer FPA compactness as defined by the ratio $\frac{R}{d}$ for C-fibers of radius R or $\frac{a}{d}$ for SQ-beams of side a), which in turns also prescribe the strengthening (torsion-like and bending-like) contributions to be accounted for according to the layer interconnection strength and characteristics.

Note that owing to a generally non zero inter distance (h) between successive layers in a pile, the alternated FPAs could be considered as separated by some fiber-free matrix layers through which only the layer (1D fiber bundle-like) interconnectors would cross. For sake of keeping simplicity in the description no third layer type is added into the laminate description and these variable densities of the fiber layers in the composite will be accounted for in varying the matrix volume fraction that embeds each of the two $\pm\vartheta$ fiber layer families, through the expression of the mean fiber density within the structure as described in the last part of this section.

It is noteworthy that this way to account for the layer inter distances in terms of fiber volume fraction in the structure does not represent any fiber pair interaction from layer to layer which are disregarded here on the argument that interactions between misoriented FPAS are expectedly low compared with cumulated interactions between parallel fibers in FPAs. This is questionable in situations when the fiber in-layer inter distance is large while the layer piling is dense, that is essentially at the beginning of a deformation process applied to the structure. Comparisons with numerical simulations will show that the neglect of these FPA interactions is

reasonable.

Hence, prior to considering additional through-layer inter-connections and prior to describing the in-plane features of a pantographic-like deformation mode, the two here considered procedures to formulate first effective properties for piled FPAs in a matrix start as follows:

1. considering first the composite as constituted by two misoriented FPA-reinforced matrix layers, each one having its effective properties calculated first from the mGO of its C-fiber or SQ-beam FPAs and secondly applying the homogenization procedure for calculating the effective properties of the equivalent homogeneous materials to this biphasic laminate material;

2. determining first, from the knowledge of the mGOs for FPAs of C-fibers or SQ-beams, the mGO of the pantographic-inspired fiber bi-layer assemblage taken as the representative pattern of the fiber networked phase and then using directly this newly built operator in the derivation of the composite effective properties.

Presentation of both procedure foundations show that they coincide for the description of the pantographic-inspired (P-I) composites here of concern. The common additional steps of introducing through-layer inter connections and in-layer pantographic-like geometrical descriptors are presented next.

4.2.1 Effective properties of P-I composites from a two-layer FPA-based laminate scheme

In the laminate-based description, we still consider a compliant matrix with stiffness tensor $\boldsymbol{C}^M$ embedding, according to various networked configurations, a single fiber phase with stiffness tensor $\boldsymbol{C}^F$and volume fraction f_F. A simple laminate structure (homogeneous layers of each) of these two phases with ω_j-oriented normal has effective stiffness estimate that reads from specializing Eq. (3.27)

$$\boldsymbol{C}_{eff}^{Lam(\omega_j)} = \boldsymbol{C}^M - f_F\Big(\big(\boldsymbol{C}^M - \boldsymbol{C}^F\big)^{-1} - \boldsymbol{t}_{\boldsymbol{C}^M}^{p\omega_j} + f_F\boldsymbol{t}_{\boldsymbol{C}^M}^{p\omega_j}\Big)^{-1} \tag{4.1}$$

with $t_{C^M}^{p\omega_j}$ the laminate operator referring to the matrix phase M. This is exemplified in Fig. 4.6 for the x_3 axis as ω_j orientation with $t_{C^M}^{px3}$ given in Tab. 3.1 last line. All phases playing equivalent roles in laminate structures, Eq. 4.1 is equivalent to referring to phase F as the matrix, $f_M = 1 - f_F$, as

$$\boldsymbol{C}_{eff}^{Lam(\omega_j)} = \boldsymbol{C}^F - f_M\Big(\big(\boldsymbol{C}^F - \boldsymbol{C}^M\big)^{-1} - \boldsymbol{t}_{\boldsymbol{C}^F}^{p\omega_j} + f_M\boldsymbol{t}_{\boldsymbol{C}^F}^{p\omega_j}\Big)^{-1} \tag{4.2}$$

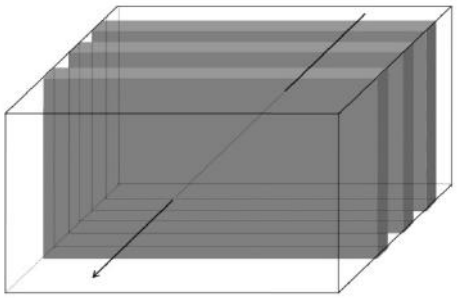

Figure 4.6: An elementary two-phase laminate structure (layers are not necessarily of same thickness, only the phase volume fraction matters in Eqs. (4.1)-(4.2).

In Eqs. (4.1)-(4.2), the laminate operator appears in two separate parts, according to the PC-W estimate: the negative full occurrence stands for the layers taken as embedded domains and the positive fractional one stands for the shape (the symmetry) of the spatial distribution of these layer-like inclusions. Both these shapes are here homothetic (and thus have the same operator) since distributing spatially infinite parallel layers can only be done according to such a layered arrangement. Also, Eqs. (4.1)-(4.2) identifiy to the two Hashin-Shtrikman bounds [95] for the phases M and F which only coincide for this case of a $1D$ laminated structure of the phases (all other relevant, necessarily in-between, estimates also coincide). The symmetric form that clearly shows this identity for laminates, discussed first in [68] to the authors knowledge, reads

$$\begin{aligned} \boldsymbol{C}_{eff}^{Lam(\omega_j)} &= \langle \boldsymbol{C} \rangle + \left(\{\boldsymbol{C}\} - \boldsymbol{C}^M \right) : \boldsymbol{t}_{\{\boldsymbol{C}\}}^{p\omega_j} : \left(\{\boldsymbol{C}\} - \boldsymbol{C}^F \right) \\ &= \langle \boldsymbol{C} \rangle - f_M f_F \left(\boldsymbol{C}^F - \boldsymbol{C}^M \right) : \boldsymbol{t}_{\{\boldsymbol{C}\}}^{p\omega_j} : \left(\boldsymbol{C}^F - \boldsymbol{C}^M \right) \end{aligned} \tag{4.3}$$

with $\langle \boldsymbol{C} \rangle = f_F \boldsymbol{C}^F + f_M \boldsymbol{C}^M$ (the Voigt average) and $\{\boldsymbol{C}\} = f_M \boldsymbol{C}^F + f_F \boldsymbol{C}^M$. The key property of this symmetric form, which is at the origin of the laminate (or platelet) system scheme of homogenization for composites with co-continuous phases, is the reference third phase of properties $\{\boldsymbol{C}\}$ which acts as a reference matrix of infinitesimal volume fraction embedding both phases F and M and in which the laminate operator is defined.

For a bi-layered laminate structure based on associating two $\pm\theta$-rotated beam alignments in the plane of normal x_1, each layer family will have effective properties obtained after rotation as

$$\boldsymbol{C}_{effPCW}^{\infty RB(\theta),\ x_1} = \mathcal{R}_{ip}(\theta)\mathcal{R}_{jq}(\theta)\mathcal{R}_{kr}(\theta)\mathcal{R}_{ls}(\theta)\boldsymbol{C}_{effPCW}^{\infty RB(0),\ x_1} \tag{4.4}$$

where $\mathcal{R}(\theta) = \begin{pmatrix} 1 & 0 & 0 \\ 0 & \cos\theta & -\sin\theta \\ 0 & \sin\theta & \cos\theta \end{pmatrix}$. Using these stiffness tensors for both constitutive layer families of the laminate structure, the effective properties of the pantographic-inspired composite can be written according to Eq. (4.3)

$$\boldsymbol{C}_{effLS}^{Lam(\pm\theta),\ x_1} = \left\langle \boldsymbol{C}_{effPCW}^{\infty RB(\pm\theta),\ x_1} \right\rangle - f_{+\theta} f_{-\theta} \left(\Delta \boldsymbol{C}_{effPCW}^{\infty RB(\pm\theta),\ x_1} \right) : \boldsymbol{t}^{p,\ x_1}_{\left\{ \boldsymbol{C}_{effPCW}^{\infty RB(\pm\theta),\ x_1} \right\}} : \left(\Delta \boldsymbol{C}_{effPCW}^{\infty RB(\pm\theta),\ x_1} \right) \tag{4.5}$$

with

$$\left\langle \boldsymbol{C}_{effPCW}^{\infty RB(\pm\theta),\ x_1} \right\rangle_{f_{+\theta}/f_{-\theta}} = f_{+\theta} \boldsymbol{C}_{effPCW}^{\infty RB(+\theta),\ x_1} + f_{-\theta} \boldsymbol{C}_{effPCW}^{\infty RB(-\theta),\ x_1} \tag{4.6}$$

$$\Delta \boldsymbol{C}_{effPCW}^{\infty RB(\pm\theta),\ x_1} = \pm (\boldsymbol{C}_{effPCW}^{\infty RB(+\theta),\ x_1} - \boldsymbol{C}_{effPCW}^{\infty RB(-\theta),\ x_1}) \tag{4.7}$$

$$\left\{ \boldsymbol{C}_{effPCW}^{\infty RB(\pm\theta),\ x_1} \right\}_{f_{+\theta}/f_{-\theta}} = f_{-\theta} \boldsymbol{C}_{effPCW}^{\infty RB(+\theta),\ x_1} + f_{+\theta} \boldsymbol{C}_{effPCW}^{\infty RB(-\theta),\ x_1} \tag{4.8}$$

Since $\left\langle \boldsymbol{C}_{effPCW}^{\infty RB(\pm\theta),\ x_1} \right\rangle_{f_{+\theta}/f_{-\theta}}$ is nothing else than the Voigt estimate (arithmetic average) for this bi-layered structure as defined, the deviation of the laminate estimate $\boldsymbol{C}_{effLS}^{Lam(\pm\theta),\ x_1}$ from the Voigt upper bound is fully carried by the second part in Eq. (4.5). This second part is only non-zero for terms related to the non-zero terms of the laminate operator $\boldsymbol{t}^{p,\ x_1}_{\left\{ \boldsymbol{C}_{effPCW}^{\infty RB(\pm\theta),\ x_1} \right\}}$ defined on the reference medium with properties $\left\{ \boldsymbol{C}_{effPCW}^{\infty RB(\pm\theta),\ x_1} \right\}_{f_{+\theta}/f_{-\theta}}$. Note that equal fractions of both layer types yield $\left\{ C_{effPCW}^{\infty RB(\pm\theta),x_1} \right\}_{f_{\pm\theta}=0.5} = \left\langle \mathrm{C}_{effPCW}^{\infty RB(\pm\theta),x_1} \right\rangle_{f_{\pm\theta}=0.5}$, that is the stiffness tensor of the reference matrix phase equals the Voigt stiffness estimate for the two-phase structure, and that the layers are not orthotropic in a same frame unless $2\theta = 90°$, yielding non zero skew symmetric parts. Writing $C_X^{\infty RB(\pm\theta),x_1} = \mathrm{C}^{O(\theta)} \pm \mathrm{C}^{SS(\theta)}$ to separate the symmetric (orthotropic O) and the skew-symmetric SS parts in these oppositely rotated tensors, the latter ones cancel each other by $\pm\theta$ symmetry such that while $\left\{ C_{effPCW}^{\infty RB(\pm\theta),x_1} \right\}_{0.5/0.5} = \left\langle \mathrm{C}_{effPCW}^{\infty RB(\pm\theta),x_1} \right\rangle_{0.5/0.5} = \mathrm{C}^{O(\theta)}$ keeps orthotropic symmetry, one has $\Delta C_{effPCW}^{\infty RB(\pm\theta),x_1} = \pm 2\mathrm{C}^{SS(\theta)}$ in Eq. (20b) where the sign of $\Delta C_{effPCW}^{\infty RB(\pm\theta),x_1}$ does not matter for only square terms of it appear in the formula of Eq. ((4.5).

It is not in the present scope to further examine the specificities of such structures, yet it is not complicated to verify, with the help of details given in [64], that owing to the property uniformity of the R and L layers with regard to their normal direction the laminate normal properties remain the common normal properties of both R,L layer types.

4.2.2 Effective properties of P-I composites from a mGO for a two-layer FPA pattern

In the stiffness averaging procedure, the construction of a global mGO for the pantographic-inspired 3D structure consists in:

1. rotating the planar alignment mGO with generic form given in Tab. 3.2 at the two opposite angles of $\pm\theta$ (from at most a $2\theta = 90°$ misorientation to a non zero minimal value depending on the distance between fiber interconnections);

2. calculating the network mGO $\boldsymbol{t}_{\boldsymbol{C}^M}^{Pant}$from averaging those of the two misoriented FPAs and using it for estimating effective properties.

This network mGO will stand for the operator $\boldsymbol{t}_{\boldsymbol{C}^M}^{V}$ in Eq. (16b) which will then provide an estimate for the effective stiffness properties of the composite, the relevant distribution operator $\boldsymbol{t}_{\boldsymbol{C}^M}^{SDist}$ for such FPA pile ups being unambiguously the operator of a laminate (plate) operator, given last line of Tab. 3.1 and to be appropriately rotated.

The mGOs of the $\pm\theta$ rotated FPAs around the transverse direction x_1 is of the form

$$\boldsymbol{t}_{\boldsymbol{C}^M}^{\infty Align(\pm\theta)} = \mathcal{R}_{ip}(\pm\theta)\mathcal{R}_{jq}(\pm\theta)\mathcal{R}_{kr}(\pm\theta)\mathcal{R}_{ls}(\pm\theta)\boldsymbol{t}_{\boldsymbol{C}^M}^{\infty Align(0)} \tag{4.9}$$

where $\mathcal{R}(\pm\theta)$ has been given and $\boldsymbol{t}_{\boldsymbol{C}^M}^{\infty Align(0)}$ is given as the sum of the interaction part from Table 4 and of the interior part from Tab. 3.1, specializing the generic form for C-fibers and SQ-beams in using the appropriate $C_i(x)$ functions as explained.

This averaging description finally just amounts to writing the mGO of the pantographic-inspired embedded network as the arithmetic mean of the two mGOs of the $\pm\theta$ rotated FPAs

$$\boldsymbol{t}_{\boldsymbol{C}^M}^{Pant} = \left\langle \boldsymbol{t}_{\boldsymbol{C}^M}^{\infty Align} \right\rangle_{+\theta,-\theta} = \frac{1}{2}\left(\boldsymbol{t}_{\boldsymbol{C}^M}^{\infty Align(+\theta)} + \boldsymbol{t}_{\boldsymbol{C}^M}^{\infty Align(-\theta)}\right) \tag{4.10}$$

As each FPA mGO, their mean value in Eq. (4.10) also varies with the fiber inter distance (d).

According to this scheme, after having obtained $\boldsymbol{t}_{\boldsymbol{C}^M}^{Pant}$, the effective properties of the composite can be simply evaluated by using Eq. (4.7) as

$$\boldsymbol{C}_{effPCW}^{Pant/Plate} = \boldsymbol{C}^M - f_{fib}\Big(\Big(\left(\boldsymbol{C}^M - \boldsymbol{C}^{fib}\right)^{-1} - \boldsymbol{t}_{\boldsymbol{C}^M}^{Pant}\Big) + f_{fib}\boldsymbol{t}_{\boldsymbol{C}^M}^{Plate}\Big)^{-1} \tag{4.11}$$

In similar manner, for the individual FPAs taken as the representative pattern of a two-phase (aligned fiber + matrix) composite, effective properties are still obtained from Eq. (4.7) as

$$\boldsymbol{C}_{effPCW}^{\infty Align(0)/Plate} = \boldsymbol{C}^M - f_{fib}\Big(\Big(\big(\boldsymbol{C}^M - \boldsymbol{C}^{fib}\big)^{-1} - \boldsymbol{t}_{\boldsymbol{C}^M}^{\infty Align(0)}\Big) + f_{fib}\boldsymbol{t}_{\boldsymbol{C}^M}^{Plate}\Big)^{-1} \quad (4.12)$$

The related effective properties for the rotated FPAs are obtained as the rotated operators

$$\boldsymbol{C}_{effPCW}^{\infty Align(\pm\theta)/Plate} = \mathcal{R}_{ip}(\pm\theta)\mathcal{R}_{jq}(\pm\theta)\mathcal{R}_{kr}(\pm\theta)\mathcal{R}_{ls}(\pm\theta)\boldsymbol{C}_{effPCW}^{\infty Align(0)/Plate} \quad (4.13)$$

or they can be directly obtained in applying Eq. (4.7) with using the rotated FPA operator as

$$\boldsymbol{C}_{effPCW}^{\infty Align(\pm\theta)/Plate} = \boldsymbol{C}^M - f_{fib}\Big(\Big(\big(\boldsymbol{C}^M - \boldsymbol{C}^{fib}\big)^{-1} - \boldsymbol{t}_{\boldsymbol{C}^M}^{\infty Align(\pm\theta)}\Big) + f_{fib}\boldsymbol{t}_{\boldsymbol{C}^M}^{Plate}\Big)^{-1} \quad (4.14)$$

The next section presents, for both descriptions, the chosen simple method for the introduction of through-layer interconnections in this structure.

4.2.3 The through-layer inter connection description from a 1D bundle of fiber-like pivot arrays

Seeing the pivot arrays that connect the fiber layers as being in the average a one directional (1D) fiber bundle, possibly ω-inclined with regard to the normal to the FPAs, we first consider this reinforcement of the matrix, which identically applies to both descriptions previously presented and keeps the validity of all presented equations provided a change of the reference matrix phase $\boldsymbol{C}^M$ to account for the characteristic in concern. Introducing the ω-oriented bundle in the matrix as shown in Fig. 4.7 simply amounts to solving the previous equations with effective properties for the bundle-reinforced matrix writing

$$\boldsymbol{C}_{eff}^{M(wB)} = \boldsymbol{C}^M - f_{Pivots}\Big(\Big(\big(\boldsymbol{C}^M - \boldsymbol{C}^{Pivots}\big)^{-1} - \boldsymbol{t}_{\boldsymbol{C}^M}^{wBundle}\Big) + f_{Pivots}\boldsymbol{t}_{\boldsymbol{C}^M}^{wBundle}\Big)^{-1} \quad (4.15)$$

In Eq. (4.15), $\boldsymbol{t}_{\boldsymbol{C}^M}^{wBundle}$ stands for the mGO of a 1D bundle of parallel fibers with direction w, going through the FPAs, $\boldsymbol{C}^{Pivots}$ is the pivot property tensor and f_{Pivots} the density of pivots in a fiber layer. All these three quantities are expectedly evolving under extension-like of the structure.

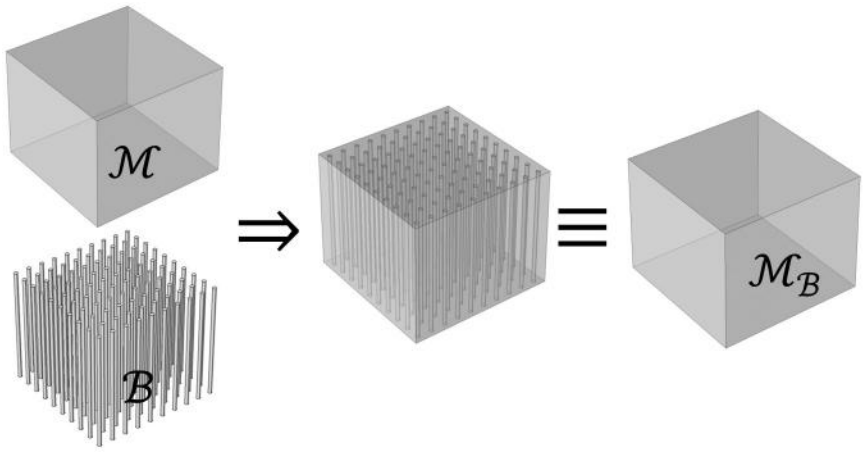

Figure 4.7: Reinforcing the matrix by an w-oriented fiber 1D bundle prior to embedding the FPA layers in it.

Basically, the pivot density is given by the cross section area ratio of a pivot and of a $PQRS$ current zone according to Fig. 4.4. The $\boldsymbol{C}^{Pivots}$ properties are not necessarily those of the fiber material and whether or not they initially (undeformed state) are, they are likely to be modified by the deformation into some effective properties as will be discussed in the next chapter.

A quite accurate form of the $\boldsymbol{t}_{\boldsymbol{C}^M}^{wBundle}$ mGO for such a fiber bundle has been obtained in [63] from also averaging the mGOs of a minimal set (typically 4) of FPAs with same fiber direction (coaxial FPAs). The shape evolution of the bundle is carried by the angular changes of the FPA orientations around their common fiber bundle. It is noteworthy that if any orientation change happens during deformation of this through-layers ω-oriented link between the planar alignments, it can be accounted for provided that the evolution law for this orientation from initial x_1 one is specified.

For a simplified first study of the effects of such through layer inter-connections on the structure behavior, one can resort to the interior Green operator of a single fiber oriented along ω (as given in Table 1 for cylindrical ones), that is one can disregard the interactions between the bundle elements as well as its shape changes and take $\boldsymbol{t}_{\boldsymbol{C}^M}^{wBundle} = \boldsymbol{t}_{\boldsymbol{C}^M}^{wCyl}$.

One next examines the in-layer characteristics that must be accounted for in relation to the type of through layer interconnections which are considered.

4.2.4 Geometric descriptors of the constraints on the in-plane pantographic-like deformation

One here describes the in-plane geometrical descriptors for the behavior under extension of that pantographic-inspired two-phase bi-continuous composite structure type which are due to such existing inter connections. As for the chosen description of the through-layer interconnections, the description we use for these in-plane geometrical descriptors is compatible with the two examined and compared (laminate-based and mGO averaging) procedures for estimating the properties of the composite of concern.

We consider, as drawn in Fig. 4.8(right), according to the micrographs of Fig. 4.8(left) a pair of (ϕ_1, ϕ_2) oppositely oriented beam layers with regard to the horizontal axis, with all beams of same rectangular cross section area $a \cdot b$, where b is the height and a the in-layer width, such that b=a for SQ-beams (this discussion is valid also in case of cylindrical fibers with cross section area πr^2 and radius r). Along each beam, regularly spaced attachments (the pivots) inter-connect at inter distance L the successive two (or more, above and below) alternated layers. The beams are considered as undeformable such that a, b and L are kept constant. The details of the pivot geometry are at first disregarded and their height (h)- which is the inter-distance between the layers - is just supposed to allow beam rotations without affecting the structure, although behavior differences are highly expectable whether (h) is small (dense layer piling) or large (distant layers).

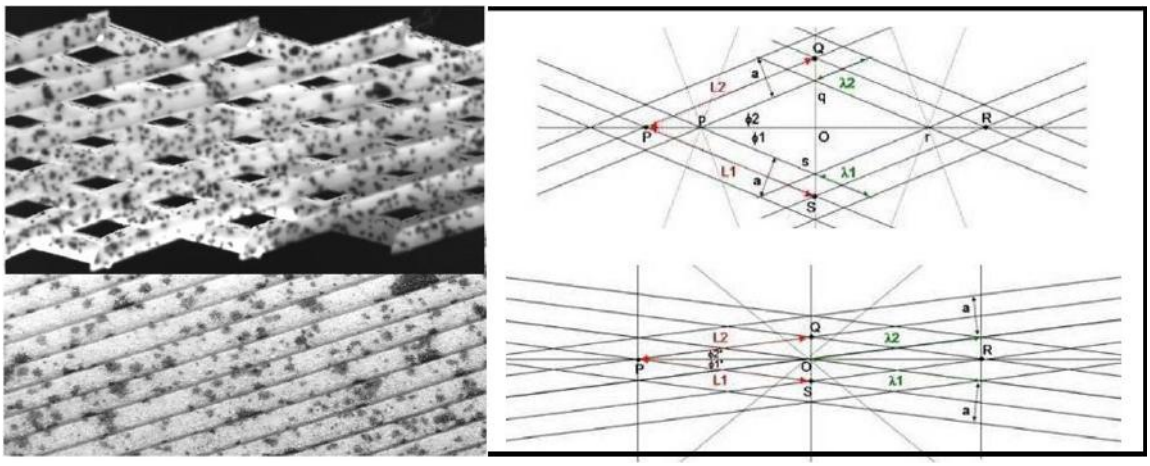

Figure 4.8: Micrograph (left) and one-cell schematic (right) of current (top) and maximal (bottom) extension shape for a bi-layered interconnected beam network element.

Thus, as viewed along the normal to the layers (top view), the four interconnecting pivots of an elementary representative domain are firstly reduced to points (Fig. 4.8), as the $PQRS$ set from Fig. 4.4, such that we a priori disregard possible deformation of the pivots as bending (distortion from straight cylinders) or inclination with regard to the z normal to x-y layers (say the w orientation is kept parallel to z). In ideal symmetric and homogeneous extension along a line going through P and R (a priori neglecting also beam distortions at the pivot level as well as between pivots along beams), the main current characteristic of the elementary representative cell $PQRS$ is that the two diagonal segments PR and QS remain orthogonal, with $L_1 = L_2 = L$ and $\phi_1 = -\phi_2 = \theta$ (for notation consistency with previous sections). If the two beam layer types are initially orthogonal, the decrease of $\pm\theta$ ranges from $\pm\frac{\pi}{4}$ to $\pm\theta^*$. In terms of beam misorientations, the current length of the network is given by $PR = 2L\cos\theta$, from $\sqrt{2}L$ and the current structure extension is

$$\alpha = \frac{PR - PR_0}{PR_0} = \sqrt{2}\cos\theta \ - 1 \tag{4.16}$$

The current area of the $PQRS$ "cell" is $\mathcal{A}_{PQRS} = \frac{1}{2}PR \cdot QS = 2L^2\cos\theta \sin\theta \ = L^2\sin 2\theta$. Similarly, the area of the commonly "free" interspace $pqrs$ between the fibers of successive layers is given by $\mathcal{A}_{pqrs} = \frac{1}{2}pr \cdot qs \ = (L-\lambda)^2\sin 2\theta$, where $\lambda = a/\sin 2\theta$ is the side length of the beam superposition area and is equal to a initially.

Consequently, the inter-distance (d) between any two parallel beams varies with θ as

$$d = (L-\lambda)\sin 2\theta \ = L\sin 2\theta - a \tag{4.17}$$

When beams are at contact (Fig. 4.8(right)), $\mathcal{A}_{pqrs} = 0$ and $\lambda = L$ such that $d = 0$ and the minimal misorientation is $\theta^* = \frac{1}{2}\sin^{-1}\frac{a}{L}$. The maximal extension follows as

$$\alpha^* = \sqrt{2}\cos\theta^* \ - 1 = \sqrt{2}\cos\left(\frac{1}{2}\sin^{-1}\frac{a}{L}\right) - 1 \tag{4.18}$$

The limit for the extension when a/L goes to 0 is $\sqrt{2} - 1 \approx 41,42\%$ and it is still 41% when $a/L \approx 0,15$ and 40% when $a/L \approx 0,28$.

As for the in-plane inter distance (d) between fibers, the inter distance between layers is zero for layers at contact, in which case the inter connecting pivots have a zero height (h). For a general (h) value, an elementary volume element is $\mathcal{V}_{PQRS} = (h+b)\,\mathcal{A}_{PQRS} = (h+b)L^2\sin 2\theta$. For compact layers (h=0), the void part equals twice the interlayer spacing along a segment L

$$\mathcal{V}_{void(h=0)} = \mathcal{V}_{voidmin} = 2\,(Ld)\,(\frac{b}{2}) = bL(L\sin 2\theta \ - a) \tag{4.19}$$

and for (h) being general

$$\mathcal{V}_{void(h)} = \mathcal{V}_{voidmin} + hL^2\sin2\theta \ = (b+h)L^2\sin2\theta \ - bLa \tag{4.20}$$

Thus, the void volume fraction, which also is the embedding matrix volume fraction, reads

$$f_{void(h)} = \frac{(b+h)L^2\sin2\theta \ - bLa}{(h+b)L^2\sin2\theta} = 1 - \frac{ba}{(h+b)L\sin2\theta} \tag{4.21}$$

with $f_{void(h=0)} = 1 - \frac{a}{L\sin2\theta} = \frac{L-\lambda}{L} = 1 - \frac{a(L-\lambda)}{Ld}$.

The fiber volume fraction which appears in Eqs. (4.11)-(4.12) conversely has the form

$$f_{fib(h)} = \left(\frac{b}{h+b}\right)\frac{a}{L\sin2\theta} = \left(\frac{b}{h+b}\right) f_{fib(0)} \tag{4.22}$$

It is noteworthy that in the cases when the pivots between fiber layer are allowed to bend, there is no more equivalency between the pivot height and the layer inter-distance unless initially (no extension yet): if the bending angle κ is the one given by the pivot orientation (ω) and the normal (z) to the fiber layers, say $\kappa = (\omega, z)$, the layer inter distance will decrease, possibly down to a null value if that bending can drive the fiber layers to contact. The relation of this bending angle κ to the misorientation angle θ is another geometric descriptor. This bending influence can be also simply examined from considering different values of the layer inter distance (h), as is done next.

In the case of SQ-beams (as for rectangular beams with same height b), the planar alignments at maximal extension become compact laminate layers what corresponds to Fig. 4.7, with two alternated layer types of all same thickness, and with minimal misorientation $2\theta^*$.

The above described geometric changes for a pantographic-inspired beam or fiber structure explicates the in-plane links between the structure extension, the layer misorientation, the in-plane fiber inter-distances (d) and the fiber layer inter distance (h).

It is noteworthy that any description taking into account the inter distance (h) between fiber layers (FPAs) potentially allows to also account for torsion of the pivots, the torsion being in first approximation simply given by the ratio $2\theta/h$, for the layer inter distance (h) also is the pivot height as long as no bending has occurred. This torsion amount is also connected to the inter distance (d) between the fibers of a layer through the θ angle current value. This torsion can be further related to a torsional stress contribution provided the knowledge of a torsion stiffness modulus for the

pivots which will depend on the pivot structure in real materials. But it can also enter the characteristics of the 1D bundle introduced in the P-I fiber network description, through a variation of stiffness moduli (and especially of the shear modulus) related to the pivot torsion. One can for example consider a stiffness increase (in pure elastic regime without neither plasticity nor damage) with torsion, as $\mu_B(\theta)/\mu_B = \chi(\theta - \frac{\pi}{4}) \geq 1$, with a function χ that may be determined from experimental and/or numerical data. In comparison, the pivot bending effect which is the decrease of the fiber layer (FPAs) inter distance (h) can be more easily considered in the modeling, via the variation law for the fiber volume fraction as explained next on.

The various relations synthesized in Eqs. (4.16)-(4.22), here called geometric descriptors, are pantographic-inspired in the sense that, as described, the interconnections between the fiber layers (FPAs) correspond to typical behavior of pantographic structures as for example examined in [4, 96] among other ones. These relations correspond to the assumption of fixed pivot type, already pointed to correspond to a one-placement-field description as discussed in [5]. Other types of pivots (or fiber layer interconnections) could be considered, in which case other relations would hold between the same geometric descriptors, in place or in addition to the here presented ones. When the elements of the 1D fiber bundle that goes through the FPAs are allowed to become w-inclined in the extension direction with regard to the normal of the FPA plane, in the pointed necessary alternated manner at the scale of successive FPA pairs (to be illustrated in section 4), this corresponds as said already to the two-placement fields assumption examined in (Spagnuolo *et al.*, 2017), yet with no global inclination of the pivot arrays, in the average.

The next Section first exemplifies analytical results from the proposed extension modeling and validating with numerical comparisons of the variation of the overall Young and shear moduli follow. At last, comparisons with numerically obtained typical force-displacement curves of 2D pantographs, where the so called pivot strength effects have a variable - from high to low - contribution, establish that the proposed analytical model can integrate these observed effects via several of the explicitly introduced geometric descriptors and, when not enough (namely in case of high pivot strength effects), via a possibly *pivot-strength-induced* variation of the matrix stiffness itself with the FPA misorientation increase. A typical fitting variation law for the matrix shear modulus with the misorientation angle is extracted, as example, from the performed comparisons.

4.3 Effective property evolution and force-displacement relation of stretched P-I composite

The here exemplified analytical data result from the use of the averaging procedure description for the pantographic-like bi-layers taken as the representative element of the matrix-embedded P-I fiber network with SQ-beams that we previously characterized in the details. The modified matrix property form in Eq. (4.15) is used to account for the trans-layer effective or apparent stiffness of the P-I composite structure, which results from the fiber bundle-like pivot arrays that physically ensures the FPA interconnections and preserves a non vanishing transverse stiffness of the P-I composite.

A first consequence of the alternated *R-L-R...* FPA layering in the considered P-I fiber network is the presence of alternated torsions on successive pivots along each array. Although not easily evidenced, neither on numerical nor on experimental experiments (pivots need be marked along their axis to follow that torsion which can be stiff or not depending on the pivot type), this alternated behavior is obvious as can be inferred from looking at Fig. 4.1 and imagining a stretch of it in the here considered extension symmetry conditions. On the contrary, there is a less obvious behavior of the pivots for the same reason of alternated layering, which finds immediate experimental evidence (to be exemplified in the following): the pivot arrays do not strictly remain straightly normal to the fibers layers (the FPAs) but are alternately bent between successive *R-L* and *L-R* layer pairs such as to remain straightly normal to the layers in the average.

These pretty much homogeneous trans layer effects (the pivot distribution remains discretely homogeneous together during homogeneous extension of the matrix embedded P-I fiber network) are always present in pantographs, in complement to and independently from the more heterogeneous in-layer features which are localized at the interconnections between homogeneous zones and that we here disregard. Both these two (torsion-due and bending-due) through-layer features that also result from the in-plane deformation are likely to impact the effective stiffness of the bundle-like pivot array and in turn the overall P-I composite behavior. What means that considering some relevant evolution form for both the effective stiffness and the geometry of this bundle-like pivot array is a possible way to indirectly account for these important characteristics of the P-I composite structure type, that we here called globally the pivot strength effects. Both identified effects involve the layer inter distance (h) which enters the proposed P-I composite descriptions from the expression given to the mean volume fraction of the fiber phase in the previous section.

4.3.1 Modulus evolutions and force-displacement plot for the pantographic-inspired structure

We here consider two isotropic and nearly incompressible phases having relative shear moduli of 1 (matrix) and 50 (fibres) with respective Poisson ratio of 0.49 and 0.499. The fiber-like bundle that represent the pivot array is considered to a priori have the same moduli as the fibers, with considering a possible torsion-due increase of the pivot shear modulus. The initial fiber inter distance (d) is taken equal to 20 times the fiber width a.

From using the relations between the so-called geometric descriptors, giving successive extensions $e = \Delta L/L0$ of the representative cell ($PQRS$) of the structure, allows two calculations:

i. on the one hand, determining the misorientation angles $\pm\theta(e)$ and from them the fiber inter distance d(e) in the layers, that is the two necessary terms allowing to determine effective elastic properties C^{eff}(e,h) according to the averaging description we have presented before, given a few different values for the h/a layer relative inter distance. This calculation provides the effective axial Young modulus for the extended structure Y(e,h) as well as all other effective moduli;

ii. on the other hand, the axial strain in the $PQRS$ cell is obtained using a logarithmic strain $\epsilon(e) = Ln(1+e)$, from which an axial stress $\sigma(e,h)$ is calculated as $Y\,(e,h) \cdot \epsilon(e)$, which stands for a tensile force per unit cross section area of the structure, say

$$F_{S0=1}(e,h) = \sigma\,(e,h) = Y\,(e,h) \cdot Ln(1+e) \tag{4.23}$$

This force identifies the pantograph behavior to the homogeneous extension of its central zone as simplified in Fig. 4.4 left (or right, up to a body rotation), what is realizable provided appropriate loading boundary conditions. The Fig. 4.9 shows the so estimated axial Young modulus variation with angle 2θ at different values of h/a from 0 (layers at contact) to 10 (distant).

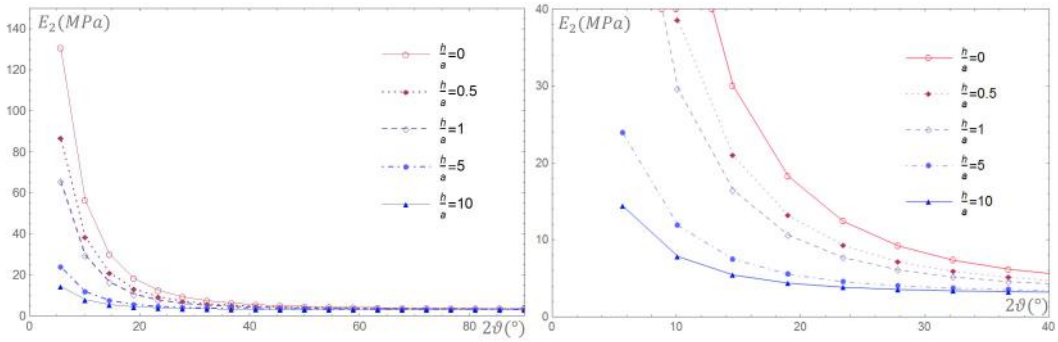

Figure 4.9: Variation (left) of axial Young modulus versus 2θ for different, from contact (0) to distant (10), h/a values without matrix reinforcing bundle and (right) a zoom of the left side.

The Fig. 4.10 similarly reports the same axial Young modulus evolution with the additional effect of through-layer fiber bundle reinforcement, according to Eq. 4.15. The bundle is simplified to a single cylindrical fiber to represent a pivot array and the current volume fraction of fibers in the bundle (or pivots in the bilayers) is taken as $a^2/(L^2 \sin\theta \cos\theta)$. The pivot elastic properties are those of the fibers and no additional (torsion-like or bending-like) effect is considered. Since in this example the a/d ratio is taken equal to 1/20, the initial low fraction of 25.10^{-4} increases to a/d=5.10^{-2} at compact contact. There is no noticeable difference, as expected, on the *axial* Young modulus.

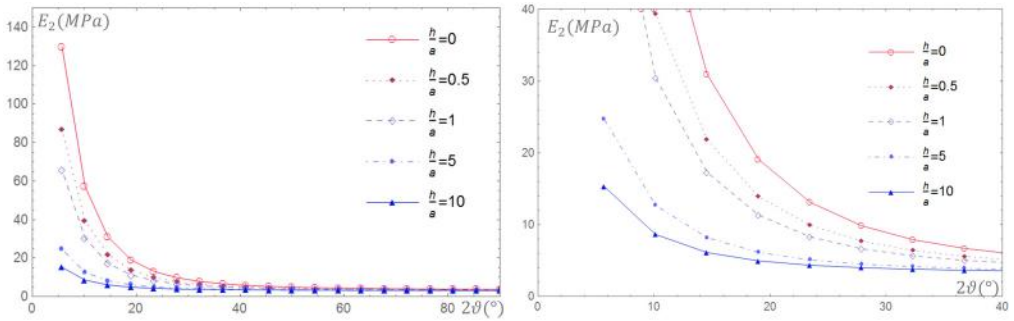

Figure 4.10: Variation (left) of axial Young modulus versus 2? for different, from contact (0) to distant (10), h/a values, with matrix reinforcing bundle and (right) a zoom of the left side.

The Figs. 4.11-4.12 show the corresponding maximal (i.e. at contact h=0 inter distance) variations with 2θ , with and without bundle effect, of the other effective

elastic moduli, which are much less evolving, in extension, than the axial Young modulus, but with a more pronounced effect especially on the two other (normal and transverse) Young moduli, while none of the 3 shear moduli (along and around the bundle fiber direction) appears affected, as expected as well.

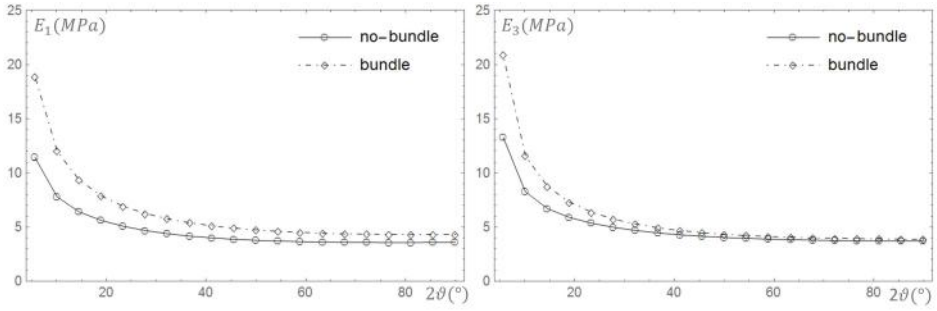

Figure 4.11: Compared evolutions without and with bundle effect at h=0 (layer contact) of the normal (left) and the transverse (right) Young modulus with layer misorientation angle 2θ.

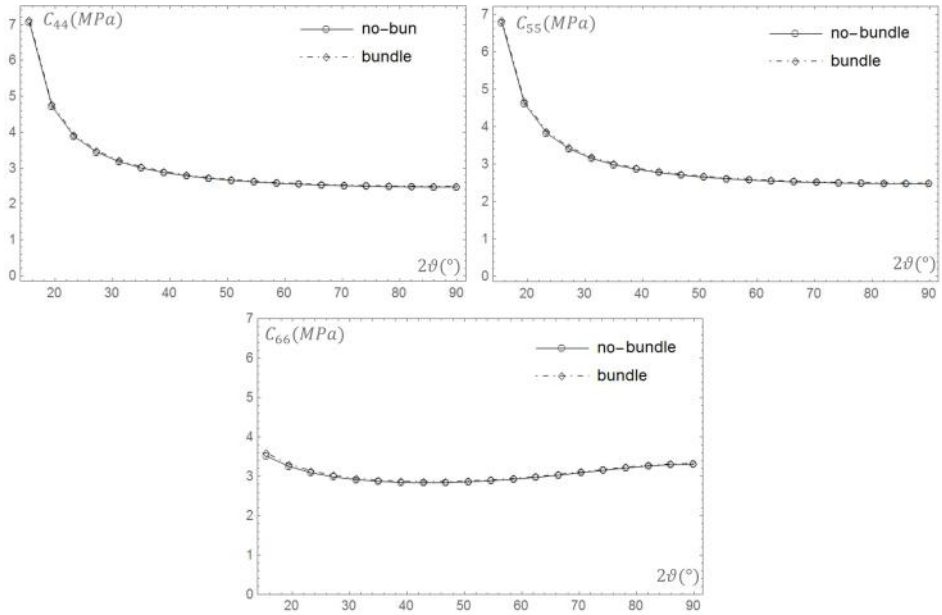

Figure 4.12: Compared evolutions without and with bundle effect at h=0 (layer contact) of the lateral $x_1 - x_3$ (top, left), the $x_1 - x_2$ facial (top, right) and the in-plane $x_2 - x_3$ (bottom) shear modulus with layer misorientation angle 2θ.

The related axial force (per cross section area unit) evolutions, obtained as explained in the beginning of that section from using that axial Young modulus analytical estimate, have the form plotted on Fig. 4.13 (respectively versus the 2θ layer angle, left, and versus the normalized extension Δ_L/Δ_{Lmax}, right), without and with bundle effect at h=0, without appearing noticeable differences. The extension normalization for the analytical curves uses the maximal extension that corresponds to fiber contact in the FPAs. The force-displacement curves of Fig. 4.13 right have the well known qualitative form of the force-displacement curves of 2D pantograph prior entering into any plastic or damaged stage. The final sharp increase corresponds to the start of the elastic behavior of the nearly aligned and fully compact FPA families at minimal misorientation angle θ.

The next subsection reports some comparisons with numerical validating results.

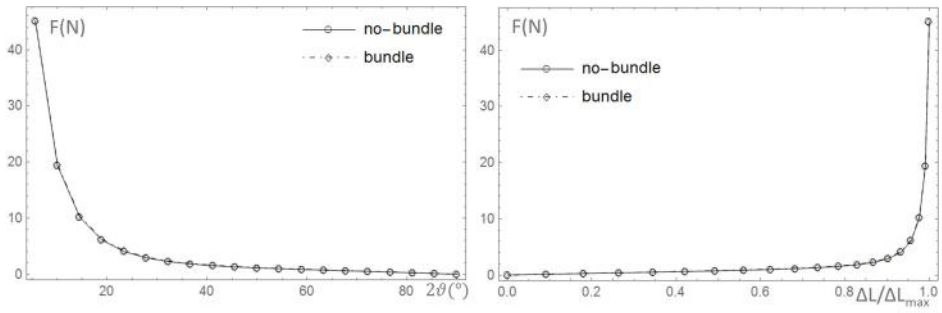

Figure 4.13: Axial force evolution for h=0 (layer contact) versus (left) the 2θ layer misorientation angle and (right) the normalized Δ_L/Δ_{Lmax} structure extension, without and with bundle stiffness contribution.

4.3.2 Compared numerical and analytical elastic modulus evolutions during extension

Comparisons with numerical simulations are performed from using the cell shown in Fig. 4.14, in which the layer (relative) inter-distance (h/a) is explicitly present. The two-phase elastic moduli are the same as for the analytical calculations. There are physically no pivot inter connectors in the cell.

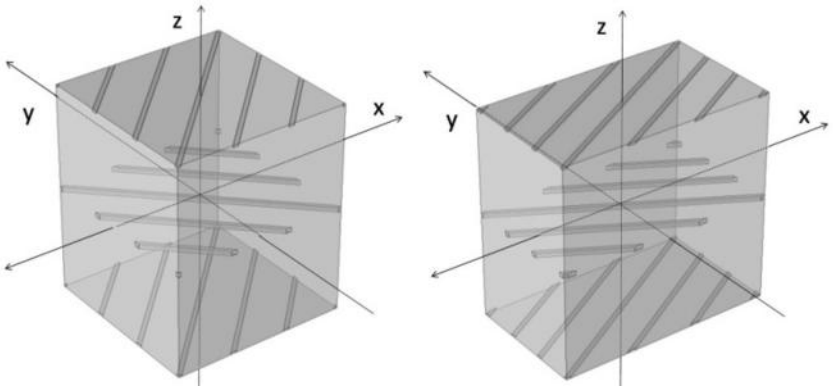

Figure 4.14: Initial (left) and x-extended (right) periodic cell for numerical estimates of effective modulus evolutions.

The fiber initial inter distance (d) in the layers is taken to be 20 times the beam side length and the relative layer inter distance h/a is varied from contact (0) to distant as in the analytical estimates. In order to remain close to the procedure used for the analytical estimate changes with a change of the layer misorientation angle (that is with various extension steps and no distorsion of the structure), the cell structure has been step-wise extended in changing that misorientation angle and on each successive cell with extended structure, 6 elementary loads are applied to determine the 3 Young moduli and the 3 shear ones. So doing, the cell remains homogeneously deformed at each extension step and not internal stresses are stored.

The first performed calculations are for the variation of the effective axial Young modulus with respect to the layer relative inter distance, from close to distant. These variations are reported in Fig. 4.15 as a function of the FPA misorientation angle 2θ for different values of the FPA h/a relative inter distance. The corresponding analytical estimates are also plotted for comparison. It is seen that both calculations pretty well correspond for the different h/a values (0, 1, 3) which cover the range of typical ratios in pantographs.

The Figs. 4.16-4.17 similarly report the numerically calculated other (Young and shear) moduli using the same cell, for the case h=0 only. These plots show how the tendencies well corresponds with the analytical estimates which are also reported.

The final step of this work consists in examining possible additional description, in the proposed analytical modeling, of torsion-like and bending-like strengthening effects on the total force-displacement curve from the pivot arrays, as is the case during in-plane extension of 2D pantographs, that we call for short pivot strength effects.

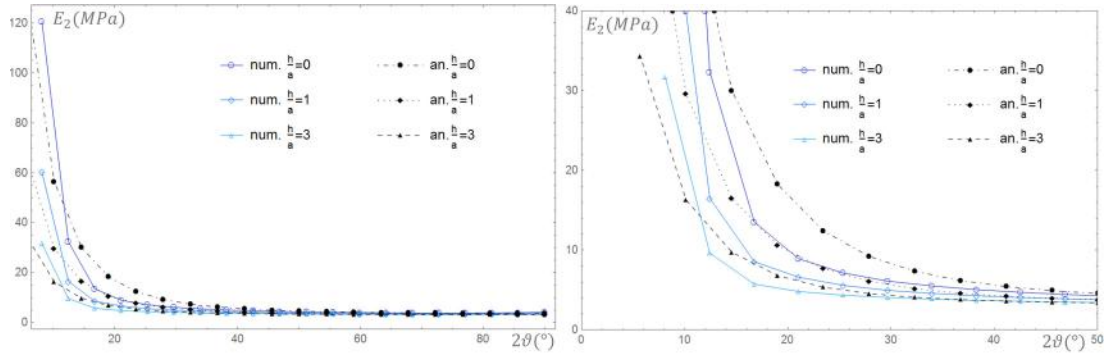

Figure 4.15: Compared (left) numerical and analytical axial Young modulus estimated evolutions with FPA misorientation angle 2θ at different (h/a) values and (right) a zoom of the left side.

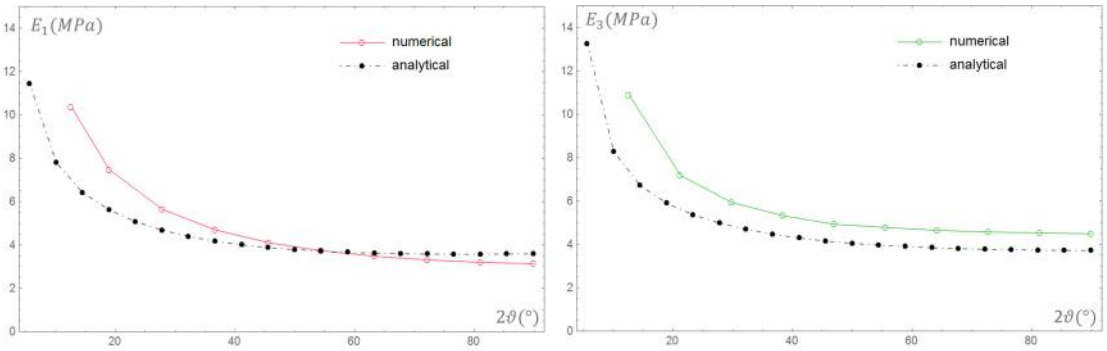

Figure 4.16: Compared numerical and analytical simulations of estimated evolutions with layer misorientation angle 2θ of the normal (left) and the transverse (right) Young modulus at h=0.

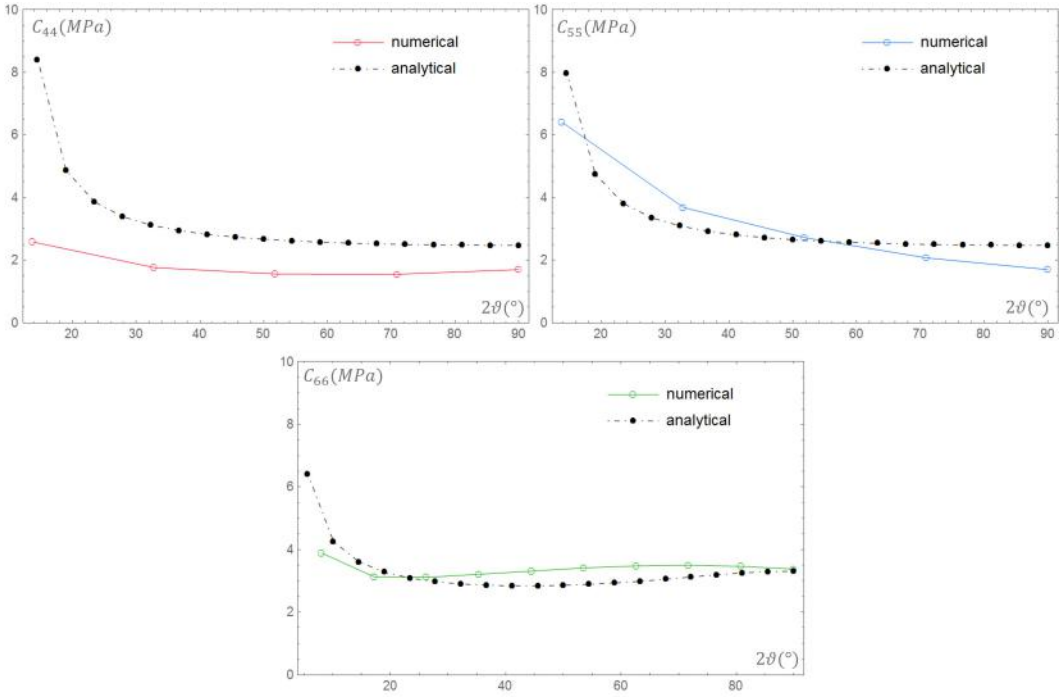

Figure 4.17: Compared numerical and analytical simulations of estimated evolutions with layer misorientation angle 2θ of the lateral $x_1 - x_3$ (top, left), the $x_1 - x_2$ facial (top, right) and the in-plane $x_2 - x_3$ (bottom) shear modulus at h=0.

4.3.3 Compared numerical and analytical force-extension curves with pivot strength effects

We compare a typical numerical force-displacement curve of a 2D pantographic structure, which is homogeneously in-plane stretched thanks to appropriately prescribed boundary conditions that suppress the heterogeneous second gradient effects, to the force-displacement curves obtained from the presented analytical modeling which is pivot strength free as built.

The boundary descriptions for these comparative numerical simulations are defined such that the whole 2D pantographic structure is homogeneously strained as the central zone. So doing, compared with the pure extension that is described in the proposed analytical homogenization-based model, the numerical one is only complemented with a discretely homogeneous pivot strength field coming from the specific torsion or/and bending features. Depending on this pivot strength, the difference between the total force-displacement curve of the pantographic structure and

its pure extension part can be either dominant or minor. This section stresses the two following results:

i. it is possible to pretty well match an analytically obtained $F/\Delta L$ curve from the proposed modeling, as the one shown in Fig. 4.13, characterized by a low matrix to fibers stiffness ratio and which is pivot strength free as built, in adjusting appropriately the pivot strength part in the total pantographic structure $F/\Delta L$ extension curve;

ii. it is conversely possible to pretty well match a numerical pantographic structure $F/\Delta L$ curve with low or moderate pivot strength contribution in accounting in the model for either a torsion-due stiffness increase of the bundle-like pivot arrays or for a bending-due decrease of the fiber layer inter distance (h), or for both effects; when these two effects (of limited influence) prove insufficient (say in case of high pivot strength contribution), a good match is accessible with assuming the matrix stiffness to increase according to some fiber misorientation dependency, the form of which can be deduced from the analytical versus numerical comparisons. These 3 influences are exemplified.

Numerically matching the analytical pivot strength free reference curve

Fig. 4.18 reports in full lines the force-displacement curve from the analytical modeling that corresponds to the case ($h = 0, \mu_M = 1$) plotted in Fig. 4.13 right, together with two numerical curves that correspond to a 2D pantograph under in-plane extension, the parameters of which are collected in Tab. 4.1. We call the stiffest of these two curves, the reference numerical simulation curve (the torsion modulus of which is denoted ref in Tab. 4.1) and the second one, which is the numerical adjustment on the analytical curve is called the low torsion numerical simulation curve (ℓT in Tab. 4.1). The pretty good adjustment is here obtained from reducing the torsion modulus by a factor 3 from the value of the reference numerical curve

For other μ_M values in the analytical curve, the necessary variation on the pantograph torsion modulus for matching the numerical and analytical curves are to be adjusted accordingly. For one discussion point to come next on, it is worth to stress here that adjusting analytical curves obtained with a smaller μ_M matrix modulus (keeping same h value) would be reasonably well obtained in decreasing similarly further the pantograph torsion modulus in the numerical simulation, such that a no torsion strength limit in the pantograph extension numerical simulation expectedly calls for a vanishing matrix stiffness in the proposed analytical modeling.

a	A	$k_e = EA$	k_p^{ref}
$10^{-3}m$	a^2	$149.9\ N$	$1225 \cdot 10^{-5} N\ m^{-1}$
h_p	r_p	$\overline{\ell}$	$k_p^{(lT)}$
$10^{-3}m$	$5 \cdot 10^{-4}m$	$25 \cdot 10^{-3}\ m^{-1}$	$428 \cdot 10^{-5} N\ m^{-1}$

Table 4.1: Data for the plots of the force-displacement numerical curves in Fig. 4.18. h_p, r_p are the pivot heigth and radius, $\overline{\ell}$ is the inverse of the interdistance ℓ between pivots and $k_p = \frac{\mu \pi r_p^4}{2h_p}\overline{\ell}^2$ *(Spagnuolo et al., 2017).*

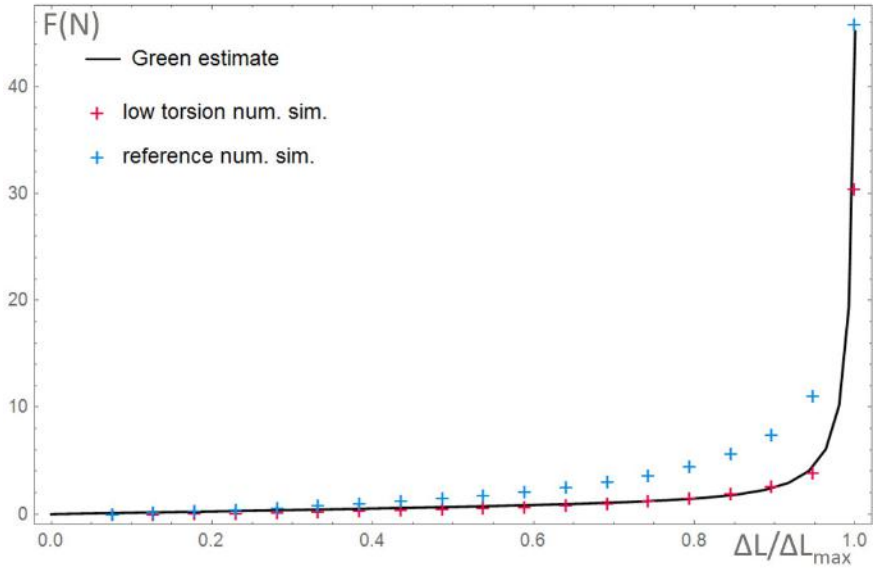

Figure 4.18: Matching the analytical force-displacement curve for h=0 and μ_M (full line) in lowering the torsion modulus from the 2D pantographic structure (upper crosses) numerical reference curve to the low torsion one.

Analytically matching the numerical reference curve with adding pivot strength effects

Considering first the pivot strength effects to be purely torsional, a first possible input in the proposed modeling is on the pivot effective stiffness that explicitly appears in the description given to the bundle-like pivot array that reinforces the embedding matrix according to Eq. (4.15). A pivot stiffness increase can be accounted for in

giving some evolution for in particular their shear modulus with the misorientation angle between fiber layers. A qualitative evidence that alternated torsion of successive pivots along fiber-like arrays is unavoidable, although hard to observed either experimentally or numerically, can be inferred from imagining the extension of the multi-layered P-I structures exemplified in Fig. 4.1. In order to check this effect, we have considered an evolution law of the bundle shear stiffness, under the simple form

$$\mu_B(\theta/h) = \mu_B \left(1 + c \left(\left| \frac{\pi}{4} - \theta \right| \frac{b}{h+b} \right)^N \right) \tag{4.24}$$

where c and the exponent N remain as adjustable coefficients, while the absolute value results from assumed equal stiffness increase whether the θ angle decreases or increases from the unstressed $\pi/4$ position.

In order to examine a *bending* interpretation of the pivot strength effects, a simple possibility to introduce it in the analytical modeling is to consider that the main pivot bending effect is to reduce the distance (h) between FPA layers, with at the most, layers reaching contact if bending goes to its geometrical limit (without damage). This alternated bending of pivots along fiber-like arrays has established existence as exemplified on Fig. 4.19 (left), from some performed experiments not to be commented in the present scope. It is also observable that the assumption of this (not totally regular) alternated bending to be null in the average over the layers is reasonable in gross approximation and sufficient for a schematic description as shown in Fig. 4.19 (right). The bending is assumed to remain in the plane made by the extension direction and the pivot array initial orientation normal to the FPA layers (the drawing plane) although each fiber-like pivot array connect fibers which are alternately $\pm\theta$ misoriented on each side of it. The bending angle can be estimated from the projections of the FPA layers in that bending plane as defined and drawn. A pivot bending of (mean) angle $\pm\kappa = (\pm w, z)$, with $\pm w$ and z being the pivot (alternated) direction and FPA normal respectively, changes the FPA inter distance as $h''(\mathrm{w},\mathrm{z})' = (h+b)\cdot\cos(\kappa) - b$. The limit bending angle κ_{lim} at layer contact (h=0) may be restricted by some minimal h_{min} value corresponding to a κ_{max} angle lower than κ_{lim}, in which case $h''(\kappa_{max}) = (h+b)\cdot\cos(\kappa_{max}) - b = h_{min}$ and $\kappa_{max} = \arccos\left(\frac{h_{min}+b}{h+b}\right)$. Note that in comparison with the possibly significant decrease of h if approaching or reaching contact ($h_{min} = 0, \kappa_{max}=\kappa_{lim}$), the pivot bending contribution to the structure extension is a negligible axial translation of the left-oriented FPAs with regard to the right-oriented ones $(h+b)\cdot\sin(\kappa_{max})$. The introduction in the modeling of this pivot bending effect on (h) can then pass by

Eq.(4.22) to increase faster the fiber volume fraction as

$$f_{fib(h,\kappa)} = \left(\frac{b}{h"(\kappa)} + b\right)\frac{a}{L\sin 2\theta} = \left(\frac{b}{h"(\kappa)+b}\right) f_{fib(0)} \tag{4.25}$$

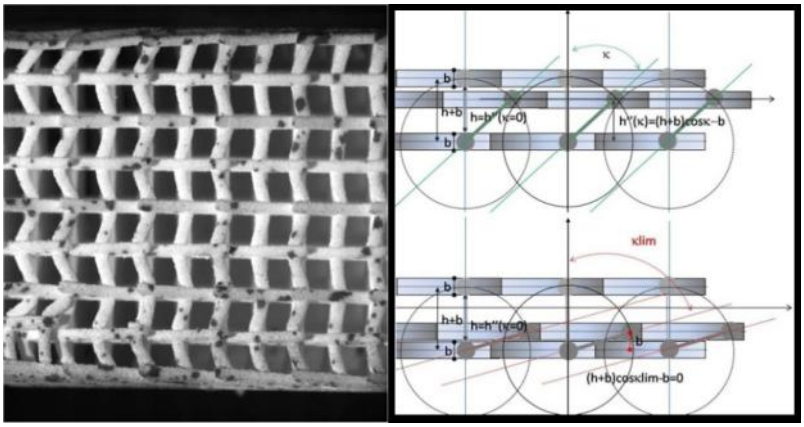

Figure 4.19: A lateral (left) view of a stretched multilayered pantographic structure showing alternated pivot bending along arrays and (right) a schematic description with (top) current and (bottom) limit positions (the intermediate third layer in the drawings is the extended position of the upper one, the lower layer being kept as fixed reference).

The use of Eq. (4.25) needs to determine or fix an evolution of κ/κ_{max} in terms of θ/θ_{max} or of any related geometric descriptor as defined. For the present purpose, only variations of $F/\Delta L$ curve with different constant h/a values have been compared.

These two effects are exemplified in Fig. 4.20(left) for the pivot stiffness (shear modulus) variation according to Eq. (4.24) and in Fig. 4.20(right) for the bending stiffness effect from changing the (kept constant) value of the layer inter distance (h/a), without using Eq. (4.25). It is noteworthy regarding the pivot height changes due to bending, a division by two may be likely thus the transition amounts from10 to 5 or from 1 to 0.5 which are exemplified in Fig. 4.20(right).

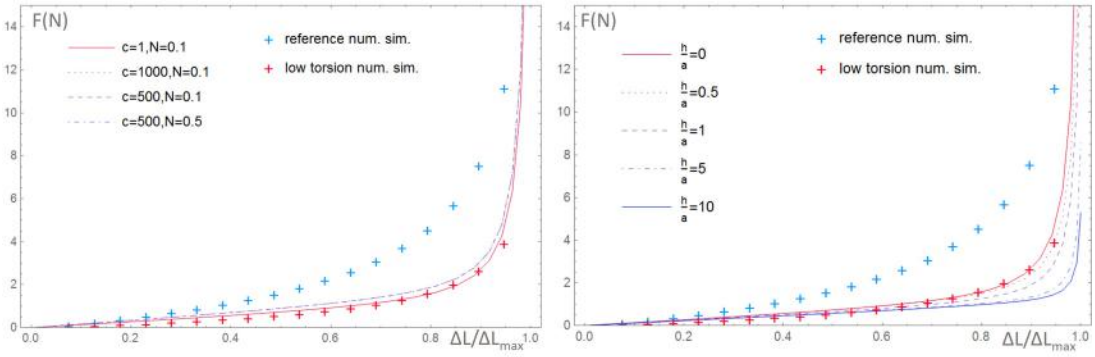

Figure 4.20: Amplitude and shape changes of the analytical force-displacement curve from (left) increasing the pivot shear modulus according to Eq. (4.24) (several sets of c,N parameters) and (right) decreasing the h/a inter distance.

From these Figures, where both the reference numerical curve and the low torsion one are plotted, the amount of variation allowed for a force-displacement curve by these two effects, either alone or together, both on the amplitude and on the shape of the curve of pantographs only appears convenient to adjust weak or moderate pivot strength effects.

On the contrary, when the contribution of pivot strength effects to the total curve is dominant, as is the case for the numerical reference curve in Figs. 4.18-4.20, these two effects are not sufficient. In which case, a last possibility to indirectly consider a pivot-due effect of torsion-type in the proposed analytical modeling is through a dependency of the matrix stiffness with the misorientation angle between the fiber layers. The Fig. 4.21(left) reports again the reference numerical curve with a set of analytical ones for different phase contrasts μ_M/μ_F, starting from $\mu_M = 0.02\mu_F$ (the contrast with $\mu_M = 1$ used in most of the previous plots) to end with $\mu_M = 0.98\mu_F$. Collecting the intersections of these analytical curves with the reference numerical one yield a μ_M/μ_F versus displacement $\Delta L/L_{max}$ relation which in turn yields the μ_M/μ_F versus 2θ angle variation law plotted in Fig. 4.21(right). Using in the modeling a close analytical expression (as the dotted curve) will quite well restitute analytically the reference numerical curve.

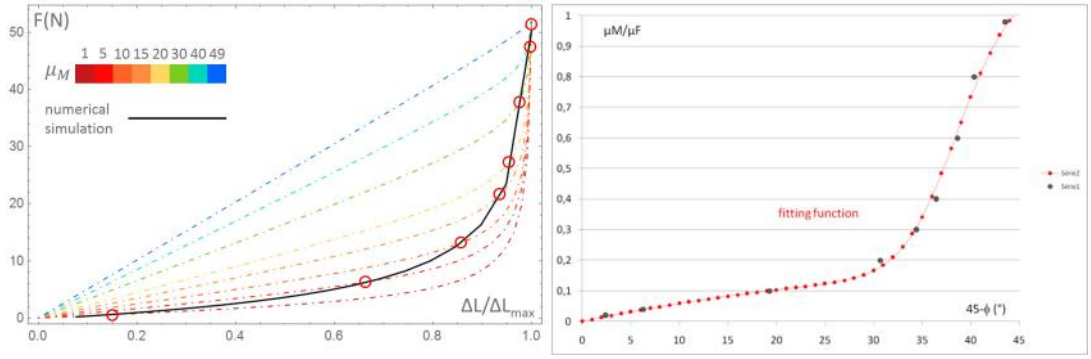

Figure 4.21: Amplitude and shape variations (left) of the analytical force-displacement curve for different values of μ_M and (right) the resulting $\mu_M(\theta)$ variation law that allows analytical matching with the reference numerical plot.

4.4 Conclusion

In this Chapter we have presented a description for two phase bi-continuous composites made of a 3D continuous fiber network embedded in a compliant matrix, the main characteristic of which is to obey a pantographic-inspired behavior due to the pantographic-like nature of the fiber arrangements and interconnection characteristics. This description which is based on considering the fiber network as an alternated piling of fiber planar alignments (FPAs) of cylindrical or square cross section allows to propose a homogenization-based model for the elastic behavior of such a composite structure, thanks to mean Green operators (mGOs) made available in previous works by authors and co-workers for such FPAs. Homogenization-based modeling amounts to estimating the effective (here elastic or elastic-like but also other) properties of a composite structure in accounting as precisely as possible for this structure, such as to be capable to follow the evolutions of these properties during the deformation of the structure and to estimate the stress-related evolutions. The pantographic-inspired characteristics of the structure are defined from geometric descriptors which link, in a 2D pantographic structure, on the one hand the fiber layer misorientation change to their network extension and to the fiber inter-distances in each constitutive layer, what also modifies the fiber network volume fraction in a representative volume element of the composite. On the other hand, that same fiber layer misorientation is linked to the strengthening behavior of the pivots that inter-connect the fiber layers which constitutes a more or less important contribution to the total force-displacement curve.

From comparisons with numerical estimates of the evolutions of the effective elastic moduli obtained for such a structure, it is shown that the proposed description which has the advantage of being analytical provides satisfying estimates of the effective Young and shear modulus variations when such a composite is submitted, at least piece wisely, to in-plane axial homogeneous extension.

Comparisons with numerically obtained force-displacement curves of an axially strained typical 2D pantograph have then shown that a quite good match is obtained with an analytically obtained force-displacement curve (from the effective axial Young modulus estimate) provided adjusting the pivot-strength-related contribution in the pantographic numerical extension simulation. Converse simulations have also shown that a quite good match of a numerical pantograph force-displacement curve can be obtained from the analytical modeling with accounting for (i) a torsion-due stiffness increase of the fiber-bundle like pivot arrays or/and (ii) a bending-due decrease of the fiber layers inter-distance or/and (iii), for high pivot strength effects, with assuming the embedding matrix of the composite to have a fiber misorientation-due stiffness increase during straining. These matching possibilities show that such pantographic-inspired composites can also be to some extent pantograph-equivalent.

Chapter 5

Damage analysis in pantographic fabrics

Here we further discuss the issue of damage and failure in pantographic structures. The ensuing discussions are based upon experimental data published [5, 6, 97].

5.1 Introduction

In this Chapter, we deal with some aspects concerning damage and rupture in pantographic structures. The discussions presented below can easily be linked to the topics discussed in the previous Chapter. In fact, in the previous Chapter it was suggested that, by modifying the properties of the matrix, one can approach the description of the onset of plasticity and damage in the pantographic-inspired composite material.

As we have already pointed out several times, there is a strong analogy, also supported by the identification analyses between the two models presented above, between the matrix of the pantographic-inspired composite and the pivots of the pantographic structures.

In this final Chapter we show how most of the phenomenology of damage and fracture in pantographic structures is attributable to the deterioration of pivots.

5.2 Mechanisms of rupture

Experimentally, three different mechanisms of rupture have been observed: one concerning the fibers and two related to the pivots. The fiber rupture occurs when the maximum elongation is reached related to the geometrical and material features of

the fiber in a considered sample. On the other hand, the pivots can experience failure depending on two different mechanisms: (i) the shear of the pivot and (ii) its torsion. Needless to say, the failure occurs when reaching certain thresholds, in shear (i) or torsion (ii) of the pivot. As a qualitative observation, it is possible to forecast which of these last mechanisms will prevail by considering the shape ratio of the pivots: for "slim" pivots it has been observed that the *shear mechanism* prevails, while for "stubby" pivots the *torsion mechanism* plays the fundamental role.

In the following paragraphs we quantitatively analyze the aforementioned mechanisms.

5.2.1 Fiber elongation mechanism

From a quantitative viewpoint for characterizing rupture, the discrete quasi-static Hencky spring model described in the previous Chapter can be modified by considering a simple irreversible rupture mechanism for the extensional springs as discussed in [97]. An extensional spring fails if its deformation level exceeds a certain threshold. Experimental data for a displacement-controlled bias extension test (Fig. 5.1) are provided in [12]. The first fiber failure is observed at the corners of the specimen, where the elongation of fibers attains its maximum, as also predicted by the second gradient continuum model discussed in the first Chapter.

This predicted failure initiation has also been confirmed by means of a displacement-controlled shear test [97] (see Fig. 5.2). It was also observed that in this case the elongation of fibers attains its maximum at the corners ofthe specimen. We note that in the proposed second gradient model, the assumed damage mechanism was that of the fibers due to their elongation.

5.2.2 Pivot shear mechanism

In [5], a pivot damage mechanism due to shearing of pivots, i.e. fibers detaching due to relative sliding in correspondence of pivots, is taken into account, allowing the sliding between the two layers (families) of fibers. Thus, the non-linear homogenized quasi-static model for the discrete system discussed in the first Chapter is modified by introducing, in the spirit of mixture theory, two independent placement functions χ^1 and χ^2 (the placement functions of body points belonging to horizontal and vertical fibers, respectively) defined on the same reference domain and, accordingly, considering the following nonlinear (elastic) strain energy to be minimized

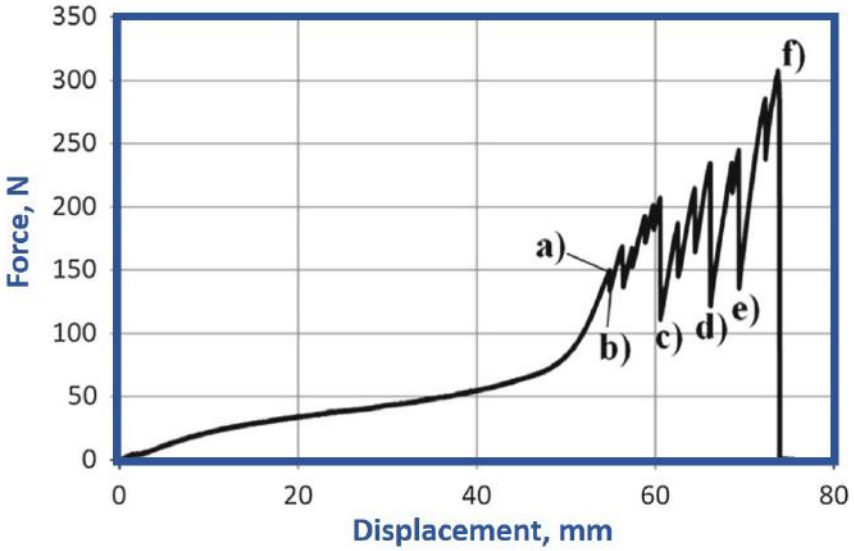

Figure 5.1: Force versus prescribed displacement for a bias extension test. (a) Sample before first beam breakage (i.e. breakdown onset); (b) upper-left corner beam breakage; (c)-(f) further fiber breakages.

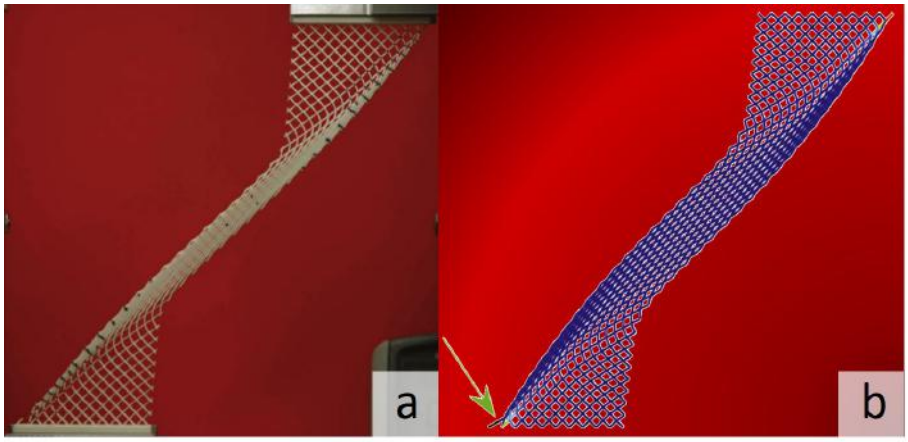

Figure 5.2: (a) Damage onset ($\lambda = 0.976$) of a shear test. (b) The broken fiber is in black and it is pointed by the arrow.

$$\int_{\mathcal{B}_0} \underbrace{\sum_{\alpha=1,2} \frac{K_e^\alpha}{2} \|F^\alpha \hat{e}_\alpha - 1\|^2}_{\text{extension of horiz. and vert. fibers}} + \int_{\mathcal{B}_0} \underbrace{\frac{K_s}{2} \left| \arccos\left(\frac{F^1\hat{e}_1 \cdot F^2\hat{e}_2}{\|F^1\hat{e}_1\| \cdot \|F^2\hat{e}_2\|} \right) - \frac{\pi}{2} \right|^\xi}_{\text{shear (pivots torsion) contribution}} +$$

$$+ \int_{\mathcal{B}_0} \underbrace{\sum_{\alpha=1,2} \frac{K_b^\alpha}{2} \left[\frac{\|\nabla F^\alpha |\hat{e}_\alpha \otimes \hat{e}_\alpha\|^2}{\|F^\alpha \hat{e}_\alpha\|^2} - \left(\frac{F^\alpha \hat{e}_\alpha \cdot \nabla F^\alpha |\hat{e}_\alpha \otimes \hat{e}_\alpha}{\|F^\alpha \hat{e}_\alpha\|^2} \right)^2 \right]}_{\text{bending of horiz. and vert. fibers}} + \tag{5.1}$$

$$+ \int_{\mathcal{B}_0} \underbrace{\frac{K_{int}}{2} \|\chi^1 - \chi^2\|^2}_{\text{relative sliding of the two layers}}.$$

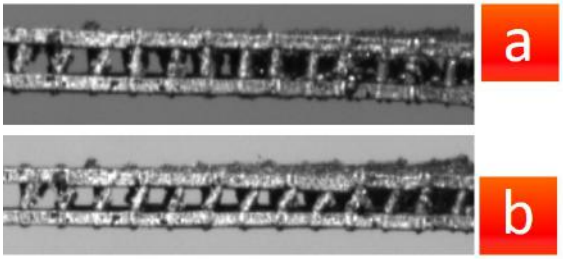

Figure 5.3: Experimental observation of the shear of pivots: (a) reference configuration and (b) shear deformation. We are grateful to Dr. X. Pinelli (LMT, ENS Paris-Saclay/CNRS/Université Paris-Saclay) for the photos.

where K_{int} (resistance to the relative sliding of the two layers) evolves following a criterion based on thresholds for the relative distance $\delta = \|\chi^1 - \chi^2\|$ between χ^1 and χ^2. Depending on the geometrical features of the considered pantographic structure, one can then predict a relative displacement between the fibers in the corner of the rigid triangles near the short side of the structure or on the long sides of the sheet (see Figs. 5.4-5.5).

One can then qualitatively forecast the development of fracture in the pantographic sheet by allowing the beams to slide one respect to the other in correspondence of the pivots as introduced in [5] and [4]. Indeed, the algorithm developed in [4] is able to forecast the onset of fracture, by considering a *mechanism* based on a threshold of the relative displacement (corresponding to the shear of the pivot, as experimentally observed, see Fig. 5.3). We note that in this algorithm, the considered model is based on the non-linear Euler-Bernoulli beam theory and the pivots are modelled as extensional springs whose elastic constant corresponds to the K_{int} of the homogenised model.

In Fig. 5.6 it is possible to observe the relative displacement between beams as a 3D bar graph, plotted on the shape of the pantographic sheet. A noteworthy aspect related to the introduction of the cubic factor in the *sliding* energetic term is the breaking of symmetry in the plot of relative displacement seen in Fig. 5.6. From the viewpoint of fracture initiation, it is clear from the figure that there are two maxima which correspond to two precise pivots. One of them will undergo the first rupture, due to a flexural/shear stress. This numerical prediction is validated in Fig. 5.7, where a well explicative sequence showing the load step when the first fracture occurs is presented: the broken pivot is precisely the one predicted by the model.

A dissipation problem could be suitably adapted to the relative displacement

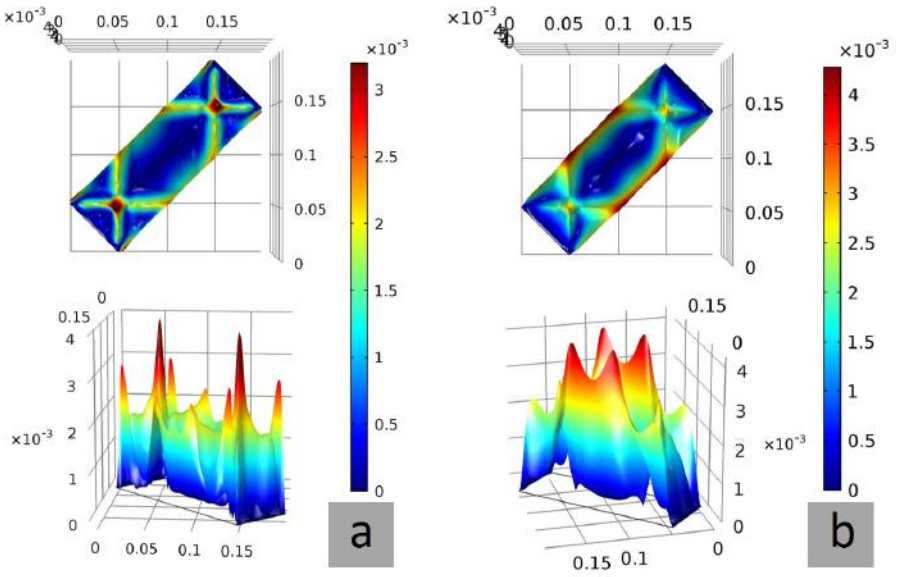

Figure 5.4: Depending on the geometrical features of the considered pantographic structure, one can predict a relative displacement between the fibers in the corner of the rigid triangles near the short sided of the structure (a) or on the long sides of the sheet (b).

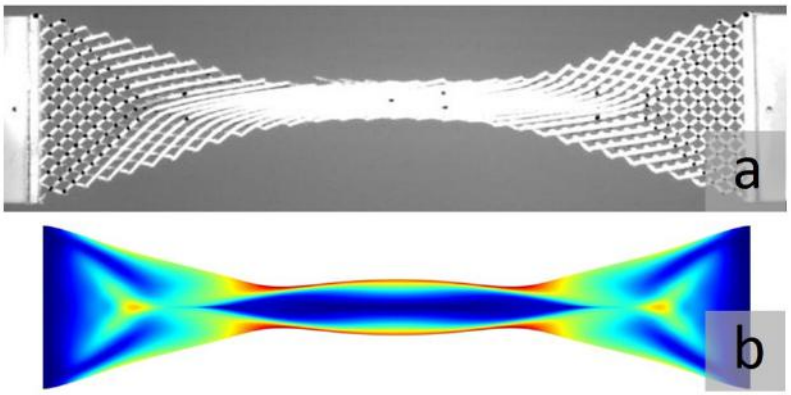

Figure 5.5: Comparison between experimental emerging of the first rupture in an aluminum pantographic structure (a) and numerical prevision (b) of the maximum of the relative displacement between the fibers (relative displacement in colour scale).

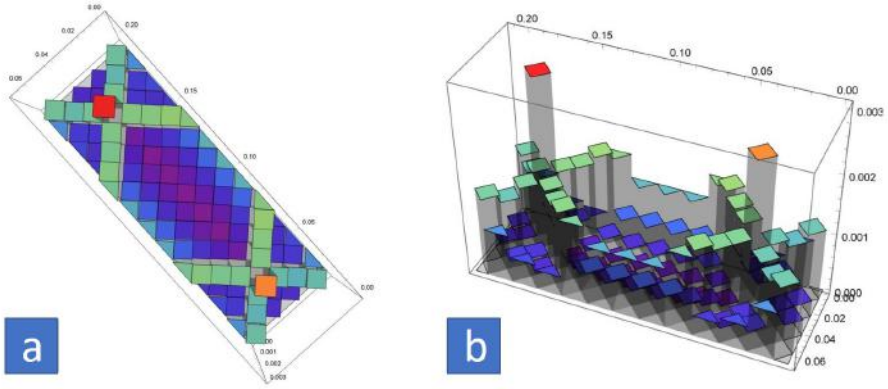

Figure 5.6: Plot of the relative displacement on the shape of the pantographic sheet in the framework of the non-linear Euler-Bernoulli beam meso-model.

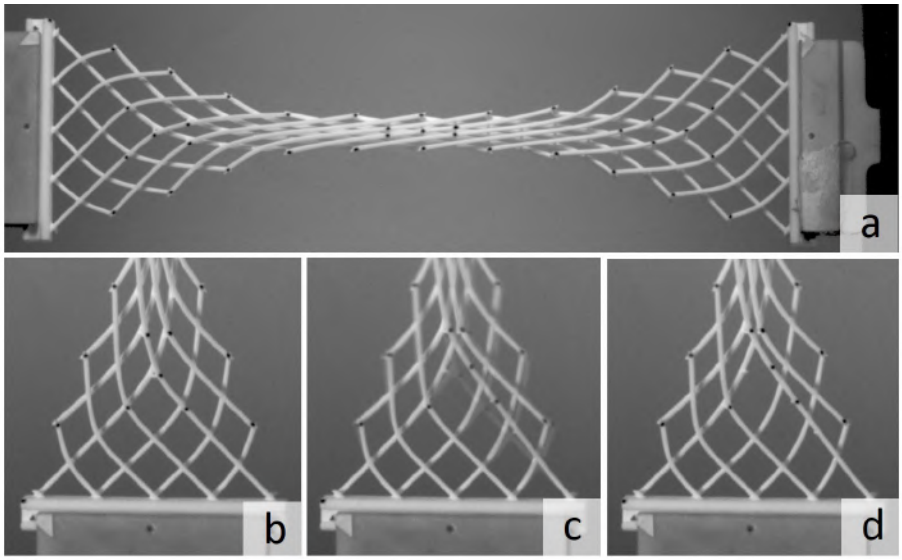

Figure 5.7: A well explicative sequence which shows the moment of the first fracture, in the pivot forecasted by the model.

description. In this case, it should be needed a preliminary analysis on the friction mechanisms, as the one presented in [99].

5.2.3 Pivot torsion mechanism

Finally, we consider a rupture criterion based on the computation of the shear angle[1] (see Fig. 5.8). One can relate the torsion of the pivots to the shear angle. For certain specimen endowed with a particular set of geometrical parameters, the rupturing evolution is controlled (and initiated) by excessive shear deformation (or torsion) of the pivots. In the displacement-controlled shear test in Fig. 5.2, the shear attains its maximum near the two internal vertices of the quasi-rigidly deforming triangles.

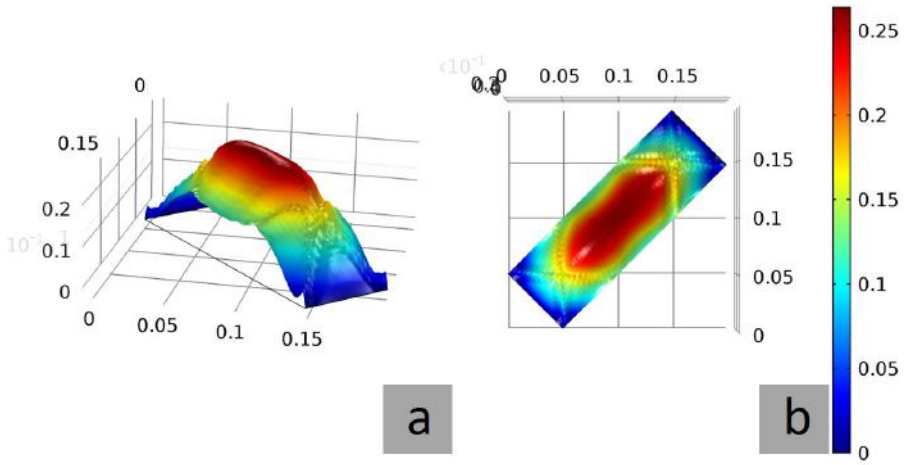

Figure 5.8: Plot of the shear angle. It is possible to use it for defining a rupture criterion based on the pivot torsion.

5.3 Quasi-perfect pivots

Technological advances in the field of additive manufacturing have made it possible to produce structures and objects with very complex geometry. Because of this peculiar ability, 3D printing has greatly increased the realization and study of metamaterials, i.e. materials that, with a microstructure decided a priori, exhibit exotic mechanical properties. Recently some pantographic structures have been moulded in Polyamide replacing the standard pivots (cylinders with no torsional stiffness) with perfect

[1]We refer here to the shear of the whole pantographic structure, different from the aforementioned shear of the pivot.

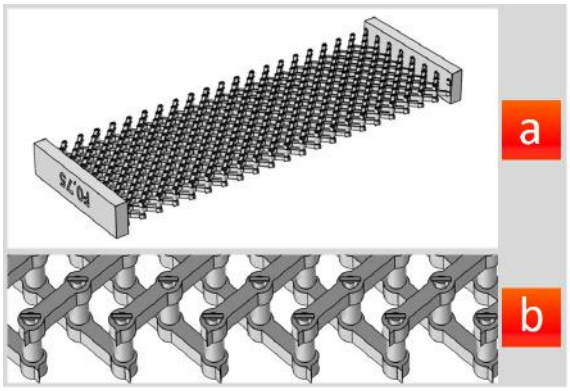

Figure 5.9: CAD model of a pantographic structure with perfect-pivots (a). In (b) the perfect pivots are shown.

pivots, which correspond to hinges (free rotations). Details of this study are given in [60].

In this section, we present pantographic structures with perfect pivots made of 316L stainless steel. As will be explained below, pivots are not exactly perfect pivots, as residual torsional stiffness is observed experimentally. The dimensions at which the perfect pivot is printed are very close to the precision ensured by the printing and at these levels also the size of the powder used for the printing is a quantity that influences the result. Despite the apparent unsuccess of printing perfect pivot metal structures, some properties of the specimens, which at first glance are underestimated, can be observed. When comparing the measurements for a standard pivot and a (nominal) perfect pivot specimen, there are considerable differences that can only be ascribed to the different types of pivots. For this reason, they will be referred to as quasi-perfect pivots. An extensive explanation of the process of printing metal pantographic structures is given in [96].

Deformation energy of a pantographic sheet

In the first Chapter of this thesis, it has been illustrated how to reach a macroscopic model of second gradient continuum by means of a process of homogenization (which actually consists in performing a procedure of identification of the energy of macro-deformation, that is a macroscopic lagrangian density, in terms of constitutive parameters appearing in the postulated expressions of the microdeformation energy) of a postulated micromodel.

5.3.1 The shear energy

The second integral in Eq. (5.1) can be interpreted as a shear deformation energetic contribution at the macro level. At the micro level it may be associated with pivot torsional energy. The form of this energy term depends on the angle between the interconnected fibers by the pivot elevated to a certain power γ: this last parameter can be obtained from experimental data fitting and in general it depends on the type of material in which the structure is fabricated. As will be explained below, the energy of shear can be modeled in other ways too. For example, a model that more accurately captures phenomenology is due to Ogden [**?**, 100]. A version of Ogden shear energy adapted to pantographic structures has been introduced in [**?**]

$$\begin{aligned}\mathcal{W}_s(\vartheta, \mathcal{J}) = \mathrm{K}_{s1}\left[\left(1+\left(\frac{\vartheta}{\vartheta_0}\right)^2\right)^{\beta} - 1\right] \\ -\mathrm{K}_{s2}(\log(\mathcal{J}-\mathcal{J}_0) - (\log(1-\mathcal{J}_0) - \mathcal{J} + 1)\end{aligned} \tag{5.2}$$

where ϑ is the angle between the fibers in correspondence of the interconnecting pivot and $\mathcal{J}$ the module of its cosinus, while ϑ_0 and $\mathcal{J}_0$ are the values of the angle and of its cosinus in some particular points of the deformation history. These last two parameters will be described with more precision in a future work. The two constants K_{si} $(i = 1, 2)$ substitute the shear stiffness K_s of Eq. (5.1).

5.3.2 Experiments and numerical simulations: quasi-perfect pivots (QPP)

Two specimens, one with standard pivots and one with quasi-perfect pivots, were tested in a BIAS extension test. The two specimens' shapes are, in the reference configuration, rectangles of sides $L_1 = 30\,mm$ and $L_2 = 90\,mm$. An image of the QPP-sample (Quasi Perfect Pivot sample) can be observed in Fig. 5.10. Both the specimens are made of 316L stainless steel. Since additive manufacturing does not produce homogeneous but highly porous samples [101, 102], the mechanical characteristics of the objects tested must be considered different (lower) than those of the material of which they are made up. The specimens have been created by using the SLM125HL set-up from SLM solutions. This machine is equipped with a 400W YAG laser (YLR-400-WC) at a wavelength of 1070 nm. The scanning speed varies from 400 to 1500 mm/s, while the thickness of the powder layer lies in the range between 30 and 100 μm. The minimum diameter of the laser at the focal point is about 70 μm. The powder employed is 316L stainless steel having spherical particles whose lowest

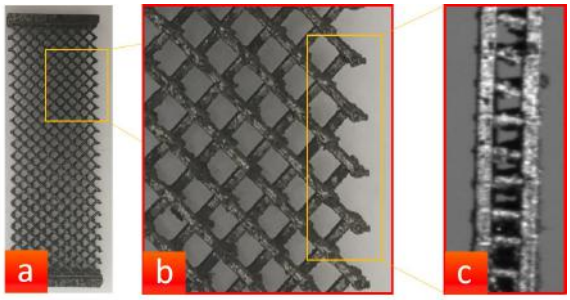

Figure 5.10: QPP specimen (a) and details of the pivots (b,c).

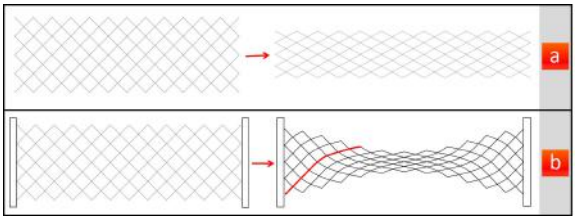

Figure 5.11: Schematic description of a BIAS extension test. (a) A pantograhic structure with no clamping deforms as a truss; (b) when the short sides are clamped, the bending of the fibers is observed.

diameter is 37 μm (CILAS 920).The manufacturing of the part is preceded by the proper positioning of the 3D geometry in the printing volume using the MAGICS-Materialize Software.

BIAS extension test in pantographic structures

A BIAS extension test is simplest experimental test one can perform on pantographic structures [37] (it is specifically called BIAS extension and not only extension, because it is performed along a biased direction respect to the fiber direction, see Fig. 5.11). This particular test is performed by tightening the short sides of the pantographic structure to observe the effects of the second gradient. In fact, as it can be seen in Fig. 5.11, if the short sides are not blocked, then, in theory, a zero strain energy (a so-called floppy mode) should be measured: up to the point where all the fibers become parallel the extension energy is zero (or negligible). If the short sides are not tightened, the bending energy (second gradient) is also cancelled out. This test was therefore specifically designed to observe the effect of the second gradient in pantographic structures.

K_e	K_b	K_s
$EA\backslash p$	$EI\backslash p$	$G\pi d^4\backslash(32hp^2)$

Table 5.1: Theoretical expressions for the stiffnesses. E is the Young modulus, G the shear modulus, A the cross-section of the fibers, I the cross-sectional moment of inertia. Finally, p is the interdistance between two pivots on the same fiber, d the diameter and h the height of the pivot.

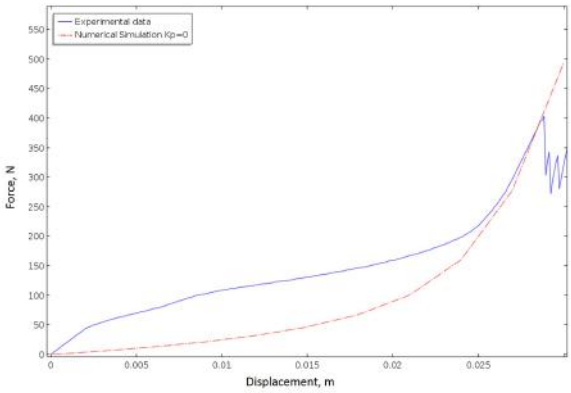

Figure 5.12: Comparison between the experimental measurements of reaction force for a pantographic structure with quasi-perfect pivots (blue) and the numerical simulation for a structure with perfect pivots (red, dot-dashed). The numerical simulation is lower than the experimental measure.

The perfect pivots did not work at a first look

BIAS extension tests were performed for the specimen of Fig. 5.10. The reaction force versus prescribed displacement was measured and plotted in Fig. 5.12. A first remark must be done by observing Fig. 5.12: by comparing the measured reaction force with the theoretically expected one (obtained via numerical simulation with the prescription that the shear stiffness K_s is zero), it is evident that a substantial part of the deformation energy (the area under the reaction force curve) is missing in the numerical simulated case. In other words, we cannot pose the shear stiffness to zero for the present sample and we cannot say that the pivots are perfect. The theoretical expressions for the stiffnesses used in the umerical simulations are reported in Tab. 5.1.

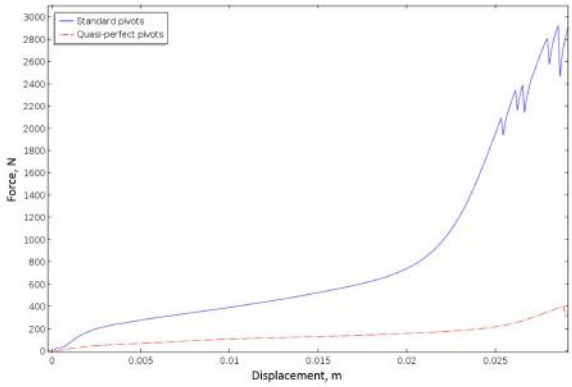

Figure 5.13: Comparison between the experimental measurements of reaction force for a pantographic structure with standard pivots (blue) and a structure with quasi-perfect pivots (red, dot-dashed).

Comparison with standard pivots

A second comparison must be done, with the experimental curve relative to a BIAS extension test of a pantographic structure made of the same material (316L stainless steel) but with standard pivots (SP). The comparison of the force-displacement curves for the two specimens is shown in Fig. 5.13.

An observation can be done immediately. If, on the one hand, it has been remarked that the reaction force measured for the specimen with perfect pivots is significantly higher than that which should be observed if the pivots were really perfect, by comparing it with the curve for the standard pivot specimen, it is clear that the measured force is much lower than in the standard case. In this sense one can conclude that the perfect pivots are not perfect from the microscopic point of view, but they are sufficiently perfect, we say quasi-perfect, from a global macroscopic point of view. The QPP specimen has, infact, a total structural stiffness lower compared to the SP specimen. If the difference between the two mechanical behaviors is ascribed solely to the pivots, then it makes sense to examine the ratio between the shear stiffnesses of the two specimens. Both the values are identified by using the theoretical expressions in Tab. 5.1. We obtain

$$\frac{K_s(QPP)}{K_s(SP)} = 0.1 \tag{5.3}$$

We can therefore conclude that the manufacturing process of perfect pivots has been partially successful, having produced pivots with torsional stiffness of an order of

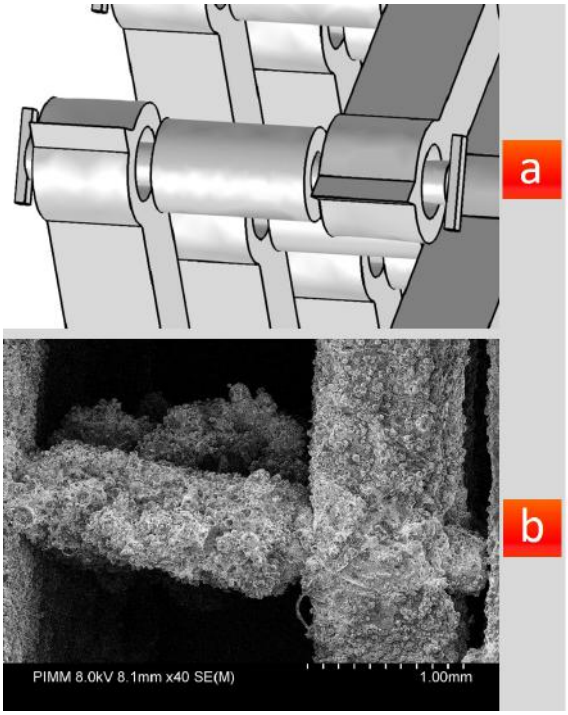

Figure 5.14: Comparison betwen the CAD model (a) of a perfect pivot and its practical realisation (b) in 316L stainless steel via additive manufacturing.

magnitude lower than the case of standard pivots. The reason for the incomplete success of the perfect pivots can be easily understood by observing Fig. 5.14 in which the CAD design of a perfect pivot and its realization by additive manufacturing are compared. The photo shows precisely the porosity that prevents the mechanism of the perfect pivot from working properly. In the phase of fabrication, the specimens were positioned orthogonally to the building platform even though a tilt angle of 45^o would have been preferable for the realization of the pivots. Despite the significant technological achievements represented by such manufacturing technologies, the objects obtained are very sensitive to the location and the number of supports whose inadequate positioning could result in widespread microstructural flaws. Furthermore, the rough surfaces in Fig. 5.14b show porosity which can potentially be suppressed by heat treatments such as Hot Isostatic Pressing (HIP), resulting in almost-fully dense metallic alloys [103] (such post processing was not performed on the samples).

5.4 Conclusion

In this final Chapter we discussed some aspects concerning the damage and rupture of pantographic structures. The qualitative and phenomenological analyses presented represent yet another point of contact between pantographic metamaterial and pantographic-inspired composite material. In fact, in the previous Chapter it was suggested that the properties of the matrix, which plays a similar role to that of pivots in pantographic structures, can be modified to describe phenomena such as damage or rupture in pantographic-inspired composite.

Conclusion

Collaboration and mutual exchange between different entities always leads to new and unknown scenarios. The risk of failure when trying to connect distant backgrounds is very high, but if one succeeds in obtaining a result then the originality and innovation of the project are guaranteed.

This thesis is the result of the contact between two scientific fields which are originally very distant: composites (and the relative homogenisation framework by means of Green's operators) and metamaterials (which imply the constant introduction of new models and generalised theories). The idea described above is obviously very complex and presents several challenges forcing to face very hard mathematical and technical problems. In this thesis work, we explained the first attempt to achieve this very ambitious project.

The first chapter of this thesis is dedicated to the description of the pantographic metamaterial. As we have pointed out many times, the presence of the microstructure makes it necessary to adopt a second gradient model to take into account all its exotic effects. The deformation of the pantographic metamaterial is extremely heterogeneous and it is possible to localize different zones with different deformation behaviors: the description of the pantographic-inspired composite has been made only for the homogeneous zones of the structure, not taking into account the interface between these, where the flexion of the fibers is observed and therefore second gradient contributions are necessary for the mathematical modeling.

In the second chapter we have presented some experimental data about the pantographic structures that motivated the adoption of the homogenization framework of the Green tensors to model the material of pantographic inspiration.

In chapters 3 and 4, the techniques of Green's tensor homogenization framework were applied to research into the actual properties of pantographic-inspired composite.

In the last chapter a phenomenological analysis of the damage has been approached. The discussion of the damage is linked to the deformation characteristics of the interconnecting pivots: this allowed us to make some comparisons with the

pantograph-inspired material, where the role of the pivots is played by the matrix.

Appendix A

DIC applied to pantographic structures

A.1 Application to a BIAS extension test

In the following, a BIAS extension test performed on a steel pantographic structure is analyzed. In total, a series of 55 pictures will be analyzed for which no damage was observed. Figure A.1 shows the picture of the initial configuration, and three loaded configurations corresponding to the 17th, 34th and 51st studied steps. In the present case, the pivots of the pantograph were marked in black, and a random pattern was created by spraying black and white paint on the grips. The fact that the grips were patterned helps the DIC code to converge even though very large displacement levels occur during the experiment.

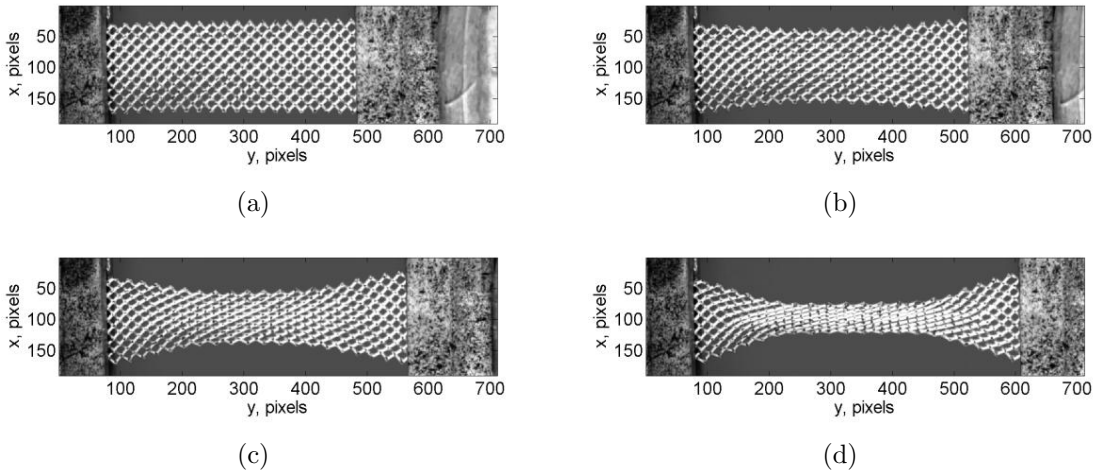

Figure A.1: Gray level images of the pantograph in the reference configuration (a), 17th (b), 34th (c) and 51st (d) loading steps

Macro- and mesoscale analyses will be reported in the sequel. For macroscale analyses, the rectangular region of interest was meshed with T3 elements independently of the underlying mesostructure. Such discretizations may then be compared with numerical simulations performed at the macroscale [2]. Four different mesh densities were considered (Fig. A.2(a-d)). The characteristic mesh size, which is defined as the square root of the average element surface, was equal to 28 pixels for the first mesh, 13 pixels for the second one, 8 pixels for the third one, and 6 pixels for the last. These four meshes will be utilized for convergence analyses of the DIC results at the macroscale.

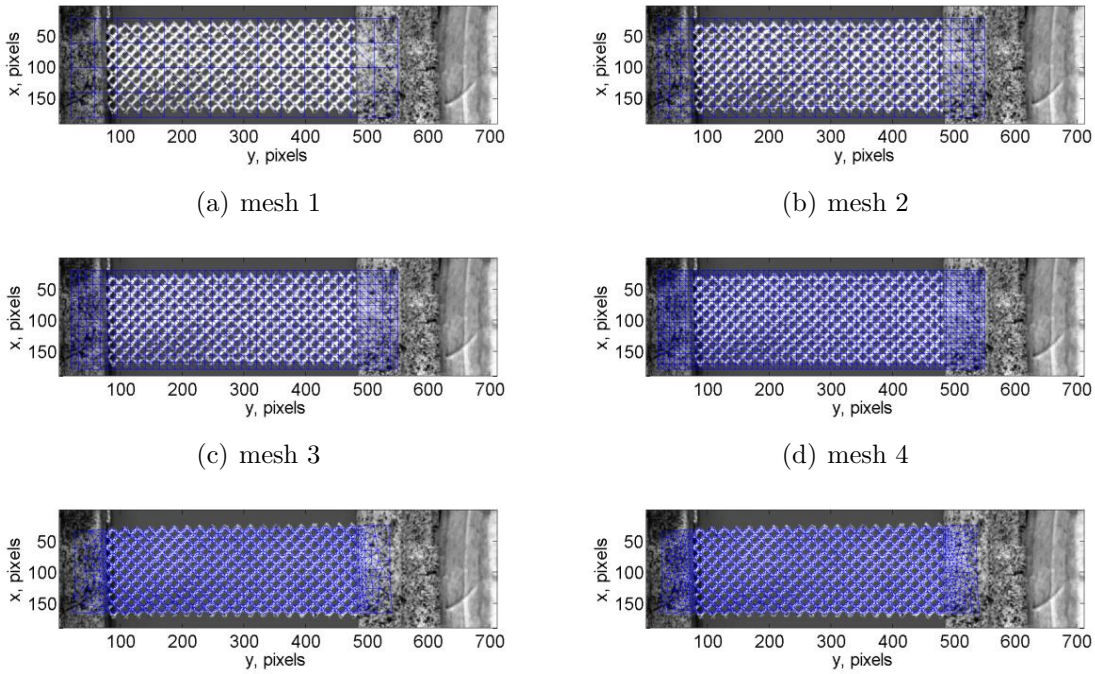

(a) mesh 1 (b) mesh 2

(c) mesh 3 (d) mesh 4

(e) mesh 5 (f) mesh 6

Figure A.2: Finite element meshes overlaid with the gray level picture of the reference configuration.

Two additional meshes were tailored to the pantograph mesostructure (Fig. A.2(e-f)). Contrary to the polyamide pantograph for which simple morphological operations were performed in order to construct the mesoscale mesh from a mask [2], the procedure was different herein. The starting point was the nominal geometry of the pantograph, which would be used, say, in FE simulations. From this information, the mesh was created with Gmsh [104] (Fig. A.3(a)) and a picture of the corresponding mask (Fig. A.3(b)). A DIC analysis was run between the reference picture and the mask to deform it so that the mesh can be backtracked onto the actual pantograph surface. In such an analysis, an auxiliary (coarse) mesh was used (Fig. A.3(c)). Once the DIC analysis converged, the original mesh was consistent with the actual geometry of the pantograph (Fig. A.3(d)).

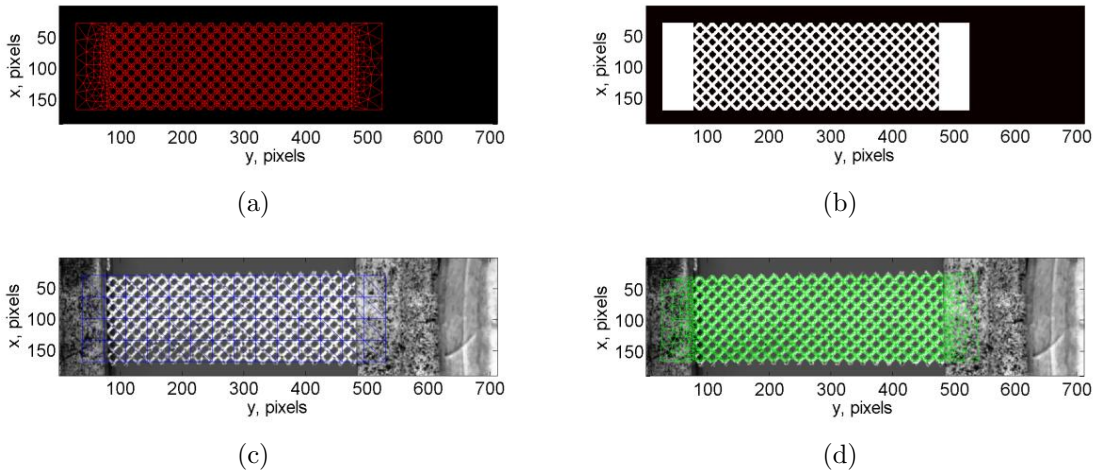

Figure A.3: Illustration of the back-tracking procedure. Initial mesh (a) and corresponding mask (b). (c) Reference picture and mesh used to register the mask. (d) Overlay of back-tracked mesh and reference picture.

This back-tracking procedure was applied to two meshes (Fig. A.3(e-f)). The corresponding characteristic mesh size is equal to 3.7 and 3.6 pixels, respectively. It is worth noting that such discretizations can only be considered thanks to regularization techniques since the correlation length of the pantographic structure is of the order of 10 pixels. Only so-called direct calculations will be reported in which each considered picture is registered with respect to the reference image. To speed-up convergence, a first incremental analysis is run in which the reference configuration becomes the deformed configuration of the previous analysis step. These first results are used as initialization to the direct registrations. The regularization length was chosen equal to 30 pixels. The convergence condition on the norm of the mean displacement correction was set to 10^{-3} pixel, which is very low since the measured displacement amplitudes will be significantly higher (*i.e.* more than 130 pixels in the longitudinal directions, and $\pm$ 50 pixels in the transverse direction).

In global DIC, the registration quality is assessed with gray level residual fields, which correspond to the pixel-wise gray level difference between the picture in the reference configuration and the picture in the deformed configuration corrected by the measured displacement. The quantity to be minimized is the L^2-norm of the gray level residuals over the region of interest [59]. The root mean square (RMS) level is reported in Fig. A.4 for all six meshes considered herein. The first general tendency is that the registration quality degrades as more steps are analyzed, thereby signaling that the measured fields become very complex at the end of the experiment (Fig. A.1).

Such type of observation was already made for the polyamide pantograph [2, 105]. Second, there is a significant difference between the first four meshes and the last two. This proves that meshes tailored to the actual pantograph surface better capture the kinematics of the test, even with the same regularization length as for coarser meshes. Third, in both cases, a converged solution is obtained in terms of mesh density with respect to the chosen regularization length. More precisely, meshes 3 and 4 at the macroscale, meshes 5 and 6 at the mesoscale have the same residual levels. Consequently, there is no need to further refine the discretization with the chosen regularization length.

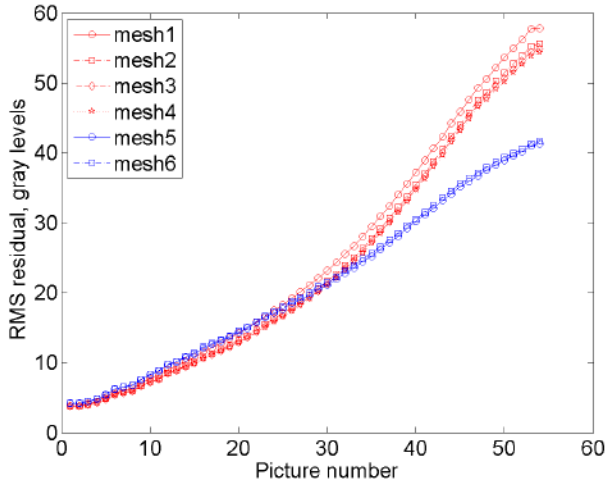

Figure A.4: RMS gray level residual as functions of the picture number for the six meshes shown in Fig. A.2.

In the following discussion, only two sets of results are reported, namely, those of meshes 4 (at the macroscale) and 6 (and the mesoscale). Figure A.5 shows the longitudinal and transverse displacements measured for the 17th picture. The transverse displacement field u_x shows a very important contraction, which is of the same order of magnitude as the longitudinal motions u_y. Since the width of the sample is one third of its length, the transverse deformations are much more important than the longitudinal component. This observation applies to both scales. In the present case, both measurements have approximately the same quality in terms of overall registration residuals (Fig. A.4).

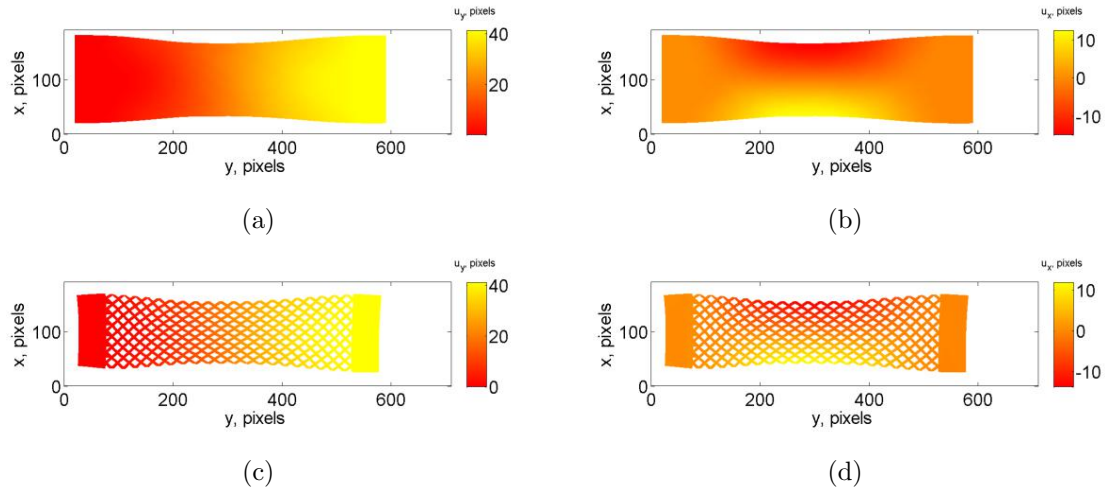

Figure A.5: Longitudinal (a-c) and transverse (b-d) displacement fields measured with meshes 4 (a-b) and 6 (c-d) for the 14th picture. The fields are shown on the deformed configuration.

In Fig. A.6 the same fields are shown for the 34th picture. The main features of the transverse and longitudinal displacement fields are identical to the previous step, yet with higher overall levels. The displacement ranges still are of the same order of magnitude for the longitudinal and transverse displacements. Consequently the central part of the sample is thinner. The deformed shapes are very close for both meshes, which translates into the same levels of registration residuals (Fig. A.4).

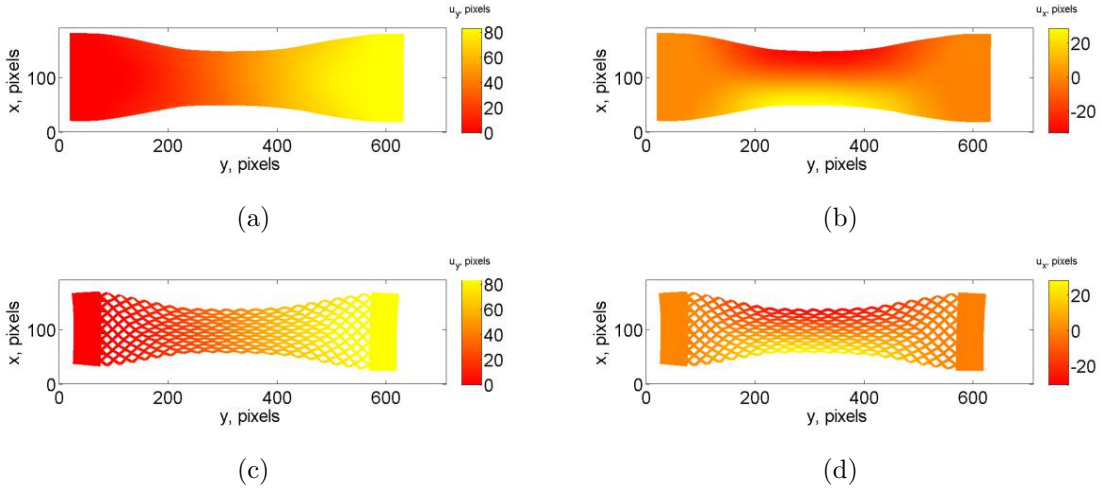

Figure A.6: Longitudinal (a-c) and transverse (b-d) displacement fields measured with meshes 3 (a-b) and 4 (c-d) for the 34th picture. The fields are shown on the deformed configuration.

One of the last steps is reported in Fig. A.7. In that case the gray level residuals (Fig. A.4) are significantly higher for mesh 4 (at the macroscopic scale) in comparison with mesh 6 (at the mesoscopic scale). There is a clear difference in the deformed shape whose width is lower for the mesoscopic analysis in comparison with the macroscopic result. The highly deformed region has grown toward both ends of the pantographic sheet, which can be understood by the fact that when struts touch each other, the deformation mechanism moves away from these zones.

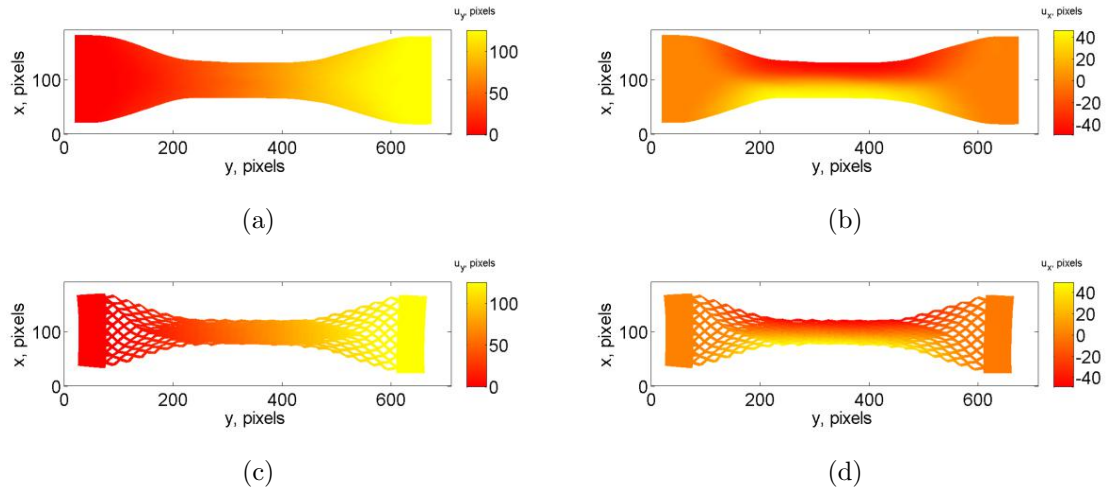

Figure A.7: Longitudinal (a-c) and transverse (b-d) displacement fields measured with meshes 3 (a-b) and 4 (c-d) for the 51th picture. The fields are shown on the deformed configuration.

The results reported herein confirm that DIC analyses can be run on pantographic structures at macroscopic scales [2, 105] and mesoscopic levels [2] with regularized DIC on very fine meshes (*i.e.* down to 3.6 pixel elements). Important gains were observed in terms of registration quality by moving from the macroscopic to the mesoscopic scale (*i.e.* more than a factor of one and a half at the end of the picture series). The final gray level residuals indicate that even more advanced approaches should be followed. What is missing in the mesoscopic analysis is the special kinematics provided by the pivots.

A.2 Application to a shear test

Shear tests have also been reported for pantographic structures [97]. This second example deals with 1,000 pictures with an 8-bit digitization and a definition of 1388×1038 pixels. The physical size of one pixel is equal to 110 µm. The first part of the experiment was monitored very finely, and then the acquisition rate was decreased (Figure A.8(a)).

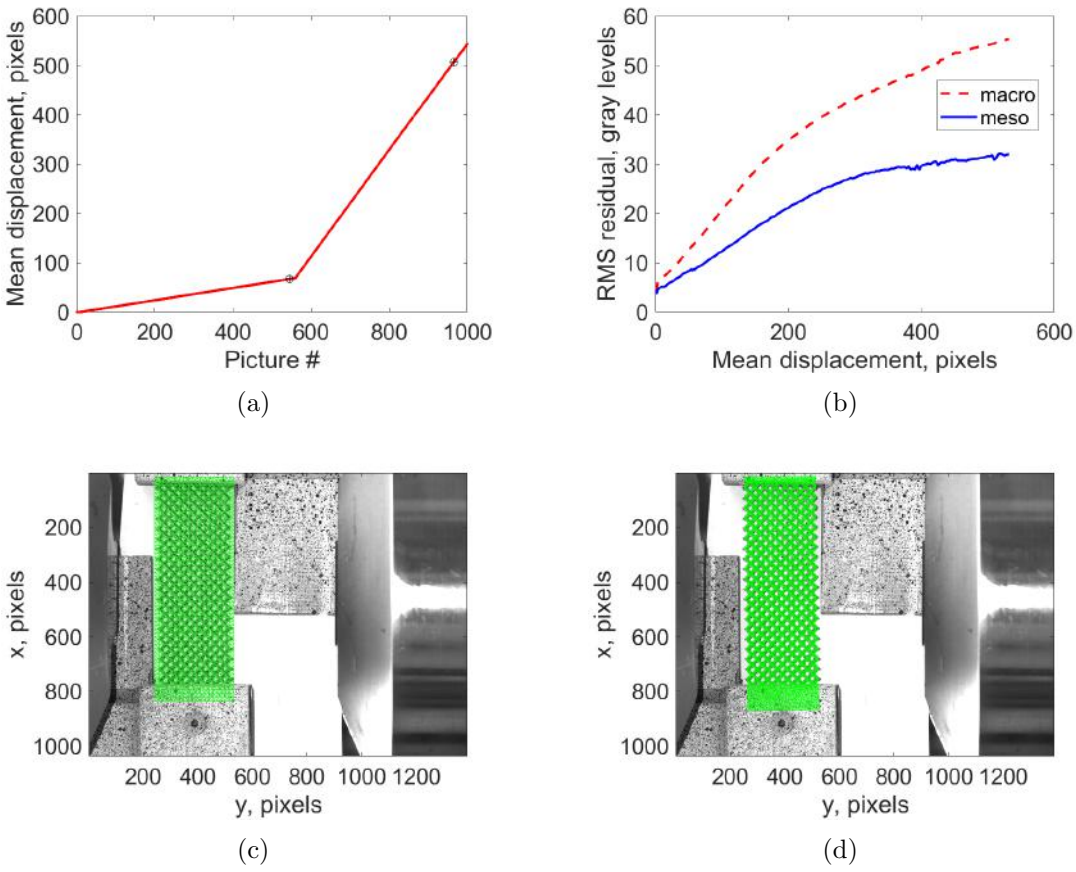

Figure A.8: (a) Mean transverse displacement of the crosshead. The black symbols depict the two states that are analyzed hereafter. (b) RMS gray level residuals for the whole image sequence. Meshes at the macro- (c) and meso- (d) scales overlaid on top of the image of the reference configuration.

In the following DIC analyses, the two scales of measurements are discussed. The mesh at the macroscopic level encompasses the whole pantograph and a small part of the grips (Figure A.8(c)). The mean characteristic mesh size was equal to 10 pixels. Conversely, the mesh at the mesoscale only covers the external surface of the pantograph (Figure A.8(d)). Its characteristic size was equal to 5 pixels on average. It was backtracked by following the same procedure as in the BIAS test. In the present case, the regularization length was equal to 75 pixels (*i.e.* higher than in the previous case) since the regularization strategy was now applied to incremental displacements (*i.e.* Hencky-type elasticity) and not to total displacements. When studying the gray level residuals, there is a gradual degradation as the applied displacement increases.

This trend shows that the selected kinematic bases and regularization strategy are not able to fully describe the experiment. Contrary to the previous, there are clearer differences between macroscopic and mesoscopic kinematic bases, namely, the former leading to higher residuals than the latter.

Figure A.9 shows the displacement fields measured for the 545-th picture (Figure A.8(a)), which are overlaid on top of the picture in the deformed configuration. Even though the gray level residuals were higher than those at the very early stages of the experiment (Figure A.8(b)), the results are still reasonably consistent with the underlying mesostructure. In terms of overall pattern, the mesoscopic and macroscopic fields are close.

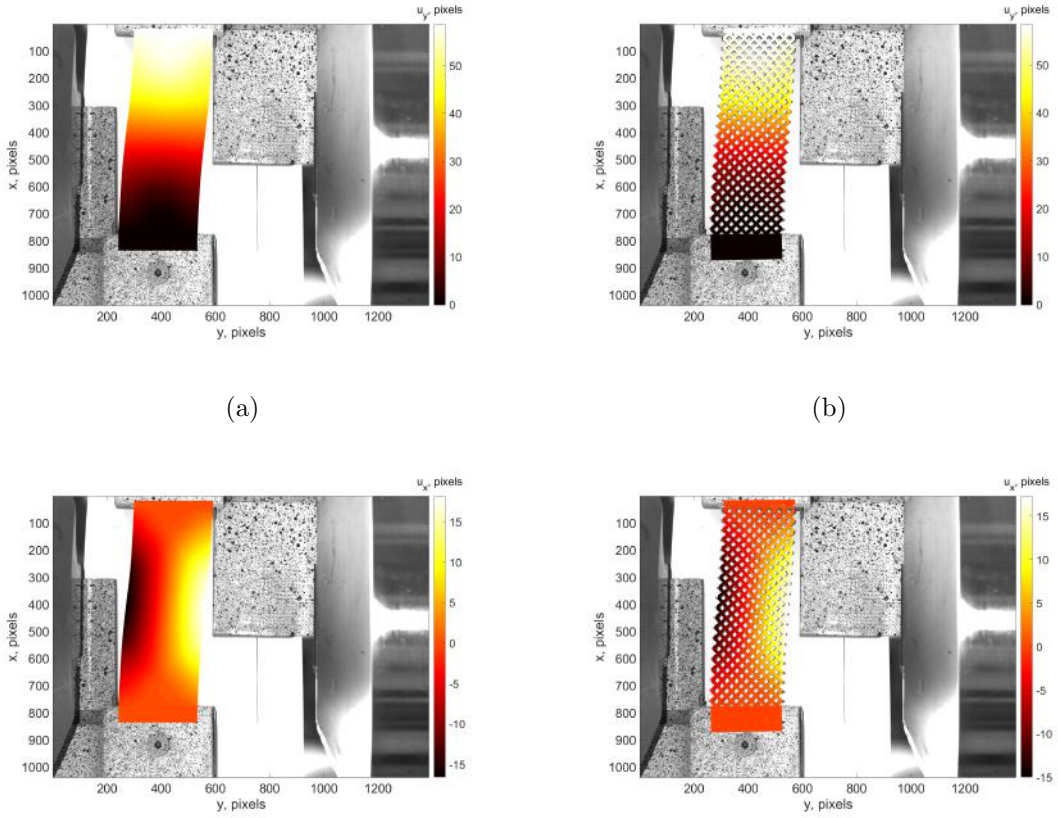

Figure A.9: Transverse (a-b) and longitudinal (c-d) displacement fields measured with macro (a-c) and meso (b-d) meshes for the 545th picture. The fields are overlaid on top of picture in the deformed configuration.

The gray level residual fields are reported in Figure A.10 for the two types of discretizations. Significant differences are observed between the two fields. The mesostructure appears in the residuals of the macroscopic calculations (Figure A.10(a)). This observation proves that the macroscopic kinematics does not fully capture the actual sample deformation. Conversely, the mesoscopic kinematics better describes the underlying deformation process. As a consequence, the gray level residuals are lower than those observed with the macroscopic mesh (Figure A.10(b)).

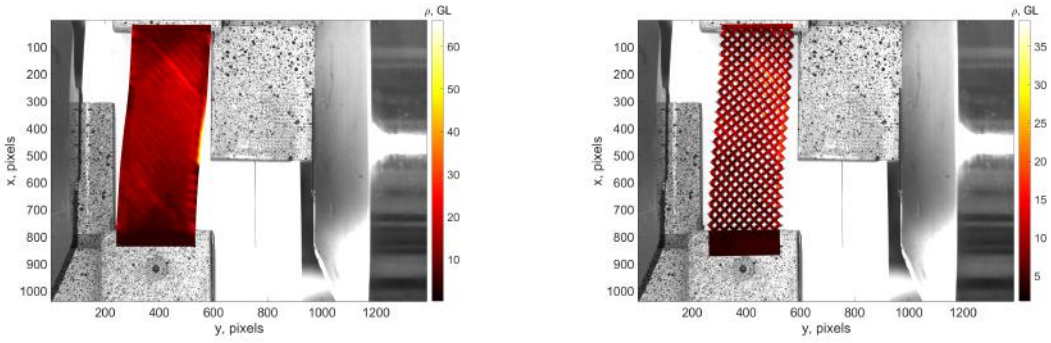

(a) (b)

Figure A.10: Gray level residual fields with the macro (a) and meso (b) meshes for the 545th picture. The fields are overlaid on top of picture in the deformed configuration.

Green Lagrange strain fields are reported in Figure A.11 for both discretizations. It is interesting to note that even though elastic regularization was considered, some details of the mesostructure appear in the macroscopic fields associated with the normal strain components (Figure A.11(a,c). The shear strain levels (Figure A.11(e) remain rather small in comparison with the normal strain amplitudes (Figure A.11(a,c)). The mesoscopic mesh, which is more closely related to the underlying mesostructure, enables higher strain magnitudes to be measured in comparison with the macroscopic discretization.

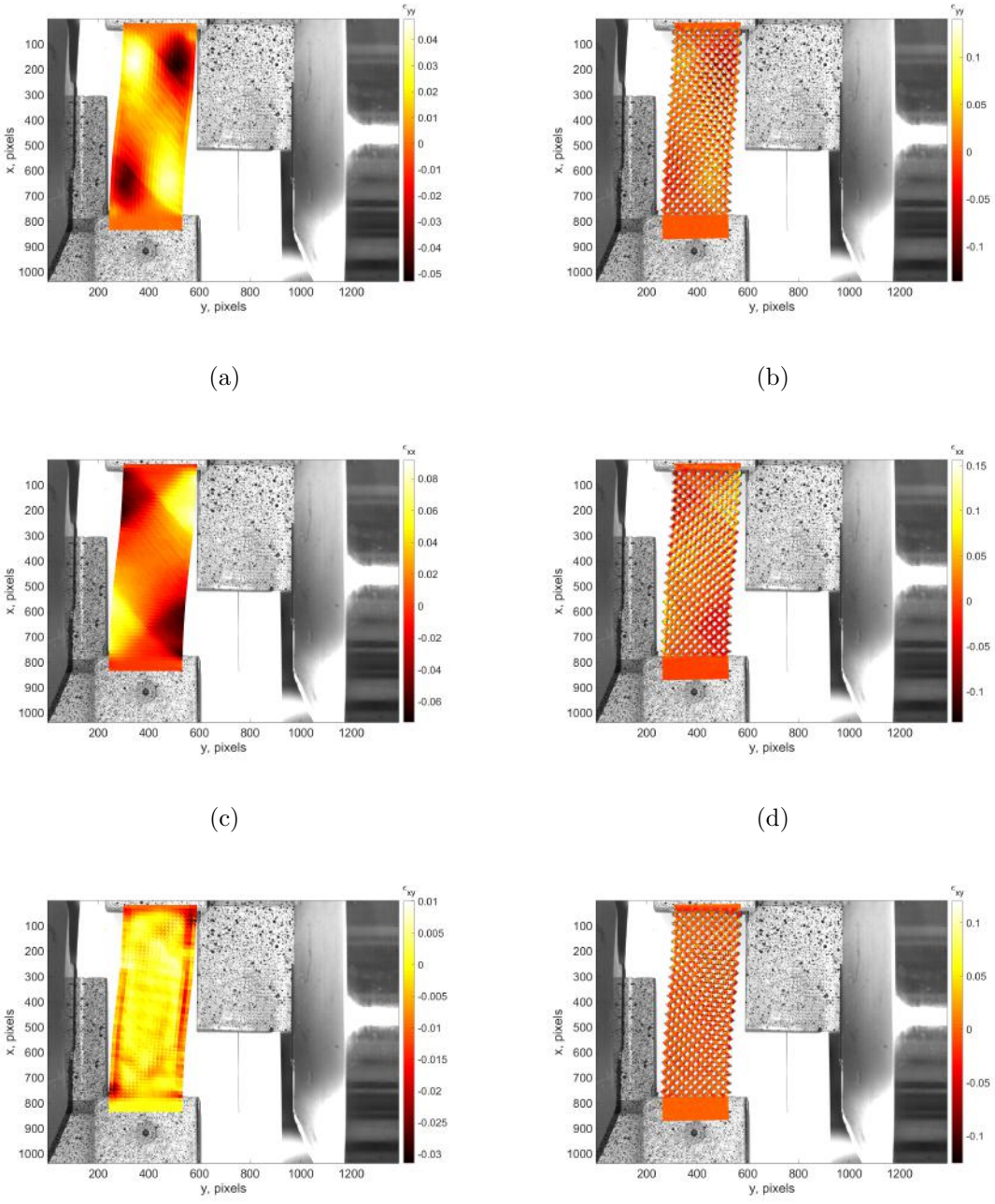

Figure A.11: Normal transverse (a-c), longitudinal (b-d) and shear (e-f) strain fields measured with macro (a-c) and meso (b-d) meshes for the 545th picture. The fields are overlaid on top of picture in the deformed configuration.

One of the last step of the experiment (*ie* 965-th picture, see Figure A.8(a)) is now analyzed. This configuration is significantly deformed and leads to a crosshead displacement level greater than 60 % of the sample height. The displacement field pattern is again similar for macroscopic (Figure A.12(a,c)) and mesoscopic analyses (Figure A.12(b,d)).

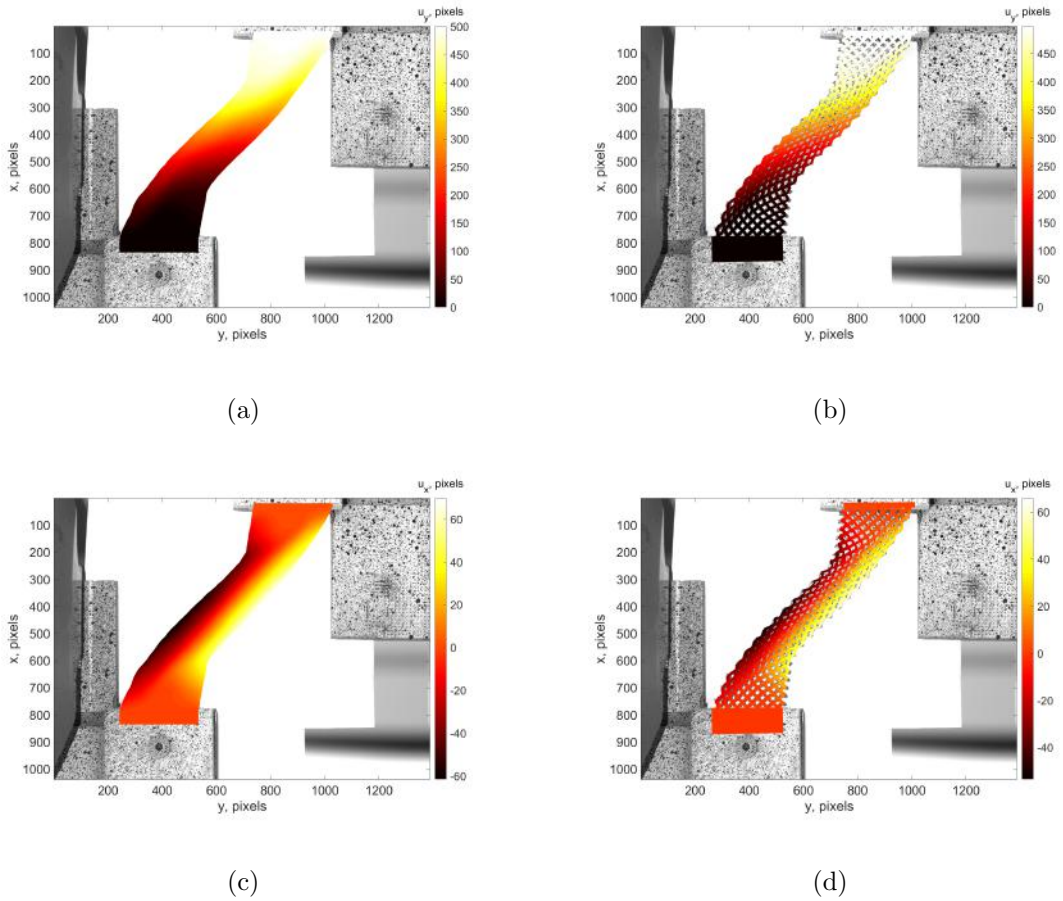

Figure A.12: Longitudinal (a-c) and transverse (b-d) displacement fields measured with meshes 3 (a-b) and 4 (c-d) for the 965th picture. The fields are shown on the deformed configuration.

The gray level residual field corresponding to the macroscopic discretization (Figure A.13(a)) indicates that the kinematic description is too crude to properly capture local details. This phenomenon leads to overall levels that are about two times

higher than the mesoscopic analysis (Figure A.8(b)). At the end of the analysis, the mesoscopic mesh and corresponding discretization of the displacement field is more trustworthy than the macroscopic mesh. Even though the mesoscopic mesh is better suited, it still does not fully capture the actual deformation (Figure A.13(b)). An even more detailed description is need (*eg* describing the local kinematics around pivots).

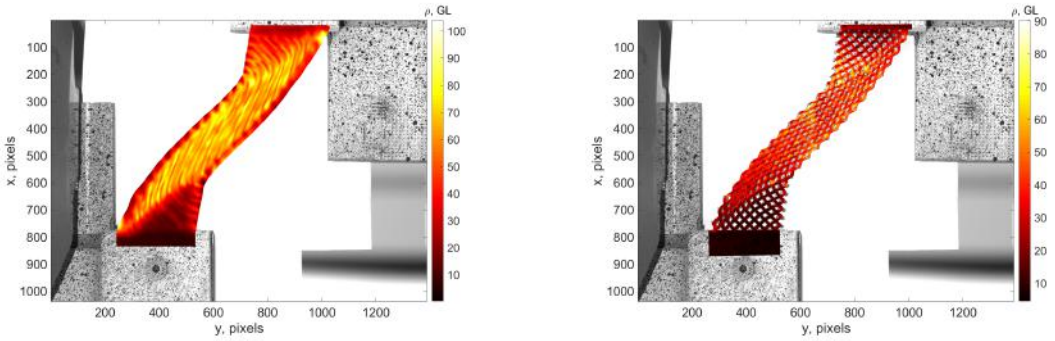

(a) (b)

Figure A.13: Gray level residual fields with the macro (a) and meso (b) meshes for the 965th picture. The fields are overlaid on top of picture in the deformed configuration.

Green Lagrange strain fields are shown in Figure A.11 for the two different discretizations. Significant differences are observed in any of the reported fields, except in the areas close to the grips where the pantograph does not deform too much. It is worth noting that the strain levels are higher with the mesoscopic mesh in comparison with the macroscopic discretization.

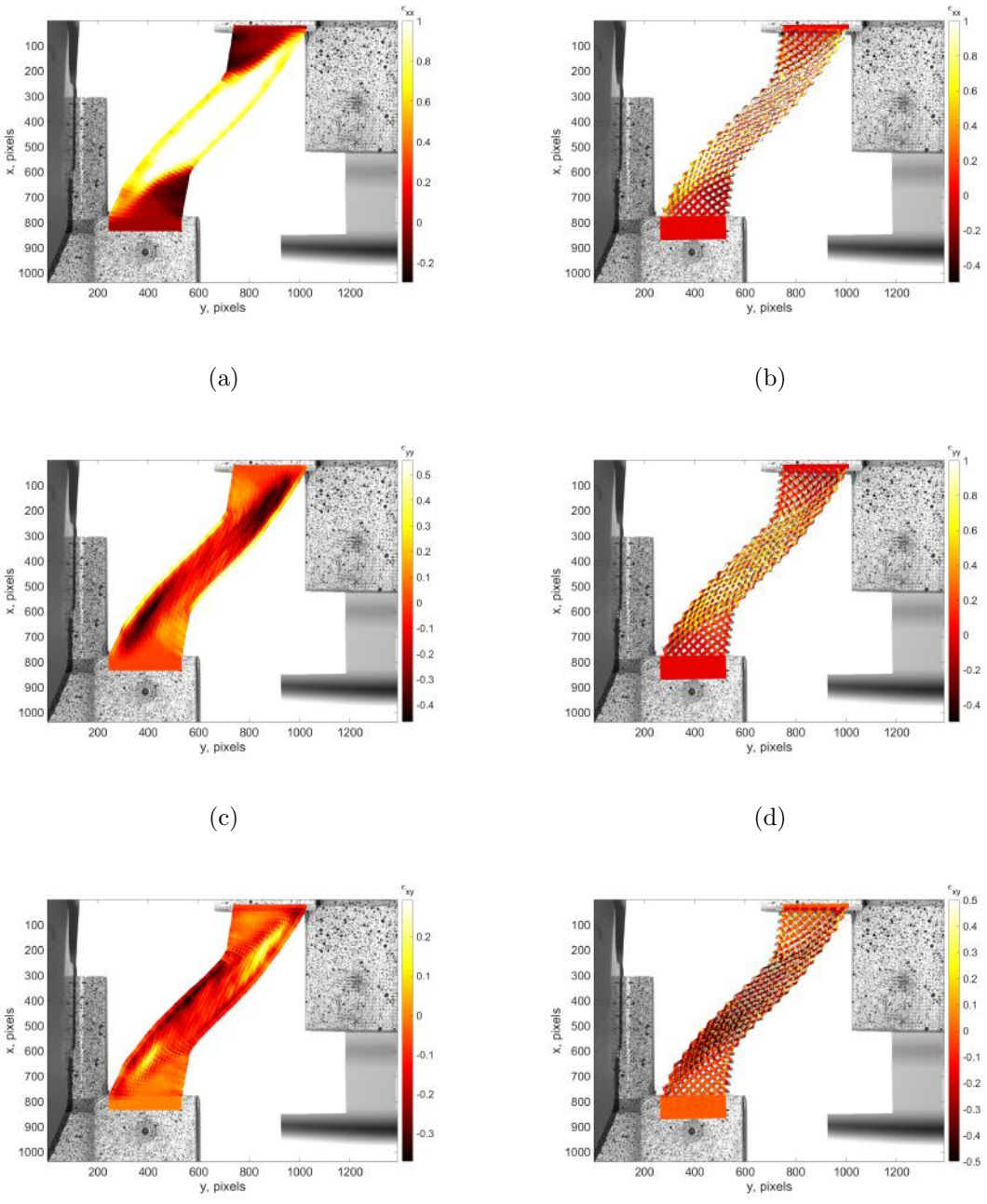

Figure A.14: Normal transverse (a-c), longitudinal (b-d) and shear (e-f) strain fields measured with macro (a-c-e) and meso (b-d-f) meshes for the 965th picture. The fields are overlaid on top of picture in the deformed configuration.

Appendix B

The mean Green interaction operator between two infinite parallel cylinders.

Main calculation steps are in part A1, additional calculation details are given in parts A2 and A3.

B.1 Integrals for two ellipsoids

For two ellipsoids V1, V2 (of volume v1 and v2 respectively), with centers I1,I2 at distance ±Lfrom the frame origin O along the x3 axis, the weight function to be calculated reads:

$\overline{\psi_{\mathrm{v}}^{\mathrm{V1,V2}}}(\omega)=\int_{z_{(\omega)}^{\min}}^{z_{(\omega)}^{\max}} \frac{2\left(\mathrm{s_{V1}}'(\mathrm{z}+\eta_\omega,\omega)\mathrm{s_{V2}}'(\mathrm{z}-\eta_\omega,\omega)\right)}{8\pi^2\mathrm{v}}\,\mathrm{dz}=\frac{\mathrm{P_{(1,2)}}}{D_1(\omega)^3 D_2(\omega)^3}\left(\frac{\mathrm{z}^3}{3}-\eta_\omega^2\mathrm{z}\right)_{z_{(\omega)}^{\min}}^{z_{(\omega)}^{\max}}$ (B1.1),

with $\mathrm{P_{(1,2)}}=\frac{9\mathrm{v1v2}}{16\pi^2(\mathrm{v1+v2})}$. $\mathrm{s'_{Vi}(z,\omega)}$ is the first z-derivative of the section area of Vi by the plane of equation $\mathrm{z}=\omega.\mathbf{r}$, $D_1(\omega)$ is the breadth of Vi in direction $\omega=(\theta,\phi)$ and $\eta_\omega=L\cos\theta$. The direction $\omega=(0,\phi)$ corresponds $\forall\phi$ to the x3 axis around which θ is counted and ϕ runs in the x1-x2 plane from 0 along direction x1. Taking η_ω positive corresponding to the half $\theta\in(0,\pi/2)$ domain, Eq. B1.1 yields, with $\left\{\mathrm{z^{min}},\mathrm{z^{max}}\right\}=\left\{\eta-\mathrm{D_2},\mathrm{D_1}-\eta\right\}$ for $0\le\eta\le(\mathrm{D_1}+\mathrm{D_2})/2$ (the ω-dependencies are here omitted for brevity) and with $D_1(\omega)=D_2(\omega)=D0(\omega)\ \forall\omega$ when V1=V2=V0:

$\overline{\psi_{\mathrm{v}}^{\mathrm{V1,V2}}}(\omega)=\frac{\mathrm{P_{(1,2)}}}{{\mathrm{D_1}^3}{\mathrm{D_2}^3}}\left(\frac{{\mathrm{D_1}^3}}{3}+\frac{{\mathrm{D_2}^3}}{3}-\eta\left({\mathrm{D_1}^2}+{\mathrm{D_2}^2}\right)+\frac{4\eta^3}{3}\right),\ \forall\phi$ (B1.2).

For spheroids of semi axes (a,c,a) with $(c//x2)$, aspect ratio $\zeta=c/a>1$ and volume $\mathrm{v_0}=4\pi a^3\zeta/3$ such that $\mathrm{P_{(1,2)}}=\mathrm{P}=\frac{9{\mathrm{v_0}}^2}{16\pi^2(2\mathrm{v_0})}=\frac{3a^3\zeta}{8\pi}$, the breadths read

$\mathrm{D}_0(\theta,\phi) = \mathrm{a}\sqrt{1+(\zeta^2-1)\sin^2\phi\sin^2\theta} = \mathrm{a}\sqrt{1+(\lambda^2(\phi)-1)\sin^2\theta}$ and the interior and interaction weight functions:
$\psi_{\mathrm{x2}}^{\zeta-\mathrm{sph}}(\theta,\phi) = \frac{1}{4\pi}\frac{\zeta}{\left(1+(\zeta^2-1)\sin^2\phi\sin^2\theta\right)^{3/2}} = \frac{1}{4\pi}\frac{\zeta}{\left(1+\left(\lambda(\phi)^2-1\right)\sin^2\theta\right)^{3/2}}$ (B1.3a),

$$\overline{\psi_{\mathrm{x2(x1)}}^{2\mathrm{sph}\zeta}}(\theta,\phi) = \frac{\mathrm{P}}{{\mathrm{D}_0}^6(\theta,\phi)}\left(\frac{2{\mathrm{D}_0}^3(\theta,\phi)}{3} - 2\eta_{(\theta,\phi)}\mathrm{D}_0(\theta,\phi)^2 + \frac{4{\eta_{(\theta,\phi)}}^3}{3}\right)$$

$= \frac{\zeta}{4\pi}\left(\frac{1}{\left(1+(\lambda(\phi)^2-1)\sin^2\theta\right)^{3/2}} - 3\frac{L\cos\theta}{a\left(1+(\lambda(\phi)^2-1)\sin^2\theta\right)^{2}} + 2\frac{L^3\cos^3\theta}{a^3\left(1+(\lambda(\phi)^2-1)\sin^2\theta\right)^{3}}\right)$(B1.3b).
Eq. B1.3b can be formally written:
$\overline{\psi_{\mathrm{x2(x1)}}^{2\mathrm{sph}\zeta}}(\theta,\phi) = I_{2sph\zeta}^{0,0} = \sum_{i(m,n)=1}^{3} F_{i(m,n)}^{0,0}(\theta,\phi) = \sum_{i(m,n)=1}^{3}\frac{\zeta}{4\pi}K_{i(m,n)}\frac{\cos^m\theta}{\left(1+(\lambda(\phi)^2-1)\sin^2\theta\right)^n}$ (B1.4),
the three elements $i(m,n) = 1,2,3$ of which correspond to $(m,n) = (0,3/2),(1,2),(3,3)$ and with the appropriate coefficients, $K_{i(m,n)} = 1$, $-3L/a = -3/\rho_0$ and $2(L/a)^3 = 2/{\rho_0}^3$ as appearing. For an isotropic reference matrix, the integrals to be calculated belong to the set ([44,22]):
$I_{2sph\zeta}^{p,q} = \sum_{i(m,n)=1}^{3} I_{i(m,n)}^{p,q} = \sum_{i(m,n)=1}^{3}\left(\int_{\phi=0}^{2\pi} 2\int_{\theta=\theta_{\min}}^{\pi/2} F_{i(m,n)}^{p,q}(\theta,\phi)\sin\theta d\theta d\phi\right),\ p,q = 0,1,2$ (B1.5),
where: $F_{i(m,n)}^{p,q}(\theta,\phi) = \frac{\zeta}{4\pi}K_{i(m,n)}\frac{\cos^m\theta}{\left(1+(\lambda(\phi)^2-1)\sin^2\theta\right)^n}\cos^{2p}\theta\cos^{2q}\phi$ (B1.6).
The value of $\theta_{\min}$which depends on ϕ corresponds with $\tan(\theta_{\min}) = \tan(\theta(\phi)_{\min}) = \frac{1}{\lambda(\phi)}\sqrt{\frac{L^2-a^2}{a^2}}$. $\theta_{\min} = 0$ when $L = a$ (contact) for all ϕ angles. Then, with $1+\tan^2(\theta_{\min}) = \cos^{-2}(\theta_{\min})$, it comes:
$\cos(\theta(\phi)_{\min}) = \sqrt{\frac{\lambda^2(\phi)}{(\lambda^2(\phi)-1)+(L^2/a^2)}} = \frac{\rho_0\lambda(\phi)}{\sqrt{{\rho_0}^2\lambda^2(\phi)+(1-{\rho_0}^2)}} = \rho(\phi) \le \rho_0 \le 1$ (B1.7).
The case $p,q = 0,0$ in Eqs B1.5,B1.6 corresponds to the integrals of the elements of the mean pair interaction weight function itself in Eq. B1.1, for which we know that they always fulfil together the null value $\int_{\phi=0}^{2\pi} 2\int_{\theta=\theta_{\min}}^{\pi/2}\overline{\psi_{\mathrm{v}}^{\mathrm{V1,V2}}}(\theta,\phi)\sin\theta d\theta d\phi = \sum_{i(m,n)=1}^{3}\left(\int_{\phi=0}^{2\pi} 2\int_{\theta=\theta_{\min}}^{\pi/2} F_{i(m,n)}^{0,0}(\theta,\phi)\sin\theta d\theta d\phi\right) = 0$.
As will appear next on, for parallel infinite cylinders, only the cases $p = 0,1,2$ with $q = 0$ suffice to obtain all the interaction operator terms, say nine double integrals of the form:

$$I_{i(m,n)}^{p,0} = \int_{\phi=0}^{2\pi} 2\int_{\theta=\theta_{\min}}^{\pi/2} F_{i(m,n)}^{p,0}(\theta,\phi)\sin\theta d\theta d\phi = 8\int_{\phi=0}^{\pi/2}\int_{\theta=\theta_{\min}}^{\pi/2} F_{i(m,n)}^{p,0}(\theta,\phi)\sin\theta d\theta d\phi$$

$= \frac{8\zeta}{4\pi}K_{i(m,n)}\int_{\phi=0}^{\pi/2}\int_{\theta=\theta_{\min}}^{\pi/2}\left(\frac{\cos^m\theta}{\left(1+(\lambda(\phi)^2-1)\sin^2\theta\right)^n}\cos^{2p}\theta\right)\sin\theta d\theta d\phi$ (B1.8).

The variable and notation changes $\cos\theta = x$ and $\lambda(\phi)^2 - 1 = \alpha(\phi)^{-2} \geq 0$ (for prolate spheroids) yield:

$$I^{p,0}_{i(m,n)} = \frac{2\zeta}{\pi} K_{i(m,n)} \int_{\phi=0}^{\pi/2} \left(\alpha(\phi)^{2n} \int_{\mathrm{x}=0}^{\mathrm{x}_{mx}} \frac{\mathrm{x}^{m+2p}}{\left(1+\alpha(\phi)^2 - \mathrm{x}^2\right)^n} \mathrm{dx} \right) d\phi = \frac{2\zeta}{\pi} K_{i(m,n)} \int_{\phi=0}^{\pi/2} G^{p,0}_{m,n}(\alpha(\phi)) d\phi,$$

(B1.9) where $\mathrm{x}_{mx} = \mathrm{x}_{\max}(\phi) = \cos(\theta(\phi)_{\min}) = \rho(\phi)$. The calculation steps for the nine x-integrals $G^{p,0}_{m,n}(\alpha(\phi))$ are given in **part B.2**. Also using ${\mathrm{x}_{mx}}^2 = \frac{{\rho_0}^2(1+\alpha(\phi)^2)}{{\rho_0}^2+\alpha(\phi)^2}$ and $\frac{{\mathrm{x}_{mx}}^2}{1+\alpha(\phi)^2-{\mathrm{x}_{mx}}^2} = \frac{{\rho_0}^2}{\alpha(\phi)^2}$ arrives at:

$G^{0,0}_{0,3/2}(\alpha(\phi)) = \frac{\alpha(\phi)^2}{1+\alpha(\phi)^2}\rho_0$ (B1.10a),

$G^{1,0}_{0,3/2}(\alpha(\phi)) = \alpha(\phi)^3 \left(\frac{\rho_0}{\alpha(\phi)} - \tan^{-1}\left(\frac{\rho_0}{\alpha(\phi)}\right)\right)$ (B1.10b),

$G^{2,0}_{0,3/2}(\alpha(\phi)) = \frac{\left(\alpha(\phi)^3+\alpha(\phi)^5\right)}{2} \left(\frac{\rho_0\alpha(\phi)}{{\rho_0}^2+\alpha(\phi)^2} + 2\frac{\rho_0}{\alpha(\phi)} - 3\tan^{-1}\left(\frac{\rho_0}{\alpha(\phi)}\right)\right)$ (B1.10c),

$G^{0,0}_{1,2}(\alpha(\phi)) = \frac{\alpha(\phi)^2}{1+\alpha(\phi)^2}\frac{{\rho_0}^2}{2}$ (B1.11a),

$G^{0,0}_{3,3}(\alpha(\phi)) = \frac{\alpha(\phi)^2}{1+\alpha(\phi)^2}\frac{{\rho_0}^4}{4}$ (B1.11b),

$G^{1,0}_{1,2}(\alpha(\phi)) = \frac{\alpha(\phi)^4}{2} \left(\frac{{\rho_0}^2}{\alpha(\phi)^2} - \ln\left(\frac{{\rho_0}^2+\alpha(\phi)^2}{\alpha(\phi)^2}\right)\right)$ (B1.12a),

$G^{1,0}_{3,3}(\alpha(\phi)) = \frac{\alpha(\phi)^6}{2} \left(\frac{1}{2}\frac{{\rho_0}^4}{\alpha(\phi)^4} - \frac{{\rho_0}^2}{\alpha(\phi)^2} + \ln\left(\frac{\alpha(\phi)^2+{\rho_0}^2}{\alpha(\phi)^2}\right)\right)$ (B1.12b),

$G^{2,0}_{1,2}(\alpha(\phi)) = \frac{\left(\alpha(\phi)^4+\alpha(\phi)^6\right)}{2} \left(\frac{{\rho_0}^2}{\alpha(\phi)^2} + \frac{{\rho_0}^2}{{\rho_0}^2+\alpha(\phi)^2} - 2\ln\left(\frac{\alpha(\phi)^2+{\rho_0}^2}{\alpha(\phi)^2}\right)\right)$ (B1.13a),

$$G^{2,0}_{3,3}(\alpha(\phi)) =$$

$\frac{\left(\alpha(\phi)^6+\alpha(\phi)^8\right)}{2} \left(\frac{1}{2}\frac{{\rho_0}^4}{\alpha(\phi)^4} + 3\ln\left(\frac{{\rho_0}^2+\alpha(\phi)^2}{\alpha(\phi)^2}\right) - \frac{{\rho_0}^2}{{\rho_0}^2+\alpha(\phi)^2} - 2\frac{{\rho_0}^2}{\alpha(\phi)^2}\right)$ (B1.13b).

Eqs B1.10-B1.13 also hold for more general ellipsoids than x_2-oriented spheroids ($\beta = 1$) , using $\lambda(\phi)^2 - 1 = \alpha(\phi)^{-2} = (\zeta^2 - \beta^2)\sin^2\phi + (\beta^2 - 1) \geq 0$ in Eq. B1.3 and following ones. At the sphere pair limit ($\beta = 1$, $\zeta = 1$), the ϕ integrals becomes independent of θ and simply amounts to multiplying the functions $G^{p,0}_{m,n}(\alpha)$ by a factor $\pi/2$in Eq. B1.9 with the value for α being its infinite limit. Taking the $\alpha \to \infty$ (or $\bar{\alpha} \to 0$) limits in Eqs B1.10-B1.13 well provides the sphere pair expected values, as recalled in part B.2 (elliptic cross sections $\beta \neq 1$ yield a $(\beta, 1, 1)$ spheroid pair limit).

Back to the x_2-oriented spheroids, the second ϕ integrations in Eq. B1.9 with using the functions $G^{p,0}_{m,n}(\alpha(\phi))$ are solved using a second (ϕ to α) variable change from $\alpha(\phi)^2 = \frac{1}{\lambda(\phi)^2-1} = \frac{\sin^{-2}(\phi)}{\zeta^2-1}$, what yields $\frac{d\left(\alpha(\phi)^2\right)}{d\phi} = -2\frac{\sin^{-3}(\phi)}{\zeta^2-1}\cos(\phi) = -\frac{2\alpha(\phi)^2}{\tan(\phi)}$ such

that $d\phi = -\tan(\phi)\frac{d\alpha}{\alpha}$ with $\tan(\phi) = \left((\zeta^2-1)\alpha^2-1\right)^{-1/2}$. That finally arrives at $d\phi = -\left((\zeta^2-1)\alpha^2-1\right)^{-1/2}(d\alpha/\alpha)$. The reference integral form becomes (the minus sign on dϕ vanishes when inverting the integration bounds on α):
$I^{p,0}_{i(m,n)} = \frac{2\zeta}{\pi} K_{i(m,n)} \int_{\phi=0}^{\pi/2} G^{p,0}_{m,n}(\alpha(\phi))d\phi = \frac{2\zeta}{\pi} K_{i(m,n)} \int_{\alpha=(\zeta^{\infty 2}-1)^{-1/2}}^{\infty} \frac{G^{p,0}_{m,n}(\alpha)}{\sqrt{(\zeta^2-1)\alpha^2-1}} \frac{d\alpha}{\alpha}$ (B1.14a).
This complicated integral type simplifies for infinite cylindrical fibers $\zeta \to \infty$ as:

$$^{\zeta^\infty} I^{p,0}_{i(m,n)} =$$

$\frac{2}{\pi} \frac{K_{i(m,n)}\zeta^\infty}{\sqrt{\zeta^{\infty 2}-1}} \int_{\alpha=(\zeta^{\infty 2}-1)^{-1/2}}^{\infty} \frac{G^{p,0}_{m,n}(\alpha)}{\sqrt{\alpha^2-(\zeta^{\infty 2}-1)^{-1}}} \frac{d\alpha}{\alpha} \to \frac{2}{\pi} K_{i(m,n)} \int_{\alpha=0}^{\infty} \frac{G^{p,0}_{m,n}(\alpha)}{\alpha} \frac{d\alpha}{\alpha}$ (B1.14b).
After some more manipulations summarized in **part B.3**, analytical solutions (either from the direct α integration or in terms of its inverse $\bar{\alpha} = 1/\alpha$, since $\int_{\alpha=0}^{\infty} G^{p,0}_{m,n}(\alpha)\,(d\alpha/\alpha^2) = \int_{\bar{\alpha}=0}^{\infty} G^{p,0}_{m,n}(\bar{\alpha})d\bar{\alpha}$), are obtained (infinite elliptic fibers, $\beta \neq 1$ and $\zeta \to \infty$, here disregarded can be treated similarly).
The variable change from ϕ to α highlights why integrals of Eq. B1.9 with $q = 1, 2$ as $I^{p,q}_{i(m,n)} = (2\zeta/\pi)\, K_{i(m,n)} \int_{\phi=0}^{\pi/2} G^{p,q}_{m,n}(\alpha(\phi)) \cos^{2q}(\phi) d\phi$ are equal to the corresponding $I^{p,0}_{i(m,n)}$ integral when $\zeta \to \infty$: with using $\cos^{2q}(\phi) = \left(1 - \frac{1}{(\zeta^2-1)\alpha^2}\right)^q$, Eq. B1.14a becomes:
$^{\zeta^\infty} I^{p,q}_{i(m,n)} = \frac{2}{\pi} \frac{K_{i(m,n)}\zeta^\infty}{\sqrt{\zeta^{\infty 2}-1}} \int_{\alpha=(\zeta^{\infty 2}-1)^{-1/2}}^{\infty} \frac{G^{p,0}_{m,n}(\alpha)}{\sqrt{\alpha^2-(\zeta^{\infty 2}-1)^{-1}}} \left(1 - \frac{1}{(\zeta^{\infty 2}-1)\alpha^2}\right)^q \frac{d\alpha}{\alpha}$ (B1.15).
When $\zeta \to \infty$, this additional factor equals unity for any non zero α value and does not affect the integral such that $\lim_{\zeta\to\infty} I^{p,q}_{i(m,n)} = \lim_{\zeta\to\infty} I^{p,0}_{i(m,n)}$, $q = 1, 2$. For the same reason, as is easily verified for the integrals that correspond to the terms of the cylinder interior weight function and interior operator, which are known from direct simple calculation, one has $\lim_{\zeta\to\infty} (2\zeta/\pi)\, K_{i(m,n)} \int_{\phi=0}^{\pi/2} G^{p,q}_{m,n}(\alpha(\phi)) \sin^{2q}(\phi) d\phi = 0$.

B.2 The nine x-integrals $G^{p,0}_{m,n}(\alpha(\phi))$

Integrals with regard to $\mathrm{x} = \cos\theta$. With $n = 3/2$, one obtains, taking $\mathrm{u} = \frac{\mathrm{x}}{\sqrt{1+\alpha^2}}$:
1°) $G^{0,0}_{0,3/2}(\alpha) = \alpha^3 \int_0^{\mathrm{x}_{mx}} \frac{1}{(1+\alpha^2-\mathrm{x}^2)^{3/2}}\,\mathrm{dx} = \frac{\alpha^3}{1+\alpha^2} \int_0^{\mathrm{u}_{mx}} \frac{1}{\left(\sqrt{1-\mathrm{u}^2}\right)^3}\,\mathrm{du} = \frac{\alpha^3}{1+\alpha^2} \frac{\mathrm{u}_{mx}}{\sqrt{1-\mathrm{u}_{mx}{}^2}}$
$= \frac{\alpha^3}{1+\alpha^2} \sqrt{\frac{\mathrm{x}_{mx}{}^2}{1+\alpha^2-\mathrm{x}_{mx}{}^2}} = \frac{\alpha^3}{1+\alpha^2}\frac{\rho_0}{\alpha} = \rho_0 \frac{\alpha^2}{1+\alpha^2}$; $Sphere\, \lim_{\alpha\to\infty} = \rho_0$ (B2.1).
2°) $G^{1,0}_{0,3/2}(\alpha) = \alpha^3 \int_0^{\mathrm{x}_{mx}} \frac{1}{(1+\alpha^2-\mathrm{x}^2)^{3/2}}\,\mathrm{x}^2\mathrm{dx} = \alpha^3 \int_0^{\mathrm{u}_{mx}} \frac{1-\left(1-\mathrm{u}^2\right)}{(1-\mathrm{u}^2)^{3/2}}\,\mathrm{du} = \alpha^3 \left(\frac{\mathrm{u}_{mx}}{\sqrt{1-\mathrm{u}_{mx}{}^2}} - \sin^{-1}(\mathrm{u}_{mx})\right)$
$= \alpha^3 \left(\sqrt{\frac{\mathrm{x}_{mx}{}^2}{1+\alpha^2-\mathrm{x}_{mx}{}^2}} - \sin^{-1}\left(\sqrt{\frac{\mathrm{x}_{mx}{}^2}{1+\alpha^2}}\right)\right)$
$= \alpha^3 \left(\frac{\rho_0}{\alpha} - \tan^{-1}\left(\frac{\rho_0}{\alpha}\right)\right)$; $Sphere\, \lim_{\bar{\alpha}\to 0} = \frac{{\rho_0}^3}{3}$ (B2.2).

In Eq. A2.2 we have used $\sin^{-1}\left(\sqrt{\frac{{\rho_0}^2}{{\rho_0}^2+\alpha^2}}\right)=\tan^{-1}\left(\frac{\rho_0}{\alpha}\right)$.

3°) $G^{2,0}_{0,3/2}(\alpha(\phi))=\alpha^3\int_0^{x_{mx}}\frac{1}{(1+\alpha^2-x^2)^{3/2}}x^4dx=\alpha^3\left(1+\alpha^2\right)\left(\int_0^{u_{mx}}\frac{\left(1-u^2\right)^2+2u^2-1}{\left(1-u^2\right)^{3/2}}du\right)$

$=\alpha^3\left(1+\alpha^2\right)\left(\frac{1}{2}\left(\sin^{-1}(u_{mx})+u_{mx}\sqrt{1-{u_{mx}}^2}\right)-2\sin^{-1}(u_{mx})+\frac{u_{mx}}{\sqrt{1-{u_{mx}}^2}}\right)$

$=\alpha^3\left(1+\alpha^2\right)\frac{1}{2}\left(\sqrt{\frac{{x_{mx}}^2}{1+\alpha^2}}\sqrt{1-\frac{{x_{mx}}^2}{1+\alpha^2}}+2\sqrt{\frac{{x_{mx}}^2}{1+\alpha^2-{x_{mx}}^2}}-3\sin^{-1}\left(\sqrt{\frac{{x_{mx}}^2}{1+\alpha^2}}\right)\right)$

$=(\alpha^3+\alpha^5)\,\frac{1}{2}\left(\frac{\rho_0\alpha}{{\rho_0}^2+\alpha^2}+2\frac{\rho_0}{\alpha}-3\tan^{-1}\left(\frac{\rho_0}{\alpha}\right)\right)$; $Sphere\lim_{\bar{\alpha}\to 0}=0{\rho_0}^3+\frac{{\rho_0}^5}{5}$ (B2.3).

For the 6 remaining integrals (with $n=2$ and $n=3$), taking the variable change $z=\frac{x^2}{1+\alpha^2}$ yields:

4°) $G^{0,0}_{1,2}(\alpha(\phi))=\alpha^4\int_0^{x_{mx}}\frac{x}{(1+\alpha^2-x^2)^2}dx=\frac{\alpha^4}{2(1+\alpha^2)}\int_0^{z_{mx}}(1-z)^{-2}\,dz=\frac{\alpha^4}{2(1+\alpha^2)}\left((1-z_{mx})^{-1}-1\right)$

$=\frac{\alpha^4}{2(1+\alpha^2)}\left(\frac{{x_{mx}}^2}{1+\alpha^2-{x_{mx}}^2}\right)$

$=\frac{\alpha^4}{2(1+\alpha^2)}\frac{{\rho_0}^2}{\alpha^2}=\frac{\alpha^2}{2(1+\alpha^2)}{\rho_0}^2$; $Sphere\lim_{\alpha\to\infty}=\frac{{\rho_0}^2}{2}$ (B2.4).

5°) $G^{0,0}_{3,3}(\alpha(\phi))=\alpha^6\int_0^{x_{mx}}\frac{x^3}{(1+\alpha^2-x^2)^3}dx=\frac{\alpha^6}{2(1+\alpha^2)}\int_0^{z_{mx}}\frac{z}{(1-z)^3}dz$

$=\frac{\alpha^6}{2\left(1+\alpha^2\right)}\left(\int_0^{z_{mx}}\frac{dz}{(1-z)^3}-\int_0^{z_{mx}}\frac{dz}{(1-z)^2}\right)=\frac{\alpha^6}{2\left(1+\alpha^2\right)}\left(\frac{1}{2}\left((1-z_{mx})^{-2}-1\right)-\left((1-z_{mx})^{-1}-1\right)\right)$

$=\frac{1}{2}\left(\frac{{x_{mx}}^2}{1+\alpha^2-{x_{mx}}^2}\right)^2=\frac{\alpha^6}{2(1+\alpha^2)}\frac{1}{2}\left(\frac{{\rho_0}^2}{\alpha^2}\right)^2=\frac{\alpha^2}{4(1+\alpha^2)}{\rho_0}^4$; $Sphere\lim_{\alpha\to\infty}=\frac{{\rho_0}^4}{4}$ (B2.5).

6°) $G^{1,0}_{1,2}(\alpha(\phi))=\alpha^4\int_0^{x_{mx}}\frac{x}{(1+\alpha^2-x^2)^2}x^2dx=\frac{\alpha^4}{2}\int_0^{z_{mx}}\frac{z}{(1-z)^2}dz=\frac{\alpha^4}{2}\left(\frac{z_{mx}}{1-z_{mx}}+\ln\left(1-z_{\max}\right)\right)$

$=\frac{\alpha^4}{2}\left(\frac{{x_{mx}}^2}{(1+\alpha^2)-{x_{mx}}^2}+\ln\left(\frac{(1+\alpha^2)-{x_{mx}}^2}{1+\alpha^2}\right)\right)$

$=\frac{\alpha^4}{2}\left(\frac{{\rho_0}^2}{\alpha^2}-\ln\left(\frac{{\rho_0}^2+\alpha^2}{\alpha^2}\right)\right)$;$Sphere\lim_{\bar{\alpha}\to 0}=\frac{{\rho_0}^4}{2}$ (B2.6)

7°) $G^{1,0}_{3,3}(\alpha(\phi))=\alpha^6\int_0^{x_{mx}}\frac{x^3}{(1+\alpha^2-x^2)^3}x^2dx=\frac{\alpha^6}{2}\int_0^{z_{mx}}\frac{z^2}{(1-z)^3}dz=\frac{\alpha^6}{2}\int_0^{z_{mx}}\frac{1-2(1-z)+(1-z)^2}{(1-z)^3}dz$

$=\frac{\alpha^6}{2}\left(\frac{z_{mx}\left(2-z_{mx}\right)}{2\left(1-z_{mx}\right)^2}-2\frac{z_{mx}}{1-z_{mx}}-\ln\left(1-z_{mx}\right)\right)=\frac{\alpha^6}{2}\left(\frac{{x_{mx}}^2\left(3x_{mx}-2(1+\alpha^2)\right)}{2\left(1+\alpha^2-{x_{mx}}^2\right)^2}-\ln\left(\frac{1+\alpha^2-{x_{mx}}^2}{1+\alpha^2}\right)\right)$

$=\frac{\alpha^6}{2}\left(\left(\frac{1}{2}\frac{{\rho_0}^4}{\alpha^4}\right)-\left(\ln\left(\frac{\alpha^2}{\alpha^2+{\rho_0}^2}\right)+\frac{{\rho_0}^2}{\alpha^2}\right)\right)$; $Sphere\lim_{\bar{\alpha}\to 0}=\frac{{\rho_0}^6}{6}$ (B2.7).

8°) $G^{2,0}_{1,2}(\alpha(\phi))=\alpha^4\int_0^{x_{mx}}\frac{x}{(1+\alpha^2-x^2)^2}x^4dx=\frac{\alpha^4\left(1+\alpha^2\right)}{2}\int_0^{z_{mx}}\frac{1}{(1-z)^2}z^2dz$

$=\frac{\alpha^4\left(1+\alpha^2\right)}{2}\int_0^{z_{mx}}\frac{1-2\left(1-z\right)+\left(1-z\right)^2}{\left(1-z\right)^2}dz=\frac{\alpha^4\left(1+\alpha^2\right)}{2}\left(\frac{{x_{mx}}^2}{(1+\alpha^2)-{x_{mx}}^2}+2\ln\left(\frac{(1+\alpha^2)-{x_{mx}}^2}{1+\alpha^2}\right)\right.$

$= \frac{\left(\alpha^4+\alpha^6\right)}{2}\left(\frac{{\rho_0}^2}{\alpha^2}+\frac{{\rho_0}^2}{{\rho_0}^2+\alpha^2}-2\ln\left(\frac{\alpha^2+{\rho_0}^2}{\alpha^2}\right)\right)$; $Sphere\lim_{\bar{\alpha}\to 0}=0{\rho_0}^4+\frac{{\rho_0}^6}{3}$ (B2.8).

9°) $G^{2,0}_{3,3}(\alpha(\phi))=\alpha^6\int_0^{\mathrm{x}_{mx}}\frac{\mathrm{x}^3}{(1+\alpha^2-\mathrm{x}^2)^3}\mathrm{x}^4\mathrm{dx}=\frac{\alpha^6\left(1+\alpha^2\right)}{2}\int_0^{\mathrm{z}_{mx}}\frac{\mathrm{z}^3}{(1-\mathrm{z})^3}\mathrm{dz}$

$$=\frac{\alpha^6\left(1+\alpha^2\right)}{2}\left(\frac{\mathrm{z}_{mx}\left(2-\mathrm{z}_{mx}\right)}{2\left(1-\mathrm{z}_{mx}\right)^2}-3\frac{\mathrm{z}_{mx}}{1-\mathrm{z}_{mx}}-3\ln\left(1-\mathrm{z}_{mx}\right)-\mathrm{z}_{mx}\right)$$

$$=\frac{\alpha^6\left(1+\alpha^2\right)}{2}\left(\frac{{\mathrm{x}_{mx}}^2\left(5{\mathrm{x}_{mx}}^2-4(1+\alpha^2)\right)}{2\left((1+\alpha^2)-{\mathrm{x}_{mx}}^2\right)^2}-3\ln\left((1+\alpha^2)-{\mathrm{x}_{mx}}^2\right)-(1+\alpha^2){\mathrm{x}_{mx}}^2\right)$$

$$=\frac{\left(\alpha^6+\alpha^8\right)}{2}\left(\frac{1}{2}\frac{{\rho_0}^4}{\alpha^4}+3\ln\left(\frac{{\rho_0}^2+\alpha^2}{\alpha^2}\right)-\frac{{\rho_0}^2}{{\rho_0}^2+\alpha^2}-2\frac{{\rho_0}^2}{\alpha^2}\right);Sphere\lim_{\bar{\alpha}\to 0}=0{\rho_0}^6+\frac{{\rho_0}^8}{8}$$

(B2.9)

B.3 Integrals with regard to $\alpha=\left((\zeta^2-1)\sin^2\phi\right)^{-1/2}$

Integrals with regard to $\alpha=\left((\zeta^2-1)\sin^2\phi\right)^{-1/2}$, also using $\kappa=\alpha/\rho_0$, at limit .

1°) ${}^{\zeta\infty}I^{0,0}_{0,3/2}=\frac{2}{\pi}K_{1(0,3/2)}\int_{\alpha=0}^{\infty}\frac{G^{0,0}_{0,3/2}(\alpha)}{\alpha}\frac{d\alpha}{\alpha}=\frac{2}{\pi}(\mathbf{??})\int_{\alpha=0}^{\infty}\left(\frac{\alpha^2}{1+\alpha^2}\rho_0\right)\frac{d\alpha}{\alpha^2}=\frac{2\rho_0}{\pi}\int_0^{\infty}\left(\frac{1}{1+\alpha^2}\right)d\alpha$
$=\frac{2\rho_0}{\pi}\frac{\pi}{2}=\rho_0$; $Contact\lim_{\rho_0\to 1}=1$ (B3.1).

2°) ${}^{\zeta\infty}I^{1,0}_{0,3/2}=\frac{2}{\pi}K_{1(0,3/2)}\int_{\alpha=0}^{\infty}\frac{G^{1,0}_{0,3/2}(\alpha)}{\alpha}\frac{d\alpha}{\alpha}=\frac{2}{\pi}(\mathbf{??})\int_{\alpha=0}^{\infty}\left(\alpha^3\left(\frac{\rho_0}{\alpha}-\tan^{-1}\left(\frac{\rho_0}{\alpha}\right)\right)\right)\frac{d\alpha}{\alpha^2}$
$=\frac{2{\rho_0}^2}{\pi}\int_0^{\infty}\left(\left(1-\frac{\alpha}{\rho_0}\tan^{-1}\left(\frac{\rho_0}{\alpha}\right)\right)\right)d\frac{\alpha}{\rho_0}=\frac{2{\rho_0}^2}{\pi}\frac{\pi}{4}=\frac{{\rho_0}^2}{2}$; $Contact\lim_{\rho_0\to 1}=1/2$ (B3.2).

3°) ${}^{\zeta\infty}I^{2,0}_{0,3/2}=\frac{2}{\pi}K_{1(0,3/2)}\int_{\alpha=0}^{\infty}\frac{G^{2,0}_{0,3/2}(\alpha)}{\alpha}\frac{d\alpha}{\alpha}=\frac{2}{\pi}(\mathbf{??})\int_{\alpha=0}^{\infty}\left(\frac{\left(\alpha^3+\alpha^5\right)}{2}\left(\frac{\rho_0\alpha}{{\rho_0}^2+\alpha^2}+2\frac{\rho_0}{\alpha}-3\tan^{-1}\left(\frac{\rho_0}{\alpha}\right)\right)\right)\frac{d\alpha}{\alpha^2}$

$$=\frac{2}{\pi}\left(\frac{{\rho_0}^2}{2}\int_{\kappa=0}^{\infty}\left(\frac{\kappa^2}{1+\kappa^2}+2-3\kappa\tan^{-1}\left(\frac{1}{\kappa}\right)\right)d\kappa+\frac{{\rho_0}^4}{2}\int_{\kappa=0}^{\infty}\left(\frac{\kappa^4}{1+\kappa^2}+2\kappa^2-3\kappa^3\tan^{-1}\left(\frac{1}{\kappa}\right)\right)d\kappa\right)$$

$=\frac{2}{\pi}\left({\rho_0}^2\frac{\pi}{8}+{\rho_0}^4\frac{\pi}{16}\right)=\frac{2{\rho_0}^2+{\rho_0}^4}{8}$; $Contact\lim_{\rho_0\to 1}=3/8$ (B3.3).

4°) $I^{0,0}_{1,2}=\frac{2}{\pi}K_{2(1,2)}\int_{\alpha=0}^{\infty}\frac{G^{0,0}_{1,2}(\alpha)}{\alpha}\frac{d\alpha}{\alpha}=\frac{2}{\pi}(-\frac{3}{\rho_0})\int_{\alpha=0}^{\infty}\left(\frac{\alpha^2}{1+\alpha^2}\frac{{\rho_0}^2}{2}\right)\frac{d\alpha}{\alpha^2}$
$=\frac{2}{\pi}\left(\frac{-3}{2\rho_0}\right){\rho_0}^2\int_0^{\infty}\left(\frac{1}{1+\alpha^2}\right)d\alpha=-\frac{3\rho_0}{2}$; $Contact\lim_{\rho_0\to 1}=-3/2$ (B3.4).

5°) ${}^{\zeta\infty}I^{0,0}_{3,3}=\frac{2}{\pi}K_{3(3,3)}\int_{\alpha=0}^{\infty}\frac{G^{0,0}_{3,3}(\alpha)}{\alpha}\frac{d\alpha}{\alpha}=\frac{2}{\pi}(\frac{2}{{\rho_0}^3})\int_{\alpha=0}^{\infty}\left(\frac{\alpha^2}{1+\alpha^2}\frac{{\rho_0}^4}{4}\right)\frac{d\alpha}{\alpha^2}$
$=\frac{2}{\pi}\left(\frac{2}{4{\rho_0}^3}\right){\rho_0}^4\int_0^{\infty}\left(\frac{1}{1+\alpha^2}\right)d\alpha=\frac{\rho_0}{2}$; $Contact\lim_{\rho_0\to 1}=1/2$ (B3.5).

$6°)\ {}^{\zeta^\infty}I^{1,0}_{1,2} = \frac{2}{\pi}K_{2(1,2)}\int_{\alpha=0}^{\infty}\frac{G^{1,0}_{1,2}(\alpha)}{\alpha}\frac{d\alpha}{\alpha} = \frac{2}{\pi}(-\frac{3}{\rho_0})\int_{\alpha=0}^{\infty}\left(\frac{\alpha^4}{2}\left(\frac{{\rho_0}^2}{\alpha^2}-\ln\left(\frac{{\rho_0}^2+\alpha^2}{\alpha^2}\right)\right)\right)\frac{d\alpha}{\alpha^2} =$
$\frac{2}{\pi}\left(\frac{-3}{\rho_0}\right)\frac{1}{\rho_0}\frac{{\rho_0}^4}{2}\int_0^{\infty}\left(\left(1-\kappa^2\ln\left(\frac{1+\kappa^2}{\kappa^2}\right)\right)\right)d\kappa = \frac{2}{\pi}\left(\frac{-3}{\rho_0}\right)\frac{1}{\rho_0}\frac{{\rho_0}^4}{2}\frac{\pi}{3} = -{\rho_0}^2$; $Contact\lim_{\rho_0\to 1} =$
-1 (B3.6).

$7°){}^{\zeta^\infty}I^{1,0}_{3,3} = \frac{2}{\pi}K_{3(3,3)}\int_{\alpha=0}^{\infty}\frac{G^{1,0}_{3,3}(\alpha)}{\alpha}\frac{d\alpha}{\alpha} = \frac{2}{\pi}\left(\frac{2}{{\rho_0}^3}\right)\int_{\alpha=0}^{\infty}\left(\frac{\alpha^6}{2}\left(\frac{1}{2}\frac{{\rho_0}^4}{\alpha^4}-\frac{{\rho_0}^2}{\alpha^2}+\ln\left(\frac{{\rho_0}^2+\alpha^2}{\alpha^2}\right)\right)\right)\frac{d\alpha}{\alpha^2}$

$$= \frac{2}{\pi}{\rho_0}^2\int_0^{\infty}\kappa^4\left(\ln\left(\frac{1+\kappa^2}{\kappa^2}\right)+\frac{1}{2}\frac{1}{\kappa^4}-\frac{1}{\kappa^2}\right)d\kappa = \frac{2}{\pi}{\rho_0}^2\left(\int_0^{\infty}\left(\frac{1}{2}-\kappa^2\left(1-\kappa^2\ln\left(\frac{\kappa^2+1}{\kappa^2}\right)\right)d\kappa\right)\right) = \frac{2}{\pi}\rho_0$$

$8°){}^{\zeta^\infty}I^{2,0}_{1,2} = \frac{2}{\pi}K_{2(1,2)}\int_{\alpha=0}^{\infty}\frac{G^{2,0}_{1,2}(\alpha)}{\alpha}\frac{d\alpha}{\alpha} = \frac{2}{\pi}(-\frac{3}{\rho_0})\int_{\alpha=0}^{\infty}\left(\frac{\alpha^4+\alpha^6}{2}\left(\frac{{\rho_0}^2}{\alpha^2}+\frac{{\rho_0}^2}{{\rho_0}^2+\alpha^2}-2\ln\left(\frac{\alpha^2+{\rho_0}^2}{\alpha^2}\right)\right)\right)\frac{d\alpha}{\alpha^2}$

$$= \frac{2}{\pi}\left(\frac{-3}{2}\right)\int_0^{\infty}\left(\left({\rho_0}^2\kappa^2+{\rho_0}^4\kappa^4\right)\left(\frac{1}{\kappa^2}+\frac{1}{1+\kappa^2}-2\ln\left(\frac{\kappa^2+1}{\kappa^2}\right)\right)\right)d\kappa$$

$= \frac{2}{\pi}\left(\frac{-3}{2}\right)\left(\frac{\pi}{6}{\rho_0}^2+\frac{\pi}{10}{\rho_0}^4\right) = -3\left(\frac{1}{6}{\rho_0}^2+\frac{1}{10}{\rho_0}^4\right)$;$Contact\lim_{\rho_0\to 1} = -4/5$ (B3.8).

$9°){}^{\zeta^\infty}I^{2,0}_{3,3} = \frac{2}{\pi}K_{3(3,3)}\int_{\alpha=0}^{\infty}\frac{G^{2,0}_{3,3}(\alpha)}{\alpha}\frac{d\alpha}{\alpha}$

$$= \frac{2}{\pi}\left(\frac{2}{{\rho_0}^3}\right)\int_{\alpha=0}^{\infty}\left(\frac{\alpha^6+\alpha^8}{2}\right)\left(\frac{1}{2}\frac{{\rho_0}^4}{\alpha^4}+3\ln\left(\frac{{\rho_0}^2+\alpha^2}{\alpha^2}\right)-\frac{{\rho_0}^2}{{\rho_0}^2+\alpha^2}-2\frac{{\rho_0}^2}{\alpha^2}\right)\frac{d\alpha}{\alpha^2}$$

$$= \frac{2}{\pi}\int_0^{\infty}\left({\rho_0}^2+{\rho_0}^4\kappa^2\right)\left(\frac{1}{2}+3\kappa^4\ln\left(\frac{1+\kappa^2}{\kappa^2}\right)-\frac{\kappa^4}{1+\kappa^2}-2\kappa^2\right)d\kappa$$

$= \frac{2}{\pi}\left({\rho_0}^2\frac{\pi}{10}+{\rho_0}^4\frac{\pi}{14}\right) = \frac{{\rho_0}^2}{5}+\frac{{\rho_0}^4}{7}$; $Contact\lim_{\rho_0\to 1} = 12/35$ (B3.9).

Appendix C

Angular relations for the pantographic structure's deformed axial and transverse states

In the extension case, for a θ angle in the central zone given by the extension amount, identically the strained four lateral zones correspond to a θ' angle equal to $0.5(\theta + \pi/4)$. The in-plane bending angle of the two fiber families is simply $\beta = \pi/4 - \theta$.

In the shear case, corresponding to a D transverse displacement of point P with regard to point R (and no extension), one has $\gamma = D/(L\sqrt{2})$ and the solid body rotation is r=atan(γ). The θ angle for the central zone is given from $\cos\theta = \sqrt{(1+\gamma^2)/2}$ When γ or r is zero, there is no deformation and $\cos\theta = 1/\sqrt{2} = \cos(\pi/4)$.
The two types of lateral zones correspond to an angle $0.5(\theta+\pi/4) \pm$ r and the two in-plane bending angles for the fiber families are $\pi/4 - \theta \pm r$, that is in both case the extension values with adding or substracting the rigid body rotation. A more general in-plane deformation combining extension and shear can be analyzed similarly. Pantographs with more zones than a single central one between two triangular ends and four lateral parts can be schematized in similar yet more complicated manner.

Bibliography

[1] E. Barchiesi, M. Spagnuolo, and L. Placidi, "Mechanical metamaterials: a state of the art," *Mathematics and Mechanics of Solids*, p. 1081286517735695, 2018.

[2] F. dell'Isola, P. Seppecher, J. J. Alibert, T. Lekszycki, R. Grygoruk, M. Pawlikowski, D. Steigmann, I. Giorgio, U. Andreaus, E. Turco *et al.*, "Pantographic metamaterials: an example of mathematically driven design and of its technological challenges," *Continuum Mechanics and Thermodynamics*, pp. 1–34.

[3] F. dell'Isola, P. Seppecher, M. Spagnuolo, E. Barchiesi, F. Hild, T. Lekszycki, I. Giorgio, L. Placidi, U. Andreaus, M. Cuomo *et al.*, "Advances in pantographic structures: Design, manufacturing, models, experiments and image analyses," *Continuum Mechanics and Thermodynamics*, 2019.

[4] U. Andreaus, M. Spagnuolo, T. Lekszycki, and S. R. Eugster, "A ritz approach for the static analysis of planar pantographic structures modeled with nonlinear euler–bernoulli beams," *Continuum Mechanics and Thermodynamics*, vol. 30, pp. 1103–1123, 2018.

[5] M. Spagnuolo, K. Barcz, A. Pfaff, F. DellIsola, and P. Franciosi, "Qualitative pivot damage analysis in aluminum printed pantographic sheets: numerics and experiments," *Mechanics Research Communications*, vol. 83, pp. 47–52, 2017.

[6] M. Spagnuolo, P. P, and D. C, "Phenomenological aspects of quasi-perfect pivots in metallic pantographic structures," *(submitted to) Mechanics Research Communications*, 20xx.

[7] F. dell'Isola and D. Steigmann, "Discrete and continuum models for complex (meta-)materials," *Cambridge University Press*, vol. in production, 2019.

[8] F. dell'Isola, D. Steigmann, and A. Della Corte, "Synthesis of fibrous complex structures: Designing microstructure to deliver targeted macroscale response," *Applied Mechanics Reviews*, vol. 67, no. 6, p. 060804, 2015.

[9] G. Milton, M. Briane, and D. Harutyunyan, "On the possible effective elasticity tensors of 2-dimensional and 3-dimensional printed materials," *Mathematics and Mechanics of Complex Systems*, vol. 5, no. 1, pp. 41–94, 2017.

[10] V. A. Eremeyev and W. Pietraszkiewicz, "Material symmetry group and constitutive equations of micropolar anisotropic elastic solids," *Mathematics and Mechanics of Solids*, vol. 21, no. 2, pp. 210–221, 2016.

[11] A. Bertram and R. Glüge, "Gradient materials with internal constraints," *Mathematics and Mechanics of Complex Systems*, vol. 4, no. 1, pp. 1–15, 2016.

[12] F. dell'Isola, T. Lekszycki, M. Pawlikowski, R. Grygoruk, and L. Greco, "Designing a light fabric metamaterial being highly macroscopically tough under directional extension: first experimental evidence," *Zeitschrift für angewandte Mathematik und Physik*, vol. 66, pp. 3473–3498, 2015.

[13] J.-J. Alibert, P. Seppecher, and F. dell'Isola, "Truss modular beams with deformation energy depending on higher displacement gradients," *Mathematics and Mechanics of Solids*, vol. 8, no. 1, pp. 51–73, 2003.

[14] C. Pideri and P. Seppecher, "A second gradient material resulting from the homogenization of an heterogeneous linear elastic medium," *Continuum Mechanics and Thermodynamics*, vol. 9, no. 5, pp. 241–257, 1997.

[15] L. Russo, *The forgotten revolution: how science was born in 300 BC and why it had to be reborn*. Springer Science & Business Media, 2013.

[16] S. M. Stigler, "Stigler's law of eponymy," *Transactions of the New York Academy of Sciences*, vol. 39, no. 1 Series II, pp. 147–157, 1980.

[17] F. dell'Isola, U. Andreaus, and L. Placidi, "At the origins and in the vanguard of peridynamics, non-local and higher-gradient continuum mechanics: An underestimated and still topical contribution of Gabrio Piola," *Mathematics and Mechanics of Solids*, vol. 20, no. 8, pp. 887–928, 2015.

[18] F. dell'Isola, A. Della Corte, and I. Giorgio, "Higher-gradient continua: The legacy of Piola, Mindlin, Sedov and Toupin and some future research perspectives," *Mathematics and Mechanics of Solids*, vol. 22, no. 4, pp. 852–872, 2017.

[19] P. Germain, "The method of virtual power in continuum mechanics. part 2: Microstructure," *SIAM Journal on Applied Mathematics*, vol. 25, no. 3, pp. 556–575, 1973.

[20] R. A. Toupin, "Elastic materials with couple-stresses," *Archive for Rational Mechanics and Analysis*, vol. 11, no. 1, pp. 385–414, 1962.

[21] R. D. Mindlin, "Micro-structure in linear elasticity," *Archive for Rational Mechanics and Analysis*, vol. 16, no. 1, pp. 51–78, 1964.

[22] S. R. Eugster and F. dell'Isola, "Exegesis of the Introduction and Sect. I from Fundamentals of the Mechanics of Continua** by E. Hellinger," *ZAMM-Journal of Applied Mathematics and Mechanics/Zeitschrift für Angewandte Mathematik und Mechanik*, vol. 97, no. 4, pp. 477–506, 2017.

[23] ——, "Exegesis of sect. II and III. A from Fundamentals of the mechanics of continua by E. Hellinger," *ZAMM-Journal of Applied Mathematics and Mechanics/Zeitschrift für Angewandte Mathematik und Mechanik*, vol. 98, no. 1, pp. 31–68, 2018.

[24] F. dell Isola, P. Seppecher, and A. Della Corte, "The postulations á la d alembert and á la cauchy for higher gradient continuum theories are equivalent: a review of existing results," in *Proc. R. Soc. A*, vol. 471, no. 2183. The Royal Society, 2015, p. 20150415.

[25] N. Auffray, F. dell'Isola, V. Eremeyev, A. Madeo, and G. Rosi, "Analytical continuum mechanics à la Hamilton–Piola least action principle for second gradient continua and capillary fluids," *Mathematics and Mechanics of Solids*, vol. 20, no. 4, pp. 375–417, 2015.

[26] Y. Rahali, I. Giorgio, J. Ganghoffer, and F. dell'Isola, "Homogenization à la piola produces second gradient continuum models for linear pantographic lattices," *International Journal of Engineering Science*, vol. 97, pp. 148–172, 2015.

[27] A. Bilotta, G. Formica, and E. Turco, "Performance of a high-continuity finite element in three-dimensional elasticity," *International Journal for Numerical Methods in Biomedical Engineering*, vol. 26, no. 9, pp. 1155–1175, 2010.

[28] A. Cazzani, M. Malagù, and E. Turco, "Isogeometric analysis: a powerful numerical tool for the elastic analysis of historical masonry arches," *Continuum Mechanics and Thermodynamics*, vol. 28, no. 1-2, pp. 139–156, 2016.

[29] E. Benvenuto, "An introduction to the history of structural mechanics. part i: Statics and resistance of solids. part ii: Vaulted structures and elastic systems," 1991.

[30] M. de Saint-Venant, *Mémoire sur la torsion des prismes: avec des considérations sur leur flexion ainsi que sur l'équilibre intérieur des solides élastiques en général: et des formules pratiques pour le calcul de leur résistance à divers efforts s' exerçant simultanément.* Imprimerie nationale, 1856.

[31] E. Cosserat, F. Cosserat *et al.*, "Théorie des corps déformables," 1909.

[32] F. Dell'Isola, G. Maier, U. Perego, U. Andreaus, R. Esposito, and S. Forest, "The complete works of gabrio piola: volume i," *Cham, Switzerland: Springer*, 2014.

[33] P. Casal, "La capillarité interne," *Cahier du groupe Français de rhéologie, CNRS VI*, vol. 3, pp. 31–37, 1961.

[34] ——, "Theory of second gradient and capillarity," *COMPTES RENDUS HEBDOMADAIRES DES SEANCES DE L ACADEMIE DES SCIENCES SERIE A*, vol. 274, no. 22, p. 1571, 1972.

[35] F. dell'Isola, I. Giorgio, M. Pawlikowski, and N. Rizzi, "Large deformations of planar extensible beams and pantographic lattices: heuristic homogenization, experimental and numerical examples of equilibrium," *Proc. R. Soc. A*, vol. 472, no. 2185, p. 23 pages, 2016.

[36] F. dell'Isola, A. Della Corte, R. Esposito, and L. Russo, "Some cases of unrecognized transmission of scientific knowledge: from antiquity to Gabrio Piola's peridynamics and generalized continuum theories," in *Generalized continua as models for classical and advanced materials.* Springer, 2016, pp. 77–128.

[37] P. Seppecher, J.-J. Alibert, and F. dell'Isola, "Linear elastic trusses leading to continua with exotic mechanical interactions," in *Journal of Physics: Conference Series*, vol. 319, no. 1. IOP Publishing, 2011, p. 012018.

[38] V. A. Eremeyev and F. dellIsola, "A note on reduced strain gradient elasticity," in *Generalized Models and Non-classical Approaches in Complex Materials 1.* Springer, 2018, pp. 301–310.

[39] G. Everstine and A. Pipkin, "Boundary layers in fiber-reinforced materials," *J. Appl. Mech.*, vol. 40, pp. 518–522, 1973.

[40] M. Hilgers and A. Pipkin, "Elastic sheets with bending stiffness," *Q. J. Mech. Appl. Math.*, vol. 45, pp. 57–75, 1992.

[41] ——, "Energy-minimizing deformations of elastic sheets with bending stiffness," *J. Elast.*, vol. 31, pp. 125–139, 1993.

[42] ——, "Bending energy of highly elastic membranes ii," *Q. Appl. Math*, vol. 54, pp. 307–316, 1996.

[43] M. Hu, H. Kolsky, and A. Pipkin, "Bending theory for fiber-reinforced beams," *J. Compos. Mater*, pp. 235–249, 1985.

[44] A. Pipkin, "Generalized plane deformations of ideal fiber-reinforced materials." *Q. Appl. Math*, vol. 32, pp. 253–263, 1974.

[45] ——, "Energy changes in ideal fiber-reinforced composites," *Q. Appl. Math*, vol. 35, pp. 455–463, 1978.

[46] ——, "Some developments in the theory of inextensible networks," *Q. Appl. Math*, vol. 38, pp. 343–355, 1980.

[47] F. dell'Isola, M. d'Agostino, A. Madeo, P. Boisse, and D. Steigmann, "Minimization of shear energy in two dimensional continua with two orthogonal families of inextensible fibers: the case of standard bias extension test," *Journal of Elasticity*, vol. 122, no. 2, pp. 131–155, 2016.

[48] L. Placidi, L. Greco, S. Bucci, E. Turco, and N. Rizzi, "A second gradient formulation for a 2d fabric sheet with inextensible fibres," *Zeitschrift für angewandte Mathematik und Physik*, vol. 67(5), no. 114, 2016.

[49] R. Rivlin, "Plane strain of a net formed by inextensible cords," in *Collected Papers of RS Rivlin*. Springer, 1997, pp. 511–534.

[50] L. Greco, I. Giorgio, and A. Battista, "In plane shear and bending for first gradient inextesible pantographic sheets: numerical study of deformed shapes and global constraint reactions," *Mathematics and Mechanics of Solids*, p. 1081286516651324, 2016.

[51] M. Cuomo, F. Dell'Isola, L. Greco, and N. Rizzi, "First versus second gradient energies for planar sheets with two families of inextensible fibres: Investigation on deformation boundary layers, discontinuities and geometrical instabilities," *Composites Part B: Engineering*, vol. 115, pp. 423–448, 2017.

[52] M. Cuomo, F. dell'Isola, and L. Greco, "Simplified analysis of a generalized bias test for fabrics with two families of inextensible fibres," *Zeitschrift für angewandte Mathematik und Physik*, vol. 67, no. 3, pp. 1–23, 2016.

[53] F. dell'Isola, M. Cuomo, L. Greco, and A. Della Corte, "Bias extension test for pantographic sheets: numerical simulations based on second gradient shear energies," *Journal of Engineering Mathematics*, vol. 103, no. 1, pp. 127–157, 2017.

[54] L. Greco, I. Giorgio, and A. Battista, "In plane shear and bending for first gradient inextensible pantographic sheets: numerical study of deformed shapes and global constraint reactions," *Mathematics and Mechanics of Solids*, vol. 22, no. 10, pp. 1950–1975, 2017.

[55] I. Giorgio, "Numerical identification procedure between a micro-cauchy model and a macro-second gradient model for planar pantographic structures," *Zeitschrift für angewandte Mathematik und Physik*, vol. 67(4), no. 95, 2016.

[56] E. Turco, F. dell'Isola, A. Cazzani, and N. Rizzi, "Hencky-type discrete model for pantographic structures: numerical comparison with second gradient continuum models," *Zeitschrift für angewandte Mathematik und Physik*, vol. 67, p. 28 pages, 2016.

[57] M. Spagnuolo, F. dell'Isola, and I. Giorgio, "Astounding evidences of applicability of higher gradient models: if a continuum model is capable to predict the good results also in case of a discrete reality," *to appear*, 2018.

[58] M. Sutton, J. Orteu, and H. Schreier, *Image correlation for shape, motion and deformation measurements: basic concepts, theory and applications*. Springer Science & Business Media, 2009.

[59] F. Hild and S. Roux, "Digital image correlation," in *Optical Methods for Solid Mechanics. A Full-Field Approach*, P. Rastogi and E. Hack, Eds. Weinheim (Germany): Wiley-VCH, 2012, pp. 183–228.

[60] E. Turco, A. Misra, M. Pawlikowski, F. dell'Isola, and F. Hild, "Enhanced piola–hencky discrete models for pantographic sheets with pivots without deformation energy: numerics and experiments," *International Journal of Solids and Structures*, vol. 147, pp. 94–109, 2018.

[61] F. Hild and S. Roux, "Comparison of local and global approaches to digital image correlation," *Experimental Mechanics*, vol. 52, no. 9, pp. 1503–1519, 2012.

[62] Z. Tomičević, F. Hild, and S. Roux, "Mechanics-aided digital image correlation," *The Journal of Strain Analysis for Engineering Design*, vol. 48, no. 5, pp. 330–343, 2013.

[63] P. Franciosi, M. Spagnuolo, and O. U. Salman, "Mean green operators of deformable fiber networks embedded in a compliant matrix and property estimates," *Continuum Mechanics and Thermodynamics*, vol. 31, no. 1, pp. 101–132, 2019.

[64] M. Spagnuolo, P. Franciosi, and F. dell'Isola, "A green operator-based elastic modeling for two-phase pantographic-inspired bi-continuous materials," *submitted to International Journal of Solids and Structures*, vol. xx, 2019.

[65] R. Christensen and F. Waals, "Effective stiffness of randomly oriented fibre composites," *Journal of Composite Materials*, vol. 6, no. 4, pp. 518–532, 1972.

[66] S. Boucher, "On the effective moduli of isotropic two-phase elastic composites," *Journal of Composite Materials*, vol. 8, no. 1, pp. 82–89, 1974.

[67] R. Christensen, "Isotropic properties of platelet-reinforced media," *Journal of Engineering Materials and Technology*, vol. 101, no. 3, pp. 299–303, 1979.

[68] P. Franciosi and A. El Omri, "Effective properties of fiber and platelet systems and related phase arrangements in n-phase heterogenous media," *Mechanics Research Communications*, vol. 38, no. 1, pp. 38–44, 2011.

[69] H. Veenstra, P. C. Verkooijen, B. J. van Lent, J. van Dam, A. P. de Boer, and A. P. H. Nijhof, "On the mechanical properties of co-continuous polymer blends: experimental and modelling," *Polymer*, vol. 41, no. 5, pp. 1817–1826, 2000.

[70] J. H. Kinney, J. S. Stölken, T. Smith, J. T. Ryaby, and N. E. Lane, "An orientation distribution function for trabecular bone," *Bone*, vol. 36, no. 2, pp. 193–201, 2005.

[71] T. Clyne, A. Markaki, and J. Tan, "Mechanical and magnetic properties of metal fibre networks, with and without a polymeric matrix," *Composites Science and Technology*, vol. 65, no. 15-16, pp. 2492–2499, 2005.

[72] M. Agoras, O. Lopez-Pamies, and P. P. Castañeda, "Onset of macroscopic instabilities in fiber-reinforced elastomers at finite strain," *Journal of the Mechanics and Physics of Solids*, vol. 57, no. 11, pp. 1828–1850, 2009.

[73] T. Rangelov, G. Manolis, and P. Dineva, "Elastodynamic fundamental solutions for certain families of 2d inhomogeneous anisotropic domains: basic derivations," *European Journal of Mechanics-A/Solids*, vol. 24, no. 5, pp. 820–836, 2005.

[74] A. El Omri, A. Fennan, F. Sidoroff, and A. Hihi, "Elastic-plastic homogenization for layered composites," *European Journal of Mechanics-A/Solids*, vol. 19, no. 4, pp. 585–601, 2000.

[75] P. P. Castañeda and J. R. Willis, "The effect of spatial distribution on the effective behavior of composite materials and cracked media," *Journal of the Mechanics and Physics of Solids*, vol. 43, no. 12, pp. 1919–1951, 1995.

[76] J. D. Eshelby, "The determination of the elastic field of an ellipsoidal inclusion, and related problems," *Proceedings of the Royal Society of London. Series A. Mathematical and Physical Sciences*, vol. 241, no. 1226, pp. 376–396, 1957.

[77] M. Berveiller, O. Fassi-Fehri, and A. Hihi, "The problem of two plastic and heterogeneous inclusions in an anisotropic medium," *International Journal of Engineering Science*, vol. 25, no. 6, pp. 691–709, 1987.

[78] J. Willis, "Interfacial stresses induced by arbitrary loading of dissimilar elastic half-spaces joined over a circular region," *IMA Journal of Applied Mathematics*, vol. 7, no. 2, pp. 179–197, 1971.

[79] L. Walpole, "Elastic behavior of composite materials: theoretical foundations," in *Advances in applied mechanics*. Elsevier, 1981, vol. 21, pp. 169–242.

[80] E. Kröner, "Modified green functions in the theory of heterogeneous and/or anisotropic linearly elastic media," in *Micromechanics and inhomogeneity*. Springer, 1990, pp. 197–211.

[81] M. Bornert, C. Stolz, and A. Zaoui, "Morphologically representative pattern-based bounding in elasticity," *Journal of the Mechanics and Physics of Solids*, vol. 44, no. 3, pp. 307–331, 1996.

[82] V. Buryachenko, "Multiparticle effective field and related methods in micromechanics of composite materials," *Applied Mechanics Reviews*, vol. 54, no. 1, pp. 1–47, 2001.

[83] A. G. Ramm and A. I. Katsevich, *The Radon transform and local tomography*. CRC press, 1996.

[84] P. Franciosi, "On the modified green operator integral for polygonal, polyhedral and other non-ellipsoidal inclusions," *International Journal of Solids and Structures*, vol. 42, no. 11-12, pp. 3509–3531, 2005.

[85] ——, "A decomposition method for obtaining global mean green operators of inclusions patterns. application to parallel infinite beams in at least transversally isotropic media," *International Journal of Solids and Structures*, vol. 147, pp. 1–19, 2018.

[86] ——, "The boundary-due terms in the green operator of inclusion patterns from distant to contact and to connected situations using radon transforms: illustration for spheroid alignments in isotropic media," *International Journal of Solids and Structures*, vol. 47, no. 2, pp. 304–319, 2010.

[87] ——, "Mean and axial green and eshelby tensors for an inclusion with finite cylindrical 3d shape," *Mechanics Research Communications*, vol. 59, pp. 26–36, 2014.

[88] P. Franciosi, S. Barboura, and Y. Charles, "Analytical mean green operators/eshelby tensors for patterns of coaxial finite long or flat cylinders in isotropic matrices," *International Journal of Solids and Structures*, vol. 66, pp. 1–19, 2015.

[89] P. Franciosi, "Laminate system schemes for effective property estimates of architectured composites with co-(dis) continuous phases," *Mechanics Research Communications*, vol. 45, pp. 70–76, 2012.

[90] ——, "Transversally isotropic magneto-electro-elastic composites with co-(dis) continuous phases," *International Journal of Solids and Structures*, vol. 50, no. 6, pp. 1013–1031, 2013.

[91] P. Franciosi and Y. Charles, "Effective property estimates for n-phase composites with from all to none co-continuous phases," *International Journal of Solids and Structures*, vol. 96, pp. 110–125, 2016.

[92] G. Postma, "Wave propagation in a stratified medium," *Geophysics*, vol. 20, no. 4, pp. 780–806, 1955.

[93] W. Voigt, "Ueber die beziehung zwischen den beiden elasticitätsconstanten isotroper körper," *Annalen der physik*, vol. 274, no. 12, pp. 573–587, 1889.

[94] A. Reuss, "Account of the liquid limit of mixed crystals on the basis of the plasticity condition for single crystal," *Z. Angew. Math. Mech*, vol. 9, pp. 49–58, 1929.

[95] Z. Hashin and S. Shtrikman, "A variational approach to the theory of the elastic behaviour of multiphase materials," *Journal of the Mechanics and Physics of Solids*, vol. 11, no. 2, pp. 127–140, 1963.

[96] M. De Angelo, M. Spagnuolo, F. Dannibale, A. Pfaff, K. Hoschke, A. Misra, C. Dupuy, P. Peyre, J. Dirrenberger, and M. Pawlikowski, "The macroscopic behavior of pantographic sheets depends mainly on their microstructure: experimental evidence and qualitative analysis of damage in metallic specimens," *Continuum Mechanics and Thermodynamics*, pp. 1–23, 2019.

[97] E. Turco, F. dell'Isola, N. Rizzi, R. Grygoruk, W. Müller, and C. Liebold, "Fiber rupture in sheared planar pantographic sheets: Numerical and experimental evidence," *Mechanics Research Communications*, vol. 76, pp. 86–90, 2016.

[98] G. Ganzosch, F. dell'Isola, e. Turco, T. Lekszycki, and W. Müller, "Shearing tests applied to pantographic structures," *Acta Polytechnica CTU Proceedings*, vol. 7, pp. 1–6, 2016.

[99] S. R. Eugster and C. Glocker, "Constraints in structural and rigid body mechanics: a frictional contact problem," *Annals of solid and structural mechanics*, vol. 5, no. 1-2, pp. 1–13, 2013.

[100] R. Ogden, *Non-linear elastic deformations*. Courier Corporation, 1997.

[101] J. Čapek, M. Machova, M. Fousova, J. Kubásek, D. Vojtěch, J. Fojt, E. Jablonska, J. Lipov, and T. Ruml, "Highly porous, low elastic modulus 316l stainless steel scaffold prepared by selective laser melting," *Materials Science and Engineering: C*, vol. 69, pp. 631–639, 2016.

[102] A. Haboudou, P. Peyre, and A. Vannes, "Study of keyhole and melt pool oscillations in dual beam welding of aluminum alloys: effect on porosity formation," in *First International Symposium on High-Power Laser Macroprocessing*, vol. 4831. International Society for Optics and Photonics, 2003, pp. 295–301.

[103] O. Andreau, I. Koutiri, P. Peyre, J.-D. Penot, N. Saintier, E. Pessard, T. De Terris, C. Dupuy, and T. Baudin, "Texture control of 316l parts by modulation of the melt pool morphology in selective laser melting," *Journal of Materials Processing Technology*, vol. 264, pp. 21–31, 2019.

[104] C. Geuzaine and J.-F. Remacle, "Gmsh: A 3-D finite element mesh generator with built-in pre- and post-processing facilities," *International Journal for Numerical Methods in Engineering*, vol. 79, no. 11, pp. 1309–1331, 2009.

[105] E. Turco, A. Misra, M. Pawlikowski, F. dell'Isola, and F. Hild, "Enhanced piola-hencky discrete models for pantographic sheets with pivots without deformation energy: numerics and experiments," no. submitted for publication, 2018.